Correction of scattered radiation in multi-energy radiography and tomography

Artur Sossin

N°d'ordre NNT : 2016LYSEI104

THESE de DOCTORAT DE L'UNIVERSITE DE LYON
opérée au sein de
Laboratoire détecteurs (CEA/LETI)

Ecole Doctorale N° 160
Électronique, Électrotechnique, Automatique (EEA)

Spécialité de doctorat : Traitement du Signal et de l'Image

Soutenue publiquement le 24/10/2016, par :
Artur SOSSIN
(M.Sc.)

Correction of scattered radiation in multi-energy radiography and tomography

---

Devant le jury composé de :

L. DESBAT	Professeur (Univ. Joseph Fourier)	Président
A. MOHAMMAD-DJAFARI	Directeur de Recherche (LSS-CNRS)	Rapporteur
C. MOREL	Professeur (Aix Marseille Univ.)	Rapporteur
G. POLUDNIOWSKI	Chercheur (Hôpital univ. Karolinska)	Rapporteur
V. REBUFFEL	Ingénieur Chercheur (CEA LETI)	Examinatrice
J. M. LETANG	Maître de Conférences (INSA Lyon)	Directeur de thèse
J. TABARY	Ingénieur Chercheur (CEA LETI)	Invité

Département FEDORA – INSA Lyon - Ecoles Doctorales – Quinquennal 2016-2020

SIGLE	ECOLE DOCTORALE	NOM ET COORDONNEES DU RESPONSABLE
CHIMIE	**CHIMIE DE LYON** **http://www.edchimie-lyon.fr** Sec : Renée EL MELHEM Bat Blaise Pascal 3e étage secretariat@edchimie-lyon.fr Insa : R. GOURDON	M. Stéphane DANIELE Institut de Recherches sur la Catalyse et l'Environnement de Lyon IRCELYON-UMR 5256 Équipe CDFA 2 avenue Albert Einstein 69626 Villeurbanne cedex directeur@edchimie-lyon.fr
E.E.A.	**ELECTRONIQUE, ELECTROTECHNIQUE, AUTOMATIQUE** **http://edeea.ec-lyon.fr** Sec : M.C. HAVGOUDOUKIAN Ecole-Doctorale.eea@ec-lyon.fr	M. Gérard SCORLETTI Ecole Centrale de Lyon 36 avenue Guy de Collongue 69134 ECULLY Tél : 04.72.18 60.97 Fax : 04 78 43 37 17 Gerard.scorletti@ec-lyon.fr
E2M2	**EVOLUTION, ECOSYSTEME, MICROBIOLOGIE, MODELISATION** **http://e2m2.universite-lyon.fr** Sec : Safia AIT CHALAL Bat Darwin - UCB Lyon 1 04.72.43.28.91 Insa : H. CHARLES Safia.ait-chalal@univ-lyon1.fr	Mme Gudrun BORNETTE CNRS UMR 5023 LEHNA Université Claude Bernard Lyon 1 Bât Forel 43 bd du 11 novembre 1918 69622 VILLEURBANNE Cédex Tél : 06.07.53.89.13 e2m2@univ-lyon1.fr
EDISS	**INTERDISCIPLINAIRE SCIENCES-SANTE** **http://www.ediss-lyon.fr** Sec : Safia AIT CHALAL Hôpital Louis Pradel - Bron 04 72 68 49 09 Insa : M. LAGARDE Safia.ait-chalal@univ-lyon1.fr	Mme Emmanuelle CANET-SOULAS INSERM U1060, CarMeN lab, Univ. Lyon 1 Bâtiment IMBL 11 avenue Jean Capelle INSA de Lyon 696621 Villeurbanne Tél : 04.72.68.49.09 Fax :04 72 68 49 16 Emmanuelle.canet@univ-lyon1.fr
INFOMATHS	**INFORMATIQUE ET MATHEMATIQUES** **http://infomaths.univ-lyon1.fr** Sec :Renée EL MELHEM Bat Blaise Pascal 3e etage infomaths@univ-lyon1.fr	Mme Sylvie CALABRETTO LIRIS – INSA de Lyon Bat Blaise Pascal 7 avenue Jean Capelle 69622 VILLEURBANNE Cedex Tél : 04.72. 43. 80. 46 Fax 04 72 43 16 87 Sylvie.calabretto@insa-lyon.fr
Matériaux	**MATERIAUX DE LYON** **http://ed34.universite-lyon.fr** Sec : M. LABOUNE PM : 71.70 –Fax : 87.12 Bat. Saint Exupéry Ed.materiaux@insa-lyon.fr	M. Jean-Yves BUFFIERE INSA de Lyon MATEIS Bâtiment Saint Exupéry 7 avenue Jean Capelle 69621 VILLEURBANNE Cedex Tél : 04.72.43 71.70 Fax 04 72 43 85 28 Ed.materiaux@insa-lyon.fr
MEGA	**MECANIQUE, ENERGETIQUE, GENIE CIVIL, ACOUSTIQUE** **http://mega.universite-lyon.fr** Sec : M. LABOUNE PM : 71.70 –Fax : 87.12 Bat. Saint Exupéry mega@insa-lyon.fr	M. Philippe BOISSE INSA de Lyon Laboratoire LAMCOS Bâtiment Jacquard 25 bis avenue Jean Capelle 69621 VILLEURBANNE Cedex Tél : 04.72 .43.71.70 Fax : 04 72 43 72 37 Philippe.boisse@insa-lyon.fr
ScSo	**ScSo*** **http://recherche.univ-lyon2.fr/scso/** Sec : Viviane POLSINELLI Brigitte DUBOIS Insa : J.Y. TOUSSAINT viviane.polsinelli@univ-lyon2.fr	Mme Isabelle VON BUELTZINGLOEWEN Université Lyon 2 86 rue Pasteur 69365 LYON Cedex 07 Tél : 04.78.77.23.86 Fax : 04.37.28.04.48

*ScSo : Histoire, Géographie, Aménagement, Urbanisme, Archéologie, Science politique, Sociologie, Anthropologie

Abstract

X-ray imaging coupled with recently emerged energy-resolved photon counting detectors provides the ability to differentiate material components and to estimate their respective thicknesses. However, such techniques require highly accurate images. The presence of scattered radiation leads to a loss of spatial contrast and, more importantly, a bias in radiographic material imaging and computed tomography (CT). Additionally, artifacts are also introduced in the case of the latter. The main aim of the present thesis was to develop a scatter correction approach adapted for multi-energy imaging. In order to achieve this task, a secondary objective was also set. Namely, the conception and validation of a simulation tool capable of providing energy-resolved scatter simulations in a reasonable time. Once validated through simulations and experimentally, this tool gave the ability to study the behavior of scattered radiation both in spatial and energy domains. Based on the conducted scatter analysis, a Partial Attenuation Spectral Scatter Separation Approach (PASSSA) adapted for multi-energy imaging was developed. The evaluation of PASSSA in radiographic mode through simulations and experiments revealed noteworthy results both in terms of image contrast improvement and scatter induced bias reduction. Additionally, simulation studies examined the performance of the developed approach in CT, where PASSSA also proved to be quite effective at correcting scatter induced distortions. Moreover, the performance improvement in the context of basis material decomposition in radiography after applying the designed method was also analyzed. It was concluded that the application of PASSSA results in a substantial improvement in basis material thickness estimation. Finally, based on the obtained simulated and experimental method evaluation results an analysis of perspective developments was also conducted.

Résumé

L'imagerie à rayons X couplée aux détecteurs résolus en énergie permet de différencier les matériaux présents et d'estimer leurs contributions respectives. Cependant, ces techniques nécessitent des images très précises. La présence du rayonnement diffusé conduit à une perte du contraste spatial et un biais dans l'imagerie radiographique ainsi que des artefacts dans la tomodensitométrie (TDM). L'objectif principal de cette thèse était de développer une approche de correction du rayonnement diffusé adaptée à l'imagerie multi-énergies. Pour réaliser cette tâche, un objectif secondaire a été défini : la conception et la validation d'un outil de simulation capable de fournir des images du diffusé résolu en énergie dans un temps raisonnable. Une fois validé, cet outil a permis d'étudier le comportement du diffusé dans le domaine spatial et énergétique. Sur la base de cette analyse du diffusé, une approche originale dite « Partial Attenuation Spectral Scatter Spectral Aproach » (PASSSA) adaptée à l'imagerie multi-énergies a été développée. L'évaluation de PASSSA en mode radiographique par des simulations numériques et des mesures expérimentales a révélé des résultats remarquables en termes d'amélioration du contraste d'image et de la réduction du biais induit par la présence du diffusé. De plus, des études de simulation ont permis d'évaluer la performance de l'approche développée dans la TDM, où PASSSA s'est révélée d'être très efficace pour corriger les distorsions induites par le rayonnement diffusé. D'autre part, l'amélioration de la performance dans le contexte de la décomposition des matériaux de base en radiographie après avoir appliqué la méthode développée a également été analysée : l'application de PASSSA se traduit par une amélioration substantielle de l'estimation des épaisseurs des matériaux de base. Finalement, sur la base des différents résultats de validation obtenus, une analyse des développements potentiels a été menée.

LIST OF SYMBOLS

0	Index denoting raw (no inspected object) quantities
a	Index denoting attenuator related quantities
A	True attenuation
A_m	Measured attenuation
$\mathbf{A}$	True attenuation (function of energy)
$\mathbf{A_m}$	Measured attenuation (function of energy)
b	Basis material index / diagonal matrix linked to **B**
$\mathbf{B}$	Attenuation matrix
c	Speed of light in vacuum
$\mathbf{C}$	2D discrete cosine transform
d	Exponent denoting detected quantities / grid element spacing
$D(E)$	Detector efficiency
$\mathbf{D}$	Detector response matrix
e	Electron charge
E	(Incident) X-ray photon energy / Energy channel
E'	Scattered x-ray photon energy
E_{kin}	Kinetic energy
$\mathbf{E}$	Vector of median detector bin energies
f	Particle fraction
$F(x, Z)$	Atomic form factor
$\mathbf{F}$	Scatter energy component (function of energy)
g	Scatter spatial component
$f(E,E^*,\sigma,\alpha,\beta)$	Parametric function with free parameters σ, α and β
h	Planck constant / grid strip height
$h(\bullet)$	Filter function
H	Indicator function
HU	Index for quantities measured in Hounsfield units
I	Signal intensity
$\boldsymbol{I}$	Identity matrix
k	Calibration pair index / smoothing parameter
$K(u)$	Scatter kernel
l	Material thickness / particle path length
m	Exponent denoting modified quantities
m_0	Electron rest-mass
$\mathbf{M}$	Transition matrix
n	Number of elements (e.g. materials, pixels, etc.)
N	Number of x-ray photons
$\mathbf{N}$	Number of x-ray photons (function of energy)
$NRMSE$	Normalized root-mean-square error
$\mathbf{p}$	Pixel with coordinates (x, y)
P	Index denoting primary quantities / scattering source point
$P_\varphi\{\bullet\}$	Multiple-angle projection acquisition operation
q	Object material index
$R\{\bullet\}$	Reconstruction operation / roughness quantifying operator

r	Relative noise per pixel
r_0	Classical electron radius
r_G	Grid ratio
s	Smoothing parameter
S	Index denoting scatter quantities / detector node point
$S(s,u,\varphi)$	Sinogram
$S(x, Z)$	Incoherent scatter function
SPR	Scatter-to-primary ratio
SPR	Scatter-to-primary ratio as a function of energy
t	Grid strip thickness
$T\{\bullet\}$	Scatter estimation operation
U_a	Accelerating potential
U	Image sub-region
v	Voxel with coordinates (x, y, z)
V	3D attenuation map (volume) of the object / voxel value
W	Diagonal matrix linked to **M**
x	Momentum transfer quantity
z	Scatter spatial component (sparse)
Z	Atomic number
$\mathrm{d}x$	Elementary material thickness
$\mathrm{d}\sigma/\mathrm{d}\Omega$	Differential cross-section
ΔN	Number of photon difference (function of energy)
ε_r	Average relative error per pixel
θ	Scattering angle
λ	(Incident) X-ray photon wave length
λ'	Scattered x-ray photon wave length
Λ	Diagonal matrix containing the eigenvalues of R
μ	Linear attenuation coefficient
ν	X-ray photon frequency
$\xi(\bullet)$	Scatter potential
φ	Projection angle
Ω	Solid angle / entire image region
σ	Total cross-section / standard deviation
σ	Standard deviation (function of energy)
$\boldsymbol{\sigma}_\mathbf{r}$	Relative standard deviation (function of energy)
τ_{photo}	Probability of the photoelectric effect

LIST OF ACRONYMS

ADD	Axis-to-detector distance
AP	Anteroposterior
ASG	Anti-scatter grid
BS	Beam-stop
BH	Beam-hole
CNR	Contrast-to-noise ratio
CBCT	Cone beam Computed Tomography
CPU	Central processing unit
CT	Computed Tomography
CR	Computed Radiography
CSG	Constructive solid geometry
DCT	Discrete cosine transform
DR	Digital Radiography
FDK	Feldkamp-Davis-Kress
GCV	Generalized cross-validation
GPU	Graphics Processing Unit
HE	High-energy
HU	Hounsfield Unit
LE	Low-energy
NDT	Non-destructive testing
MC	Monte Carlo
NRMSE	Normalized root-mean-square error
ODD	Object-to-detector distance
PASSSA	Partial Attenuation Spectral Scatter Separation Approach
PCD	Photon counting detector
PM	Primary modulation
PMMA	Polymethyl methacrylate
NRMSE	Relative standard deviation
SAD	Source-to-rotation axis distance
SFFD	Spectral Fixed Forced Detection
SDD	Source-to-detector distance
SK	Scatter kernel
SNR	Signal-to-noise ratio
SPR	Scatter-to-primary ratio
STD	Standard deviation
TFT	Thin film transistor
VOI	Volume of interest

TABLE OF CONTENTS

1. INTRODUCTION

Since the discovery of x-rays by Röntgen in 1895, numerous applications for x-ray imaging have surfaced, ranging from medical diagnostic to security and industrial sample testing. Significant advances can be observed in the design of various x-ray system components such as tubes, generators, detectors, collimators, computed tomography (CT) gantries, signal processing algorithms, etc.

In the last few decades several important changes in x-ray detection technology have occurred. In particular, in the beginning of the 1990s, the analog film detection has been replaced by the so-called "semi-digital" technique known as Computed Radiography (CR). The idea was based on the utilization of photo-stimulable phosphor plates, which were processed after exposure by a reader. [1]. Then, in early XXIst century, fully digital x-ray detection technology, known as Digital Radiography (DR), has been introduced. These types of detectors converted x-rays into electrical signals after exposure either through indirect or direct conversion. [2]. Both CR and DR contributed to the development of CT imaging and enabled the application of digital image processing techniques to the resulting x-ray images. These techniques enable image enhancement, restoration and the ability to perform image segmentation, as well as the development of automatic disease detection methods and etc. [3].

For the last few years, new digital x-ray detector capabilities have been investigated. For a given pixel, conventional x-ray detectors provide a signal proportional to the photon energy deposited into the detector element, integrated on the total energy range [2]. Recently emerged room temperature semiconductor photon counting detectors (PCDs) exhibit the ability to classify photons into several discrete energy channels, the number of which varies from a few bins (typically from 2 to 8) [4]–[6] to a hundred with a width of ~1 keV, depending on the electronic circuit [7], [8]. This new technology allows the development of energy-resolved imaging for all current x-ray applications. The supplemental energy information provides the ability to increase contrast-to-noise ratio (CNR) [9], reduce dose and artifacts [10]. Additionally, material components present in the object can be differentiated and their equivalent thicknesses and relative ratios (soft tissue, bone, glandular, contrast agent enhanced tissue, etc.) estimated by processing a single shot acquisition image in both radiography and CT [4], [10], [11]. In order to benefit from the material differentiation capability of multi-energy imaging, a high degree of image quality in the acquisitions is needed (low bias, low noise, absence of artifacts, etc.), especially for materials close in terms of attenuation.

Such an objective is difficult to achieve in the case of uncollimated geometries due to scattered radiation. It induces various undesirable effects in x-ray imaging such as bias, loss of contrast and artifacts in CT [12]. Additionally, this effect is object and geometry dependent [13]. Several studies have demonstrated the impact of x-ray scatter on multi-energy imaging applications [14]–[16].

A substantial number of methods have been developed for scatter correction using conventional detectors [17]. These approaches include direct methods, such as anti-scatter grids [18], increasing air gap [19] and additional collimation [20], methods based on nu-

merical modelling, such as Monte Carlo (MC) methods [21]–[23] and scatter kernels (SK) [24]–[26], physical measurement based methods, such as beam-stop (BS) [27]–[29], beam-hole (BH) [30], [31], primary modulation [32]–[34] and others [35], [36], and image post-processing methods [37]. Some of these techniques apply directly to multi-energy imaging (direct methods, physical measurement based methods) whilst others will suffer from an increase in model complexity and execution time (methods based on analytical modelling, image post-processing methods). It is important to note that the scatter correction methods applied for conventional x-ray detectors do not exploit the energy information. The evolution to relatively large size 2D energy-resolved PCDs gives more importance to the development of an x-ray scatter correction method adapted for multi-energy imaging.

The thesis includes two main objectives. The first one is the development of a simulation tool capable of performing multi-energy x-ray scatter simulations during a reasonable time, thus giving the opportunity to study the behavior of the phenomenon in more detail in the energy domain. The second and main goal of this work is to develop an x-ray scatter correction procedure adapted for multi-energy x-ray imaging and benefiting from the additional energy information provided by such technology.

The rest of the document is organized into seven chapters. Chapter 2 introduces the principles of x-ray generation, interaction with matter and detection. Then, x-ray scatter radiation is characterized and its effects demonstrated in conventional radiography and tomography as well as in material imaging (Chapter 3). The energy-resolved scatter simulation tool fulfilling the secondary goal of the thesis is presented in Chapter 4. The next chapter of the document (Chapter 5) introduces a subjective classification and examples of existing scatter correction schemes followed by an introduction of the developed novel multi-energy adapted scatter correction method. Chapter 6 evaluates the respective scatter correction approach through simulations and experiments. Based on these evaluations a series of method improvement propositions is also listed (Chapter 7). Finally, a conclusion is made and future work is discussed in Chapter 8.

2. PHYSICS OF X-RAY IMAGING

The production of x-ray images comprises several stages. Firstly, x-rays are generated by a corresponding device (Chapter 2.1). Then, various physical interactions occur within the inspected object contributing to local changes in x-ray flux (Chapter 2.2). Finally, an image receptor is used to detect these changes (Chapter 2.3) and various types of images are formed based on the measured signal (Chapter 2.4).

Chapter 2.1 investigates the physics behind x-ray generation and provides an overview of a common x-ray generation device with its key elements and parameters.

The behavior of x-ray photons in matter is examined in Chapter 2.2. Mathematical models for different physical interactions are presented and discussed. Finally, a demonstration of the net effect of these interactions on the x-ray flux is provided.

Chapter 2.3 highlights different technical solutions behind x-ray detection. Various detection modes with their virtues and drawbacks are discussed.

Finally, Chapter 2.4 provides information on key x-ray acquisition modes, such as radiography and CT. Image formation based on signals measured by different detector types is discussed and examples are given.

2.1. X-ray generation

X-rays are a form of electromagnetic radiation with a wavelength ranging from a few picometers to a few nanometers. The energy E of a given x-ray photon is proportional to its frequency ν, and can be characterized by the following formula:

$$E = h\nu = \frac{hc}{\lambda}, \tag{2.1}$$

where h is the Planck constant, c is the speed of light in vacuum and λ is the wavelength of the photon. From expression (2.1) it is apparent that higher and lower energy x-rays have a shorter and longer wavelength, respectively. The wavelength of diagnostic x-rays lies in the approximate interval of 0.1 nm to 0.01 nm, which corresponds to an energy range of about 12.4 keV to 124 keV [38].

X-ray photons are produced when a target material is struck by highly energetic electrons (kinetic energy is converted to electromagnetic radiation). During this event, most of the electron energy (>99%) is converted to heat when impinging on the target electrode. The remaining fraction is responsible for x-ray photon production through two different processes [38] that are discussed in more detail in Chapters 2.1.1 and 2.1.2.

The kinetic energy E_{kin} obtained by the electrons is equal to the product of the electron charge e and the accelerating potential U_a:

$$E_{kin} = eU_a. \tag{2.2}$$

The maximum possible energy of the generated x-ray photon is equal to the kinetic energy of the electron.

A device that fulfills the objective of x-ray generation consists of a source of electrons, an evacuated path for electron acceleration, a target electrode and an external energy supply to provide the necessary potential for electron acceleration [1] (Figure 2.1). This device is called an *x-ray tube* (Chapter 2.1.3).

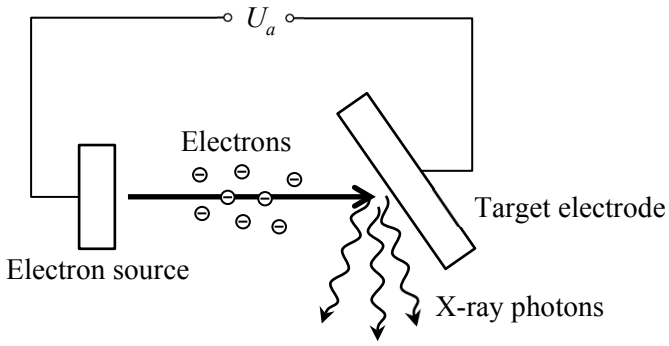

Figure 2.1. Schematic of an x-ray generation device.

2.1.1. Bremsstrahlung radiation

When an electron comes within close proximity of an atomic nucleus in the target electrode, Coulomb forces attract and decelerate the electron, causing a substantial loss of kinetic energy and a change in trajectory. This produces an x-ray photon with energy equal to the energy lost by the electron (Figure 2.2). This type of radiation is called *Bremsstrahlung*, which, when directly translated from German, means "braking radiation". [39].

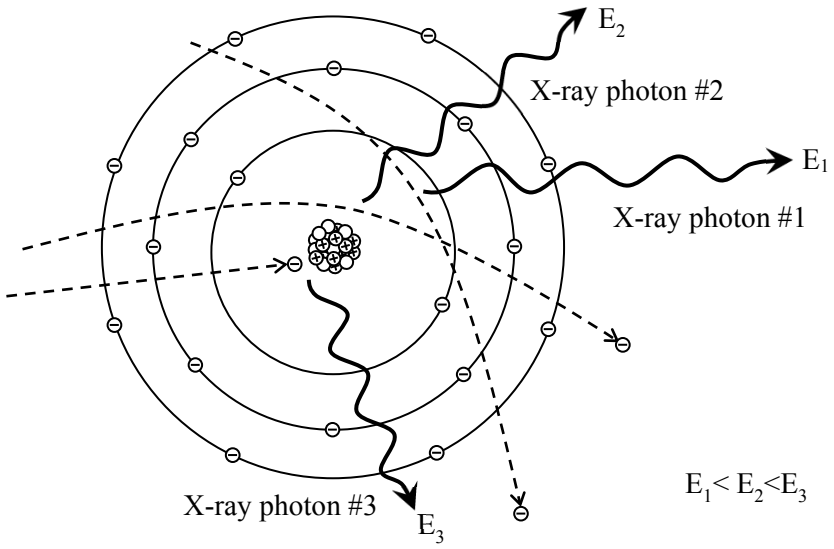

Figure 2.2. A schematic drawing of an atom of the target electrode depicting different cases of Bremsstrahlung x-ray photon production: far interaction (x-ray photon #1), close interaction (x-ray photon #2) and direct collision (x-ray photon #3).

Since Coulomb force is inversely proportional to the square of the interaction distance, the energy loss of the electron interacting with the nucleus is increased with decreasing distance. Thus, an electron passing within a longer range of the nucleus will produce a lower energy x-ray photon (x-ray photon #1 in Figure 2.2) compared to an electron passing

within shorter range (x-ray photon #2 in Figure 2.2). Additionally, in very rare cases, an electron will directly impact the nucleus, in which case all of its kinetic energy is lost and converted to an x-ray photon (x-ray photon #3 in Figure 2.2). The probability of such of an event is extremely low, since the nuclear cross-section is small compared to the size of the entire atom. Therefore, the dominant x-rays produced are low energy x-rays. The number of photons weighted by their respective energies (or *energy fluence*) decreases approximately linearly with energy up to the maximum energy of the impinging electrons [1].

The distribution of x-ray photons or energy fluence as a function of energy is called an *x-ray spectrum* (Figure 2.3). The main part is composed of Bremsstrahlung radition. According to equation (2.2), the maximum x-ray energy is determined by the acceleration voltage U_a. Due to self-absorption in the target material and due to energy dependent attenuation in the x-ray tube housing, the low energy x-ray photons undergo a stronger attenuation, thus the real energy fluence spectrum will deviate from the theoretical linear relationship discussed earlier [39].

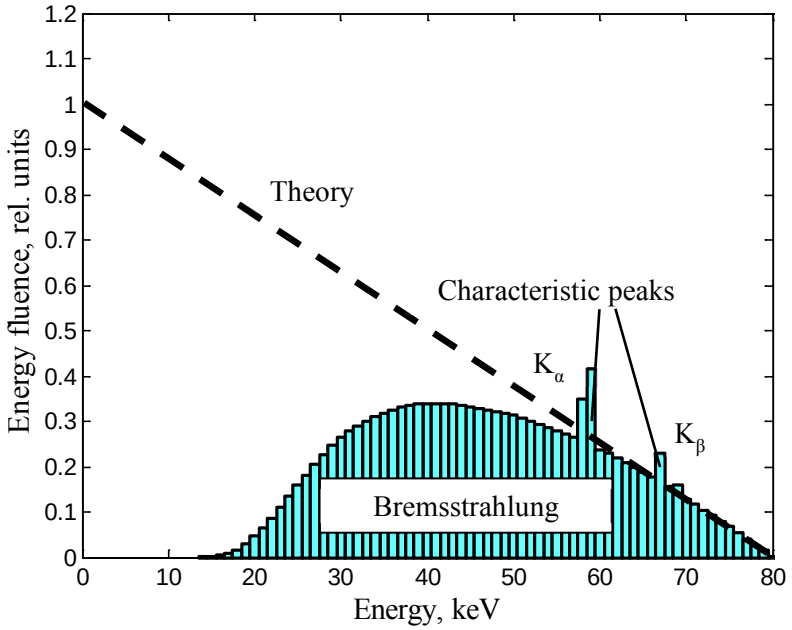

Figure 2.3. An example x-ray energy fluence spectrum produced with a tungsten anode x-ray tube (1 keV histogram bins). The acceleration voltage was set to 80 kV. The theoretical ramp spectrum is attenuated by the anode and tube housing. Energy fluence due to Bremsstrahlung photons is contained in the part of the spectrum under the dashed line while the peaks located on top of this line correspond to energy fluence due to characteristic x-ray photons, discussed in more detail in Chapter 2.1.2.

2.1.2. Characteristic x-rays

Compared to Bremsstrahlung radiation, which is produced through electron interaction with atomic nuclei of the target electrode, *characteristic radiation* (also known as *fluorescence*) is produced when the accelerated electrons interact with the atomic electrons of the target electrode (Figure 2.4a) [39]. Provided that the energy of an incident electron is greater that the binding energy of an electron of the target atom, a collision of the two electrons can eject the atomic electron and ionize the atom. The created vacancy gives rise to

an atomic shell transition. Since, in this case, the electron is transitioning to a lower energy level, the redundant energy can be transformed into a characteristic x-ray photon with energy equal to the difference in electron shell binding energies. [1].

The highest binding energy corresponds to the innermost K-shell and decreasing for other outer shells, such as L, M, N and etc. The binding energies and the characteristic radiation resulting from electron transitions from one shell to another are unique for each target electrode material. [39]. For example, for tungsten, a transition from the M-shell (2.5 keV) to the K-shell (69.5 keV) results in an emission of an x-ray photon with an energy of 67 keV. The simplified energy level diagram corresponding to a tungsten atom is presented in Figure 2.4b. Characteristic x-ray photons add to the Bremsstrahlung photons comprising the x-ray spectrum. Since only a few discrete energies are concerned, this additional fraction of photons manifests itself as peaks in the spectrum (Figure 2.3). These peaks are also called *characteristic peaks* [1].

Characteristic x-radiation is denoted with the shell letter (to which the electron transitions) and Greek indexes (α, β, etc.). The indexes indicate the origin of the transitioning electron in the atom, α – for the closest outer shell, β – for the next one and etc. [39]. Thus, for the example considered above, where a transition to the K-shell is made from the M-shell, the resulting characteristic x-ray will be denoted as K_β.

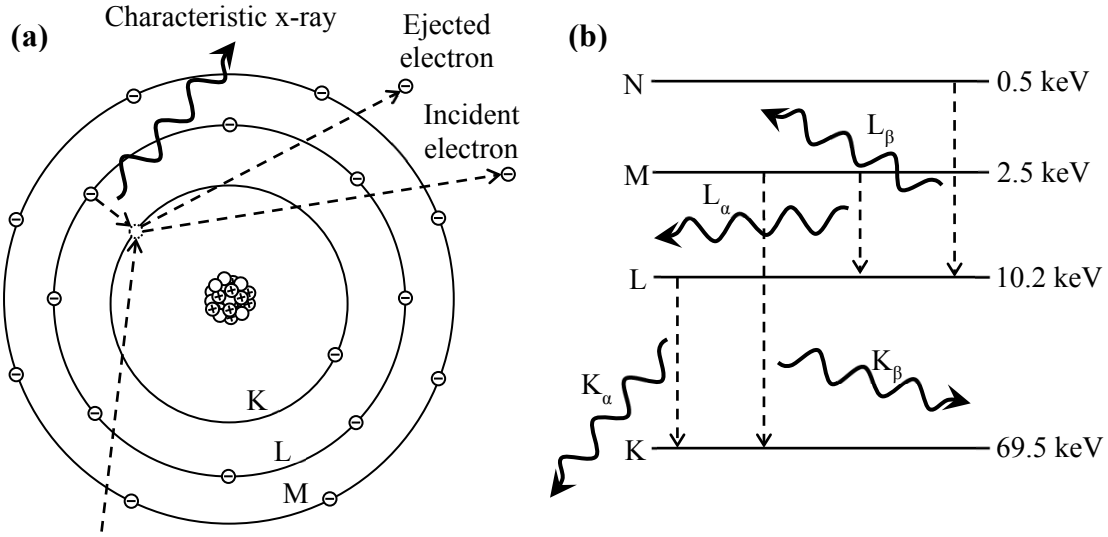

Figure 2.4. Schematic illustration of the production of a characteristic x-ray as a result of electron collision and transition (a). Simplified energy level diagram for K, L, M and N shells of a tungsten atom is also displayed (b). Note the various characteristic x-rays produced through different electron transitions.

It is also worth pointing out that reabsorption of Bremsstrahlung x-rays through an effect described later in Chapter 2.2.1 can also contribute to the production of characteristic peaks.

2.1.3. The x-ray tube

There are several solutions for an x-ray generation tube depicted in Figure 2.1. The most commonly used consists of a positively charged anode (target), a negatively charged

cathode, high voltage supply (electron acceleration), a motor for anode rotation and a glass envelope [1]. A detailed illustration can be found in Figure 2.5.

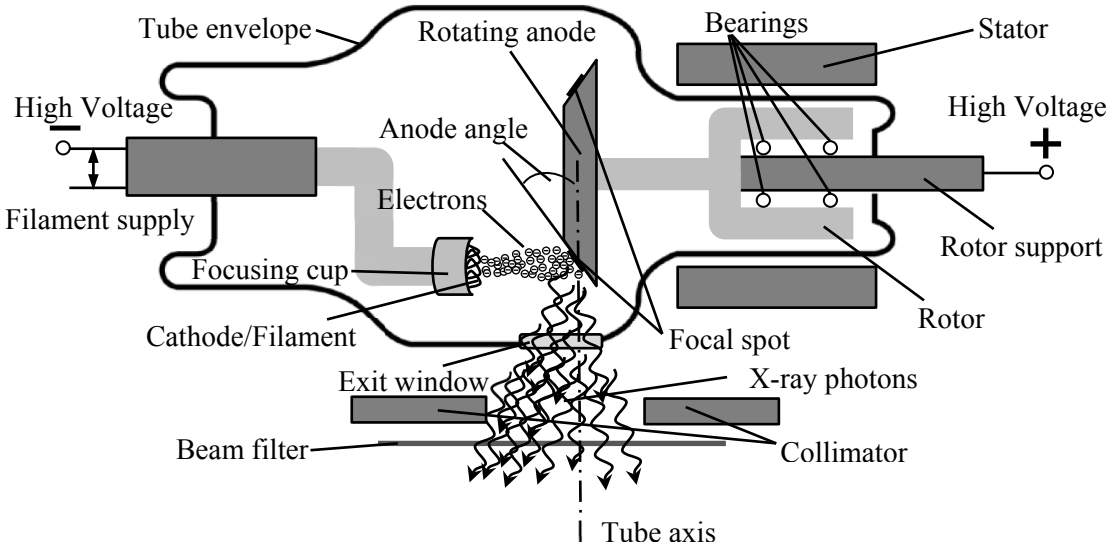

Figure 2.5. An illustration of an x-ray tube with a rotating anode, beam collimators and a beam filter.

The cathode is composed of a spiral tungsten filament surrounded by a focusing cup and acts as source of electrons for x-ray production. The filament is powered by a supply to ensure heating. Electrons are then released via a process called the thermionic emission. The high voltage applied between the cathode and anode ensures the acceleration of these electrons through the vacuum filled x-ray tube envelope. The focusing cup part of the cathode serves to shape the electron beam. The rate of electron flow from the cathode to the anode is called *tube current* and is measured in milliamperes (mA). The product of the tube current with the exposure time (in seconds) determines the amount of x-ray photons produced for a given examination. The respective product is measured in milliampere-seconds (mAs) [1].

As noted previously in the beginning of Chapter 2.1, electrons incident on the target anode deposit most of their energy in the form of heat, whilst only a small fraction is emitted as x-rays. As a result, when producing the amount of x-rays required for sufficient image quality, a large quantity of heat is generated. With its high melting point of 3422 °C and atomic number (Z), tungsten is the most commonly used anode material. The high Z is also an advantage as Bremsstrahlung production is proportional to Z. Other anode materials such as molybdenum and rhodium can be found in mammography tubes. The rotation of the anode disk by means of an induction motor insures the spreading of the impinging electron thermal energy over a large area of the disk, which is supported by a bearing-mounted rotor assembly. Thus, the rotation gives the possibility to apply higher tube currents. [39].

The *anode angle* is defined as the angle of the target electrode surface with respect to the tube axis. For diagnostic x-ray tubes, the anode angle usually ranges from 6° to 22°, with the most common being 10°–16°. [39].

The *focal spot* can be defined in two ways. The actual focal spot is the area of the anode electrode struck by the electrons. It is mostly determined by cathode filament length and focusing cup slot width. The effective focal spot is the length and width of the actual

focal spot when projected down the tube x-axis on the x-ray field. When projected, the actual focal spot will conserve the size of one of its sides while the other will decrease due to the anode angle. Note that for transmission-target tubes the electron beam spot is the true focal spot [40].

It is worth also noting that due to the anode being at an angle the x-ray photons directed toward the cathode side of the field traverse less anode material and thus experience less attenuation than those directed to the cathode side. As a result the x-ray intensity gradually increases towards the cathode side. The effect is called *heel effect* and is less prominent at larger source-to-detector distances (SDDs), because the detector views a narrower x-ray beam angle. [1].

Finally, *collimation* and *filtration* is used exterior to the x-ray tube, to shape the x-ray field spatially and spectrally. Collimator blades, typically made of lead, with electronically controlled positioning insure the desired field size. Bow-tie filtration can also be used to provide a specific (to an examined object) non-uniformity of the x-ray beam. Since the contribution of low energy photons to the measured signal is often low due to a relatively high attenuation probability in the material of the imaged object (Chapter 2.2.4), which in turn leads to additional dose, a sheet of material (typically copper or aluminum) is often inserted to insure the attenuation of these type of photons. [40].

2.2. Interaction of x-rays with matter

X-rays interact with matter through various processes, which can lead to changes in photon direction and energy or even its complete absorption. Since some of these interactions cause atom ionization, x-ray radiation is considered ionizing. This leads to its harmful effects on biological tissues. The main interactions processes relevant in diagnostic x-ray imaging are *photoelectric effect* (Chapter 2.2.1), *Rayleigh scattering* (Chapter 2.2.2) and *Compton scattering* (Chapter 2.2.3). The combination of these effects leads to the reduction of x-ray beam intensity when traversing a material. This intensity change is called *x-ray attenuation* (Chapter 2.2.4).

2.2.1. Photoelectric effect

When an incident x-ray photon with energy greater than the binding energy of an electron liberates that electron from the corresponding shell via energy transfer, a vacancy is created. This process is called photoelectric effect (Figure 2.6). The kinetic energy of the ejected electron is then equal to the difference between the photon energy and binding energy. The resulting vacancy is then filled by an outer-shell electron. This causes (as noted earlier in Chapter 2.1.2) an emission of a characteristic x-ray photon with energy equal to the difference between the binding energies of the two shells. Sometimes, the energy originating from the vacancy filling is transferred to another electron, which is ejected from the atom, instead of being emitted in the form of an x-ray photon. This second ejected electron is called an *Auger electron*. [38].

The probability of the photoelectric effect of a given material (τ_{photo}) in the diagnostic energy range can be described by the following expression:

$$\tau_{photo} \propto \frac{Z^{3\,to\,4}}{E^3}, \tag{2.3}$$

where Z is the atomic number of the material, E is the x-ray photon energy [39]. Thus, for a fixed energy, the probability of x-ray absorption through photoelectric effect increases with Z. Furthermore, for a given material the probability decreases with energy.

The elements comprising biological tissue are mostly low-Z materials, such as carbon (Z=6), hydrogen (Z=1), oxygen (Z=8) and nitrogen (Z=7). Since the K-shell binding energy is in the interval of 0.5–4 keV for these elements and the fluorescence yield is almost 0%, the characteristic x-rays become very unlikely [38]. However, when metallic implants are present in the patient, characteristic x-rays can exhibit higher energies. For example, tantalum, which is often used as metallic implant coating material [41], has a K-shell binding energy of 67.4 keV and a L-shell binding energy of 11.7 keV. In this case, the transition from L to K-shell results in the emission of a 55.7 keV x-ray photon.

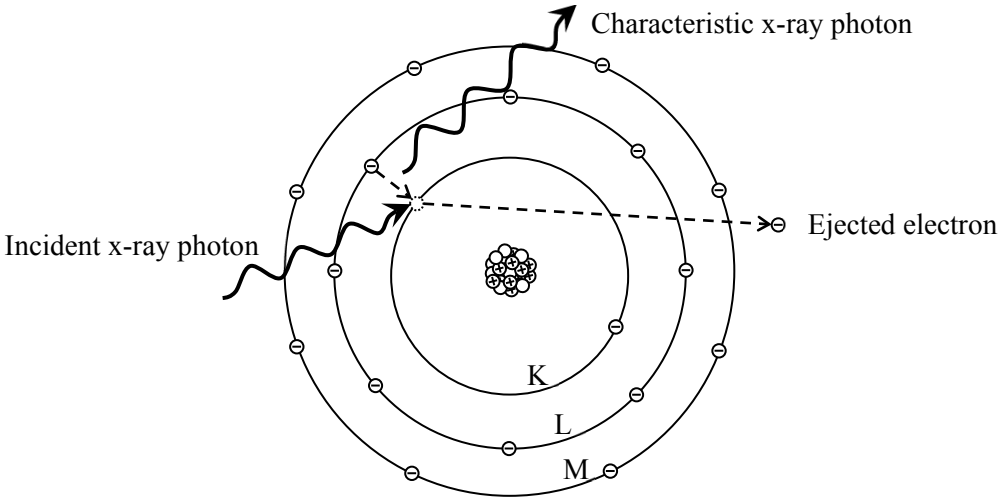

Figure 2.6. An example of the photoelectric effect. An absorbed x-ray photon causes the ejection of a K-shell electron, which leads to an electron from the L-shell to fill the vacancy. As a result a K_α characteristic x-ray is emitted.

2.2.2. Rayleigh scattering

In the process of Rayleigh scattering the x-ray photon interacts with the atom and changes direction while conserving energy (Figure 2.7a). The electrons in the atom are set into momentary vibration by the oscillating electric field of the electromagnetic wave associated with the incident photon. The vibrating electrons emit radiation of the same wavelength as the incident x-ray. A combination of these waves forms the scattered wave. Because of this, Rayleigh scattering is also known as *coherent scattering*. During this process the scattered x-ray obtains the same energy as the incident one as no energy is converted to kinetic energy or transferred to the medium. [38]. Thus, since the incident x-ray photon energy E is equal to the scattered photon energy E', then, according to (2.1), so are their wavelengths (i.e. $\lambda=\lambda'$).

In order to derive the expression for angular Rayleigh scatter probability, one starts with the expression of angular *Thompson scattering* probability, $d\sigma_{Th}/d\Omega$:

$$\frac{d\sigma_{Th}}{d\Omega} = \frac{r_0^2}{2}\left(1+\cos^2\theta\right), \tag{2.4}$$

where r_0 is the classical electron radius and θ is the scattering angle with respect to the incident photon direction. The quantity $d\sigma_{Th}/d\Omega$ is also known as the *differential Thompson cross-section*. Thompson scattering considers the case of a photon scattered through the interaction with a free electron. [39].

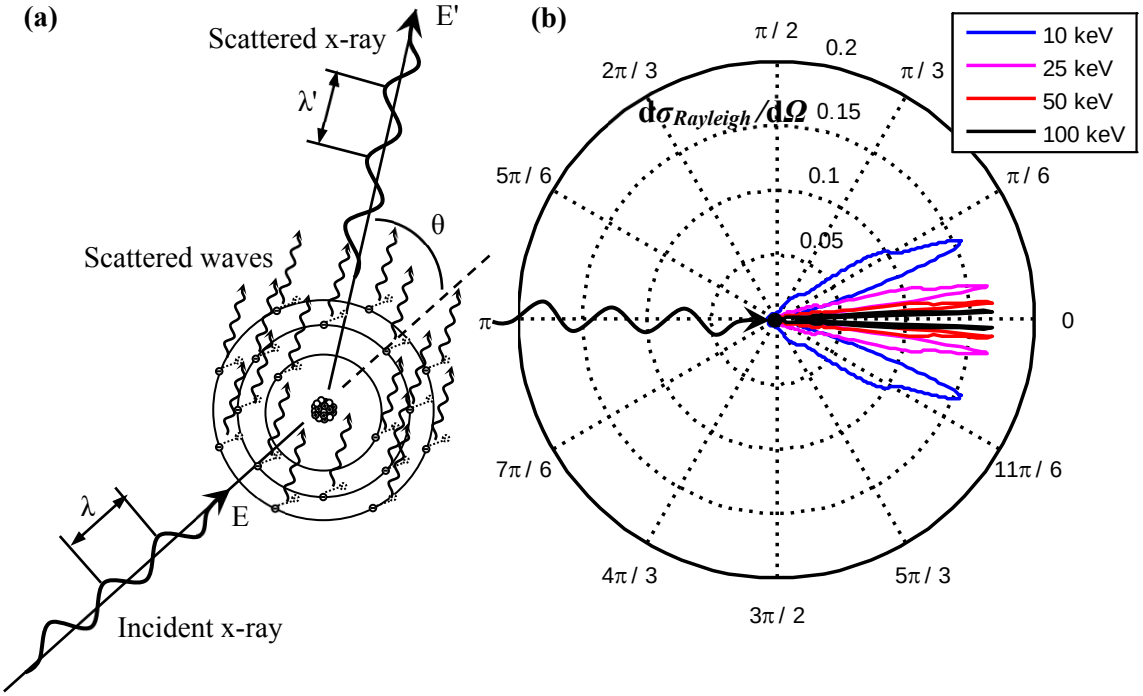

Figure 2.7. Illustration of coherent (Rayleigh) scattering (a). Incident x-ray photon energy is denoted with E and λ, respectively. The same notation is used for the scattered photon with the addition of the "prime" symbol. The scattering angle is marked with θ. In (b) a polar plot of the angular Rayleigh scattering probabilities for a water molecule at room temperature as function of scattering angle θ is presented. Note that different photon energies are also considered in (b).

Since for Rayleigh scattering an entire atom with bound electrons is considered, (2.4) must be weighted by $F(x, Z)$, a quantity known as the *atomic form factor*. This quantity takes into account the binding energies of the electrons as well as the atom configuration. Expression (2.4) thus becomes:

$$\frac{d\sigma_{Rayleigh}}{d\Omega} = \frac{d\sigma_{Th}}{d\Omega} F^2(x,Z), \tag{2.5}$$

where $d\sigma_{Rayleigh}/d\Omega$ is the angular Rayleigh scattering probability (*differential Rayleigh cross-section*), x is the momentum transfer quantity (x=sin(θ/2)/λ). Values of $F(x, Z)$ can be calculated with the aid of quantum mechanical models. [39]. Corresponding numerical tabulations also exist and can be found in [42]. For a small scattering angle θ, the value of the form factor approaches Z. In this case a collaborative action of all the electrons in the atom causes a strong forward direction for the scattering. Back-scatter is less probable, however, because F decreases with scattering angle as it becomes more difficult for all the electrons to scatter in phase without energy transfer. [39].

The form factor notion can be also extended to a molecule. In such a case coherent scattering is a result of a photon interacting with all the electrons in the molecule. It has been shown that a mixture of the respective independent angular scatter probabilities of the atoms in the molecule does not agree with the one measured in experiments [43]. The mo-

lecular form factor has been determined experimentally for a number of materials of interest for x-ray imaging [22], [43].

With the aid of equation (2.5) and using the respective molecular form factor the angular Rayleigh scattering probability can be computed. An example for a water molecule at room temperature is given in Figure 2.7b. The curve in the figure plotted for different relevant x-ray photon energies shows that the scattering probability is strongly peaked in the forward direction. This becomes more and more valid with increasing photon energy.

To obtain the Rayleigh scattering probability per material element $\sigma_{Rayleigh}$ (e.g. atom or molecule), the expression (2.5) must be integrated over the entire solid angle $\mathrm{d}\Omega$. With the aid of the substitution $\mathrm{d}\Omega=2\pi\sin\theta\mathrm{d}\theta$, the Rayleigh scattering probability in the interaction medium takes the following form:

$$\sigma_{Rayleigh} = \pi \int_0^{\pi} r_0^2 \left(1+\cos^2\theta\right) F^2\left(x,Z\right) \sin\theta \,\mathrm{d}\theta \,. \tag{2.6}$$

It is also worth noting that the probability of Rayleigh scattering is very low in the diagnostic x-ray energy range. For example, in soft tissue, this type of scattering occurs in less than 5% of interactions above 70 keV and, at most, for 12% at around 30 keV [1].

2.2.3. Compton scattering

Compared to the Rayleigh process, Compton scattering plays a more important role in x-ray imaging, since it is the predominant interaction of x-ray photons with soft tissue in the diagnostic energy range [1]. Instead of interacting with the whole atom, the incident x-ray interacts with an individual electron (most likely in the outer shell). This is the reason why the Compton process is also called *incoherent scattering*. [39].

An illustration for Compton scattering is presented in Figure 2.8a. In this type of interaction the energy of the incident x-ray photon is considerably higher than the binding energy of the outer-shell electron. The incoming photon changes its direction and energy through the interaction with the electron. A part of the x-ray photon energy is transferred to the electron (also referred to as recoil electron) ejecting it from the atom. [38].

As noted previously, the binding energy of the considered electrons is substantially lower than that of the incident x-ray photon and can be neglected. Thus, the electrons can be treated as free. With the aid of this assumption, one can derive the well-known relationship between the scattered photon energy E' and incident photon energy E through the scattering angle θ [39]:

$$E' = \frac{E}{1+\dfrac{E}{m_0 c}\left(1-\cos\theta\right)}, \tag{2.7}$$

where m_0 is the electron rest-mass.

In order to describe the probability of photon scattering by a free electron as a function of scattering angle, the *Klein-Nishina formula* is used [39]:

$$\frac{\mathrm{d}\sigma_{KN}}{\mathrm{d}\Omega} = \frac{r_0^2}{2}\varepsilon^2\left(\varepsilon+\frac{1}{\varepsilon}-\sin^2\theta\right), \quad \varepsilon=\frac{E'}{E}. \tag{2.8}$$

In (2.8) $\mathrm{d}\sigma_{KN}/\mathrm{d}\Omega$ denotes the *differential Klein-Nishina cross-section*.

As the x-ray photon is actually scattered by a bound electron, the contributions of the surrounding electrons must be taken into account in order to compute the *differential*

Compton cross-section $\mathrm{d}\sigma_{Compton}/\mathrm{d}\Omega$. This is done by weighting the expression in (2.8) by the *incoherent scattering function* $S(x, Z)$:

$$\frac{\mathrm{d}\sigma_{Compton}}{\mathrm{d}\Omega} = \frac{r_0^2}{2}\varepsilon^2\left(\varepsilon + \frac{1}{\varepsilon} - \sin^2\theta\right)S(x,Z). \tag{2.9}$$

Numerical tabulation for this function can be found in [42]. An example of angular Compton scattering probability for a water molecule at room temperature is given in Figure 2.8b.

In the forward direction the value for S is zero, thus suppressing Compton scattering. This value, however, increases with increasing x, reaching the value of Z, which is equal to the number of electrons per material atom. The increase in the value of S becomes slower with increasing Z. [39].

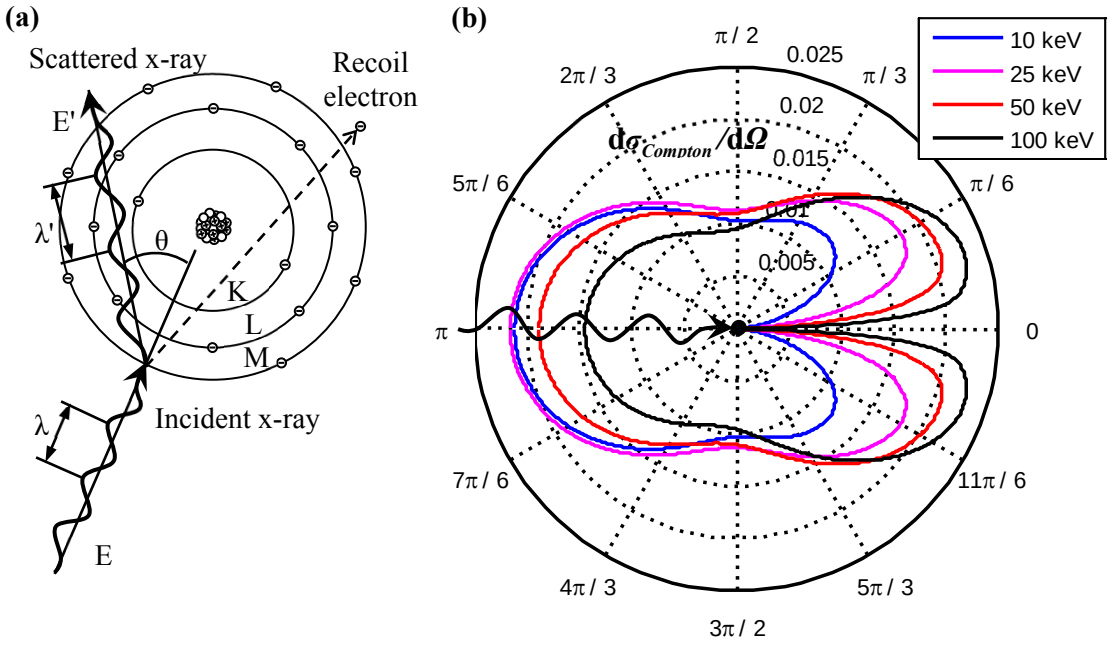

Figure 2.8. Illustration of incoherent (Compton) scattering (a). Incident x-ray photon energy is denoted with E and λ, respectively. The same notation is used for the scattered photon with the addition of the "prime" symbol. The scattering angle is marked with θ. In (b) a polar plot of the angular Compton scattering probabilities for a water molecule at room temperature as function of scattering angle θ is presented. Note that different photon energies are also considered in (b).

Compton scattering probability per material element $\sigma_{Compton}$ (e.g. atom or molecule) can be obtained in a manner similar to $\sigma_{Rayleigh}$ by integrating (2.9) over the entire solid angle $\mathrm{d}\Omega$:

$$\sigma_{Compton} = \pi\int_0^{\pi}\frac{r_0^2}{2}\varepsilon\left(\varepsilon + \frac{1}{\varepsilon} - \sin^2\theta\right)S(x,Z)\sin\theta\,\mathrm{d}\theta\,. \tag{2.10}$$

In order for the Compton interaction to take place, the x-ray photon energy must be superior to the binding energy of the electron. Consequently, the probability of Compton scattering increases with increasing incident photon energy. However, for large energies superior to the ones used in diagnostic imaging this probability becomes inversely proportional to energy. Additionally, the probability of the Compton process is electron density dependent. Since the total number of electrons per gram is relatively constant in tissue materials, the Compton interaction probability per unit mass can be considered almost inde-

pendent of Z and approximately proportional to material density when computed per unit volume of such materials. Hydrogen, however, is an exception to this trend, as the absence of neutrons in its atom leads to an approximate doubling of electron density. Hence, hydrogenous materials have a greater Compton scattering probability than non-hydrogenous materials of the same mass. [1].

2.2.4. X-ray attenuation

Photoelectric absorption, Rayleigh and Compton scattering entail a certain attenuation of the x-ray beam traversing a given material. Considering N monoenergetic x-ray photons incident on a thin slab of a given material with thickness dx and unit length interaction probability μ (Figure 2.9), the change in the number of photons dN can be given by [39]:

$$dN = -\mu N \mathrm{d}x . \tag{2.11}$$

The quantity μ is known as *linear attenuation coefficient* and, as it can be deduced from (2.11), has the unit cm^{-1}.

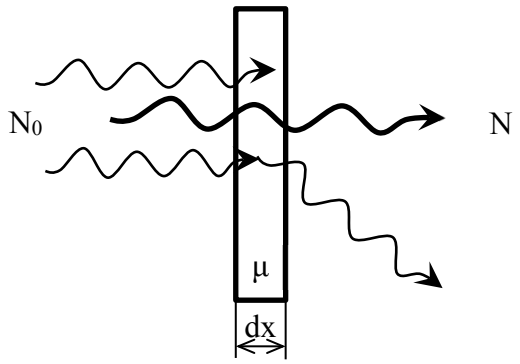

Figure 2.9. An x-ray beam attenuated by a material with thickness dx and a linear attenuation coefficient μ.

The integration of (2.11) over a material thickness l gives:

$$\int_{N_0}^{N} \frac{dN}{N} = -\mu \int_{0}^{l} \mathrm{d}x . \tag{2.12}$$

In (2.12) N_0 and N stand for incident and transmitted number of photons, respectively. The solution of (2.12) leads to the *Beer-Lambert law*:

$$N = N_0 e^{-\mu l} . \tag{2.13}$$

The observation of (2.13) reveals that the attenuation of the monochromatic x-ray beam traversing a material is an exponential phenomenon. Note that (2.13) describes the change in the number of photons that have not interacted with the material and are exiting the inspected object. These are also known as *primary photons* [39].

For a case where a polyenergetic beam traversing several materials is considered, (2.13) will take the following form:

$$N(E) = N_0(E) \exp\left(- \sum_{q=1}^{Q} \mu_q(E) l_q \right), \tag{2.14}$$

where $\mu_q(E)$ is the linear attenuation coefficient function of a given material $q \in \{1, ..., Q\}$ and l_q is the corresponding thickness. Note that Q is the total number of materials traversed.

The total linear attenuation coefficient μ_{total} is the sum of the different interaction process probabilities (Figure 2.10) [39]:

$$\mu_{total} = n_a\left(\tau_{photo} + \sigma_{Rayleigh} + \sigma_{Compton}\right), \tag{2.15}$$

where τ_{photo}, $\sigma_{Rayleigh}$ and $\sigma_{Compton}$ are the interaction probabilities probability per material element (e.g. atom or molecule) of photoelectric absorption, Rayleigh scattering and Compton scattering, respectively. In addition, n_a is the number of the corresponding material elements in a unit volume.

From Figure 2.10 it is apparent that for water the individual interaction probabilities and the resulting total attenuation are strongly dependent on incident x-ray photon energy. For low energies (<30 keV) the dominant interaction is the photoelectric effect. In contrast, Compton scattering constitutes the dominant fraction for photon energies greater than 50 keV. Although not dominant, Rayleigh scattering still remains relevant for low energy x-ray photons (<15 keV).

The probability of interaction with a given material depends on the number of atoms encountered by the x-rays per unit distance. Material density (measured in g/cm^3) has a direct influence on this number. Doubling the density results in twice as many atoms encountered per unit distance by the x-rays while traversing the material. Hence, the linear attenuation coefficient is proportional to material density. [1].

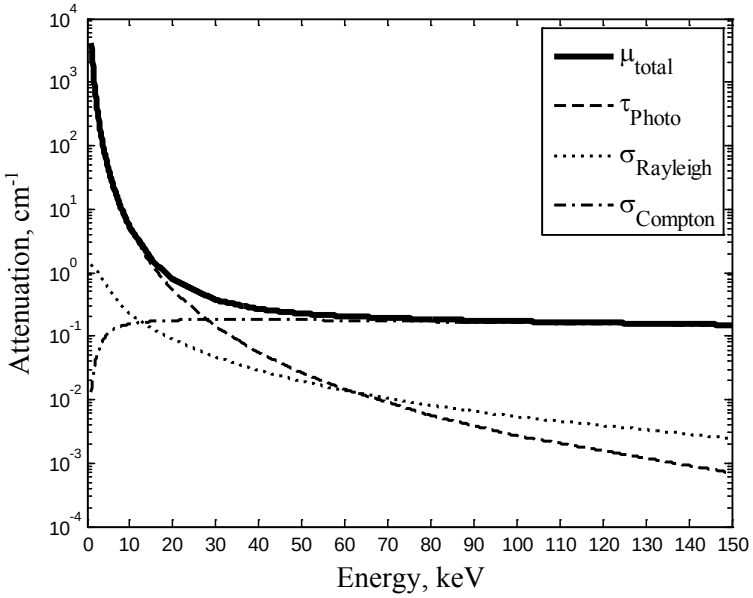

Figure 2.10. The total linear attenuation coefficient of water (μ_{total}) as a function of photon energy with its different components: photoelectric absorption (τ_{photo}), Rayleigh ($\sigma_{Rayleigh}$) and Compton ($\sigma_{Compton}$) scattering. The example was generated with the aid of an existing internal simulation tool (Chapter 4.2).

An illustration of the linear attenuation coefficient functions for water, aluminum, skeletal muscle, cortical bone, adipose tissue, iodine and tantalum is provided in Figure 2.11.

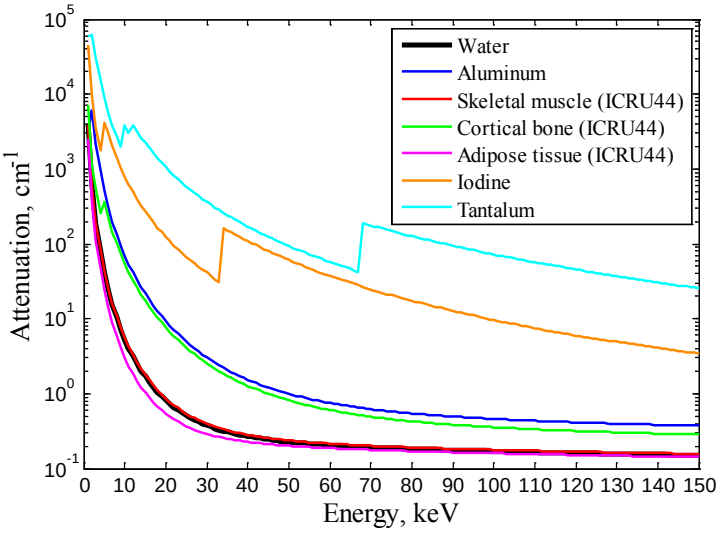

Figure 2.11. Linear attenuation coefficients as functions of energy for different materials.

Note that linear attenuation coefficients of tissue materials are close to water with the exception of cortical bone, which exhibits a higher material density. The functions presented in Figure 2.11 are mostly smooth with the exception of discontinuities visible for iodine and tantalum. These discontinuities are called "absorption edges" and they arise due to the increase of photoelectric electric effect probability when the energy of the x-ray photons begins to exceed the binding energy of the inner shell (e.g. K, L, M, etc.) electrons [1]. This entails an increase in the number of material electrons available for interaction [1].

Finally, it is also worth visualizing the attenuation of the incident x-ray photons in the inspected object (Figure 2.12). In order to do this, the x-ray tube spectrum presented in Figure 2.3 is used and (2.14) is applied for various materials with different thicknesses.

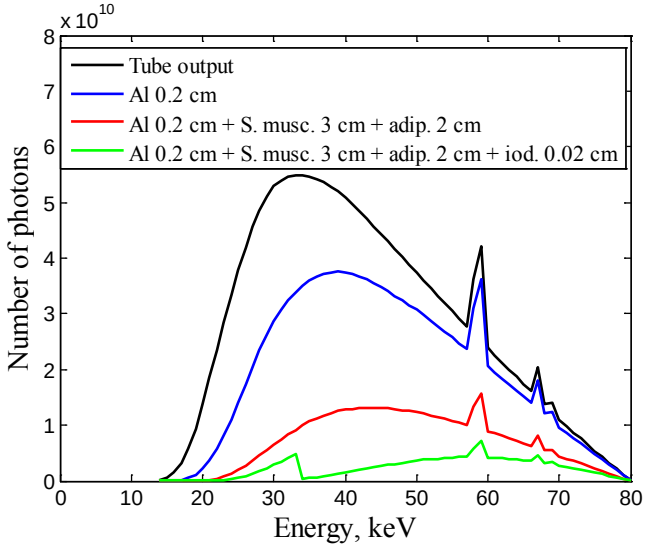

Figure 2.12. Incident x-ray spectrum (black) attenuation in the object sampled at equal 1 keV intervals. Firstly, part of the photons is lost due to added filtration of 0.2 cm aluminum (blue). Then, an additional loss occurs in skeletal muscle and adipose tissue (red). Finally, if iodine is added (green), more photons are lost and a discontinuity in the spectrum due to the K absorption edge can be visible around 33 keV. The example was generated with the aid of an existing internal simulation tool (Chapter 4.2).

2.3. Detection of x-rays

Modern day x-ray detectors are digital flat panel detectors. The technology applied in these image receptors is similar to that of a laptop computer display (Figure 2.13). [39].

Instead of wiring individual display elements (or *pixels*), a series of vertical and horizontal electrical lines are used. Combined with appropriate read-out logic, these lines can address each individual element. [1]. The technology applied in digital flat panel detectors is called *active matrix array*, because they incorporate an active switching device, which is the thin film transistor (TFT) [2], [39]. Hence the other name often attributed to the active matrix array – the *TFT array* [2].

Chapters 2.3.1 and 2.3.2 give detail on the two different types of flat panel detectors. Chapter 2.3.3 introduces key concepts behind photon counting detectors.

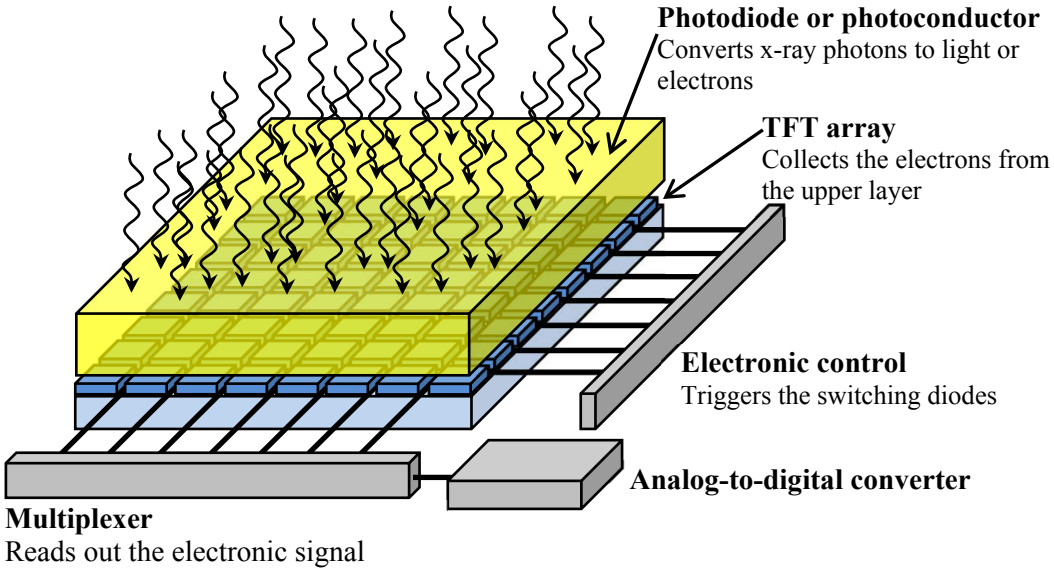

Figure 2.13. General structure of a flat panel x-ray detector.

It is also worth noting that other technologies (not covered in the present thesis) for x-ray detection also exist. These include, for example, charge-coupled devices and complementary metal-oxide-semiconductors.

2.3.1. Indirect conversion

For *indirect* conversion type flat panels a phosphor layer (typically Gd_2O_2S or CsI) is used to convert incident x-rays to fluorescent light [1]. The intensity of the light is proportional to the x-ray intensity and can thus vary from pixel to pixel in the case of a non-flat x-ray beam. This light is then converted to electric charge with the aid of photosensitive elements (photodiodes) of the detector pixels. For a given pixel, the charge level is proportional to the light intensity emitted from the phosphor in the vicinity of that pixel. This charge is stored in the detector element until the TFT array is read out. [39]. The term "indirect" stems from the fact that the x-ray energy absorbed in the phosphor layer is transmitted to the photodetector by means of visible light photons [1]. The indirect conversion based x-ray detectors are currently the most dominant types used in general digital radiography applications.

The materials used in indirect conversion x-ray detectors can be structured (CsI) or unstructured (Gd_2O_2S). Structured materials are preferred, since the crystals exhibit a needle-like shape, which reduces lateral scattering of visible light photons and increases the number of x-ray photon interactions. For unstructured materials, the light photons have a higher probability to deviate from their trajectory (lateral scattering) thus contributing to a reduction in spatial resolution [2].

2.3.2. Direct conversion

In the *direct* conversion approach, a photoconductor is used directly on top of the TFT array. The x-rays are directly converted to electron-hole pairs, which are then drawn toward the respective electrodes by means of an electric field. [2]. The electrons are directed toward the detector pixels and the generated charge is stored temporarily on the capacitance until readout. The charge magnitude among different pixels corresponds to the intensity variations of the incident x-ray beam. [39].

Two principal advantages of direct conversion are the absence of an intermediate conversion stage, which increases x-ray conversion efficiency (~8000 electrong-hole pairs for direct versus 1000–2000 for indirect), and higher spatial resolution due to lower levels of lateral scattering of electrons (direct conversion) compared to visible light photons (indirect conversion).

The most widely applied photoconductor material is a-Se, which, unfortunately due to its low Z is used primarily in mammography (thickness limitation). Other proposed photoconductors include CdTe, HgI_2 and PbO. [39].

2.3.3. Photon counting detectors

X-ray photon counting detectors utilize the principle of direct conversion with the difference that each photon is discriminated by the individual pixel electronics. Thus, for each incident x-ray photon the electronic counter is incremented (a count is recorded). A more advanced derivative of these image receptors are *photon counting energy discriminating (spectrometric) x-ray detectors*. This type of detector is able to collect energy information on the incident x-ray photons. [39]. As a result, the photons can be classified, based on their energy into several discrete *energy channels* or *energy bins*, the number of which varies from a few channels (typically 2–8) [4]–[6] to a hundred with a width of ~1 keV, depending on the electronic circuit behind the pixels [7], [8]. Materials used for the photoconductor layer in photon counting x-ray detectors include such semiconductors as Si [44] and CdTe [4], [6], [7] or its Zn doped version (CdZnTe or CZT) [8].

Despite their virtues, energy-resolved PCDs suffer from several undesirable effects degrading their performance. These include: *charge sharing* [7], fluorescence or scattering [7], *induction* and *photon pile-up* [8], [45].

In the first case (charge sharing), the charges generated from an interaction with an incident photon are collected by several adjacent pixels. The significance of the effect increases with the decrease of pixel size. It impacts detector spatial resolution and gives rise to correlations between signal and noise for adjacent pixels. [7].

Other means of disturbing the x-ray photon induced charge in reaching the correct pixel include fluorescence and scattering [7]. In the case of fluorescence, through photoelectric absorption, the incident x-ray photon gives rise to a characteristic x-ray photon. This photon may or may not arrive on the correct pixel. Additionally, through Compton scattering in the photoconductor layer, the trajectory of the incident x-ray photon may change enough

to create a charge sufficiently far from the correct detector pixel limiting the possibility of that charge to reach the respective pixel.

In the case of induction, for a given pixel, the charge collection on the electrode will give rise to a low level signal on the neighboring pixel electrodes through the induction phenomenon. This signal will appear in the low energy channels of the neighboring pixels considered.

Finally, the photon pile-up is a result of the detector electronics being incapable to discriminate between signals obtained from two photons arriving within a time interval shorter than the *dead time* of the circuit. The dead time is the limiting time interval during which the system can still discriminate between two temporally adjacent pulses. As a result of pile-up, the two photons are counted as a single photon giving rise to higher electronic pulse amplitude and, consequently, attributing a higher energy to the photon. [8].

In order to reduce the impact of the above described undesirable effects, signal processing techniques can be employed. For example, a method for correcting induction and charge sharing distortion for energy discriminating detectors can be found in [7].

The net effect of all the listed performance distortions (with the exception of pile-up) can be modeled by a *detector response function*. For a fixed detector pixel, this function describes the probability of a single photon being detected at its corresponding energy. An example of the response function measured by a prototype 16 pixel linear (1D) spectrometric CdTe detector (developed at the LDET laboratory) using a radioactive source (Co-57) is given in Figure 2.14 [8].

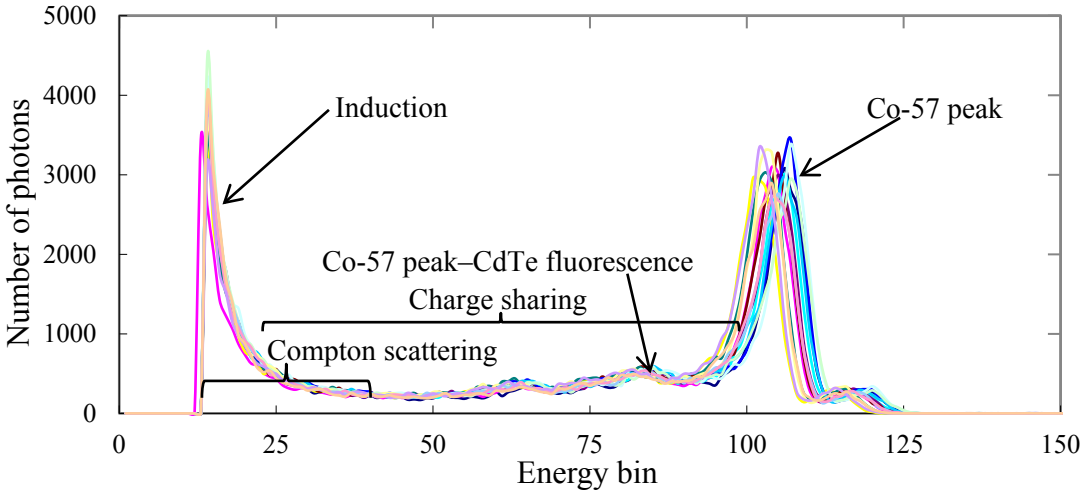

Figure 2.14. Spectral response measurements for 16 different pixels (various colors) of a spectrometric detector. Channel width is equal to 1.2 keV. Ideally one would expect a single peak around energy bin #102 corresponding to the emitted photon energy of Co-57 (122 keV). However, charge sharing, induction, scattering and fluorescence within the detector modify such an expectation.

Spectrometric x-ray detectors can give way to energy-resolved x-ray imaging for all current modalities (e.g. radiography, CT, etc.). The resulting image quality advantages are substantial. More precisely, an increase in CNR can be achieved [9] as well as dose and artefact reduction [10]. These detectors also bring new x-ray imaging capabilities into focus both in radiography and CT. These include, for example, the ability to differentiate between present material components in the object and estimate their equivalent thicknesses and relative ratios (soft tissue, bone, glandular, contrast agent enhanced tissue, etc.) by processing a single acquisition image [4], [10], [11].

2.4. From radiography to Computed Tomography

In all the multitude of x-ray imaging modalities available today, x-ray radiography and tomography remain the most common and widely used. Chapter 2.4.1 introduces the concepts behind radiography and serves as a basis for Chapter 2.4.2, which introduces the principles of x-ray tomography. Both integration mode and energy-resolved modes are discussed for each modality. For the latter corresponding specific applications are also provided.

2.4.1. Radiography

Radiography (or *projection radiography*) refers to the acquisition of a 2D x-ray projection image of a 3D object (Figure 2.15). The resulting 2D distribution reflects the variation in object attenuation viewed by different image receptor pixels. [1].

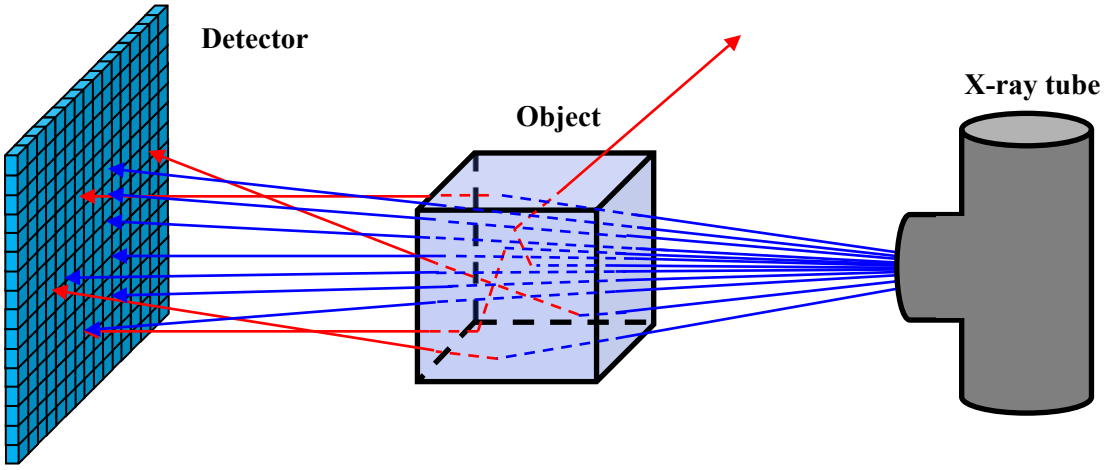

Figure 2.15. Illustration of a radiographic acquisition. Primary and scattered x-rays are marked in blue and red respectively. Note that scattered x-rays deviate from their initial trajectory through photon-matter interactions in the object.

Assuming the absence of charge sharing for each pixel $\mathbf{p}=(x,y)$ of a standard flat panel detector the following expression can be written for the measured x-ray intensity $I(\mathbf{p})$:

$$I(\mathbf{p}) = \int_{E_1}^{E_2} D(E) N(\mathbf{p},E) E \mathrm{d}E \,, \tag{2.16}$$

where E_1 and E_2 are the lower and upper energy bounds of the x-ray spectrum, $D(E)$ ($0 < D(E) < 1$) is the *detector efficiency* and $N(\mathbf{p},E)$ is the number of photons with energy E traversing the object and incident on pixel $\mathbf{p}$. Since the considered detector type performs an energy integration of the x-ray signal, it can also be called *integration mode detector*.

In order to reflect the changes in object attenuation measured by each pixel, the x-ray intensity from (2.16) is normalized by the raw x-ray intensity $I_0(\mathbf{p})$ (with no object) and a negative log transformation is applied:

$$A_m(\mathbf{p}) = -\log\left(\frac{I(\mathbf{p})}{I_0(\mathbf{p})}\right), \qquad I_0(\mathbf{p}) = \int_{E_1}^{E_2} D(E) N_0(\mathbf{p},E) E \mathrm{d}E \,, \tag{2.17}$$

where $A_m(\mathbf{p})$ is the measured x-ray attenuation and $N_0(\mathbf{p},E)$ is the number of raw x-ray photons with energy E incident on pixel $\mathbf{p}$. Examples of simulated x-ray intensity and attenuation images (scatter is not considered) are provided in Figure 2.16.

Assuming the absence of scatter, the development of (2.17) with the aid of (2.14) and (2.16) leads to an expression linking the measured x-ray attenuation $A_m(\mathbf{p})$ to the actual object attenuation $A(\mathbf{p},E)$:

$$A_m(\mathbf{p}) = -\log\left(\frac{\int_{E_1}^{E_2} D(E)N_0(\mathbf{p},E)\exp\left(-A(\mathbf{p},E)\right)E\mathrm{d}E}{\int_{E_1}^{E_2} D(E)N_0(\mathbf{p},E)E\mathrm{d}E}\right), \quad A(\mathbf{p},E) = \sum_{q=1}^{Q}\mu_q(\mathbf{p},E)l_q(\mathbf{p}), \qquad (2.18)$$

From (2.18) it is apparent that the measured x-ray attenuation is non-linearly related to the true object attenuation. $A_m(\mathbf{p})$ can be considered an "effective" attenuation, which is indicative of the total object attenuation in the direction of the considered pixel averaged over the x-ray spectrum energies. Note that for a monochromatic x-ray spectrum, the expression simplifies and the measured attenuation is directly equal to the true attenuation.

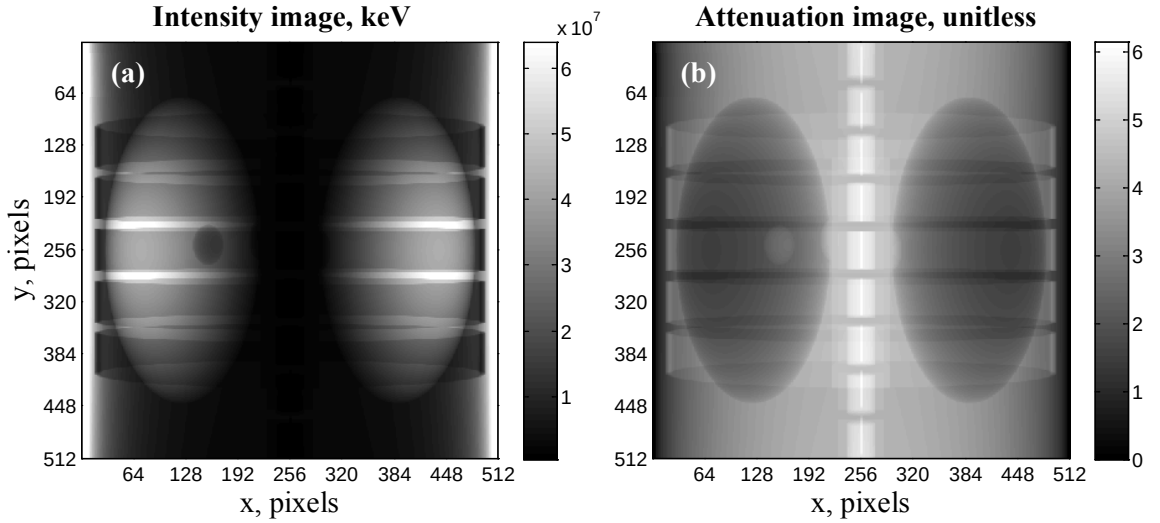

Figure 2.16. X-ray intensity (a) and attenuation (b) images acquired with the aid of an existing internal simulation tool (Chapter 4.2). Pixel size was 1 mm. Note that the attenuation image (a) provides contrast that is superior to that of the intensity image (b).

In the case of an energy-resolved PCD, photons as a function of discrete energy bins are measured per pixel. Under the assumption that the detector suffers from no or limited amount of non-linear effects (e.g. pulse pile-up), an expression equivalent to (2.16) can be obtained:

$$\mathbf{N^d}(\mathbf{p}) = \mathbf{D}\times\mathbf{N}(\mathbf{p}), \qquad (2.19)$$

where $\mathbf{N^d(p)}$ and $\mathbf{N(p)}$ are detected and incident (on the detector pixel) number of photon vectors (functions of energy channel), respectively, and $\mathbf{D}$ is the *detector response matrix* (DRM) [46]–[48].

The DRM describes the probabilities of detecting a photon in a given energy channel as a function of the respective photon energy. Thus, for example, a given element of the response matrix, $D(E,E_0)$, indicates the probability of detecting an incident photon with en-

ergy E_0 in the energy channel E [46], [47]. In the case of an ideal detector, the DRM is an identity matrix (each photon is detected only at its corresponding energy); whilst for a realistic detector it is quasi-triangular due to charge sharing effects (Chapter 2.3.3). Additionally, the DRM of a realistic spectrometric detector can also be pixel dependent. It is worth noting that the DRM does not take into account all of the inter-pixel effects comprising the point-spread-function of the detector. Finally, an illustration of a DRM corresponding to a pixel of a realistic energy-resolved PCD is provided in Figure 2.17.

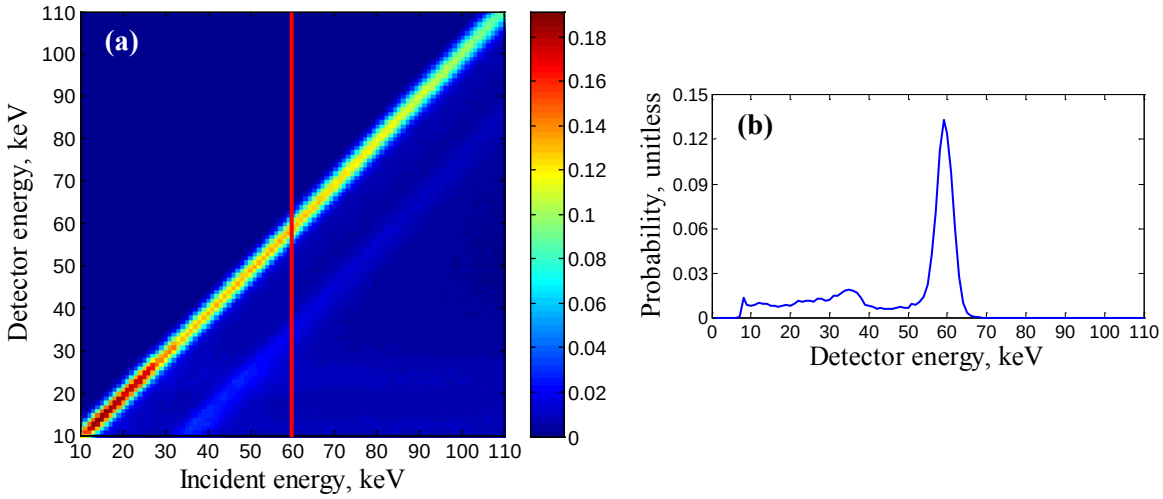

Figure 2.17. DRM of a linear CdTe detector with a 800 μm pixel size and a 3 mm thickness (a). A profile of the matrix at the incident energy of 60 keV is also presented (b). The matrix was modeled with the aid of simulations which are described in more detail in Chapter 4.3.

With the aid of (2.19) and assuming fine (~1 keV) energy channels, an expression equivalent to (2.18) can also be derived for an energy-resolved detector:

$$\mathbf{A_m}(\mathbf{p}) = -\log\left(\frac{\mathbf{D}\times[\mathbf{N_0}(\mathbf{p})\circ\exp(-\mathbf{A}(\mathbf{p}))]}{\mathbf{D}\times\mathbf{N_0}(\mathbf{p})}\right), \qquad \mathbf{A}(\mathbf{p}) = \sum_{q=1}^{Q}\boldsymbol{\mu}_\mathbf{q}(\mathbf{p})l_q(\mathbf{p}), \tag{2.20}$$

where $\mathbf{A}(\mathbf{p})$, $\mathbf{A_m}(\mathbf{p})$, $\boldsymbol{\mu}_\mathbf{q}(\mathbf{p})$ and $\mathbf{N_0}(\mathbf{p})$ are discrete counterparts (functions of energy channel) of the corresponding quantities in (2.18) and $\circ$ is the Hadamard product. Note that compared to (2.18), a more complete representation of the total object attenuation is obtained. However, the relationship between $\mathbf{A_m}(\mathbf{p})$ and $\mathbf{A}(\mathbf{p})$ is still non-linear due to $\mathbf{D}$ being non-diagonal. When $\mathbf{D}$ approaches a diagonal matrix, $\mathbf{A_m}(\mathbf{p})$ will approach $\mathbf{A}(\mathbf{p})$. Finally, similar to Figure 2.16, attenuation and number of photons images as functions of energy bin are presented in Figure 2.18.

As discussed previously in Chapter 2.3.3, energy-resolved images obtained with the corresponding PCDs enable quantification of materials present in the inspected object. According to the hypothesis of Alvarez-Makovski, the total object attenuation $\mathbf{A}(\mathbf{p})$ from (2.20) can be represented by a linear combination of independent material (*basis material*) linear attenuation coefficient functions $\boldsymbol{\mu}_\mathbf{b}(\mathbf{p})$ [49]:

$$\mathbf{A}(\mathbf{p}) = \sum_{q=1}^{Q}\boldsymbol{\mu}_\mathbf{q}(\mathbf{p})l_q(\mathbf{p}) = \sum_{b=1}^{n}\boldsymbol{\mu}_\mathbf{b}(\mathbf{p})l_b^e(\mathbf{p}), \tag{2.21}$$

where $l_b^e(\mathbf{p})$ represents the equivalent thickness of the b^{th} material and n is the total number of basis materials considered. It is worth noting that (2.21) is valid only assuming the ab-

sence of absorption edges in the considered energy interval as well as the absence of high Z materials in the object. If any of the materials considered in the linear combination is present in the total object attenuation **A(p)**, the equivalent thickness will be equal to the actual thickness of that material. [49].

The insertion of (2.21) in (2.20) leads to the following expression:

$$\mathbf{A_m}(\mathbf{p}) = -\log\left(\frac{\mathbf{D}\times\left[\mathbf{N_0}(\mathbf{p})\circ\exp\left(-\sum_{b=1}^{n}\boldsymbol{\mu}_\mathbf{b}(\mathbf{p})l_b^e(\mathbf{p})\right)\right]}{\mathbf{D}\times\mathbf{N_0}(\mathbf{p})}\right). \tag{2.22}$$

Given that the number of channels of the energy-resolved detector is greater or equal to n and $\boldsymbol{\mu}_\mathbf{b}(\mathbf{p})$ are known, (2.22) can be solved for $l_b^e(\mathbf{p})$. As for the case of total object attenuation in (2.20), the relationship between $l_b^e(\mathbf{p})$ and $\mathbf{A_m}(\mathbf{p})$ in (2.22) is also non-linear given a general (realistic) non-diagonal **D**.

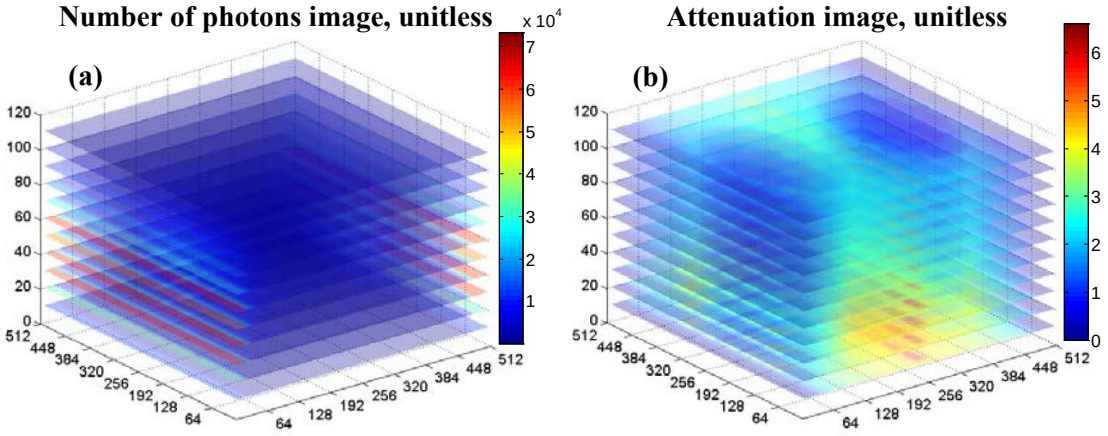

Figure 2.18. Number of x-ray photons (a) and attenuation (b) images as functions of energy channel acquired with the aid of an existing internal simulation tool (Chapter 4.2). Pixel size was 1 mm and regularly spaced 1 keV energy channels were considered. Note that with the addition of energy information the images become 3D compared to the 2D integration mode images previously displayed in Figure 2.16.

The process of solving (2.22) in terms of $l_b^e(\mathbf{p})$ is called *basis material decomposition*. In order to accomplish this, two principal techniques can be considered: direct model inversion (assuming **D** and $\mathbf{N_0(p)}$ are known) [4] or calibration based approaches [50], [51].

The calibration based method consists of learning the inverse relationship presented in (2.22) through a calibration procedure. Several approaches exist (e.g. maximum likelihood estimation) with the most common being the application of, typically, 2nd order polynomial functions [49], [50]. Since, in practice, only 2 basis materials and 2–3 energy channels are considered [49], [50], an example of a 2nd order polynomial for two basis materials and two energy channels is given:

$$\begin{aligned} l_1^e(\mathbf{p}) &= \sum_{i,j}^{2}\alpha_{1,i,j}\left(A_1(\mathbf{p})\right)^i\left(A_2(\mathbf{p})\right)^j \\ l_2^e(\mathbf{p}) &= \sum_{i,j}^{2}\alpha_{2,i,j}\left(A_1(\mathbf{p})\right)^i\left(A_2(\mathbf{p})\right)^j \end{aligned}, \tag{2.23}$$

where $\alpha_{1,i,j}$ and $\alpha_{2,i,j}$ are the polynomial coefficients and $A_1(\mathbf{p})$ and $A_2(\mathbf{p})$ correspond to the measured attenuation $\mathbf{A_m(p)}$ values in individual energy channels. In order to determine the coefficients, a set of attenuation measurements of the respective basis materials while varying their thicknesses is performed. Given known $l_1^e(\mathbf{p})$, $l_2^e(\mathbf{p})$ and $\mathbf{A_m(p)}$, the linear system from (2.23) can be solved (using the linear least squares, for example) with respect to the polynomial coefficients $\alpha_{1,i,j}$ and $\alpha_{2,i,j}$. This is why this type of technique is considered a calibration based approach. Once the coefficients are determined, (2.23) can be applied on the energy-resolved attenuation image of a given object in order to provide decomposition into the basis materials. Thus, the polynomial method consists of two stages: offline calibration (polynomial coefficient determination) and decomposition (polynomial application).

Provided that the polynomial coefficients were obtained through calibration, the two channel equivalent of the energy-resolved image from Figure 2.18b can be decomposed into water and bone, for example, with aid of (2.23). The resulting material thickness images are displayed in Figure 2.19.

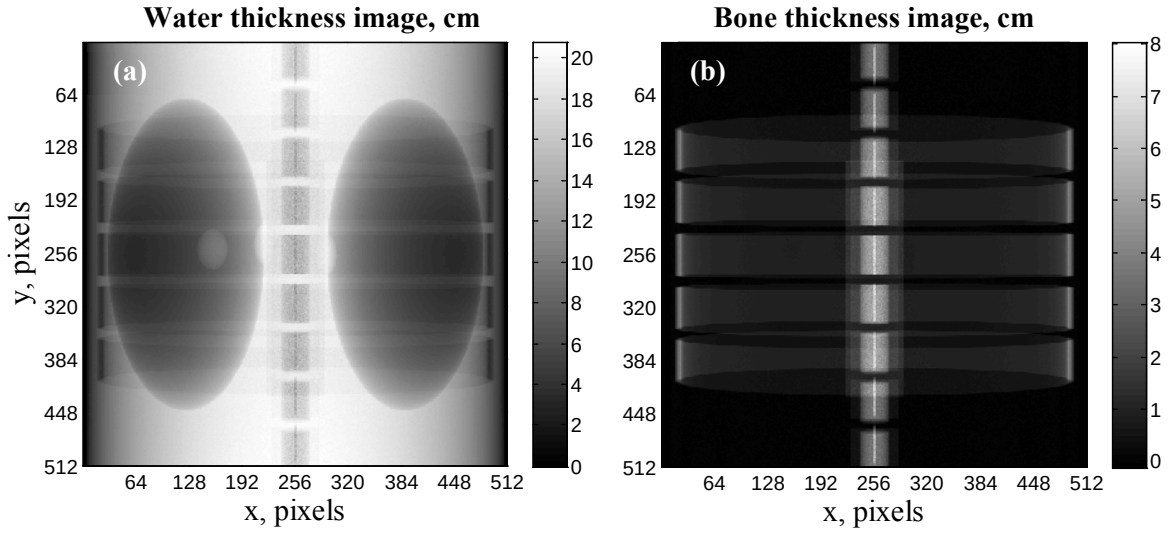

Figure 2.19. Water (a) and bone (b) thickness images produced from the two channel equivalent energy-resolved image of Figure 2.18b via (2.23). Pixel size was 1 mm.

2.4.2. Computed Tomography

As noted in Chapter 2.4.1, x-ray radiography deals with 2D attenuation projections (images) of a 3D object. Thus, superposition of imaged object structures occurs and only limited information on the geometry of these structures is available. In contrast, x-ray *Computed Tomography* is able to recover a 3D attenuation map (volume) of the studied object. In doing so, more information on object composition is made available (e.g. individual internal structure attenuation, dimensions and position).

In order to obtain a volumetric attenuation representation of a given object, several radiographic projections are acquired at different angles (Figure 2.20). The collection of these projections is called a *sinogram*. The 3D attenuation map is then obtained with the aid of a *reconstruction* operation applied on the sinogram. Since the projection data is discrete, the reconstructed attenuation volume is also discrete and comprised of volume elements or *voxels*. [38].

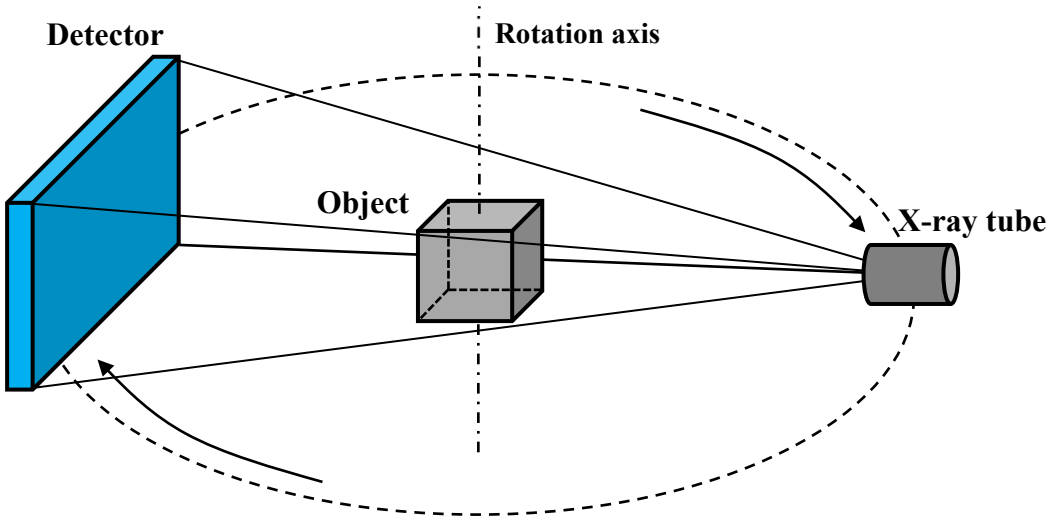

Figure 2.20. Schematic of radiographic projection acquisition during a CT scan.

For a general mathematical formulation in the case of an integration mode x-ray detector, consider that the 3D attenuation map of the object is denoted with $V(x,y,z)$. Then the application of a multiple-angle projection acquisition operation $P_\varphi\{\bullet\}$ gives rise to the sinogram $S(s,u,\varphi)$ measured by the x-ray CT system:

$$S(s,u,\varphi) = P_\varphi\{V(x,y,z)\}. \tag{2.24}$$

In (2.24), $S(s,u,\varphi)$ is a function of imaginary detector coordinates (s,u) and the projection angle φ. The imaginary detector is simply a rescaled version of the real detector placed at the rotation axis (Figure 2.21). The scale, in this case, is the SDD over the source-to-rotation axis distance (SAD). Each value of $S(s,u,\varphi)$ represents the total attenuation along the ray-path in the direction of a point (s,u) of the imaginary detector corresponding to a radiographic projection performed at angle φ.

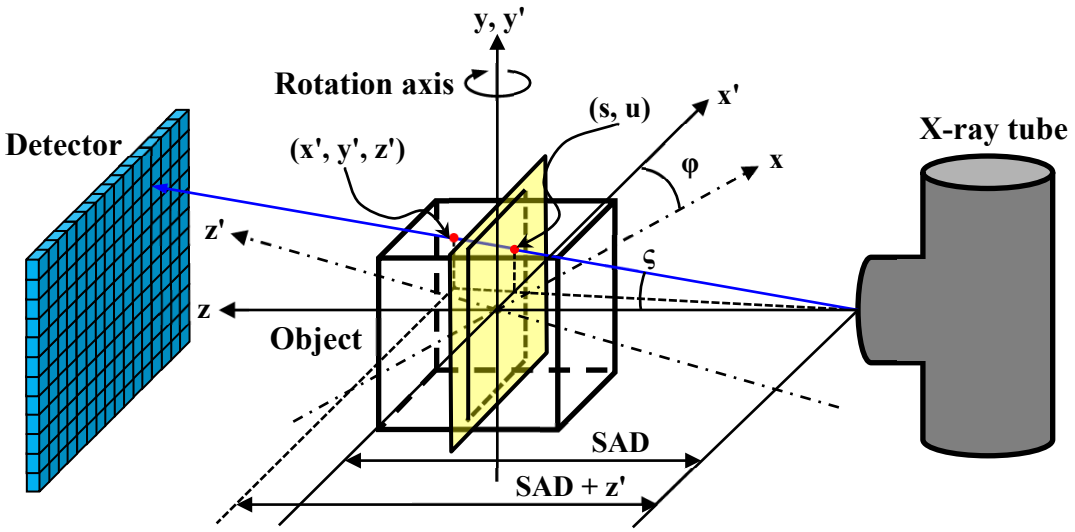

Figure 2.21. Illustration of geometrical relationships applied for CT data reconstruction.

Given a measured sinogram $S(s,u,\varphi)$, an estimated attenuation map $\tilde{V}(x,y,z)$ of the considered object can be recovered via a reconstruction operation $R\{\bullet\}$:

$$\tilde{V}(x,y,z) = R\{S(s,u,\varphi)\}. \tag{2.25}$$

Based on the geometrical relationships presented in Figure 2.21, one example of $R\{\bullet\}$, known as the Feldkamp-Davis-Kress (FDK) analytical reconstruction formula, can be derived [52].

It is important to note that the units used for CT volumes are *Hounsfield Units* (HU), which can be related to a particular total attenuation value of a reconstructed volume element in the following manner [39]:

$$\tilde{V}_{HU}(x,y,z) = \frac{\tilde{V}(x,y,z) - \mu_{water}}{\mu_{water}} \times 1000, \tag{2.26}$$

where μ_{water} is the average (in the applied energy range) linear attenuation coefficient of water. From (2.26) it is apparent that when no attenuation occurs in a given volume element, a value of -1000 HU will be obtained. On the other hand, for materials with a density far superior to that of water (bone, metal), greater values can be expected (>1000 HU). Finally a table of HU values corresponding to different tissue types is given in Table 1.

Table 1. Various tissue materials with their corresponding HU values [39].

Material	**HU value**
Compact bone	1000
Muscle	25
Water	0
Fat	-90
Air	-1000

An example section (*slice*) from a simulated projection data volume reconstruction via the FDK algorithm is presented in Figure 2.22.

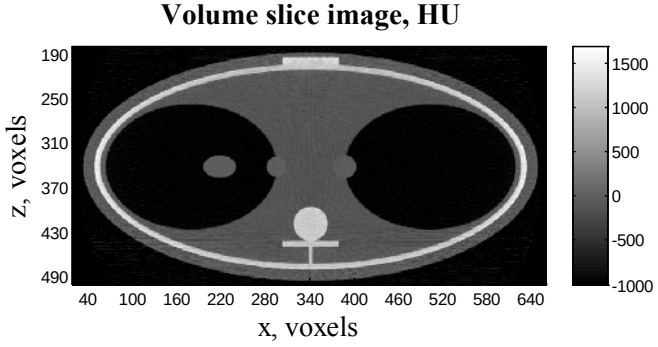

Figure 2.22. Reconstructed volume slice image from simulated projection data obtained with the aid of an existing internal simulation tool (Chapter 4.2). The reconstruction was carried with the aid of the FDK algorithm. Voxel size was 0.65 mm. Note that in comparison with the image presented in Figure 2.16, a clearer overview of the internal structure detail is visible.

A part from direct analytical reconstruction approaches, more complex iterative algebraic or statistical reconstruction techniques can be used to recover $\tilde{V}(x,y,z)$ from $S(s,u,\varphi)$. These types of algorithms aim to solve the reconstruction problem iteratively by starting from an initial estimate of the object volume and then applying a correction scheme to arrive at a final solution. Additionally, these techniques provide the ability to include prior constraints (e.g. regularization, support, etc.). [38], [53].

In iterative algebraic reconstruction methods the sinogram data is treated as system of linear equations where the attenuations of the individual voxels are the unknowns. In the case of a limited number of projections and detector size, one arrives at an ill-posed inverse problem with an equation number inferior to the number of unknowns. In order to provide a solution to such a problem, methods such as Algebraic Reconstruction Technique can be applied. [38].

In contrast to algebraic methods, statistical methods aim to model the underlying physical processes considered in the tomographic x-ray acquisition through probability distributions. This modelling leads to the so called likelihood function in terms of the volume and the corresponding projection data, which is then iteratively maximized until obtaining a stable estimate of the object volume. A well-known example of iterative statistical reconstruction methods is the Maximum Likelihood Expectation Maximization approach. [53].

Although the performance of iterative methods in terms of reconstruction accuracy is superior to that of analytical methods, the latter ones are still computationally faster. For more insight into iterative reconstruction methods the reader is referred to [38] or [53].

If, in the context of x-ray CT, a spectral x-ray detector is used, the sinogram and the reconstructed volume both get an additional dimension due to the added energy information. Another way to interpret this is that several sinograms are obtained for a given object. The number is equal to the number of detector energy channels. In this case, one can use integration mode reconstruction algorithms per channel. However, a more efficient way (especially in the case of a large number of channels), would be to apply a reconstruction algorithm adapted for the multi-energy x-ray data.

As in the case of radiography (Chapter 2.4.1), the availability of energy-resolved data in CT acquisitions will lead to the ability of quantifying individual material properties comprising the inspected object. In contrast to radiography, however, these approaches go beyond thickness estimation outlined in Chapter 2.4.1 and provide insight into individual material concentrations and atomic numbers [4], [54].

3. SCATTERED RADIATION IN X-RAY IMAGING

Scattered x-ray radiation (or simply *scatter*) refers to signals measured by detector pixels due to the contribution of secondary photons, which are produced through Compton and Rayleigh interactions occurring in the object (Figure 3.1) [39]. Fluorescence radiation can also contribute in the case of high Z material presence in the inspected object and if the corresponding absorption edges are located within the energy range used for imaging.

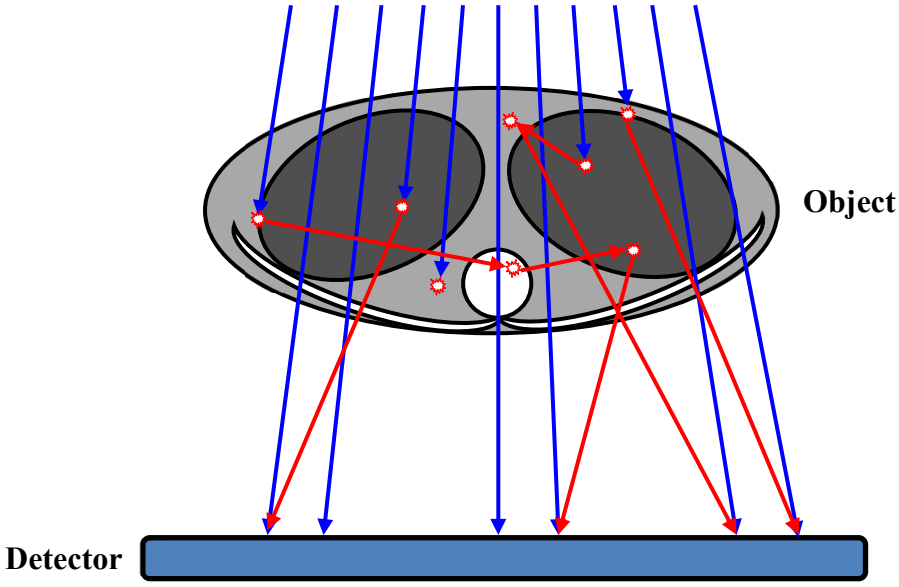

Figure 3.1. X-ray interactions in an object. Primary and scattered photons are marked in blue and red, respectively.

The next chapters describe the x-ray scatter phenomenon in more detail (Chapter 3.1) and give examples of its effect in different x-ray imaging applications (Chapter 3.2).

3.1. Characterization of the scatter phenomenon

The present chapter is sub-divided into three parts. The first one aims to present the existing observations on x-ray scatter behavior and dependencies (Chapter 3.1.1). The second and third examine scattered radiation in more depth in the energy domain through various simulations (Chapter 3.1.2) and experiments (Chapter 3.1.3).

3.1.1. Existing observations

With the presence of scattered radiation in x-ray measurements, each pixel actually measures a sum of two signals, the primary photons $N_P(E)$ that have not been stopped or

deviated by any interaction, and the scattered photons $N_S(E)$, which have been modified in direction and, possibly, energy (Compton interaction) [39]:

$$N(E) = N_P(E) + N_S(E) \tag{3.1}$$

Unlike primary radiation, which can be described by direct analytical expressions, such as (2.14), scattered radiation does not have an equivalent expression. This is due to the complex probability models describing the photon scattering interactions (Chapters 2.2.2 and 2.2.3). However, approximate models for first order scatter can still be found in the literature [16], [55], [56].

Regarding the nature of the effect, it is well known that x-ray scatter is object and geometry dependent [13]. For a fixed object-to-detector distance (ODD), also known as *air gap*, larger objects provide more scattered photons, as there is more material for the x-ray photons to interact with. This assumption is valid only if the object is entirely irradiated. Additionally, high Z materials (e.g. chrome) do not scatter as much as low Z materials (e.g. oxygen). Moreover, if one fixes the object and reduces the x-ray field until reaching a pencil beam (thus reducing the object fraction being irradiated), the scatter component decreases to negligible amounts [39]. Finally, if for a fixed object the ODD is increased, scatter tends to reduce accordingly [13], [19]. This is due to the fact that the solid angle covered by the detector reduces with respect to the scattering sources in the examined volume.

Compared to CT imaging, radiography usually uses larger field sizes and smaller ODDs. Thus, radiographic applications are likely to be more contaminated by scatter compared to CT imaging.

Another important observation concerns the spatial (function of detector pixel) behavior of x-ray scatter. More precisely, due to the randomness of interactions, the scatter spatial frequency is contained within the low frequency interval [38]. Although variations exist depending on the object and ODD, the spatial frequency of scatter remains sufficiently low to be represented by a sparse number of samples [57]. For example, it was reported through anthropomorphic phantom studies that, in diagnostic cone-beam CT (CBCT) with a SAD of 100 cm and an axis-to-detector distance (ADD) of 18–56 cm, the spatial scatter distribution can be sampled at rate as low as 5 cm^{-1} [57]. It is worth mentioning that the low spatial frequency scatter assumption is valid for a Compton interaction dominated scatter distribution (which is the most common case). However, in cases where Rayleigh scattering contribution is superior to that of Compton (e.g. after applying an anti-scatter grid), the spatial frequency tends to increase, due to the narrow angle forward directed nature of the respective interactions [13]. Moreover, in regions corresponding to object borders, the scatter distribution will exhibit higher frequency components (especially in industrial testing applications due to sharp object borders), which in turn may require an increased level of spatial sampling [28].

With respect to CT, it was also found that x-ray scatter is a slowly varying distribution as a function of projection angle, and is thus contained within a low angular frequency interval [57]. This can also be linked to the high degree of randomness of scatter interactions in the object as well as to the slow change in ODD. The previously mentioned anthropomorphic phantom studies in CBCT (SAD and ADD of 100 cm and 18–56 cm, respectively) found that an angular sampling every 25° proves sufficient for adequately representing the respective scatter distribution.

Both observations are highly important for x-ray scatter simulation (Chapter 4) and correction (Chapter 5) as the low angular and spatial frequency assumption permits subsampling both spatially and angularly. In other words, for a complete x-ray CT acquisition,

the scatter distribution can be highly accurately represented by a coarse grid of detector pixel measurements and sparse projections.

As for the behavior of scatter in the energy domain, some intuitive observations can already be made with the aid of Chapter 2.2. Firstly, since Compton scattered photons contribute to the bulk of the scatter signal, the original x-ray spectrum will be shifted to the lower energies due to the energy shift experienced during this type of interaction. Several studies have confirmed this hypothesis [14], [15], [58]. However, if compared to the spatial domain characterization, the evaluation of the behavior of x-ray scatter in the energy domain still remains limited. The advent of energy-resolved PCDs for x-ray imaging adds motivation to the investigation of energetic properties of x-ray scatter.

As the amount of x-ray scatter is a geometrically dependent phenomenon and can thus result in varying level of image degradation, an indicator of the overall scatter amount must be defined. For this purpose, a metric known as the *scatter-to-primary ratio* (SPR) is often used. It is defined by the following expression [39]:

$$SPR = \frac{I_S}{I_P} \times 100\%, \tag{3.2}$$

where I_S and I_P are the overall scatter and primary signal intensity, respectively, measured by the image receptor (or a region of interest). Table 2 provides SPR ranges based on simulations and experiments conducted within the framework of the present thesis as well as several other scatter studies [12], [13] for different x-ray modalities with limited to no collimation.

Table 2. SPR ranges based on simulations and experiments conducted during the present thesis as well as several other scatter studies [12], [13] for different x-ray modalities. The values are given for limited to no collimation.

Modality	**SPR**
Digital radiography [13]	50–160%
Multi-slice CT [12]	10–40%
CBCT [12], [13]	50–160%
Energy-resolved radiography (1D detectors)	20–40%
Energy-resolved multi-slice CT (2D detectors)	15–35%

3.1.2. Scatter behavior in the energy domain based on simulations

In order to perform x-ray scatter characterization in the energy domain, an analysis of various energy-resolved scatter images obtained with the aid of the developed simulation software (Chapter 4.3) was conducted.

The simulations were performed on a simplified numerical thorax phantom (Figure 3.2) placed in a radiographic geometry with a varying air gap (Figure 3.3). A tungsten anode (17°) x-ray tube was considered. The tube parameters were set to 110 kV and 1 mAs with 0.25 cm of aluminum filtration. A point x-ray source was considered. In order to study the scatter signals due to purely photon-object interactions, a perfect (DRM – identity matrix) 512×512 pixel energy-resolved x-ray detector was used with a pixel size of 1 mm and energy bin width of 1 keV. In addition, for the same reason, photon noise was not included.

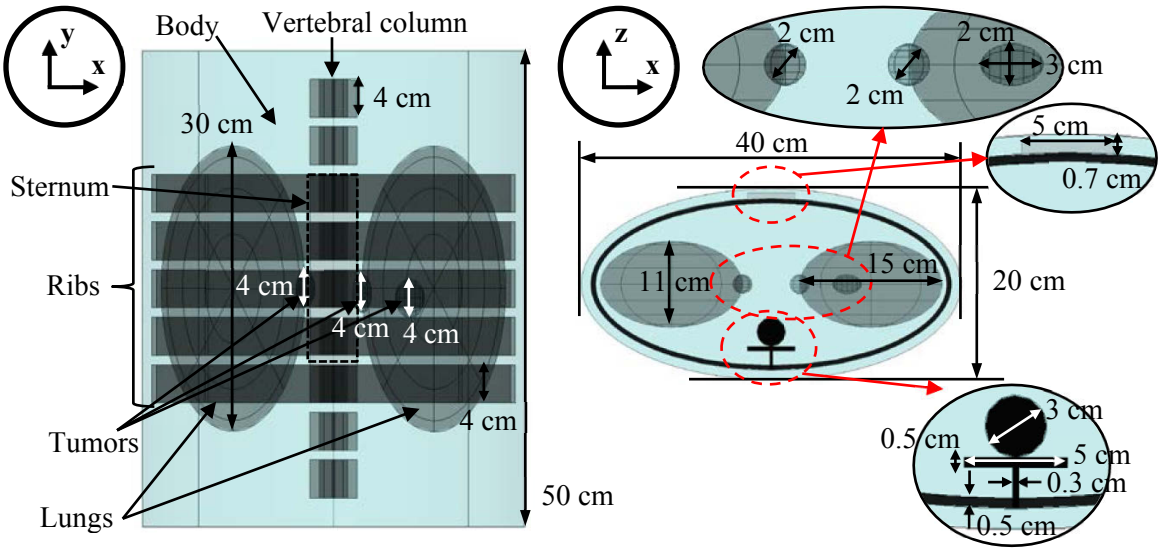

Figure 3.2. Numerical thorax phantom (x-y and x-z views). Insets for internal components are also provided for the x-z view. The body is composed of water. Vertebral column, sternum and ribs are modeled with cortical bone. Lungs are composed of air and tumor lesions are represented by polymethyl methacrylate (PMMA).

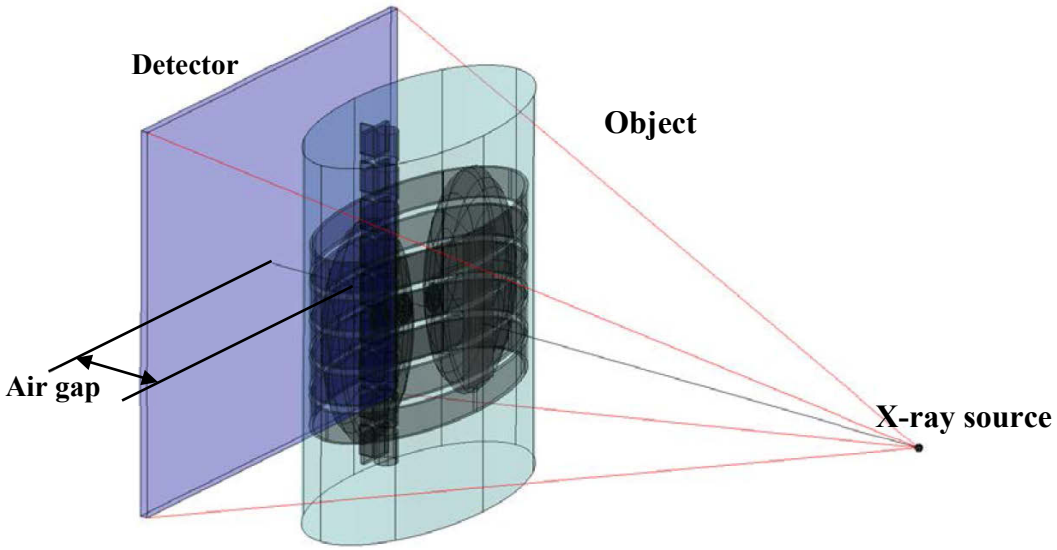

Figure 3.3. Acquisition geometry used for spectral scatter analysis. SDD was 100 cm and was fixed while the air gap was varied: 1, 10, 20 and 30 cm

Firstly, a simulated primary (scatter free) attenuation image of the inspected object (Figure 3.2) in the geometry outlined in Figure 3.3 (air gap of 10 cm) is presented to provide insight on the object structure distribution on the detector plane (Figure 3.4). The attenuation image was computed by applying a discrete version of (2.18).

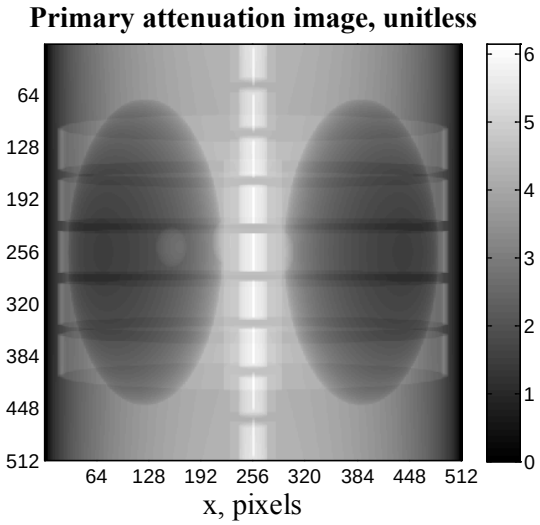

Figure 3.4. Primary attenuation image provided for phantom structure reference (pixel size 1 mm). Note the areas with low (lungs) and high attenuation (vertebral column), respectively.

The simulated x-ray scatter image (total number of photons over all energy channels) of the object from Figure 3.2 in the acquisition geometry of Figure 3.3 (air gap of 10 cm) is presented in Figure 3.5. The SPR computed via (3.2) was 77%, 65%, 62% and 60% for an air gap of 1, 10, 20 and 30 cm, respectively.

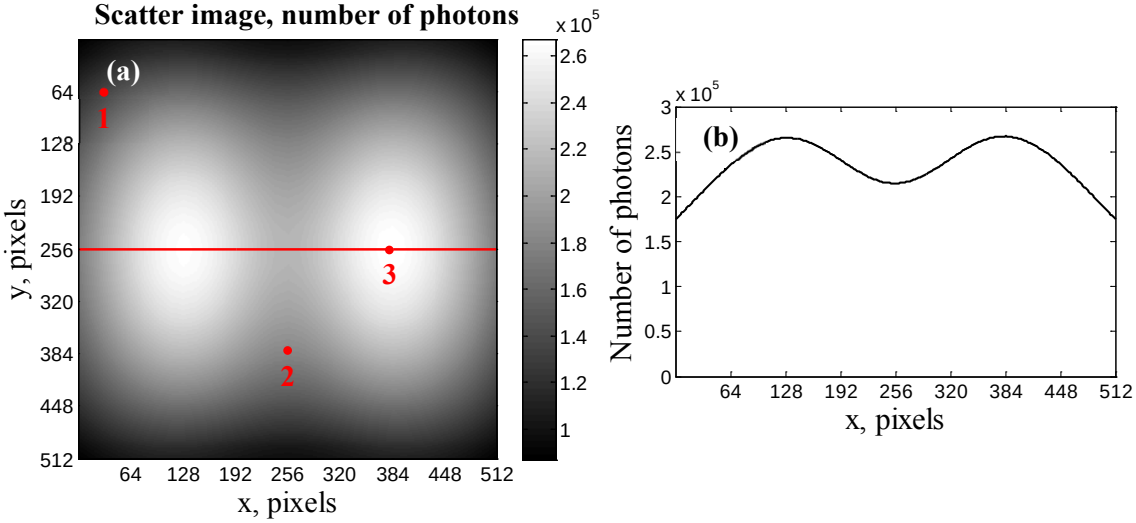

Figure 3.5. Number of photons (all energy channels) scatter image (a) with several pixels indicated for demonstration of scatter spectra (Figure 3.6). The central horizontal profile is also traced (b). Note the variations in scatter level corresponding to internal object structures: lower and higher levels are observed in the area of high (vertebral column) and low attenuation (lungs), respectively. Pixel size was 1 mm. SPR was 65%.

The scatter spectra measured at pixels marked in Figure 3.5 are depicted in Figure 3.6. These spectra have also been further separated into single (scattering after one interaction) and multiple (scattering after two or more interactions) components to provide more in-

sight on the spectrum shape origins. Additionally, primary x-ray photon spectra for the concerned points are also shown for spectrum shape comparison.

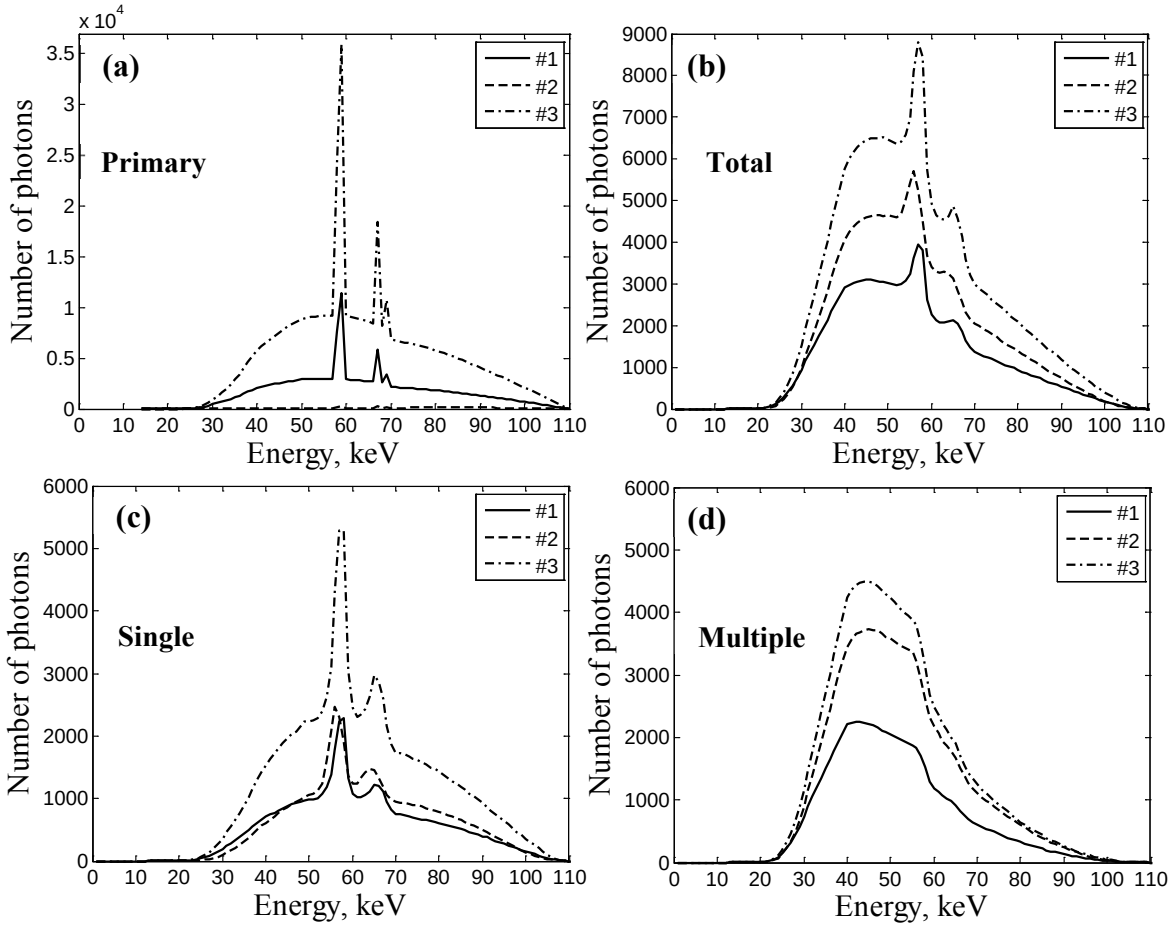

Figure 3.6. Scatter spectra measured in the pixels marked in Figure 3.5. Primary (a), total scatter (b), single (c) and multiple scatter (d) components are presented. Spectra were obtained using regularly spaced 1 keV energy bins.

From Figure 3.6a and Figure 3.6b the validity of global observations with respect to the scatter spectrum shape outlined in Chapter 3.1.1 is confirmed. Although overall the total scatter (b) exhibits a certain similarity with the primary spectrum (a), the shift towards low photon energies is apparent. By viewing the curves from (d), it can be deduced that this is mostly due to the contribution of photons undergoing multiple interactions. In contrast to the total scatter spectra, the ones obtained for single scatter interactions (c) exhibit a closer resemblance to the shape of the primary spectrum (a) with an additional broadening of characteristic peaks due to Compton interactions. Further observations of (b) indicate that the total scatter spectrum shape remains similar to a large extent across the considered pixels while the photon level changes. The same could be said for the multiple (d), but not for the single (c) scatter spectra. Additionally, note the low-energy photon part of single scatter, which tends to deform in a way similar to that of the primary spectrum. Finally, since the contribution of multiple scatter is higher or equal than that due to first order interactions (with the exception of energies around the characteristic peaks), the behavior of the total scatter spectrum is closer to that of the multiple component.

Overall, one important conclusion can be made from Figure 3.6b. The total scatter spectra exhibit mainly level variations while preserving their shape in the first approximation across various spatial locations.

In order to provide some insight on the spatial dynamic of the scatter distributions, scatter images for the extreme air gap cases (1 and 30 cm) are shown in Figure 3.7 alongside the previously inspected case of 10 cm (Figure 3.5).

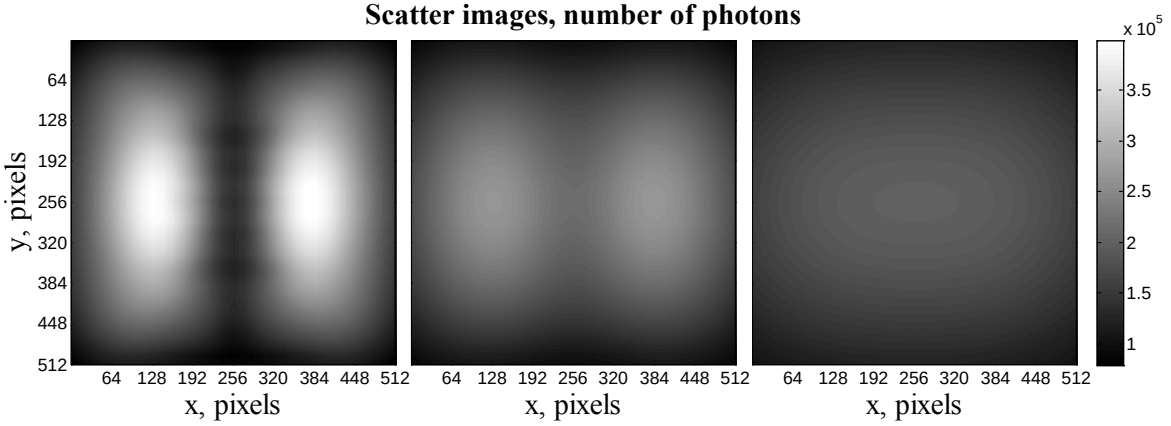

Figure 3.7. Number of photons (all energy channels) scatter images obtained with a 1 (a), 10 (b) and 30 (c) cm airgap. Note the decrease in magnitude and spatial variations with increasing airgap. Pixel size was 1 mm. SPRs for 1, 10 and 30 cm airgap images were 77%, 65% and 60%, respectively.

From Figure 3.7 one can immediately notice the decrease in scatter level as well as the spatial variability of the scatter distribution. When the object is within close proximity of the detector (1 cm) the scatter images exhibits a certain level of structural information (e.g. the zone corresponding to the vertebral column), whilst for the 30 cm air gap the image is practically flat. This behavior is consistent with existing observations of the spatial properties of scatter (Chapter 3.1.1).

For a further confirmation of the visual observation of first order shape variations of the total scatter spectral distribution, the normalized root-mean-square error (NRMSE) between an average spectrum and the individual pixel spectra as a function of energy was computed for varying airgap scatter images with the aid of the following expression:

$$NRMSE(E)=\frac{\sqrt{n_p^{-1}\sum_{\mathbf{p},E}\left(N_S(\mathbf{p},E)-\overline{N}_S(E)\left(\sum_E N_S(\mathbf{p},E)\right)\left(\sum_E \overline{N}_S(E)\right)^{-1}\right)^2}}{\overline{N}_S(E)}\times 100\%, \tag{3.3}$$

where $\boldsymbol{N_S}(\mathbf{p},E)$ is the number of scattered photons measured in pixel $\mathbf{p}$ and channel E, $\overline{N}_S(E)$ is the average number of scattered photons in channel E and n_p is the total number of pixels in the image. Note that the overall (all energy channels) photon level of $\overline{N}_S(E)$ is adjusted to that of $\boldsymbol{N_S}(\mathbf{p},E)$. This is done in order to specifically examine spectrum shape differences. The NRMSE was calculated for overall, single and multiple scatter images. Although the detector measured photons from 14 keV to 110 keV, a bandwidth limitation to 30–90 keV was performed to eliminate channels with insufficient photon statistics as numerical simulation noise may contribute to an inaccurate representation of the curves. The resulting NRMSE curves for varying air gap are visualized in Figure 3.8.

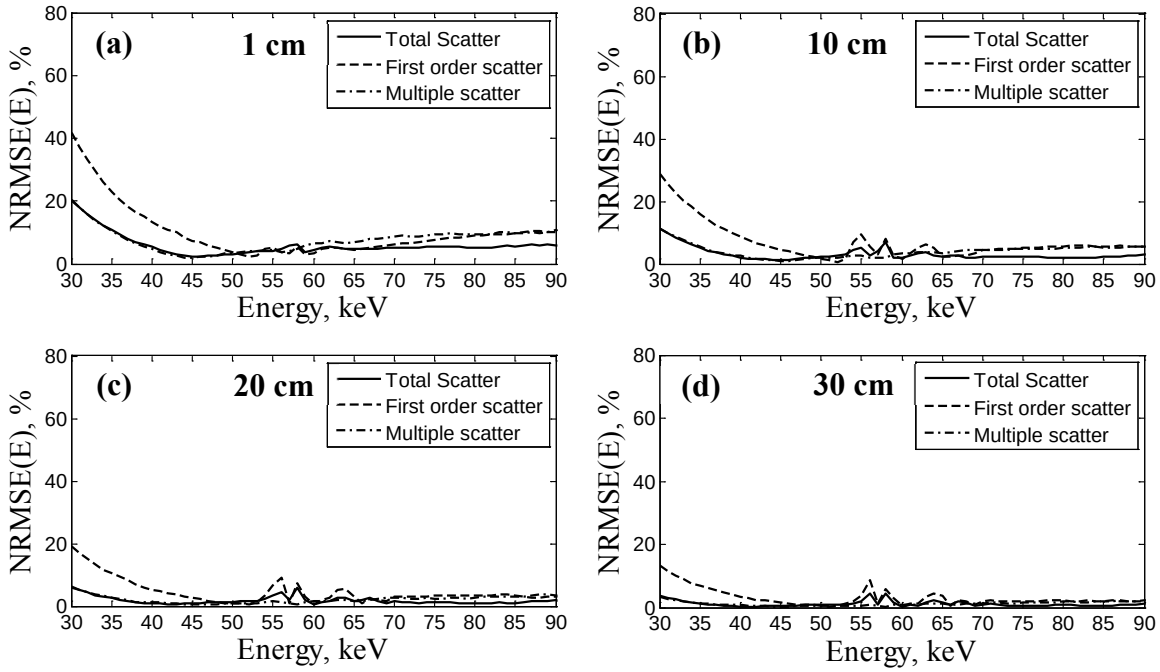

Figure 3.8. Relative standard deviation computed via (3.3) for energy-resolved scatter images of the phantom presented in Figure 3.2 with an air gap of 1 (a), 10 (b), 20 (c) and 30 (d) cm. Note that in addition to the total scatter spectra, single and multiple components were also examined.

The resulting NRMSE curves from Figure 3.8 further confirm that total and multiple scatter spectra preserve spectral shape characteristics for energies greater than 40 keV (NRMSE remains relatively constant) while the spectra corresponding to single scattering interactions change these characteristics (varying NRMSE) in the region up to 55 keV depending on the air gap. An exception to the overall trend of the total spectra can be also seen around the characteristic peak area (58 keV and 67 keV). Note that with increasing ODD the preservation of spectral shape assumption becomes even more valid. With the exception of the spectral energy range of less than 35 keV (c) and 33 keV (d), the total scatter preserves spectral shape and is more linked to the multiple scatter behavior. The latter observation is indicative of the multiple component fraction growth with respect to the single scatter component with increasing air gap. Furthermore, the single scatter displays a less variable spectral shape with increasing ODD, which also contributes to a decrease in the shape dynamics of the total spectra.

The analysis of NRMSE curves (Figure 3.8) and scatter spectra from images of a numerical phantom with a highly variable composition (Figure 3.2) indicates that the scatter spectrum preserves its shape, in the first approximation, across different detector pixels. This observation becomes more and more valid with air gaps increasing from 1 to 30 cm. Such a behavior is not totally unexpected, as multiple scatter becomes more dominant in the overall scatter spectrum with increasing air gap and it is indicative of global object attenuation. Since global object attenuation changes, the incident spectrum in an approximately equivalent manner, the spectral shape remains preserved. First order scatter events are, however, less randomly distributed in the object and thus the measure of attenuation is less global resulting in a more variable spectral shape. The combination of multiple and first order scatter has, as a result, a spectrum shape, which can be considered preserved in the first approximation.

3.1.3. Scatter behavior in the energy domain based on experiments

Several experiments involving scatter measurements have been conducted in the course of the present thesis (Chapters 4.3.3 and 6.2). In the present chapter, this data is analyzed in order to further verify the scatter spectral shape preservation hypothesis.

First experiment

In the first experiment, a cylindrical PMMA phantom with air cavities and aluminum insert (Figure 3.9) was placed at 280 cm and 2.6 cm from the x-ray source and detector, respectively. The phantom was positioned with the insert being closest to the detector and in the center of the imaged zone. A grid of beam blockers inserted between the source and the inspected object was used to completely absorb the primary radiation in selected zones of the image. Thus, only the scatter component was recorded in these regions. The acquisition parameters were 110 kV and 1 mAs with 0.2 cm of aluminum filtration. The whole object was irradiated. The energy-resolved images were acquired with a horizontally translated linear (1D) 16×1 pixel energy-resolved (1.2 keV width bins) x-ray detector (0.8 mm pixel size). A more detailed description of acquisition configuration and geometry is also available in Chapter 4.3.3.

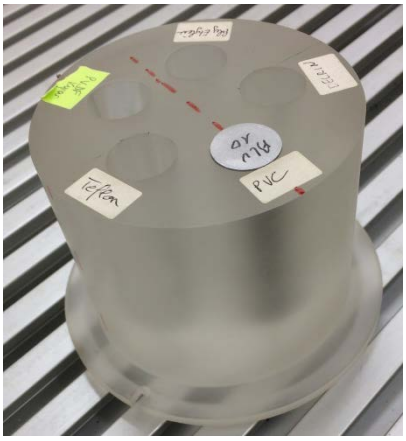

Figure 3.9. Cylindrical PMMA phantom with aluminum insert and air cavities. The height is around 9 cm and the main diameter is 10 cm (base part above flat support). The insert and cavities have a 6 cm height and a 2 cm diameter.

As previously in Chapter 3.1.1, an attenuation image is presented to provide insight on the distribution of object structures on the detector plane (Figure 3.10). Since, however, the primary signal was not readily available during measurements, a total (primary with scatter) attenuation image is presented instead. Attenuation per pixel was computed by applying a discrete version of (2.18) on each image pixel.

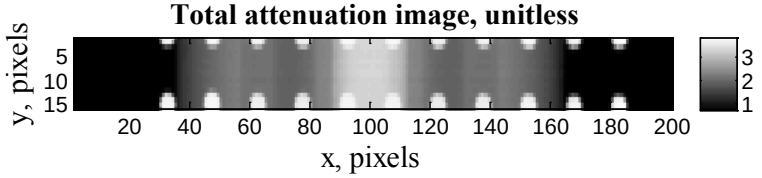

Figure 3.10. Total attenuation image provided for phantom (Figure 3.9) structure reference. Note the areas with low (air cavities) and high attenuation (aluminum insert), respectively. In addition, a segment of the BS grid is also visible (white areas). Pixel size was 0.8 mm.

In order to obtain a scatter image from the spatially sampled scatter data, spatial cubic spline interpolation was performed for each energy channel. The resulting total number of photons image along with the blocker grid image (no object) is presented in Figure 3.11. The SPR associated with the scatter image was 24%.

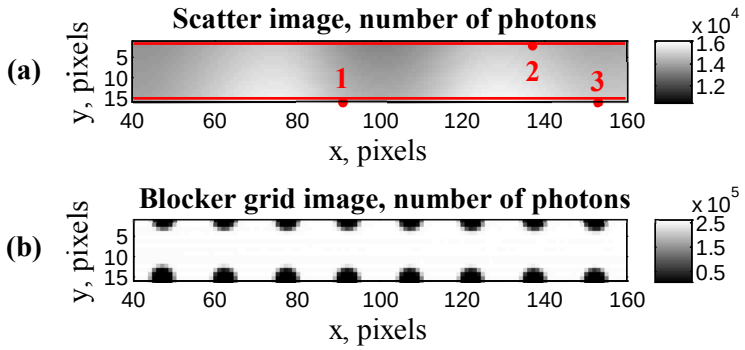

Figure 3.11. Number of photons (all energy channels) scatter (a) and beam blocker grid (b) images corresponding to the first experiment. The blocker grid image demonstrates the locations (dark zones) of scatter samples. Profile and spectrum sample locations are also indicated in (a) for further visualizations in Figure 3.12. These locations were chosen in order to capture the maximum number of true (no interpolation) scatter samples. Pixel size was 0.8 mm. The SPR was 24%.

The two profiles marked in Figure 3.11a are shown in Figure 3.12a. Note that these profiles were traced across locations corresponding to the spatially sampled scatter data. Additionally, Figure 3.12b displays the scatter spectra from various pixel locations indicated in Figure 3.11a. Note that these spectra were also taken from the directly measured scatter data without any interpolation.

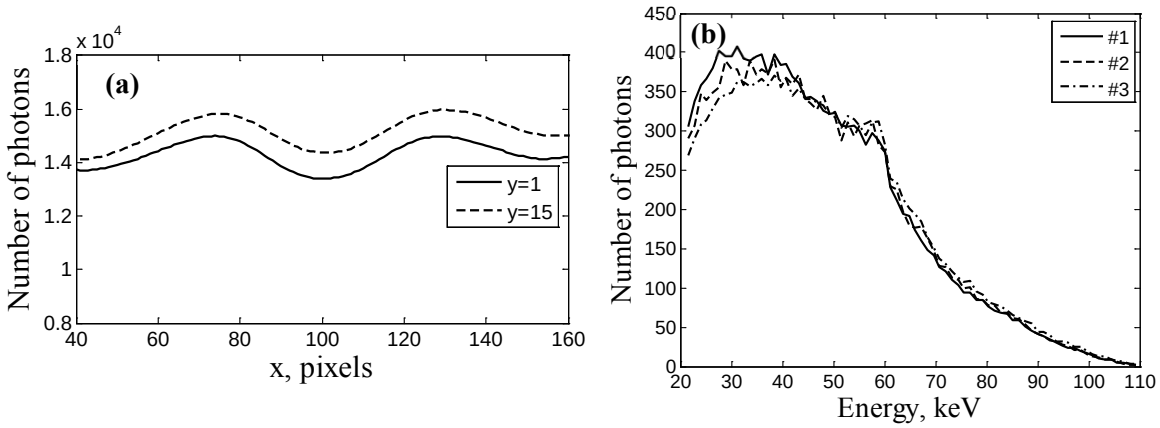

Figure 3.12. Horizontal profiles (a) and spectra (b) from locations indicated in Figure 3.11a (first experiment). Pixel size was 0.8 mm. Spectra were obtained using regularly spaced 1.2 keV energy bins.

From Figure 3.11a and Figure 3.12a it is apparent that the level of spatial variation of scatter in the considered configuration is quite low. However, zones with high and low signal can still be identified and linked to the corresponding internal structures of the phantom. The low magnitude zone (central part) corresponds to the aluminum insert while the high magnitude corresponds to air cavities. The differences in scatter spectra taken from

various pixels in the image are also not substantial and are mostly located in the low-energy interval. Additionally, the shapes of the spectra appear quite similar.

For a more quantitative evaluation of the behavior of scatter in the energy domain, the NRMSE as function of energy was computed with the aid of (3.3) for the spectra measured directly in the beam blocker influenced zones indicated in Figure 3.11b. In order to avoid the channels with immediate proximity to the energy cutoff of the detector and channels with a low photon number (noisy measurements), the energy bandwidth was set to 30–90 keV. The resulting curve is visualized in Figure 3.13.

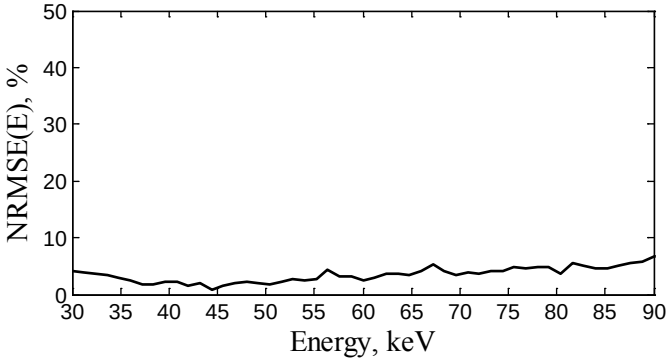

Figure 3.13. Relative standard deviation as a function of energy computed via (3.3) for the directly measured (non-interpolated) scatter spectrum samples (1.2 keV energy bins) obtained in the first experiment.

The analysis of Figure 3.13 reveals a NRMSE which is relatively constant for different energies. This indicates scatter shape preservation at a high level across various spatial sample locations. Additionally, the curve exhibits a certain level of noise, which is directly related to the noise present in the measured scatter spectra.

Despite the object from Figure 3.9 being small compared to the object considered for the simulations in Chapter 3.1.2 (Figure 3.2), it remains sufficiently heterogeneous for its scale. However, from the comparison of Figure 3.8 and Figure 3.13 it can be concluded the object considered in the experiments produces substantially less variable spectra for an equivalent air gap than the simplified thorax phantom considered in the simulation.

The first reason is the influence of the DRM. As in Chapter 3.1.2 a perfect detector was considered, this influence was not taken into account. Based on example response curves of an energy-resolved detector (e.g. Chapter 2.3.3, Figure 2.14), one can conclude that a spectrum shape deformation would occur. This will lead to a much smoother spectrum shape. Thus, a portion of the scatter energy shape variation present with a perfect detector is lost with a real detector.

The second reason is a smaller object fraction imaged in the case of experiments. This zone was about 14% and 99% for experiments and simulation (air gap of 1 cm), respectively. Thus, a larger spatial area was considered in the simulations and more variability in the scatter spectrum shape can be expected.

Second experiment

In order to further investigate the behavior of the scatter energy distribution, a second experiment with an anthropomorphic thorax phantom (Figure 3.14) was performed. Note that this object was substantially larger than the one presented in Figure 3.9. Furthermore, it was more representative of the anatomical regions examined in medical diagnostics. In

order to acquire an anteroposterior (AP) image, the thorax phantom was placed at about 183 cm and 8 cm from the source and detector, respectively. The tube was set to 110 kV and 4 mAs with 2 mm of aluminum filtration. About 90% of the object volume was irradiated. Additionally, a 128×1 pixel energy-resolved (≈2.5 keV width bins) CdTe detector with a pixel pitch of 0.8 mm was used. As in the previous experiment, the detector was translated horizontally to obtain 2D images. Finally, in order to measure scatter, 3 lead strips were placed between the source and the object. More information on the system settings and geometry can be found in Chapter 6.2.1.

Figure 3.14. Anthropomorphic thorax phantom. The phantom is about 50 cm in height with a width and thickness of 28 cm and 19 cm, respectively, at the level of the heart.

As for the first experiment, a total attenuation image corresponding to the second experiment (AP projection) is presented to provide insight on object structures positioning with respect to the detector plane (Figure 3.15).

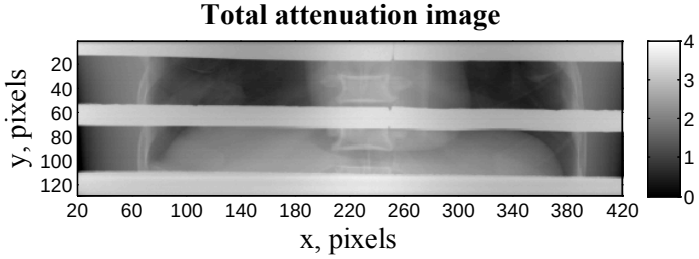

Figure 3.15. Total attenuation image provided for phantom (Figure 3.14) structure reference. Note the areas with low (lungs) and high attenuation (vertebral column), respectively. In addition, the lead strips are also visible (light gray stripes). Pixel size was 0.8 mm.

For the scatter image (AP projection), a regularized spline interpolation (Chapter 5.2.3) was applied in order to obtain the full image from the spatially sampled data. The scatter image along with the image of the lead strips (no object) is presented in Figure 3.16. The SPR for the AP projection was 33%.

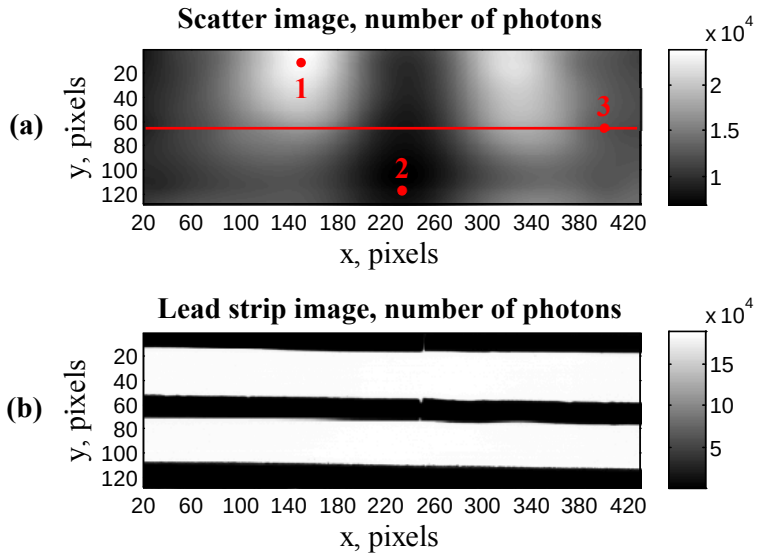

Figure 3.16. Number of photons (all energy channels) scatter (a) and lead strip (b) images corresponding to the second experiment. The latter demonstrates the locations (dark zones) of scatter samples. Additionally, profile and spectrum sample locations are indicated in (a) for further visualizations in Figure 3.17. Pixel size was 0.8 mm. SPR was 33%.

Figure 3.17a shows the profile marked in Figure 3.16a. Additionally, Figure 3.17b displays the scatter spectra from different pixel locations indicated in Figure 3.16a. Note that, as in the previous experiment, the profile and the spectra were taken from the directly measured scatter data without the influence of interpolation.

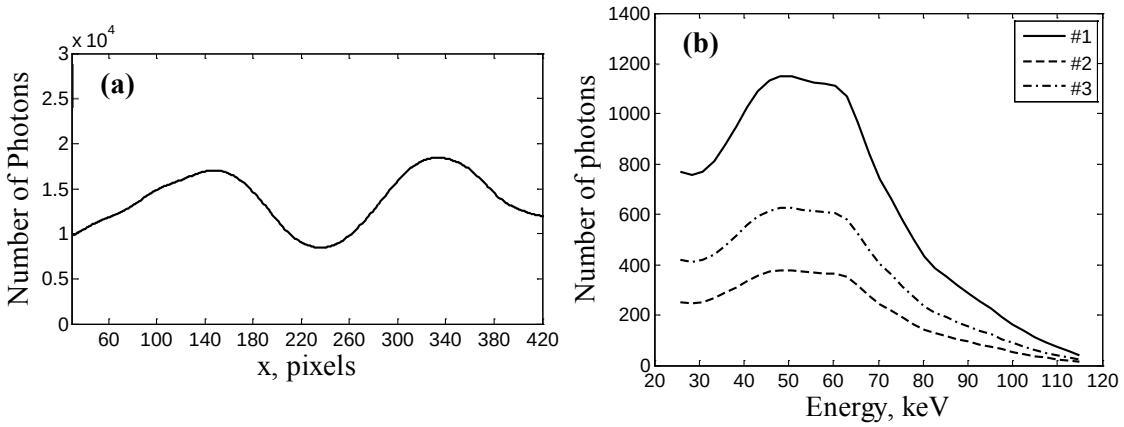

Figure 3.17. Horizontal profile (a) and spectra (b) from locations indicated in Figure 3.16a (second experiment). Pixel size was 0.8 mm. Spectra were obtained using regularly spaced 2.5 keV energy bins.

As the thorax phantom is more heterogeneous and larger than the cylindrical phantom employed previously, the level of spatial variation of the x-ray scatter distribution also becomes higher (Figure 3.16a and Figure 3.17a). Additionally, zones with high and low scatter level can be identified. These can be connected to the internal structures of the phantom, such as lungs (high magnitude zones around pixel #150 and #340) and vertebral column (low magnitude zone around pixel #230). Scatter spectra taken from different pixels

in the image also appear to vary more than the ones presented in Figure 3.12. However, the shapes of the spectra still appear to be quite similar.

In order to acquire more insight on the behavior of x-ray scatter in the energy domain for the considered phantom, additional scatter images were acquired at 45° and 90° with respect to the initial position (0°), discussed previously. The air gap remained approximately the same. The SPR for the 45° and 90° image was 30% and 33%, respectively. The NRMSE as a function of energy was then computed via (3.3) for the scatter samples taken from each of the individual images as well as from all the images. The locations for these samples in the image are indicated in Figure 3.16b (dark zones). As in the previous experiment, channels close to the energy cutoff of the detector and channels with a low photon number (noisy measurements) were neglected by using the energy bandwidth of 30–90 keV. The resulting NRMSE curves are visualized in Figure 3.18.

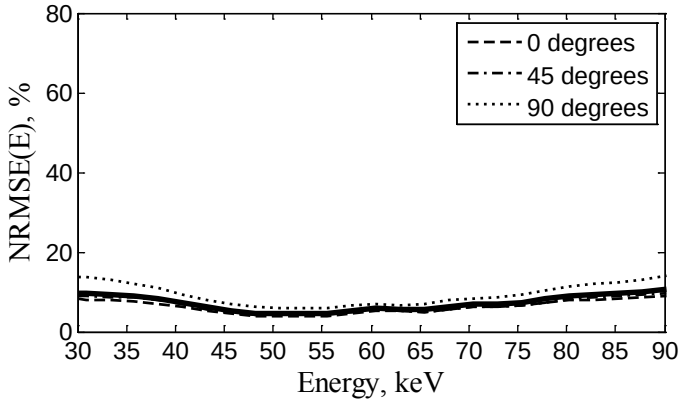

Figure 3.18. Relative standard deviation as a function of energy computed via (3.3) for the measured scatter spectrum samples (2.5 keV energy bins) from different projection images as well as from all images (second experiment).

Figure 3.18 reveals that for the 0° and 45° the NRMSE remains quite constant across different energy channels. Slightly more variability can be overserved in the 90° case, especially in channels less than 37 keV and greater than 75 keV. Finally, the curve produced based on the samples from all projections appears to display a similar dynamic to both the AP and 45° projections while differing slightly from the 90° projection. Thus, one can state that the scatter spectrum shape exhibits a low level of variability overall across different projections while some of them display a higher or lower level of variability, respectively. This phenomenon can be explained by the changing position of the object internal structures with respect to the detector plane. Another reason can be DRM differences across different detector pixels, as gain correction does not completely eliminate them. Finally, as the energy channels of the employed detector are larger than the ones of the detector used in the previous experiment, the curves do not display the noise present in the curve from Figure 3.13.

The anthropomorphic thorax phantom is much closer to the simplified version used in the simulations (Figure 3.2, Chapter 3.1.2). Thus, the fact that the individual projection NRMSE curves (Figure 3.18) remain similar to the ones obtained from the numerical thorax phantom with a similar air gap (Figure 3.8, Chapter 3.1.2) is expectable. This can be further supported by the imaged fraction of the object being about 27%. Thus a larger portion of the object is imaged compared to the previous experiment.

3.1.4. Conclusion

From the simulations presented in Chapter 3.1.2 and the experiments described in Chapter 3.1.3 it can be concluded that the scatter spectrum shape can be globally preserved for a variety of air gaps and objects. The hypothesis tends to become less valid with larger and more heterogeneous objects within close proximity of the detector. In this case, the shape variations manifest predominantly in the low-energy interval. Additionally, based on the multiple-projection experiment with the anthropomorphic phantom, one can state that scatter may also preserve its spectrum shape across varying projections of the same object. However, in order to further validate this statement, more multiple-projection acquisitions need to be performed with different air-gaps and objects.

Since the scatter spectrum shape can be considered approximately preserved, the spectral and spatial aspect of an energy-resolved scatter image can be potentially decoupled. This hypothesis is even more valid in the case of realistic energy-resolved detectors, as the corresponding energy response tends to reduce the scatter spectrum shape variations. This simplifies the representation of a given energy-resolved image, which in turn can be utilized in spectral x-ray scatter simulation as well as in scatter estimation and correction algorithms. The decoupling of spatial and energy scatter components can potentially lead to speed ups in scatter simulations and reduce the complexity of scatter correction.

3.2. Effect of scattered radiation in x-ray imaging

Having characterized x-ray scatter in the spatial and energy domains, one can describe the resulting effect in radiographic and tomographic imaging. As noted in Chapter 3.1.1, instead of measuring only the primary photons, the total signal measured by a given detector pixel is actually a sum of primary and scattered photons, thus the attenuation expressions for integration mode (2.18) and energy-resolved mode (2.20) x-ray attenuations will take the following forms:

$$A_m(\mathbf{p}) = -\log\left(\frac{\int_{E_1}^{E_2} D(E)\left(N_P(\mathbf{p},E)+N_S(\mathbf{p},E)\right)E\,\mathrm{d}E}{\int_{E_1}^{E_2} D(E)N_0(\mathbf{p},E)E\,\mathrm{d}E}\right) \tag{3.4}$$

and

$$\mathbf{A_m}(\mathbf{p}) = -\log\left(\frac{\mathbf{D}\times\left[\mathbf{N_P}(\mathbf{p})+\mathbf{N_S}(\mathbf{p})\right]}{\mathbf{D}\times\mathbf{N_0}(\mathbf{p})}\right). \tag{3.5}$$

The indices *P* and *S* in (3.4) and (3.5) refer to primary and scatter components of the concerned quantity (number of photons), respectively. As a result of the additional component (scatter), the signal measured by a given x-ray detector pixel becomes biased. The Beer-Lambert law is no longer valid as not only primary photons are measured. Thus, when comparing the scatter free cases (2.18) and (2.20) with their counterparts (3.4) and (3.5) for the scatter corrupted case, it can be concluded that a sub-estimation in attenuation will occur. This leads to local spatial contrast reduction in radiography [39] and tomography [12] as well as a certain decrease in resolution as interior object contours and small structures become less discernable (Chapter 3.2.1 and Chapter 3.2.2). It will also contribute to beam hardening and streak artifacts in CT [59].

For multi-energy applications the presence of scatter affects energy weighting aiming to improve image quality [15] and disturbs the efficacy of multi-energy applications, such as *basis-material decomposition* [14], [60].

Chapters 3.2.1 and 3.2.2 illustrate x-ray scatter effects in integration mode radiography and CT, respectively, while Chapter 3.2.3 provides insight on the influence of scatter in a typical multi-energy application (basis material decomposition).

3.2.1. In radiography

In order to give an example of scatter influence in x-ray radiography, attenuation images with and without scatter were simulated (Figure 3.19). For the former and latter attenuation was computed via (2.18) and (3.4), respectively. The numerical phantom and geometry used were those presented in Chapter 3.1.2 (Figure 3.3 and Figure 3.2) with the air gap being set to 10 cm. Additionally, a DRM corresponding to a realistic energy-resolved PCD and photon noise (Poisson model) were also incorporated in the simulations. Finally, from this point, the notions *primary image* and *total image* will be employed for the images obtained in the absence and presence of scattered radiation, respectively.

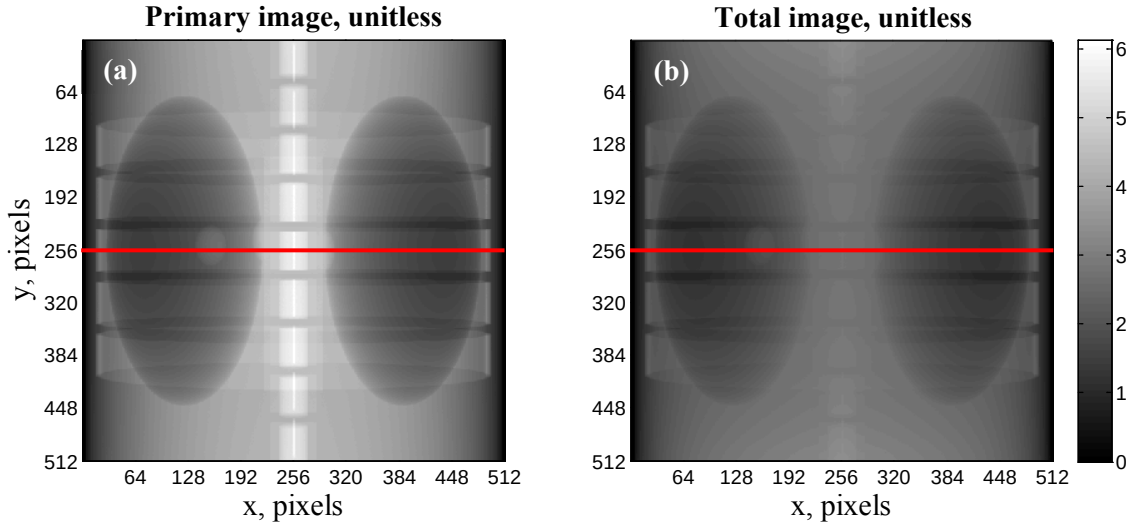

Figure 3.19. Primary (a) and total (b) attenuation images obtained with a tube set to 110 keV and 1 mAs with 2.5 mm of aluminum filtration. SPR for the total image was around 60%. The locations for the following profile visualization (Figure 3.20) are marked in red. Pixel size was 1 mm.

The analysis of Figure 3.19 indicates severe decrease in image quality when scatter is present. The total image (b) exhibits lower contrast, reduced contour visibility and an overall decrease in attenuation values when compared to the primary image (a). The vertebral column becomes nearly indiscernible. The same is true for the sternum and ribs in the central part of the image.

In order to provide more insight on scatter induced degradations, central horizontal profiles of the total and primary images were also traced (Figure 3.20).

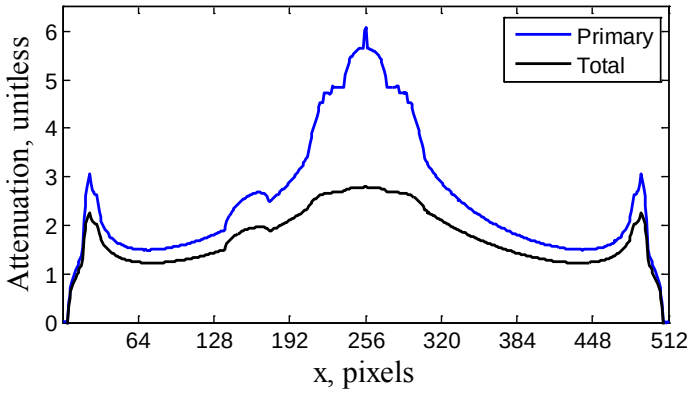

Figure 3.20. Primary and total central horizontal profiles indicated in Figure 3.19. Pixel size was 1 mm.

When analyzing the profiles from Figure 3.20 the overall bias in attenuation induced by the scatter is once again prominent. It is strongest in the middle part of the profile. Structural information in that region is almost completely lost in the presence of scatter. This can be linked to a high local SPR in the respective zone. Since this region exhibits the highest level of attenuation (a low primary signal) and the scatter signal varies relatively slowly as a function of spatial location (Chapter 3.1.1), the local SPR in the central part becomes higher compared to other image locations where much lower attenuation levels are exhibited.

Finally, one can also quantify the error induced by scatter by comparing attenuation values in each pixel of the total and primary images. In order to do this, the average relative error per image pixel ε_r is used:

$$\varepsilon_r = n_p^{-1}\left(\sum_{\mathbf{p}} \frac{\left|A_P(\mathbf{p}) - A_T(\mathbf{p})\right|}{A_P(\mathbf{p})}\right)\times 100\,\%\,, \tag{3.6}$$

Where $A_P(\mathbf{p})$ and $A_T(\mathbf{p})$ are attenuation values measured in a given pixel of the primary and total image, respectively. The application of (3.6) on the images presented in Figure 3.19 leads to an average relative error of 25.3%.

Based on the analysis in the current chapter, one can conclude that in x-ray radiography the presence of scatter introduces bias in attenuation images, the level of which is dependent on local SPR. Additionally, local contrast and object contour visibility are also reduced. Finally, it is important to note that all the previously listed negative effects of scatter are directly linked to the global SPR. Thus, for cases with a lower or higher global SPR less or more image degradation, respectively, can be expected.

The negative effects of scatter on radiographic images can lead to errors in the various domains utilizing this modality. More precisely, the decreased contrast and small structure detectability can lead to false or inaccurate diagnosis in medical radiography. The same effect can entail an inability to detect fine defects in non-destructive testing (NDT) and to identify dangerous small size objects in security.

3.2.2. In Computed Tomography

To illustrate the effect of x-ray scatter in CT, representative volumes (primary and total) were reconstructed from a set of simulated projections of the phantom presented in Chapter 3.1.2 (Figure 3.2). As previously, a DRM corresponding to a realistic energy-

resolved PCD and photon noise (Poisson model) were also incorporated in the simulations. Acquisition geometry and system information were quite similar to the ones employed in Chapter 3.1.2. More information on geometry and system parameters can be found in Chapter 6.1.1. The projection set was composed of 360 equally spaced projections (1° increments). The applied reconstruction algorithm was FDK. The reconstructed volumes were then converted to HU via (2.26). Finally, central slices (CT images) from the corresponding volumes were selected and visualized (Figure 3.21).

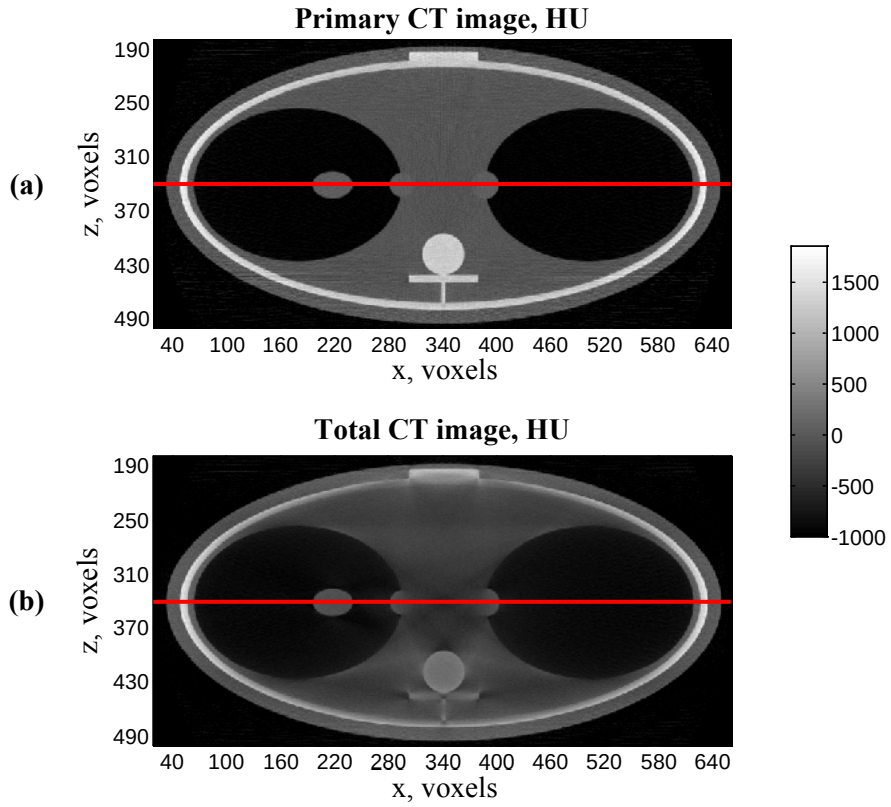

Figure 3.21. Primary (a) and total (b) CT images obtained with a tube set to 110 keV and 1 mAs with 2.5 mm of aluminum filtration. SPR for the projection dataset used to generate the total image was around 17% on average. Locations for the profile visualization in Figure 3.22 are marked in red. Voxel size was 0.65 mm.

When primary (a) and total (b) CT images from Figure 3.21 are observed, the image degradation due to scattered radiation is once again apparent. When comparing (b) to (a), contrast decrease and interior structure contour distortion in certain image regions can be observed (e.g. vertebral column, tumor inserts and sternum). Moreover, image artifacts such as beam hardening (homogeneous tissue regions of the image) and streak artifacts (vertebral column, center part of the image) can also be identified.

Note that in CT the negative effects of scatter are less uniform with contrast being almost completely preserved in some areas (e.g. left and right borders of the phantom) and the addition of artifacts. This can be linked to the reconstruction process described in Chapter 2.4.2. Because the considered CT image is the result of applying FDK on a collection of projections with different SPRs, the amount of scatter as a function of reconstructed voxel would be much more variable compared to the respective amount as a function of pixel for a fixed projection.

Additionally, one can note that, visually, the amount of degradation caused by the presence of scatter is lower than in the previously observed radiography case (Chapter 3.2.1, Figure 3.19). This can be explained by comparing the corresponding global SPRs. Since the SPR in the considered tomographic case was 17% on average for all projections over the 60% demonstrated in the radiography example, the negative effect of scatter for the examined tomographic images is also lower. In general, SPRs in CT tend to be lower than in radiography because of larger air gaps and additional detector collimation.

For further comparison of total and primary CT images, corresponding central horizontal profiles are shown Figure 3.22.

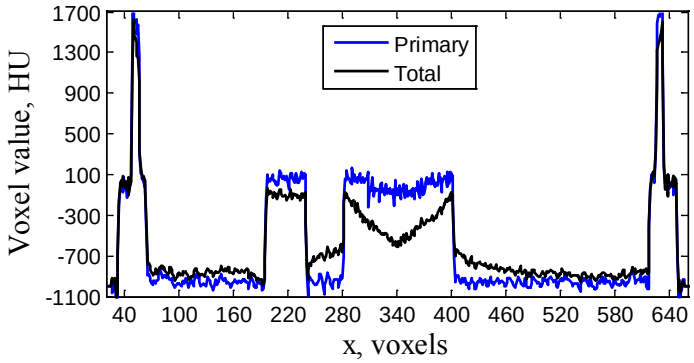

Figure 3.22. Primary and total central horizontal profiles indicated in Figure 3.21. Voxel size was 0.65 mm.

The comparison of primary and total profiles of Figure 3.22 further reveals bias and artifacts (central part) induced by scatter. Additionally, the edges linked to the elliptical structures simulating tumor lesions in the central part (voxel #310 and voxel #360) are completely absent from the total profile. However, some regions (voxels below #120 and voxels above #560) of the total and primary profiles are quite similar, which is consistent with the contrast preservation in these areas, previously observed in Figure 3.21. Another important point is that compared to attenuation in the radiography case, the scatter induced bias does not always manifest itself as sub-estimation of voxel values. This can be linked to the fact that the volume is a result of a reconstruction from several projections with varying associated scatter distributions. In addition, the filtering employed during reconstruction can also contribute to this effect as it tends to enhance high frequency details causing the production of bright streaks (over-estimation of voxel values) [59]. Scatter contributes to this effect and thus over-estimation in certain volume regions can be observed (e.g. bright steaks between the lungs and vertebral column in Figure 3.21).

In conclusion, the average relative error between the total and primary CT images per voxel was also computed via (3.6). Note that in this case the attenuation values were replaced by voxel values and the number of pixels is replaced by the number of voxels in the CT slice. The resulting error was 27.6%. This means that although visually the CT images presented in Figure 3.21 appear less degraded by scatter than the ones corresponding to a radiographic simulation (Chapter 3.2.1, Figure 3.19), quantitatively, on average, the error remains similar. Thus, in CT, the negative effect of scatter can be more severe for a given SPR than in radiography.

The negative effects from the presence of scatter in CT acquisitions can not only lead to errors in patient diagnosis but also to cancer treatment planning inaccuracies. This is because such treatments rely on the CT data in a quantitative (e.g. electron density calcula-

tion) and qualitative (e.g. structure delineation) manner [61]. Furthermore, as in the case of radiography, defect and dangerous goods detection with industrial or security scanners, respectively, can also be compromised by the presence of scatter.

3.2.3. In basis material decomposition

As previously outlined in Chapter 2.4, basis material decomposition of energy-resolved x-ray images aims at discriminating individual material components present within the inspected object. In order to examine the effect of scatter in such applications, basis material decomposition of simulated energy-resolved radiographic images was performed.

The inspected object, geometry and tube settings matched the ones applied for scatter energy shape analysis (Figure 3.3 and Figure 3.2, Chapter 3.1.2). Out of the variety of air gaps employed in Chapter 3.1.2, 10 cm was used. Additionally, the perfect (identity) DRM was replaced by one corresponding to realistic energy-resolved detector and Poisson noise was added to the data. Different scatter levels were also considered, namely SPRs of 60%, 30%, 12% and 3%, respectively. Note that the true scatter level for the considered acquisition set up was the one corresponding to the 60% SPR case. The other cases simulate partial loss of scatter level due to some form of preliminary correction or collimation. The 30%, 12% and 3% SPR cases correspond to 50%, 20% and 10% fractions of the initial scatter level. The energy-resolved primary and total images were regrouped into 2 energy bins: 14–50 keV and 51–110 keV. Then, attenuation as a function of energy channel per image pixel was computed via (2.20) and (3.5) for the primary and total images, respectively.

For the material decomposition part, 2 basis materials were considered: water and bone. A 3rd order version of the polynomial presented in (2.23) was applied on each pixel of the energy-resolved primary and total attenuation images:

$$\begin{aligned} l^e_{water}(\mathbf{p}) &= \sum_{i,j}^{3} \alpha_{1,i,j} \left(A_1(\mathbf{p})\right)^i \left(A_2(\mathbf{p})\right)^j \\ l^e_{bone}(\mathbf{p}) &= \sum_{i,j}^{3} \alpha_{2,i,j} \left(A_1(\mathbf{p})\right)^i \left(A_2(\mathbf{p})\right)^j \end{aligned}, \tag{3.7}$$

where $l^e_{water}(\mathbf{p})$ and $l^e_{bone}(\mathbf{p})$ are water and bone equivalent thicknesses, respectively and $A_1(\mathbf{p})$, $A_2(\mathbf{p})$ are attenuations corresponding to the low-energy (LE) and high-energy (HE) bins of 14–50 keV and 51–110 keV, respectively. All polynomial terms were considered in the decomposition process.

In order to estimate the polynomial coefficients from (3.7), calibration on known thickness samples of water and bone was performed in the absence of scatter. The considered water and bone thicknesses were 0–22 cm (0.5 cm step) and 0–70 cm (0.5 cm step), respectively. Then, with the aid of known $l^e_{water}(\mathbf{p})$, $l^e_{bone}(\mathbf{p})$, $A_1(\mathbf{p})$ and $A_2(\mathbf{p})$, a linear least squares estimation was applied to determine the coefficients $\alpha_{1,i,j}$ and $\alpha_{2,i,j}$ for (3.7).

The polynomials from (3.7) with their preliminarily estimated coefficients were used to decompose the primary and total attenuation images onto a water-bone materials basis. The resulting material images are shown in Figure 3.23.

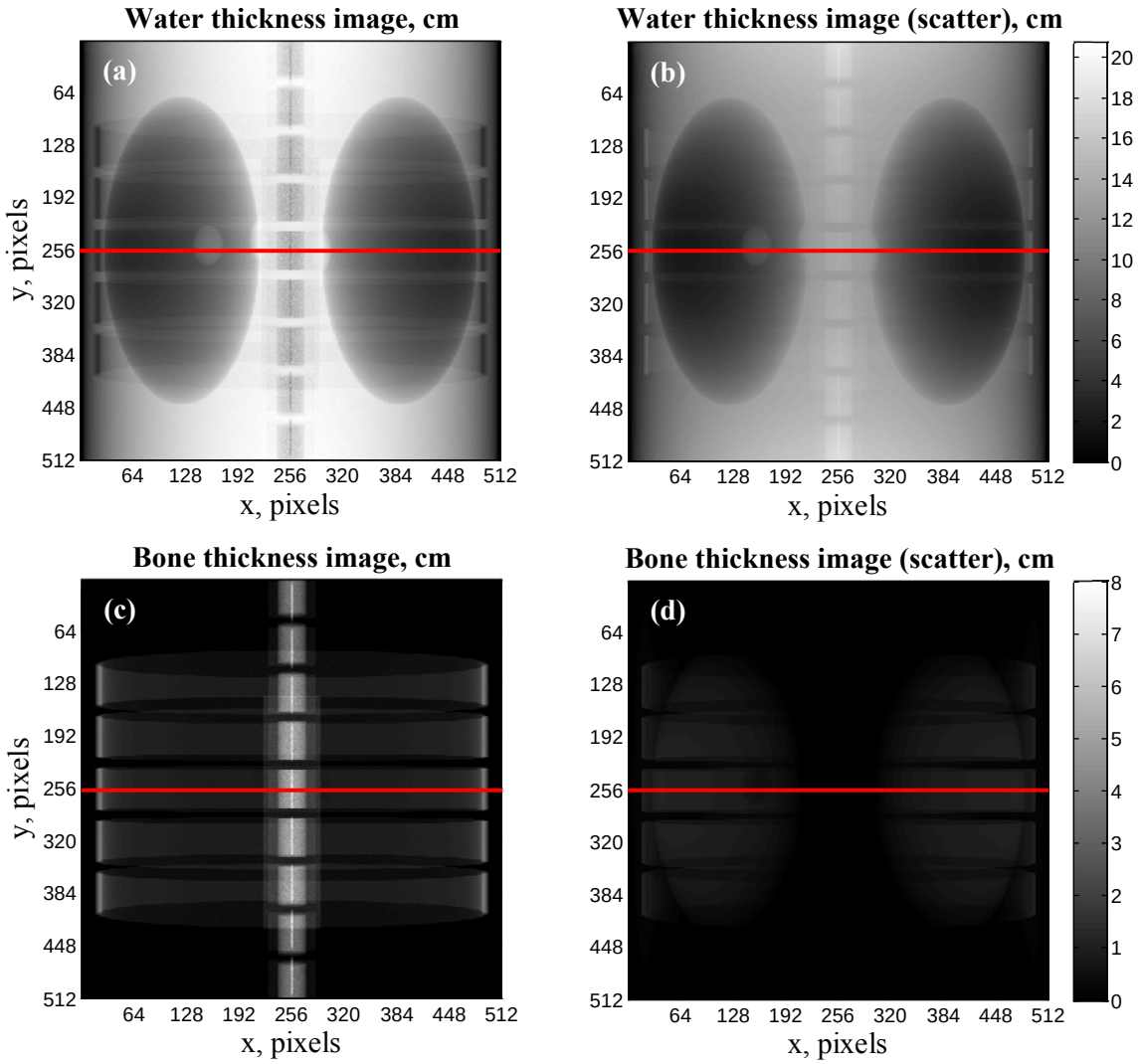

Figure 3.23. Water (a-b) and bone (c-d) thickness images. Images (a), (c) and (b), (d) were produced from primary (scatter free) and total (with scatter) attenuation images, respectively. The SPR was 60%. Additionally, locations for profile visualizations presented in Figure 3.24 and Figure 3.25 are marked in red. Pixel size was 1 mm.

The analysis of images from Figure 3.23 indicates a high level of distortion in individual material images in the presence of scattered radiation. This is especially true for the bone thickness image (d). The comparison of water thickness images produced from primary (a) and total (b) attenuation images reveals an overall thickness sub-estimation as well as a reduction in high frequency detail (e.g. vertebral column and rib contours). When compared to its scatter free counterpart (c), the bone thickness image obtained in the presence of scatter (d) exhibits a loss of structural detail related to the vertebral column, ribs and sternum. Furthermore, some structures (lungs) visible in the water thickness images (a) and (b) have propagated into the image. This can be linked to the varying influence of scatter on LE and HE energy channels. As noted previously in Chapter 3.1.1 and demonstrated in Chapters 3.1.2 and 3.1.3, the scatter spectrum shape is shifted towards the low energies. Thus, a higher amount of scatter is present in the LE channel than in HE channel. This in

turn leads to misinterpretation of materials as the attenuation characteristics in energy have changed in an inequivalent manner.

In order to provide more detail on the basis material decomposition process in the presence of scattered radiation, central horizontal profiles of the images shown in Figure 3.23 have been traced. Figure 3.24 and Figure 3.25 correspond to water and bone thickness profiles estimated with varying SPRs.

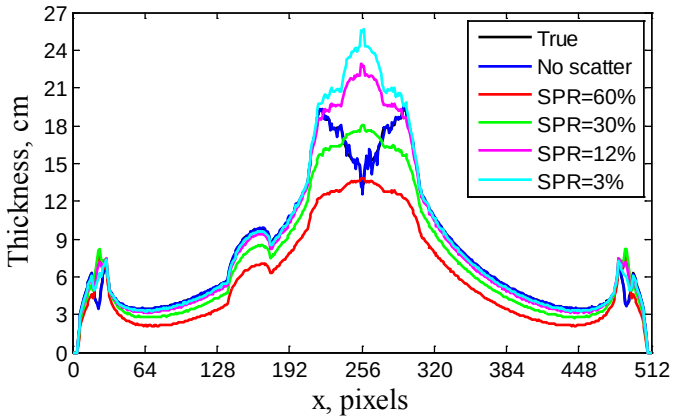

Figure 3.24. Water thickness profiles for varying levels of scatter (60%, 30%, 12%, 3% and 0% SPR). The true water thickness profile is also presented (black). Pixel size was 1 mm.

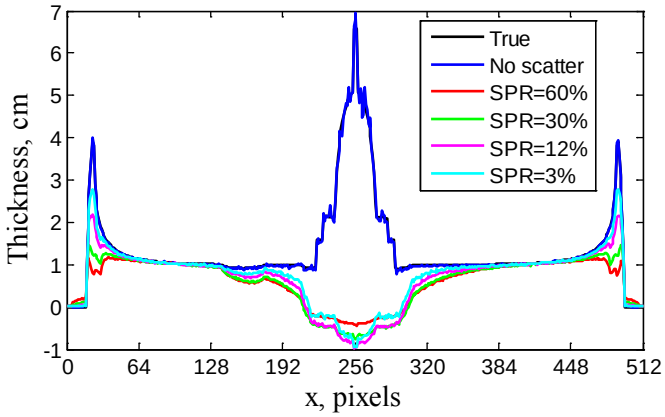

Figure 3.25. Bone thickness profiles with varying levels of scatter (60%, 30%, 12%, 3% and 0% SPR). The true bone thickness profile is also presented (black). Pixel size was 1 mm.

Central horizontal profiles from Figure 3.24 and Figure 3.25 further support the conclusions made based on the images from Figure 3.23. The water thickness profiles obtained for varying levels of scatter show varying levels of sub-estimation (Figure 3.24) with the curves approaching the true and the scatter free curves as SPR decreases. However, vertebral column related structural information propagation (around pixel #256) becomes more and more visible with decreasing overall scatter level. As for bone thickness estimation accuracy (Figure 3.25), a similar improvement with decreasing SPR can be observed. However, the middle part (around pixel #256) still exhibits a substantial bias even at a 3% SPR. Moreover, this zone begins to reveal water thickness curve related detail with decreasing scatter level.

As explained earlier, the propagation of one basis material structural information into the other is linked to the energy distortion induced by the scatter spectrum (low-energy shift). From the profiles, one can also link this phenomenon to the local SPR. Despite the overall SPR decrease, due to the low primary photon number, the SPR in the middle part of the image (vertebral column) remains substantial. This explains the corresponding thickness estimation bias and spatial distortions in the respective region.

Finally, the average relative error between the true thickness images and the material thickness images obtained with varying SPR was computed by applying (3.6). Note that in this case attenuation is replaced by the thickness value contained in the respective material image. The results are summarized in the form of a graph presented in Figure 3.26.

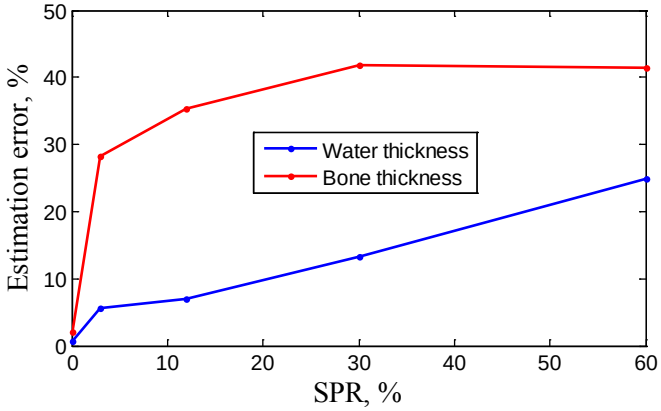

Figure 3.26. Water and bone thickness estimation errors for varying scatter levels.

From Figure 3.26 it can be noted that in the absence of scatter the chosen decomposition method preforms almost perfectly with an estimation error of around 2.1% and 0.7% for bone and water thickness, respectively. When scatter is present, an approximately linear increase from 5.6% to 24.9% can be observed for the water thickness estimation error. For bone thickness, this trend is not linear. An increase from 28.4% at minimum scatter level (3% SPR) towards 41.8% (30% SPR) can be observed. This is followed by an approximately constant trend towards 41.4% at 60% SPR. In general, the estimation error for bone thickness is always higher than for water thickness. It is also worth noting that the water thickness estimation error is quite similar to scatter induced error obtained in integration mode radiography (Chapter 3.2.1) for the same SPR. The corresponding error for bone thickness, however, is about 1.5 times higher.

Higher estimation errors for bone thickness can be linked to the fact that most of the structural information related to bone objects remains in areas with strong attenuation (e.g. vertebral column). This in turn leads to a substantially higher estimation error than for water due to the high SPR corresponding to these regions.

In conclusion, the conducted simulation study showed that the presence of scattered radiation in energy-resolved radiographic data subjected to basis material decomposition poses a great issue. Even for low global scatter levels, areas with high attenuation exhibited severe scatter induced distortion. Furthermore, structural information from one material image can propagate into the other due to spectrum shape distortions induced by scatter. This is especially prominent in regions with high local SPR.

3.3. Objectives of the thesis

As noted previously in Chapter 3.1.1, there have not been many studies involving scattered radiation in the context of energy-resolved x-ray imaging. Thus, it was necessary to perform additional research in order to provide a more detailed characterization of the behavior of scattered radiation in the energy domain (Chapters 3.1.2 and 3.1.3). For the experimental part, prototype detectors were available in the LDET laboratory. For the simulation part, a tool capable of performing multi-energy x-ray scatter simulations during a reasonable time needed to be developed and validated (Chapter 4.3). This was the first objective of the present thesis.

Based on the demonstration of the x-ray scatter effect in both integration mode and energy-resolved x-ray applications (Chapter 3.2), it can be concluded that the presence of scatter in the measured x-ray signal is an important issue that needs to be treated accordingly. In Chapter 2.4 it was stated that energy-resolved PCDs provide additional energy information of the measured signal. The second and main aim of the present thesis was to use this additional information in combination with the knowledge of scatter behavior in the energy domain, acquired through various simulations (Chapter 3.1.2) and experiments (Chapter 3.1.3), and existing scatter correction procedures (Chapter 5.1), in order to develop an x-ray scatter correction procedure adapted for multi-energy x-ray imaging and benefiting from the energy information (Chapter 5.2).

4. ENERGY-RESOLVED SCATTER SIMULATION

Computer simulation tools often facilitate the design and testing of radiographic and tomographic x-ray systems and corresponding image processing techniques. These simulations can be divided into two main categories: *analytical simulation* and *statistical simulation* [38]. A block diagram illustrating the main components of an x-ray simulation is presented in Figure 4.1.

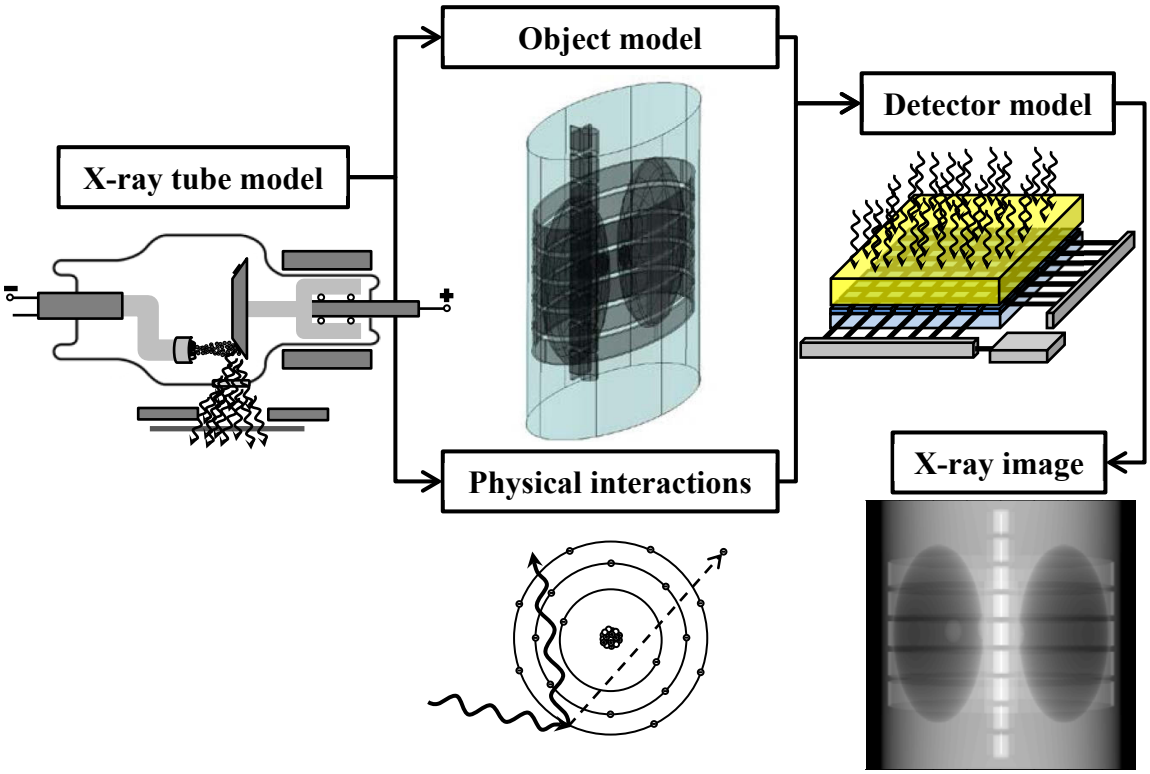

Figure 4.1. A schematic depicting key components of an x-ray simulation.

A representative example of analytical x-ray simulations is the primary x-ray photon propagation simulation through an object [38]. Using the object, which is described as a combination of simple geometrical shapes (cylinder, sphere, ellipsoid, box and etc.) with corresponding attributed materials, the total attenuation for photons directed from a given source point in the direction of a given detector pixel can be computed with the aid of (2.14).

Compared to analytical simulations, statistical simulations apply random number generators coupled with probability distributions corresponding to different interaction processes to model a given x-ray system behavior [38]. Note that this makes this type of simulation substantially more computationally demanding than an analytical simulation. A typi-

cal example is a *Monte Carlo* (MC) simulation using the interaction probabilities described in Chapter 2.2 to model scattered and/or primary radiation.

In the following chapters, more detail is given on MC simulations in the context of x-ray imaging (Chapter 4.1), a simulation tool developed in the LDET laboratory is presented (Chapter 4.2) [62], [63] and an updated version of this tool [64], developed during the course of the present thesis, is also introduced (Chapter 4.3).

4.1. Monte Carlo x-ray simulations

As noted previously, the general idea of a MC x-ray simulation is to model the photon transport through an inspected object in the direction of the detector by means of interaction probabilities and random number generators.

Firstly, a certain number of photons with an energy distribution following a given x-ray tube spectrum (for example, the one illustrated in Figure 2.3, Chapter 2.1.1) is chosen. Additionally, a model of the inspected object is built. This model can be both simplified (consisting of a few basic shapes) or complex (composed of many different shapes or utilizing CT volume data directly).

The next step is to send photons from the x-ray source in the direction of the object (Figure 4.2). Each photon is tracked into the inspected medium. Using the corresponding probability density function and a random number generator, the distance of interaction in the object is computed. Thereafter, the type of interaction is determined (photoelectric absorption, Compton or Rayleigh scattering) by means of a random draw from the respective probability distributions. These can be directly computed with aid of (2.15) for a given material. In the case of scattering the direction change is calculated using (2.5) and (2.9) for Rayleigh and Compton effects, respectively. For the latter, the energy shift is also computed via (2.7). Note that the photon can also traverse the object directly without any interaction at all. [38].

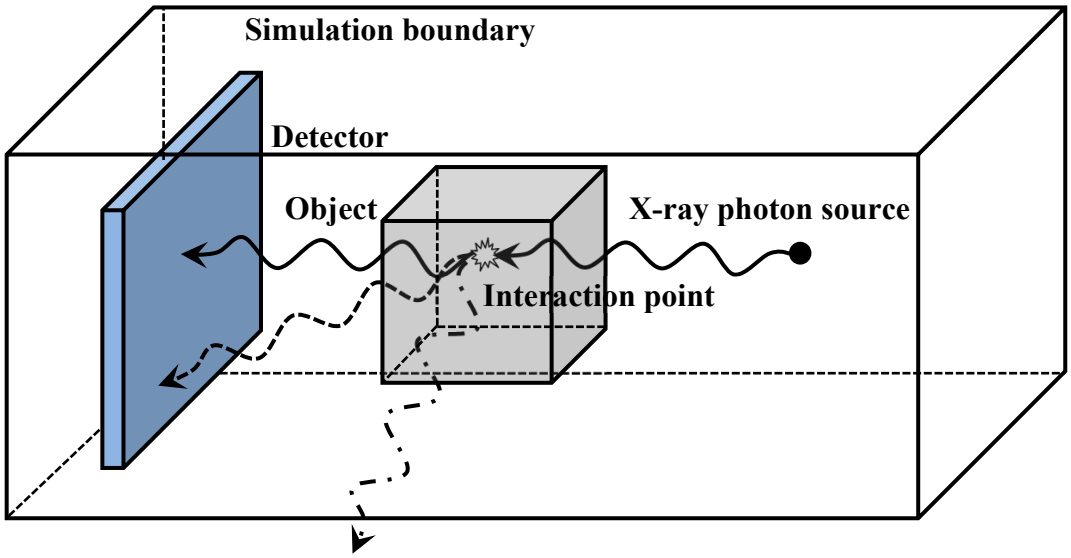

Figure 4.2. Illustration of the x-ray photon tracking applied in MC simulations. The photon is followed from the x-ray source to an interaction point in the object where it is either absorbed or scattered toward the detector (dashed line) or outside the simulation boundary (dashed-dot line). Additionally, it can undergo no interaction at all and arrive at the detector (solid line). It is also worth noting that a given photon may also undergo a chain of subsequent interactions in the object.

The tracking of each individual x-ray photon continues until it is either completely absorbed in the object, it reaches a given detector element or it exits the boundaries of the simulation. Note that all of these events can occur either after one or several interactions in the inspected object. [38].

In order to have a good estimate of the resulting x-ray image (primary and/or scatter), a very large number of photons is often required (for example ~10^9 for scatter images [21]). This leads to MC simulations being computationally expensive.

An acceleration of an MC simulation can be achieved by means of optimization techniques also termed *variance reduction techniques*. Examples of these include forced detection [65], interaction splitting [66] and Russian roulette [66]. Additionally, MC codes can be accelerated through parallelization via a Graphics Processing Unit (GPU) [67].

Overall, despite their complexity, MC simulations are the most accurate approach to simulate x-ray photon transport as they have the capability to incorporate all the required physical models.

4.2. Sindbad

The simulation tool *Sindbad* (developed in the LDET laboratory) [62], [63] is capable of modelling any radiographic system. Three main components comprising the software are (Figure 4.3): photon beam generation from an x-ray source, photon-matter interaction in the object and photon detection. Moreover, Sindbad is also capable of performing CT acquisitions by permitting the user to rotate and translate the x-ray system.

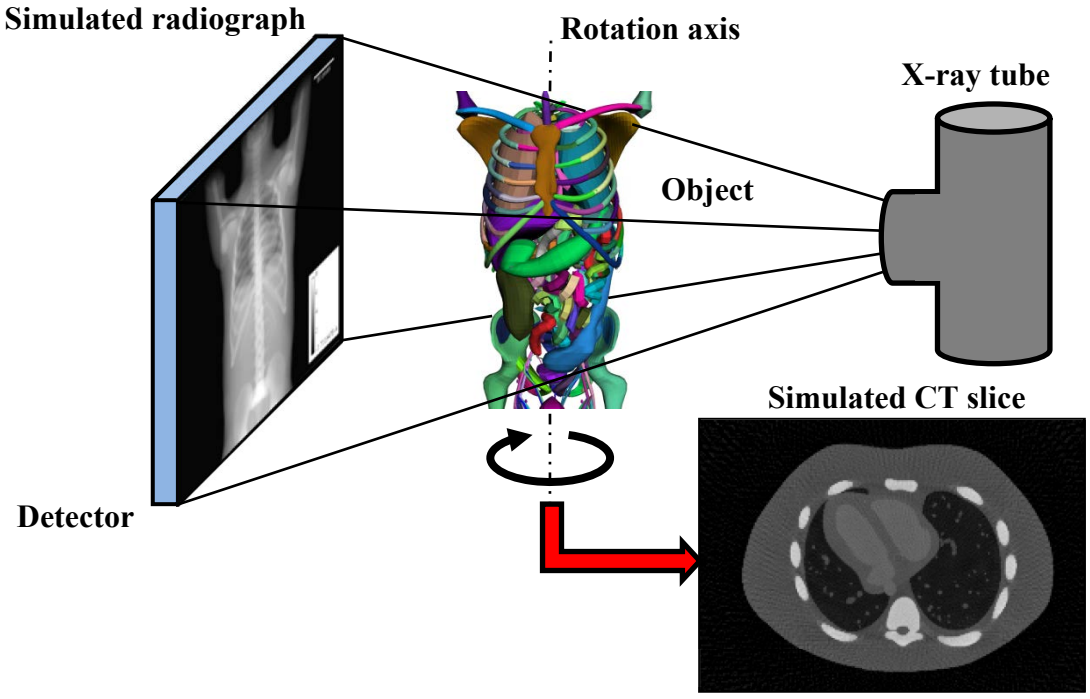

Figure 4.3. Illustration of different Sindbad components and a simulation of a realistic phantom [68] in radiographic and tomographic modes.

The x-ray generation part of the tool gives the user the ability to configure all the necessary tube parameters (anode material and angle, mAs, kV, filtration, focal spot, etc.) as well as a choice between several semi-empirical models (one example is discussed in Chapter 4.3) for the x-ray tube spectrum.

The interactions of x-ray photons with matter are managed by means of analytical (Beer-Lambert law) and MC simulations in order to obtain primary and scatter images, respectively. The scatter simulation part incorporates a hybrid approach to reduce computational time involving the reduction of photon statistic with subsequent spatial filtering of the scatter distribution [69]. Both simple and complex anthropomorphic phantoms (such as the one illustrated in Figure 4.3) are supported by Sindbad under either voxelized, faceted or constructive solid geometry (CSG) format.

The detection part of the tool gives the ability to choose between various detector models (flat panel, film, scintillating screen coupled to a charge-coupled device, photomultiplier), which exhibit differences in the way the incident x-ray signal is converted to the resulting measured one. In any case, all the listed image receptors provide a single value per pixel, corresponding to the deposited energy integrated over the energy range.

Recently, additional functionalities have been incorporated into Sindbad in order to produce energy-resolved radiographic and tomographic x-ray images. The modification consisted of keeping energy information about the photons incident on the detector and modelling the DRM for a given spectrometric detector. However, only the primary photon generation part was concerned by this modification. [47].

4.3. A tool for multi-energy x-ray simulation

One of the primary objectives of the thesis was the development of a simulation tool based on the existing libraries of Sindbad that would permit the simulation of both energy-resolved primary and scattered radiation during a reasonable time. Such a tool would permit to perform various studies aiming to provide more insight on the behavior of scatter in the spatial and, most importantly, in the energy domain. In addition, it would enable to further evaluate the influence of scatter in multi-energy imaging.

Chapter 4.3.1 presents key principles behind the developed simulation framework followed by cross-validation (Chapter 4.3.2) and experimental validation (Chapter 4.3.3). Finally, a conclusion is given and future developments are outlined in Chapter 4.3.4.

4.3.1. Sindbad-SFFD

As discussed previously in Chapter 2.4.1, an energy-resolved x-ray image can be represented by a 3D matrix (Figure 2.18), where each pixel **p** (part of the entire image region **Ω)** contains a spectrum sampled at a certain rate (depending on the number of channels of the detector). Assuming the absence of pile-up effects (linear detector model), this spectrum is a sum of two components, primary radiation $\mathbf{N_P(p)}$, coming linearly from the detector and measuring the photons that have not been stopped or deviated by any interaction, and the scattered radiation $\mathbf{N_S(p)}$, consisting of interacted photons that have been modified in direction and energy (Compton interaction):

$$\mathbf{N_T(p)} = \mathbf{N_P(p)} + \mathbf{N_S(p)}, \quad \forall \mathbf{p} \in \mathbf{\Omega}\,. \tag{4.1}$$

It is also worth noting that in (4.1) the incident direction of the photons is not scored.

Both primary and scatter signals are discrete functions of the number of output energy channels of a given spectrometric detector. Thus, for example, for a fixed pixel **p** and channel E, $N_P(\mathbf{p},E)$ corresponds to the number of primary photons measured in that pixel and energy channel.

As noted earlier (Chapter 4.2), the simulation of the first term was already possible with the recent version of Sindbad. For the scatter term an analog MC simulation can be used. This has been done in several studies on energy-resolved scattered radiation [14], [15], [58]. However, in this case, the introduction of energy information substantially increases computational demand. In order to have accurately resolved x-ray spectra in each image point, a higher number of photons would need to be used in the simulation.

In order to provide reasonable computation times while not sacrificing accuracy, a Spectral Fixed Forced Detection (SFFD) approach was employed in combination with Sindbad. The resulting new simulation software, called *Sindbad-SFFD*, is capable of energy-resolved primary and scatter simulation within a reasonable time. The SFFD approach, responsible for the energy-resolved scatter simulation part of the tool, is based on a combination of MC and deterministic calculations [65] with an addition of spatial sub-sampling of the detector. Figure 4.4 provides an illustrative summary of this technique.

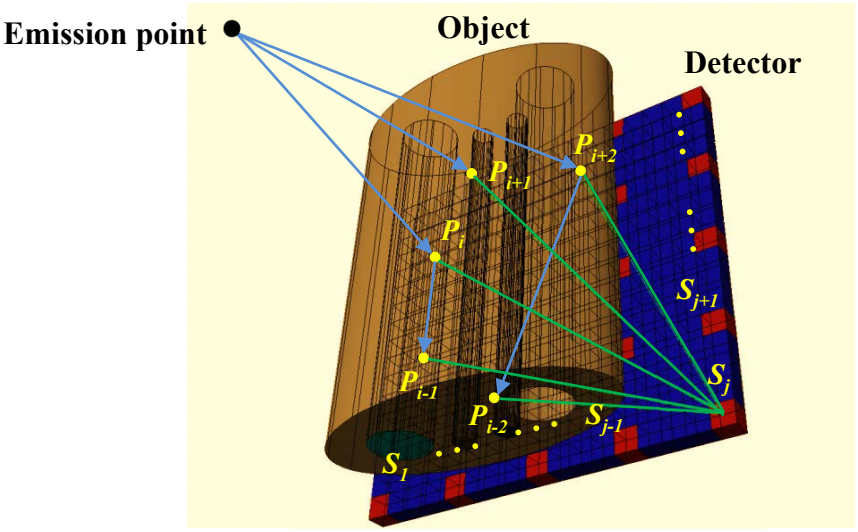

Figure 4.4. Schematic reflecting different parts of the SFFD x-ray scatter simulation approach. The MC generated particles are shown interacting with the object and producing a set of scattering points of different order followed by a sum of particle fractions in the direction of the given node.

Firstly, the MC part determines the set of scattering points $\{P_1,\ldots, P_{i-1}, P_i, P_{i+1},\ldots, P_I\}$ in the object by tracking each particle from the emission point until being absorbed or exiting the boundaries of the simulation. Coordinates, propagation direction, incident photon energy, event type (Compton or Rayleigh) and event order are recorded for each interaction point P_i. Fluorescence is not handled as it begins to add a substantial contribution only when a fair amount of high atomic number material is present in the object.

The second part of the method applies a deterministic calculation of the particle fractions $f_{ij}(E_i,E_{ij}^*)$ arriving from each scattering point P_i on a given node point $S_j \in \{S_1,\ldots, S_J\}$ located on the detector:

$$f_{ij}\left(E_i, E_{ij}^*\right) = \frac{1}{\sigma_i\left(E_i\right)} \frac{\mathrm{d}\sigma\left(\theta_{ij}, E_i\right)}{\mathrm{d}\Omega} \exp\left(-\sum_{q=1}^{Q} \mu^q\left(E_{ij}^*\right) l_{ij}^q \right) \Omega_{ij} , \tag{4.2}$$

where $\sigma_i(E_i)$ is the total cross-section as a function of the incident photon energy E_i for scattering from P_i over 4π sr, $\mathrm{d}\sigma(\theta_{ij},E_i)/\mathrm{d}\Omega$ is the differential cross section, θ_{ij} is the scattering angle, $\mu^q(E_{ij}^*)$ is the linear attenuation coefficient of a given material $q \in \{1, \ldots, Q\}$ constituting the object, function of the scattered photon energy E_{ij}^*, l_{ij}^q is the path length traversed by the scattered particle fraction in the respective material and Ω_{ij} is the solid angle seen by the scattering source P_i on the node point S_j corresponding to a given detector pixel. Note that a MC particle weight of 1 is assumed in (4.2). For certain variance reduction techniques (e.g. Russian roulette) a weighting function may be used for the initial MC particle.

Assuming a perfect detector (DRM identity and infinitely fine channels), the continuous scatter spectrum $N_j(E_{ij}^*)$ (the sub-index S has been omitted to simplify notation) in each node point S_j can be computed using the following expression:

$$N_j\left(E_j^*\right) = \sum_{i=1}^{I} f_{ij}\left(E_i, E_{ij}^*\right). \tag{4.3}$$

The final part of SFFD consists of determining the spectra for the entire detector by interpolating between the acquired samples S_j. Sub-sampling was implemented bearing in mind that scattered radiation is spatially slowly varying distribution (Chapter 3.1.1).

To this point, one only considered a perfect detector. In order to account for a realistic detector, one needs to apply a corresponding DRM on (4.3). The developed simulation tool takes the DRM as a parameter to simulate the detector response. An option of adding photon noise to the signal is also present.

For the present study, an accurate model, capable of predicting the detector response at any energy, has been used [70]. Based on a MC code (Penelope [71]), this model first simulates all physical interactions of photons and electrons inside a given semiconductor to provide the position and the number of carriers created at each interaction. The second step performs a numerical integration of the transport equation for each cloud of carriers along their trajectories toward the collecting anodes. By using the Schockley-Ramo theorem [72], drift transport, diffusion, trapping Coulomb repulsion and charge sharing and are taken into account to provide accurate estimation of the transient signals induced on collecting and neighbor anodes. Finally, electronics modeling, including realistic noise, is performed to obtain the final pulse waveforms. The detector response is calculated for all energies and the result stored in a DRM format.

Another way of estimating the DRM is with the aid of experiments. One example to perform such estimation is to measure the detector response under several radiation sources at different energies and apply a parametric model [45].

Finally, it is worth noting that for CT x-ray scatter simulations, the SFFD procedure described thus far can be applied for each projection separately.

In subsequent chapters Sindbad-SFFD is validated through simulation and experiments in a radiographic set up. This gives the opportunity to decouple the validation of different parts comprising the developed tool. Chapter 4.3.2 (cross-validation) will not consider detector modeling, thus focusing on particle interactions and geometry whilst Chapter 4.3.3 (experimental validation) will incorporate detector modelling, thus evaluating the full simulation chain.

4.3.2. Cross-validation

In order to examine the accuracy of the developed software in terms of x-ray scatter simulation performance (SFFD approach), a comparison with acquisitions provided by another simulator (GATE [73]) was carried out. GATE simulations can be considered as analog MC simulations as no additional variance reduction techniques were applied. The validation of the primary x-ray image generation part of Sindbad-SFFD was not considered as it is completely based on the previous version of the software (Sindbad), which was validated in [47].

A cylindrical PMMA numerical phantom with air cavities and an aluminum insert was used to validate the simulation software (Figure 4.5). The phantom and geometry were chosen so that the scatter spatial distribution would not be entirely flat. An additional reason was to best fit available experimental equipment.

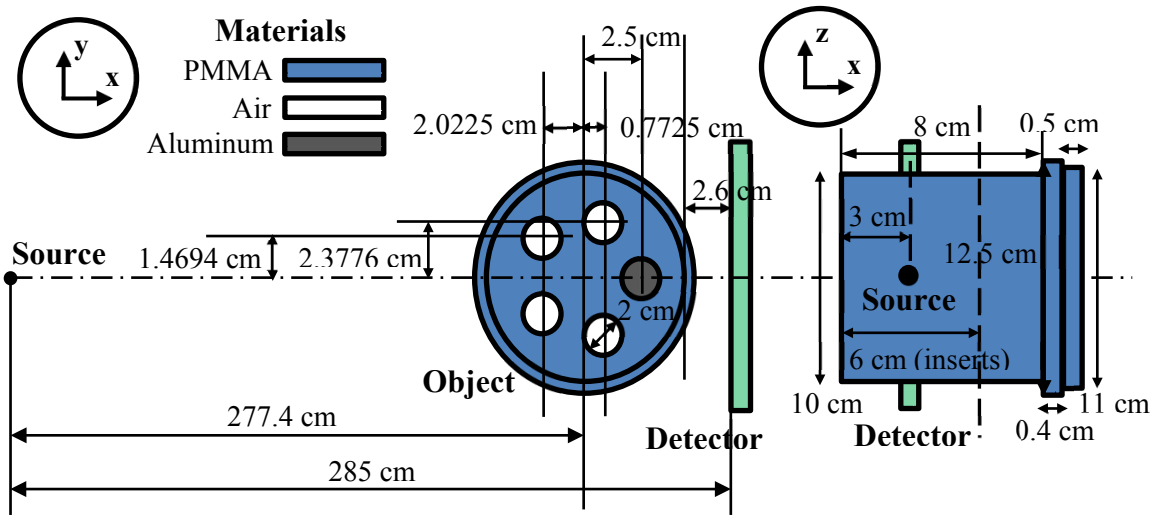

Figure 4.5. Object and geometry used in the validation process in y-x and z-x views.

Numerical constructive solid geometry (CSG) and voxelized representations were created for simulations with Sindbad-SFFD and GATE. Tube parameters were set to 110 kV, 1 mAs and 10.4° conic emission with 0.8 mm and 2 mm of aluminum and beryllium filtration, respectively. The x-ray tube spectrum modeling was based on the semi-empirical model proposed by Birch and Marshall [74]. A perfect (DRM identity, 1 keV width channels) 16×201 pixel detector was modeled (pixel pitch of 0.8 mm). The choice of detector size was motivated by the prototype available in the lab as well as by object structure (relatively homogeneous in the *y* direction). GATE simulations were set up with 3.17×10^{11} initial photons. For Sindbad-SFFD, 10^7 initial photons and a 4×50 regular node grid followed by a cubic spline interpolation between the node points were applied. Additionally, for both simulators, a 6 m^3 box of air centered at the object was added to simulate the environment. Sindbad-SFFD code was run on a single core 2.83 GHz Central processing unit (CPU) while GATE was run on a cluster with an average 2.6 GHz per CPU core. The time used for simulations with the developed software was ≈1.5 h compared to the ≈2417 h (per CPU core) for GATE.

Firstly, an attenuation image computed from the energy-resolved primary component of the signal via a discrete version of (2.18) was produced (Figure 4.6). This image will aid in linking object structures (e.g. cavities and aluminum insert) with the scatter images.

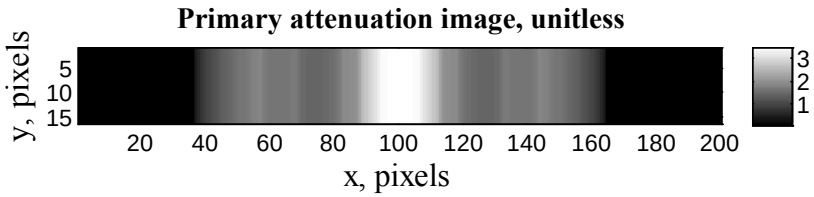

Figure 4.6. Primary attenuation image obtained with Sindbad-SFFD (pixel size of 0.8 mm).

From Figure 4.6 the aluminum insert as well as the air cavities are clearly visible. Additionally, the image indicates that the object occupies the interval of #38–#162 pixels in the *x* direction.

In order to compare the developed tool in terms of spatial scatter distribution accuracy, total incident energy scatter images were generated (Figure 4.7). The images were produced by applying the following expression on the energy-resolved scatter component:

$$I(\mathbf{p}) = \sum_{E} \mathbf{N_S}(\mathbf{p}) \circ \mathbf{E}\,, \tag{4.4}$$

where **E** is a vector of median detector bin energies. Additionally, in the case of Sindbad-SFFD, a mean of 10 realizations with corresponding standard deviation (STD) were used to evaluate the dependence on MC initialization.

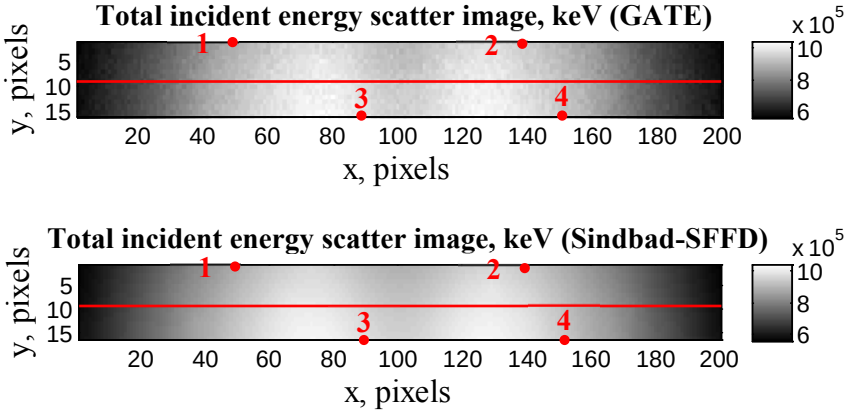

Figure 4.7. Total incident energy scatter images obtained with GATE and Sindbad-SFFD. Horizontal profile and spectrum locations used for visualizations in Figure 4.8 and Figure 4.9, respectively, are marked in red on both GATE and Sindbad-SFFD images. Pixel size was 0.8 mm.

In addition to the total incident energy images presented in Figure 4.7 central horizontal profiles were also traced (Figure 4.8).

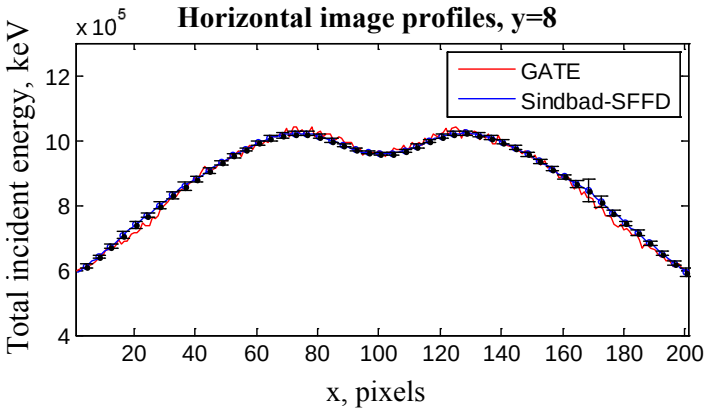

Figure 4.8. Horizontal profiles from GATE and Sindbad-SFFD scatter images shown in Figure 4.7. Markers with error bars (STD) correspond to the SFFD grid points. STDs for GATE are not present as they would not be visible at this scale. Pixel size was 0.8 mm.

The results presented in Figure 4.7 show scatter images consistent with the imaging geometry. Note the maxima in the profile in the parts where air cavities are present. Additionally, the minimum in the center of the profile (Figure 4.8) is caused by the increase in attenuation in that region (high thickness of PMMA and an aluminum insert). Globally, both scatter images and profiles, obtained from two different simulators, depict a high level of agreement. Simulations with GATE are, as expected, noisier compared to Sindbad-SFFD. This is due to the part analytical nature of the SFFD approach compared to the fully statistical nature of GATE. Additionally, the low STDs, which can be observed on the traced horizontal profile, show that the number of photons chosen was sufficient to provide a stable simulation relative to MC initialization. Finally, it can also be seen from the profile that there are areas where the STD is higher than in other profile areas (around pixel #160). This indicates that in one or several realizations provided by Sindbad-SFFD a peak was present.

The agreement between Sindbad-SFFD and GATE is further confirmed in the energy domain through the observation of the incident scatter spectra in Figure 4.9. The differences between the spectra are primarily due to the presence of photonic noise present in GATE simulations. Note that Sindbad-SFFD spectra #1 and #2 display an increase in STDs in the interval of 40–50 keV – an indication of a peak artifact presence in one of the realizations.

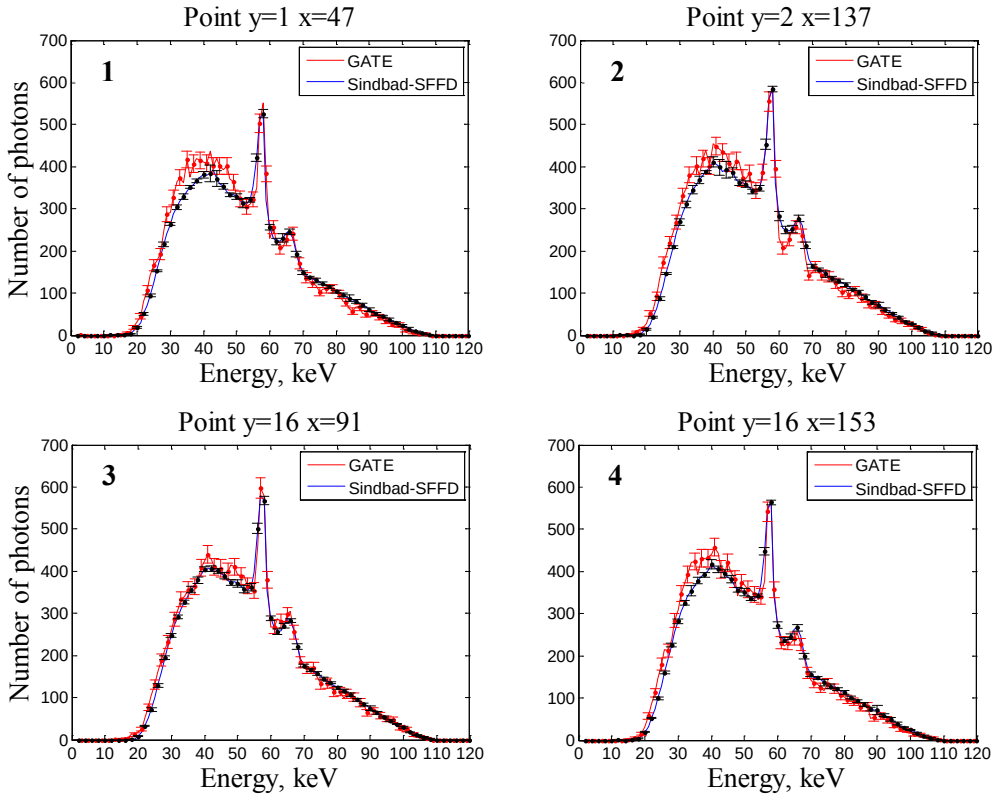

Figure 4.9. Incident scatter spectra on several control pixels on the detector (Figure 4.7). Curves provided by the developed tool and GATE are marked in blue and red, respectively. Uniform 1 keV energy bins were used. STDs are also added for both Sindbad-SFFD and GATE spectra.

In order to quantify the differences in total incident energy scatter images, a metric known as the NRMSE was used:

$$NRMSE_I = \frac{1}{I_{GATE}(\mathbf{p})}\sqrt{\frac{\sum_{\mathbf{p}}\left[I_{GATE}(\mathbf{p}) - I_{SFFD}(\mathbf{p})\right]^2}{n_p}}, \tag{4.5}$$

where I_{GATE} and I_{SFFD} are the total incident energy scatter images generated by GATE and SFFD, respectively.

For the generated spectra, a similar metric was applied in the energy interval 22–100 keV. This eliminates the contribution of channels with a low number of photons:

$$NRMSE_S = \frac{1}{\mathbf{N_{GATE}}(\mathbf{p})}\sqrt{\frac{\sum_{E}\left[\mathbf{N_{GATE}}(\mathbf{p}) - \mathbf{N_{SFFD}}(\mathbf{p})\right]^2}{n_E}}. \tag{4.6}$$

In (4.6) $\mathbf{N_{GATE}(p)}$ and $\mathbf{N_{SFFD}(p)}$ are the scatter spectra (sub-index S omitted for simplicity of notation) generated by GATE and SFFD, respectively, and n_E is the number of detector channels.

The $NRMSE_I$, when comparing the designed tool with GATE, was 1.5 %. It is also more indicative of the global spatial SFFD performance in terms of total scatter energy images. To quantify the spectral performance of the tool, $NRMSE_S$ was computed giving the following results for the four spectra presented in Figure 4.9: 6.2% – spectrum #1,

5.5% – spectrum #2, 3.7% – spectrum #3, 5.1% – spectrum #4. As noted previously, these differences can be mainly explained by the absence of noise in the Sindbad-SFFD simulations. This is confirmed by the calculation of the average relative STD for GATE data, which gives around 7% for each spectrum.

The local peaks responsible for the increase in STDs in the simulations provided by the developed tool are due to sparse first order Rayleigh scatter events with a high scatter probability [75]. As the number of photons increases, the events will become less sparse and the artifact will tend to disappear. However, such a tactic will lead to a proportional increase in computation time. Note, additionally, that increasing the distance will also reduce such peaks as the number of first order events reaching the detector plane is lower because of the reduced solid angle. The last option is not convenient for radiography simulation as the object is often located close to the detector. There are several solutions than can be applied to remedy this artifact without any geometrical dependence. Firstly, the model provided in (4.2) can be expanded to include a weight based on the probability of interaction type (Rayleigh or Compton). Such an operation would give less weight to the isolated Rayleigh events responsible for the artifact. However, this will also double computation time, as the particle fraction computation would now be done per event type. The second solution is to sub-divide the total number of launched photons into packages with different MC initialization with a subsequent application of a mean-median, which, however, might bias the result. Finally, due to the forward peaked nature and absence of photon energy change in the case of Rayleigh scattering (Chapter 2.2.2), one can also consider neglecting it altogether.

4.3.3. Experimental validation

A further investigation of the developed tool was carried out through comparison with experimental acquisitions. The focus still remained on the scatter simulation part of Sindbad-SFFD.

The geometry and phantom considered remained the same as those used for the cross-validation (Figure 4.5). An image of the corresponding experimental test bench is presented in Figure 4.10. Tube parameters were also kept unchanged. The experiments utilized an YXLON Y.TU 160-D02 x-ray tube and a 16×1 pixel linear CdTe spectrometric detector (1.2 keV width bins) with a pitch of 0.8 mm and a thickness of 3 mm which was horizontally translated to acquire images equivalent to a 16×201 pixel detector. An energy threshold of 21 keV was applied to reduce the noise in the output spectra. Gain correction was also applied. A 11×11 BS grid composed of small lead elements was used to block the primary radiation in certain zones. Thus, these zones recorded only scatter signals. The spacing between the element centers was 10 mm and the maximum thickness of each was around 7 mm. The grid was inserted at a distance of 218 cm from the source in front of the inspected object. An average of 10 acquisitions was used to reduce photon noise.

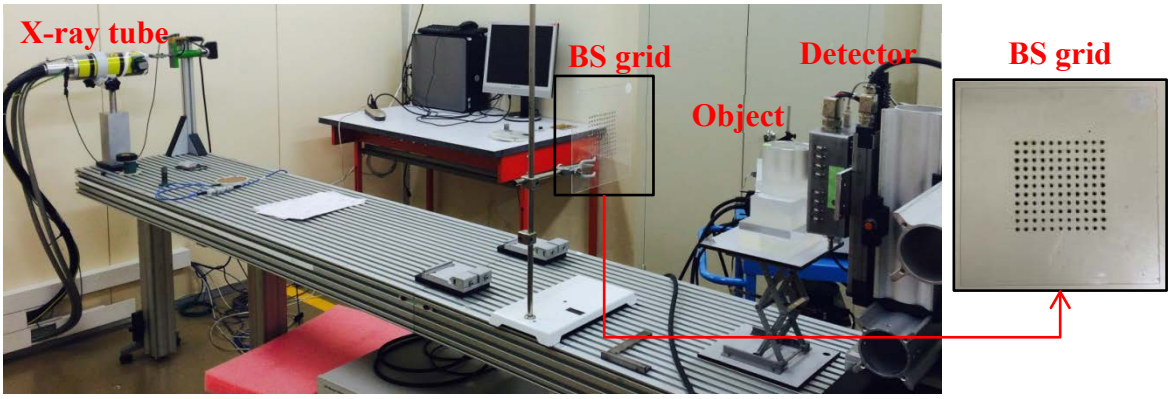

Figure 4.10. Test bench corresponding to the geometry presented in Figure 4.5. An magnified version of the BS grid is also provided.

In order to create a realistic simulation with Sindbad-SFFD, a DRM characterizing the experimental detector was applied. Other effects, such as diffusion and photon pile-up have not been considered as the experimental set up was optimized to make them negligible. To account for the environment in the experiment, the box of air considered in the cross-validation part was left in place.

Firstly, an image with no object present was experimentally acquired to verify whether the spectrum shape and tube output level were adequately modeled by the developed simulation tool (Figure 4.11).

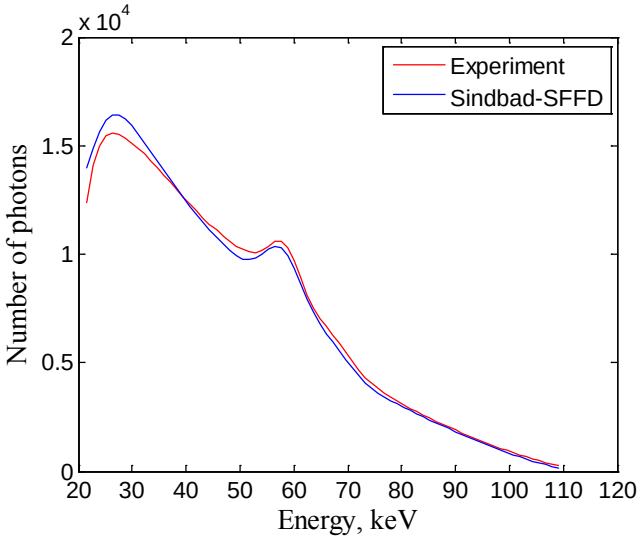

Figure 4.11. Experimental and simulated raw flux spectra. Regular 1.2 keV energy channels were used.

Both spectra presented in Figure 4.11 seem quite similar with the exception of the low energy region where the experimental spectrum exhibits a slight deformation. The agreement was considered sufficient enough to conduct scatter measurement and comparison.

Next, an experimental acquisition of the object with the BS grid was done and converted to an attenuation image generated with the aid of a discrete version of (2.18). The result is displayed in Figure 4.12. Note the 2×11 segment of the grid visible on the image. The air cavities and the aluminum insert are also clearly visible.

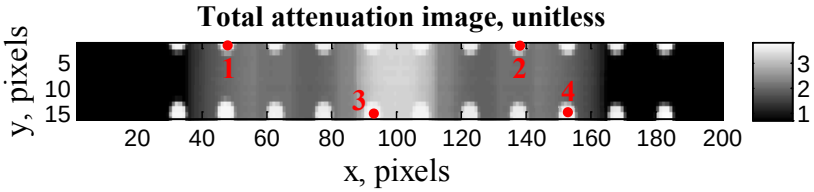

Figure 4.12. Experimental total attenuation image of the examined phantom with the added BS grid. Image pixels used for spectrum visualization in Figure 4.15 are marked in red.

In order to isolate the points concerned by the BS modification, an acquisition with only the grid in place was produced and points with maximum attenuation per BS element projection were determined through thresholding.

Having obtained a sparse scatter measurement, a cubic spline interpolation was applied to acquire a full scatter image presented in Figure 4.13, which was compared to an equivalent image produced by Sindbad-SFFD. Additionally, two horizontal profiles corresponding containing the initial sparse scatter measurements were traced (Figure 4.14). Finally, the images and profiles were limited to an interval of 45–155 pixels in the *x* direction in order to not consider parts influenced by the experiment surroundings (table, grid, object and detector support, etc.).

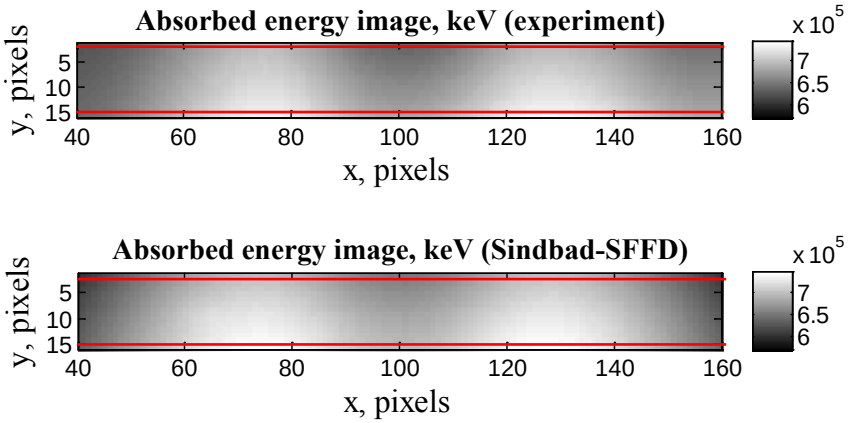

Figure 4.13. Absorbed energy scatter images obtained through experimentation and with Sindbad-SFFD. Horizontal profile locations used for visualizations in Figure 4.14 are marked in red on both experimental and Sindbad-SFFD images. Pixel size was 0.8 mm.

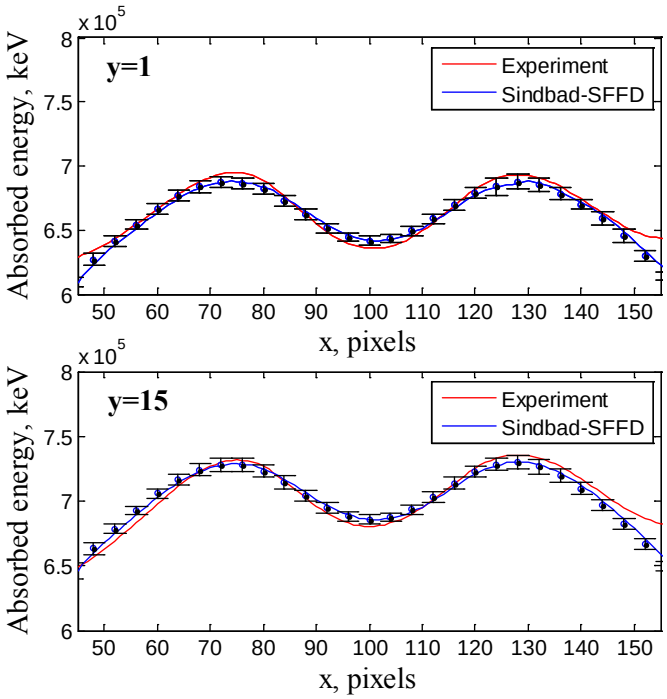

Figure 4.14. Horizontal profiles from positions indicated in Figure 4.13. Markers with error bars (STD) correspond to the SFFD grid points. Pixel size was 0.8 mm.

While the analysis of Figure 4.13 shows a globally high degree of similarity between simulated and experimental results, there are certain differences that are prominent. Firstly, through the observation of horizontal profiles (Figure 4.14) it is clearly visible that experimental scatter level is higher starting from pixel #145 for both profiles. The same can be also seen for the *y=1* profile for the pixels before pixel #50. These differences can be explained by the influence of ambient scatter coming from the environment that is still present close to the borders of the object projection. Additionally, the asymmetry in deviations between experimental and simulated curves can be explained since the environment viewed by the detector plane is also asymmetric. Further investigation of the image profiles shows that the experimental curve exhibits slight asymmetry between the maxima. This could be due to an inaccuracy in the geometrical alignment of the object with the respect to the detector plane. Finally, the differences in aluminum composition could be the cause of the dissimilarity of the central minima in the experimental and simulated profiles.

Further comparison of Sindbad-SFFD simulations with the data obtained from experiments considered scatter spectra measured in several control points contained within the BS element projections (Figure 4.15).

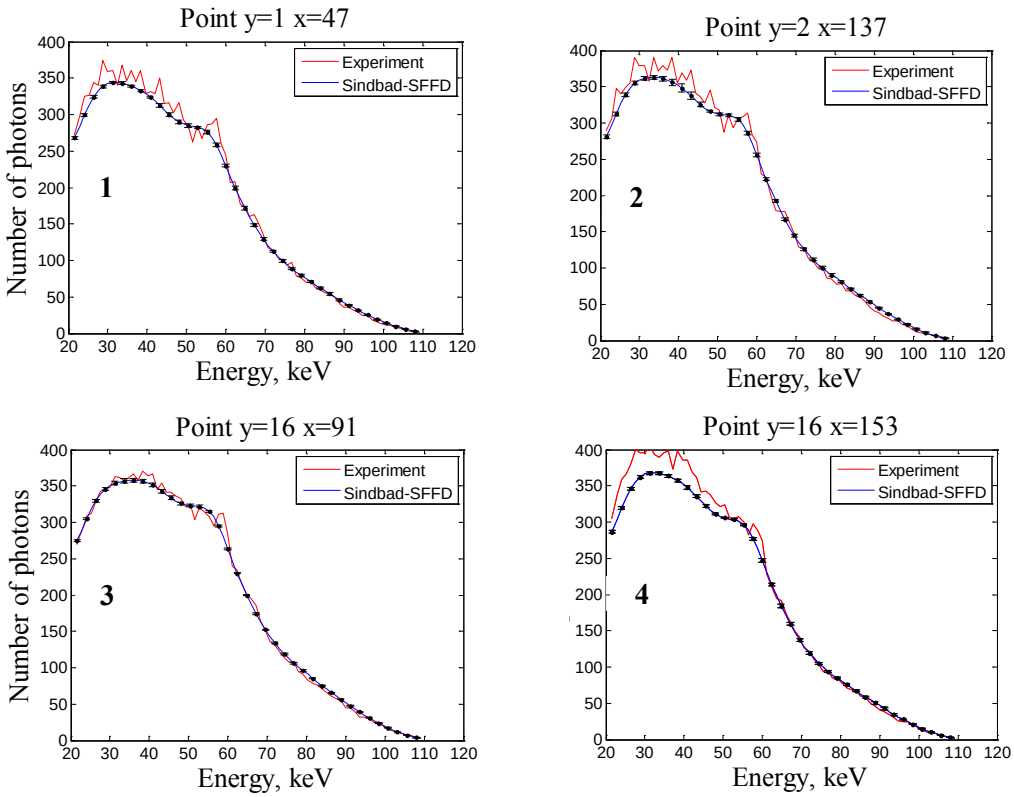

Figure 4.15. Scatter spectra measured by several control pixels of the detector located within the BS projections (Figure 4.12). Curves provided by the developed tool and the experiment are marked in blue and red, respectively. Uniform energy bins of 1.2 keV were used.

A quantitative evaluation of the results presented in Figure 4.13 and Figure 4.15 was carried out using the metrics provided by (4.5) and (4.6) where the quantities indexed GATE are replaced by the corresponding experimental quantities.

The $NRMSE_I$ computed for the images presented in Figure 4.13 was equal to 1.8% confirming the global agreement between experiments and the developed tool in terms of spatial scatter distribution. In terms of spectral aspect of the scatter, for the four spectra presented in Figure 4.15, the $NRMSE_S$ was 6.4% (#1), 6.5% (#2), 3.6% (#3), 8.4% (#4), respectively. As expected, spectrum #4 exhibits the highest error due to the difference in low energy photon level for that point. Other spectra also depict quantitative differences comparable with those seen in Figure 4.15.

4.3.4. Conclusion

Generally, Sindbad-SFFD simulations proved to be consistent with those provided by GATE with an error of 1.5% observed for total incident energy images and a maximum error for the compared control point spectra being around 6%. Such differences can arise from photonic noise (present in GATE simulations), varying MC engines and phantom representations (voxelized vs CSG).

Although photon noise could be added to Sindbad-SFFD simulated scatter distributions, it is not always a direct necessity. Namely, within the framework of scatter correction methods the corresponding distribution is mostly considered smooth (noise free) as

this leads to superior noise properties in the resulting corrected image. Thus, scatter simulation studies linked to the respective correction methods are likely to employ noiseless scatter images.

It is also worth noting that while being relatively close to GATE simulations, the developed tool requires much less computation time. In a CT configuration the improvement would be even more substantial as several radiographic projections are considered.

Further agreement is observed between the simulations obtained from the developed tool and experiments with the difference in absorbed energy images being 1.8% and the maximum difference for the examined spectra being around 8.5%. Ambient scatter, geometric positioning inaccuracies and photon noise were identified as the most probable causes of dissimilarity. Overall, the resulting performance of the presented simulation tool confirms its potential of becoming a valuable instrument for scatter radiation estimation and correction studies in multi-energy x-ray imaging.

One part of future work will be devoted to the inclusion of incident photon direction in the calculation of the spectra measured by the detector, as for small air gaps this direction is considerably different from the normal of the detector, which in turn influences the detector response.

Futures studies will also focus on the elimination of the sparse Rayleigh scatter point artifact. Additionally, an automatic selection of the number grid nodes and initial photons will also be studied. For CT simulations angular sub-sampling of x-ray scatter with subsequent interpolation will also be exploited, as it has been shown that scatter varies slowly with projection angle [57]. Moreover, other variance reduction techniques and GPU-based parallelization mentioned in Chapter 4.1 may also be explored.

5. SCATTER CORRECTION

Chapter 3 demonstrated the impact x-ray scatter has on different imaging applications and concluded that this phenomenon can sufficiently compromise the accuracy of both integration and energy-resolved mode x-ray applications. Thus, there is a great need for *scatter correction* for various x-ray modalities.

In Chapter 5.1 one aims to introduce and classify different existing scatter correction approaches applied in integration mode x-ray imaging. For each of the considered categories method examples with detailed description are also given.

It is important to note that before the present thesis, no scatter correction method that would exploit the energy information provided by energy-resolved PCDs was ever proposed. The evolution to relatively large size energy-resolved 2D detectors gives more importance to the development of an x-ray scatter correction method adapted for multi-energy imaging. A scatter correction method developed in the course of the present thesis aiming to fulfill this objective is presented in Chapter 5.2.

5.1. Existing methods

Various x-ray scatter correction schemes have been developed so far for integration mode detectors [17]. A subjective classification of such approaches can yield the following categories: *direct methods*, *numerical modeling based methods*, *physical measurement based methods* and *image post-processing*.

Examples of direct methods include, *anti-scatter grids* (ASG) [18], *increasing air gap* [19] and *additional collimation* [20]. A more detailed discussion of these techniques is provided in Chapter 5.1.1.

MC [21]–[23] and *Scatter kernel (SK)* [24]–[26] *methods* are classical examples of numerical modelling based methods. Chapter 5.1.2 provides thorough analysis of these approaches and gives examples from each category.

Physical measurement based methods include several key approaches: *beam-stop* (BS) [27]–[29], *beam-hole* (BH) [30], [31], *primary modulation* (PM) [32]–[34] and others [35], [36]. A more detailed description with examples is presented in Chapter 5.1.3.

Finally an example of an *image post-processing* approach [37] as a way to correct for scatter influence on x-ray images is given in Chapter 5.1.4.

5.1.1. Direct methods

There are a number of scatter correction approaches that aim at directly influencing the factors responsible for scatter presence in the final x-ray image without any preliminary estimation of the relevant scatter distribution. Hence, the attribution of the term *direct* to such approaches. The nature of the direct methods makes them the fastest existing scatter correction methods.

Increasing air gap

This technique originates from the idea of reducing the solid angle covered by the detector. This reduces the solid angle of the object "seen" by the detector, thus contributing to a reduction of scatter magnitude. Hence, increasing the air gap between the object and the detector can substantially reduce the resulting scatter magnitude [13], [19].

The effectiveness of the air gap technique is field and object dependent. It has been shown that air gap increase leads to a more substantial scatter reduction in the case of small scattering volumes (thin objects) and field sizes [19].

Finally, it is worth noting that the air gap approach can reduce scatter, but cannot completely correct it as x-ray acquisition experiments are limited to a certain maximum SDD due to the magnification effects and practical considerations, such as x-ray room designs. Thus, the increasing air gap technique can be considered a *scatter reduction* and not a scatter correction approach.

Anti-scatter grid

An ASG usually consists of thin strips of highly attenuating material (usually lead) fixed within a highly transmissive material (carbon fiber, plastic, aluminum, etc.). The grid elements are focused in the direction of the x-ray source. A large portion of the primary x-ray photons passes between the strips whilst the scattered photons are mostly absorbed in the septa (Figure 5.1). [3].

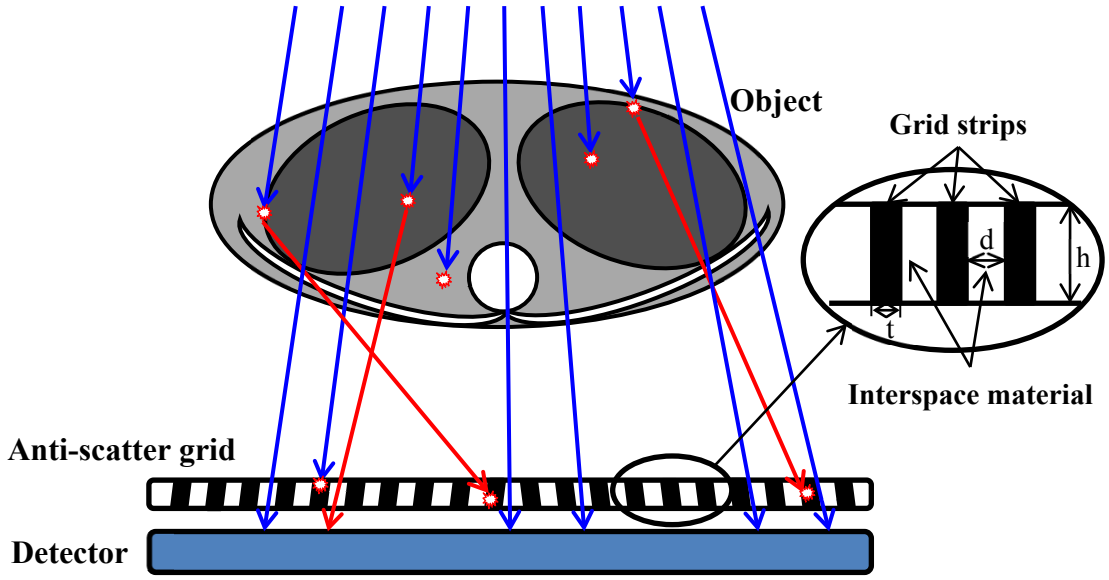

Figure 5.1. Schematic illustration of the principle of an anti-scatter grid. Primary and scattered photons are marked in blue and red, respectively. Note that not all scattered photons are absorbed and not all primary photons are transmitted. Additionally, an inset of a grid section is given to visualize the most important parameters of the grid: strip thickness (t), spacing between the elements (d) and height (h).

Grids are usually classified based on the so called *grid ratio* r_G (Figure 5.1), which is defined as the ratio of grid strip height (h) and the grid element spacing (d) [39]: $r_G=h/d$. Increasing grid ratio increases the scatter rejection efficiency of a particular ASG. This can be confirmed through observation of Figure 5.1, from which it is apparent that all scattered x-ray photons with an angle of incidence lower than arctan(r_G) will impinge on a lead el-

ement. If this is achieved through a larger *h*, primary photon transmission decreases, as they would need to traverse a greater bulk of interspace material. Another option is to incorporate thicker strips or to increase strip frequency, this also increases the fraction of primary photons being absorbed by the grid. In comparison thinner strips and/or more sparsely distributed strips contribute to a lower absorption of scattered photons. Grids can also be 2D, in which case, once again, the scatter rejection efficiency and primary x-ray beam absorption are increased simultaneously. Hence, ASG design is always a compromise between scattered x-ray photon absorption and primary x-ray photon transmission.

To avoid artifacts due to lead strips in the resulting x-ray image, the grid is usually inserted in a special holder ("Bucky") which vibrates the grid [3]. The holder, being not entirely transparent to x-rays, contributes to the attenuation of primary radiation caused by the grid.

Since the strips of an ASG are made to match the divergence of a particular x-ray beam at a chosen SDD, the use of one grid is limited to that distance within a permissible tolerance. In the opposite case, a progressive increase of primary x-ray beam attenuation will be observed toward the edge of the grid. [39].

Because any ASG contributes to a loss of a fraction of primary radiation, the tube current must be increased accordingly to ensure the necessary amount of x-ray signal be delivered to the image receptor to ensure the desired image quality [3]. This results in increased x-ray dose to the inspected object, which is a drawback in the case of medical imaging applications. Nevertheless, ASGs are quite common in radiographic imaging (with the exception of extremities) [39] and are also sometimes used for CT [18].

With appropriate design, an ASG is capable of removing 80–90% of the scatter, while transmitting more than 75% of the primary x-ray radiation. The downsides are, as noted previously, that it will be matched to a particular focal distance, which limits its generality, and that it will require an increased dose to the patient. This is true for radiographic applications.

In the case of CT, the SDD is mostly fixed, thus it makes the ASG more applicable. However, since SPRs in CT are generally lower than radiography (Table 2), the improvement might not prove to be substantial. It has been shown that despite ASGs contributing to the reduction of artifacts caused by scatter in CT images and improving contrast, there is a low level of motivation to apply grids in CBCT with respect to CNR and global image quality under most examinations (exceptions being cases with SPR>100%) [18].

Another important drawback of the ASGs is that the remaining scatter fraction changes its spatial frequency with the low-frequency assumption (highlighted in Chapter 3.1.1) being no longer valid. This is due to the dominant fraction of this signal being composed of forward directed Rayleigh scattering events. [13]. Thus, the scatter remaining after the application of the ASG substantially more complicated to correct as it occupies a much larger spatial frequency bandwidth.

Finally, it has also been shown that grids alter scatter spectrum characteristics [14]. This is expected, as the resulting scattered photons are only those that scatter at small angles (resulting in low energy loss both in the case of Compton and Rayleigh) and those that have sufficient energy to penetrate the lead strips. Additionally, the fraction of multiple events also reduces in this case.

Additional collimation

As indicated previously in Chapter 3.1.1, reduction of x-ray field size can contribute to a reduction of the irradiated object volume. The ideal case would be to scan a given object

with a highly collimated pencil beam obtaining a full radiographic image as a combination of sub-zones. This in turn substantially increases acquisition time in both radiography and tomography, which becomes inacceptable in the respective imaging applications. Thus, collimation can only limit x-ray scatter to a certain degree, similar to the air gap technique. An important virtue of collimation is the reduction of patient dose as a result of beam size limitation.

In CBCT, for example, volume of interest (VOI) imaging (realized with the aid of beam collimation) has shown high levels of scatter reduction with SPR decrease by up to 10 times and simultaneous dose decrease of up to 1.3 times [20].

Overall, as with the air gap approach, the amount of scatter reduction achieved with the aid of increased collimation is, generally, limited.

5.1.2. Numerical modelling based methods

Another category of scatter correction methods aims either at modelling the scatter distribution on the detector (MC methods) with subsequent subtraction or at correcting the scatter effects on the image using a form of filtering operations (SK methods). Due to computational load involved in their implementation, these techniques are slower than the previously described direct methods (Chapter 5.1.1).

Monte Carlo methods

As noted in Chapter 4.1, MC simulations can be used to model photon transport through a model object. A model of the inspected object is available as the reconstructed volume in CT. Thus, using this model in combination with the corresponding source and detector modelling, a MC simulation can be performed to estimate the x-ray scatter distribution on the detector [21].

Although the MC approach provides an accurate modeling of the scatter interaction physics in the object, the corresponding computation time is quite high. For example, in one study the reported time was around 430 h on a single core desktop PC [21]. Additionally, due to the reconstructed volume being biased to a certain degree by the present scatter (depending on the object and geometry), the simulated scatter distribution will suffer from a loss in accuracy as well.

The application of variance reduction techniques, sparse detector and projection sampling can drastically reduce computational time. This was implemented alongside several reconstruction iterations aimed at reducing the scatter distribution estimation error present in the object model [22]. The paper also reported an impressive ~2 min computation time on desktop PC. Despite scatter artefact correction, bias was still observed in HU values for some materials. [22].

Finally, a more recent method proposes another approach at MC method acceleration, implementing, similarly to [22], detector plane and projection space sub-sampling, but also adding the aspect of using simultaneous MC simulations running for x-ray scatter simulation at different projection angles. The latter is coupled with a low number of photons chosen per simulation with a subsequent application of a spatial fitting algorithm to recover a less noisy estimate of the corresponding scatter distribution. The authors reported a similar computation time of up to 2 min. However, this was achieved on a 16 core machine. [23]. This can be further increased with the use of variance reduction techniques similar to [22]. Nevertheless, the problem of scatter estimate inaccuracies due to the initial reconstructed volume errors still remained valid [23].

MC scatter correction methods are quite promising with ongoing research directed at computational time reduction and improving scatter estimate accuracy. However, they remain highly sensitive to the acquisition set-up modeling. Furthermore, they are not as easily applicable for radiographic applications, as an accurate inspected object volumetric model is required. Finally, it also worth mentioning the noise increase in the scatter corrected images due to the subtractive nature of the MC approaches. Because part of the signal (scatter) is subtracted and the noise linked to the total signal remains, the resulting signal-to-noise ratio (SNR) decreases. This is valid for any scatter correction method based on subtracting the scatter distribution and can be accounted for (to some extent) with the aid of image denoising methods.

Scatter kernels

Another class of numerical approaches models the scatter component I_S in a particular image pixel as a function of the primary component I_P taken from a certain region **U** centered the corresponding pixel [24]:

$$I_S = \int_U \xi\left(I_p(u)\right) K(u)\, du\,, \tag{5.1}$$

where $K(u)$ represents the scatter kernel and $\xi(\bullet)$ the scatter potential. In some cases the former is omitted [25] and (5.1) reduces to a pure deconvolution problem. The kernel function is obtained either through preliminary calibration [24] or simulation [25] procedures with different objects. For the scatter potential empirical models are used [24]. Furthermore, in CT, local thickness-variation adaptive kernels have been proposed to improve scatter correction performance (although at the cost of computation time increase) [26]. Moreover, further improvements in scatter correction accuracy in this type of technique have recently been reported through a more advance kernel modelling approach [76].

It is apparent that SK approaches are faster than MC methods because of their analytical nature (compared to the statistical of MC). However, they are similar to MC in the sense that they require accurate knowledge of system parameters to preform estimation of $K(u)$. Additionally since these are performed on objects approximating the objects to be imaged, residual bias induced by scatter will still remain to some level.

Nevertheless, SK methods achieve a high degree of scatter induced artifact reduction in CT while remaining relatively fast and are still subjects of continuing research.

5.1.3. Physical measurement based methods

In contrast to direct methods and numerical modelling techniques, physical measurement based methods apply beam modifiers to measure the x-ray scatter distribution followed by its subtraction from the total signal. The term *physical measurement* refers to the way in which the information about the scattered distribution is extracted. Additionally, these methods are faster than the ones mentioned in Chapter 5.1.2, as they incorporate direct scatter measurements coupled with interpolation and subtraction. However, they still remain slower than direct methods (Chapter 5.1.1), which do not utilize any additional computational procedures.

Beam-stop method

The BS method uses an array of highly absorbing elements (tungsten or lead) placed between the x-ray source and the object [27]. These elements are, in most cases, cylindrical and have a sufficient thickness to completely attenuate the incident x-ray beam. This en-

sures that no primary radiation is detected in the detector areas influenced by the BS elements. Thus, the only signal present in these zones is assumed to be scattered radiation. Figure 5.2 provides an illustration of an acquisition influenced by a BS grid.

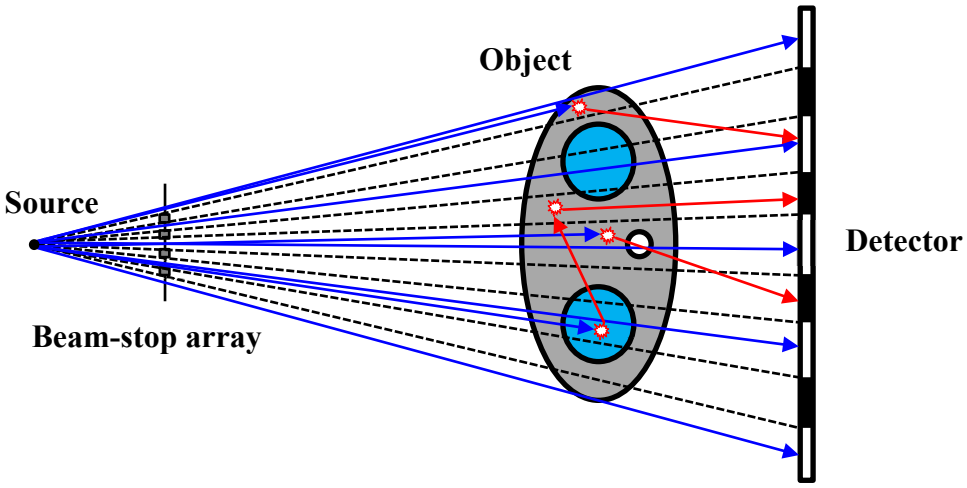

Figure 5.2. A schematic describing the principle behind the BS method. Primary and scatter radiation are marked in blue and red, respectively. The BS array blocks the primary radiation for certain image pixels (black zones on the detector). In this case, the signal measured in these zones is thus only due to the scatter component. Note that in the white zones (no BS elements), both scatter and primary components are measured.

Having obtained scatter signals in several isolated zones via an acquisition with a BS grid (Figure 5.2) and bearing in mind the low spatial frequency assumption the entire scatter distribution can be spatially interpolated from the respective areas. A second acquisition without the BS array is then performed to obtain a total image of the object without the blocked primary and the estimated scatter is subtracted. [28].

Although being considered as one of the most efficient and robust methods for x-ray scatter correction and estimation [28], the BS method has one serious drawback for medical imaging applications. More precisely, the additional acquisition required for the method contributes to an increase in patient dose. This is especially true for radiography, while in CT several strategies to avoid this effect have been proposed.

One of such strategies involves taking the measurement of scatter on a sparse set of projections with a subsequent application of cubic spline interpolation. The authors claim that the overall patient exposure increase in such a case is less than 4% [27].

Another technique proposes the application of a moving BS array with an exploitation of the inherent projection data redundancy to correct for the missing primary radiation in BS acquisitions. In such a case, a complimentary acquisition is not required and patient dose is even decreased as a result of a fraction of the primary being attenuated by the BS elements. [29].

Finally, in order to once again exploit the projection data redundancy, one paper proposed to use lead strips to cover only one half of the detector. This reduces the amount of primary spatial information loss. For each projection, scatter is interpolated/extrapolated using the 1D cubic B-spline approach and subtracted. Using a modified FDK reconstruction coupled with image post-processing techniques the authors acquire a reconstructed scatter corrected volume. Note that the post-processing is also aimed at reducing residual noise from the scatter subtraction [77].

Another drawback of the BS method is the increase in x-ray examination time due to the extra acquisition. This is valid mostly for CT as it is a collection of radiographic projections. Note that the techniques based on a single acquisition, proposed in [29] and [77], do not suffer from this disadvantage.

Furthermore, depending on the portion of the incident beam being blocked by the BS array, the change in the resulting scatter amount can be substantial enough to differ from the distribution obtained with a BS free acquisition. In this case a scatter estimation error occurs and the resulting primary (obtained through subtraction) is biased. Once again, this is only valid in the case of a classical BS approach based on 2 acquisitions.

Despite its downsides, the BS method is still a reliable and robust tool to study x-ray scatter in experimental conditions. Additionally, it can be used in conjunction with phantoms to validate the performance of other scatter estimation and correction procedures. Finally, the BS scatter correction method can also be applied in x-ray imaging domains where patient dose is not of importance (for example, industrial sample testing) [28].

Beam-hole method

A complementary approach to the BS array is the BH method. Instead of positioning an array of lead elements between the source and object, an array of apertures in a lead sheet is used instead (Figure 5.3). This permits the acquisition of sparse x-ray primary samples. Since the individual beams from the apertures can be considered pencil beams, the resulting samples have negligible scatter and can be considered purely primary. The next step is to acquire a similar image without the BH array and subtract the sampled primary giving a sampled x-ray scatter distribution. Finally, as in the BS method, a spatial interpolation of the scatter component is performed and subtracted from the BH array free image. [30].

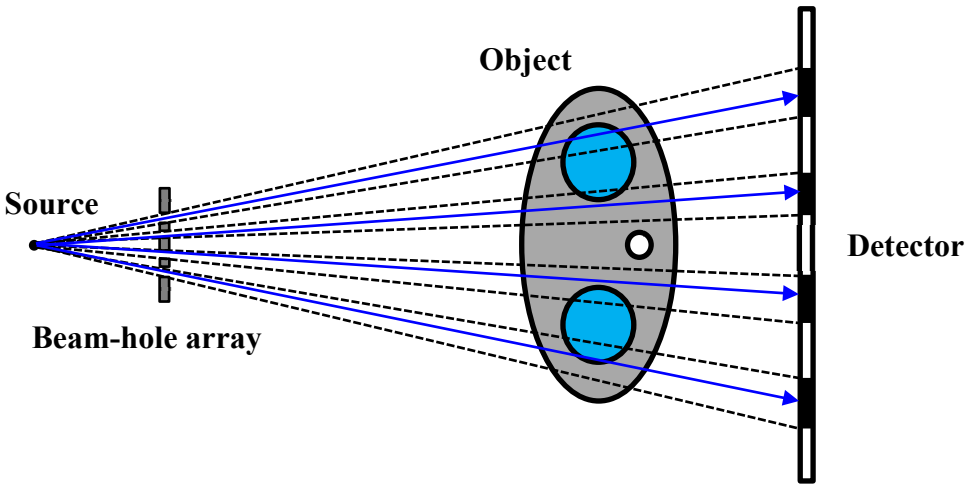

Figure 5.3. An illustration describing the idea behind the beam-hole method. The BH array produces pencil beams covering pixel zones (black zones on the detector) where only primary component (blue) is measured. Note that in white zones the primary signal is completely blocked by the BH array.

It is obvious that the BH approach requires much less of additional dose depending on the amount of the beam being passed by the apertures. A study in radiography showed the additional requirement to be around 4% [30]. In a breast CT application this number was claimed to be less than 1% [31]. Additionally, despite the indirect scheme of scatter sample

measurement, the BH method can show comparable or even superior performance to the BS method in some cases [78].

Several drawbacks are still valid for the BH method. The first being the increase in acquisition time, especially in the case of CT, unless strategies of sparse angular sampling, similar to the ones employed for MC methods (Chapter 5.1.2), are implemented. Furthermore, the measured primary samples may be corrupted by detector scattering thus inducing errors in scatter estimation.

The BH method is less popular and studied than the BS method. However, it has potential to become as widely applicable (and perhaps even more) than the BS approach.

Primary modulation

Instead of using a BS or BH array, the PM method proposes an insertion of a non-uniformly attenuating sheet of material Figure 5.4. The non-uniformity consists of thickness variations arranged spatially in such a way that they form a checkerboard pattern of a high frequency. This performs a modulation of the primary x-ray signal in the spatial frequency domain. As a result, the primary component is replicated as it is convolved with a Dirac comb (in theory) whose frequency is the reciprocal of the checkerboard pattern period. This produces a spatial frequency domain dominated by unmodulated primary and scatter signals with superimposing primary frequency copies. With the assumptions that these copies are not affected by unmodulated signals (no overlap is present), an exact recovery of primary signals is theoretically possible. The maximum spatial frequency that can be reconstructed in this case is equal to half of the modulation pattern frequency. [32].

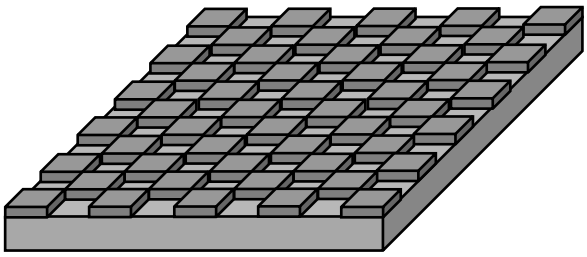

Figure 5.4. Schematic drawing of an example primary modulator.

The PM approach does not increase patient dose and acquisition time when compared to BS and BH methods in both radiographic and tomographic acquisitions. However, its efficiency is compromised by strong spatial frequency assumptions (non-overlapping of the modulated and unmodulated signals). Studies indicate that this leads to ringing artifacts [33]. The authors of the idea also point out beam-hardening and penumbra effects to degrade performance [33]. The former can be reduced with the choice of an adequate modulator material [79]. Furthermore, the theoretical limit on the spatial frequency of the restored primary puts more constrains on modulator design (pattern must exhibit a sufficiently high frequency).

An evolved version of the method considers the same modulation pattern continuously displaced during a CT projection and thus providing the same concept of modulation in the temporal domain. The authors indicate that this reduces beam-hardening and completely removes the ringing artifacts compared to the previous version of the method. Furthermore, the primary spatial frequency is now limited by the detector spatial frequency. [33]. However, no additional scan time in such a case is only valid for CT acquisitions. For a radio-

graphic acquisition, either two images with different modulator positions must be taken or fast electronics are required to record several x-ray frames (note the increased noise in each frame in this case).

Recently, the concept of PM has been revisited with the aim to implement the idea purely in the spatial domain. The concept takes advantage of the fact that scatter estimation in the context of a modulated primary can be formulated as an optimization problem. Firstly, the modulation pattern is known and its effect on the beam can be inversed. Thus, if one has a primary x-ray image corrupted by the pattern, a division of the image by the pattern image obtained in the same geometry (with no object) eliminates the effect. [34]. This is true with a modulator material optimized for a particular tube spectrum, such that the amount of attenuated signal would not depend on the imaged object area considered [79]. Unfortunately, one measures the sum of primary and scatter signals. However, with the aid of the low-frequency assumption, it can be considered that scatter is constant within a subzone of the image plane. Thus, if a suitable constant for a given subzone is subtracted and the compensation for the modulation pattern is performed a correct estimate of the primary image can be obtained. Hence, for each sub-zone, one searches for an estimate of the scatter intensity that minimizes the residual modulation pattern in the estimated primary image. The amount of residual modulation pattern can be quantified using an image smoothness indicator. Once obtained, the estimates provide samples for a subsequent spatial interpolation of the full scatter spatial distribution. [34].

As it can be seen, PM method is a promising scatter correction technique with ongoing research directed to improve performance. Thus, it shows potential of becoming a commercially used scatter correction method for various x-ray imaging applications.

Collimator shadow

A simple method, to be considered a particular form of the BS method, is the collimator shadow scatter correction approach. The idea, originally applied in CBCT, lies in the measurement of scatter signals near detector edges where primary is blocked by tube collimation. A subsequent 2D interpolation is performed to estimate the full scatter distribution. [35].

The obvious advantages include no dose or examination time increase due to supplemental acquisitions (scatter is measured simultaneously). The disadvantages lie in a much lower accuracy of scatter spatial distribution estimation compared to previously introduced methods. Increasing the amount of primary blocked by the collimators can contour this fact, but it will also limit the imaged object area. Finally, often in radiographic and sometimes in tomographic x-ray applications, the entire detector area is dedicated to the object. In this case, there are no zones where scatter can be measured.

Overall, as the authors themselves have pointed out, the method can be used as preliminary step for more advanced scatter correction algorithms requiring an idea of the scatter distribution [35]. One example of such a method, which uses the collimator shadow method in combination with a SK type of approach (Chapter 5.1.2) and compressed sensing, can be found in [80].

Additional scan data based scatter correction

For CBCT applications used for image-guided radiation therapy, a method based on additional multi-slice CT scan data, which is acquired in the treatment planning process, can be employed. It is assumed that the multi-slice CT dataset exhibits a negligible scatter level. This is ensured through collimation and the employment of an ASG. Firstly, an esti-

mate of the primary CBCT projection data is produced through forward projection of the multi-slice CT volume that is spatially registered to a preliminary CBCT volume reconstruction. The difference between the estimated and raw CBCT projections is then low-pass filtered in order to separate low spatial frequency components corresponding to the scatter distribution. Finally, the scatter estimate is subtracted from the raw CBCT projections and a reconstruction of the corrected projection data is performed. Note that since only low-frequency components of the primary are used in the method, high-frequency registration errors can be tolerated. This means that a high degree of scatter correction can be achieved without the need of an accurate volume registration. [36].

The additional scan data based scatter correction approach is fast in implementation and is consistent with current radiation therapy work flow. It has showed high levels of scatter correction performance in both phantom [36] and patient studies [81], not only improving the CBCT images visually, but also in terms of HU value accuracy. The former, as noted in Chapter 3.2.2, plays an important role in dose calculations performed during radiotherapy treatment planning. A phantom study confirmed the improvement in dose calculation accuracy after the application of the considered scatter correction approach [82].

Despite the impressive performance of this method at the very low cost of scan and computational times, it is worth pointing out that it remains application specific. This is due to the requirement of having a reference scatter free CT dataset of the same patient, which is not normally the case for diagnostic x-ray imaging applications. Nevertheless, based on the concept discussed in this chapter, one can, for example, imagine a scatter free radiographic and CT image database, which can be coupled with a more advanced registration protocol, in order to combine scatter free and scatter corrupted images of different patients. Then, the respective method can be applied on the registered images.

It is worth noting that the additional scan data based scatter correction method can be also readily implemented in NDT x-ray imaging and would be especially beneficial for applications, which require the repetitive analysis of identical machine parts. In this case a preliminary scatter free (e.g. acquired with a multi-slice CT) or scatter corrected (e.g. by the BS method) dataset of the object can be acquired. The scatter free dataset can be then used in to correct each identical examined machine part.

5.1.4. Image post-processing

The main inconveniences of scattered radiation presence in x-ray images are the resulting bias, loss of contrast and artifacts in CT images (Chapter 3.2). Thus, the problem of scatter correction can be approached as a pure image post-processing task.

One paper proposed the use of empirical scatter models (for example [83]) to produce scatter distribution estimates with a subsequent subtraction from the projection data followed by reconstruction. A flatness criterion for the resulting reconstructed images is applied, which aims to find the right weighting coefficients for these estimates to minimize artifacts due to scatter presence. [37].

The technique is simple (no system knowledge or complex modelling) and relatively fast. However, the method aims at correcting artifacts, thus it is not as efficient in improving quantitative data accuracy. Furthermore, its performance is limited by the inherent empirical models used in the estimation of scattered radiation. Finally, as the weighting coefficients are determined by the amount of artifacts present in the CT images it is directly applicable only to CT.

Overall the approach presented in [37] can be useful for fast clinical image improvement (e. g. contours of internal object structures) and thus increasing the accuracy of image-based diagnoses. However, it is not suitable for applications requiring accurate quantitative CT data (e.g. radiotherapy treatment planning).

In general, modern image processing approaches can be applied to increase the contrast and to sharpen object edges in scatter corrupted images in both radiography and tomography. The reduction of artifacts can also be addressed for CT. But these techniques will always be limited to purely visual improvements due to their lack of modelling of the underling physical phenomenon (x-ray scatter).

5.2. A novel method for multi-energy x-ray imaging

Some of the x-ray scatter correction techniques, mentioned in Chapter 5.1, apply directly to energy-resolved imaging (direct methods, physical measurement based methods) whilst others will suffer from an increase in model complexity and execution time (numerical modelling based methods, image post-processing methods). However, the scatter correction techniques applied for integration mode x-ray detectors do not exploit the energy information provided by spectrometric image receptors. In this chapter a Partial Attenuation Spectral Scatter Separation Approach (PASSSA) exploiting multi-energy information is introduced. Chapter 5.2.1 presents the main idea behind the developed approach, followed by Chapters 5.2.2 and 5.2.3, which examine some key components of the method in more detail. Some concluding remarks are also given in Chapter 5.2.4.

5.2.1. Concept

Previously, in Chapter 4.3.1, it was stated that under a linear energy-resolved detector response model (e.g. no or limited amount of pile-up), it can be considered that the each pixel of detector measures a sum of primary and scatter components, which lead to (4.1). Thus, for each pixel, one has an equation with two unknowns: primary and scattered radiation. Given an estimator of the scattered radiation $\tilde{\mathbf{N}}_{\mathbf{S}}(\mathbf{p})$, an estimator of the primary radiation $\tilde{\mathbf{N}}_{\mathbf{P}}(\mathbf{p})$ can be found via subtraction from the total radiation $\mathbf{N}_{\mathbf{T}}(\mathbf{p})$ measured by the pixel:

$$\tilde{\mathbf{N}}_{\mathbf{P}}(\mathbf{p}) = \mathbf{N}_{\mathbf{T}}(\mathbf{p}) - \tilde{\mathbf{N}}_{\mathbf{S}}(\mathbf{p}), \quad \forall \mathbf{p} \in \boldsymbol{\Omega}. \tag{5.2}$$

In order to correct for scattered radiation via (5.2), an approach for obtaining $\tilde{\mathbf{N}}_{\mathbf{S}}(\mathbf{p})$ for the entire spectral image is needed.

Consider now modifying the acquisition presented in Figure 2.15 (Chapter 2.4.1) by inserting a mask of attenuating elements (*attenuators*) between the object and the source (Figure 5.5). The insertion of the mask produces zones (shadows) on the detector with a supplemental amount of attenuation due to the mask. The shape of these shadows corresponds to the magnified spatial pattern of the attenuator mask. From this point, two acquisitions of the inspected object are considered (with and without the mask). Let the total, primary and scatter quantities from the acquisition containing the attenuator mask be denoted with exponent *m*.

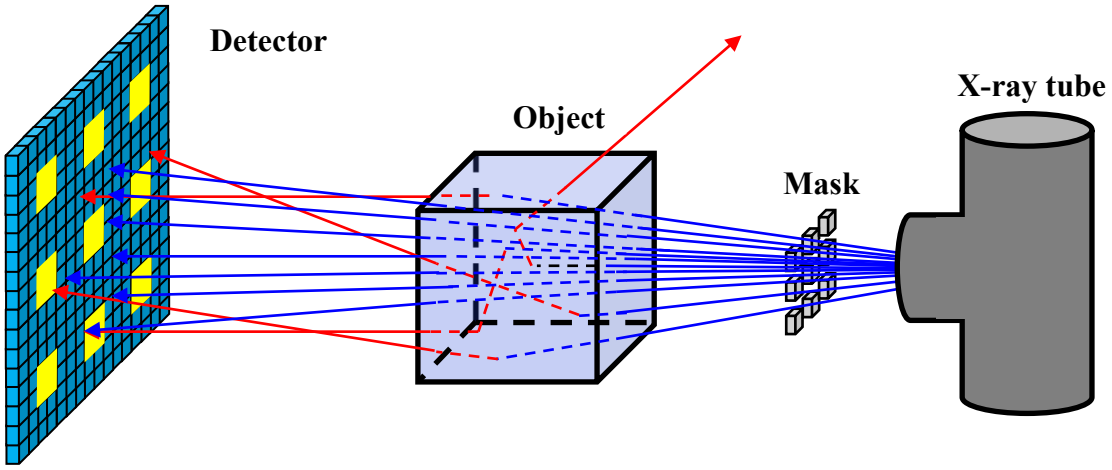

Figure 5.5. Schematic of an x-ray acquisition modified by an attenuator mask. Primary and scatter radiation are marked in blue and red, respectively. Pixel zones influenced by the insertion of the mask are marked in yellow on the detector.

Firstly, with aid of expression (2.20), one can write expanded versions of the primary component for a given pixel $\mathbf{p'}$ from the image sub-region $\mathbf{U}\subset\boldsymbol{\Omega}$ corresponding to attenuator shadows in both acquisitions:

$$\mathbf{N_P}(\mathbf{p'}) = \mathbf{D}\times\left[\mathbf{N_0}(\mathbf{p'})\circ\exp\left(-\sum_{q=1}^{Q}\boldsymbol{\mu}_\mathbf{q}(\mathbf{p'})l_q(\mathbf{p'})\right)\right],\quad \forall\mathbf{p'}\in\mathbf{U} \tag{5.3}$$

and

$$\mathbf{N_P^m}(\mathbf{p'}) = \mathbf{D}\times\left[\mathbf{N_0}(\mathbf{p'})\circ\exp\left(-\boldsymbol{\mu}_\mathbf{a}(\mathbf{p'})l_a(\mathbf{p'})-\sum_{q=1}^{Q}\boldsymbol{\mu}_\mathbf{q}(\mathbf{p'})l_q(\mathbf{p'})\right)\right],\quad \forall\mathbf{p'}\in\mathbf{U}\,. \tag{5.4}$$

In (5.3) and (5.4) $\mathbf{N_0(p')}$ is the incident tube spectrum. Additionally, the quantities $\boldsymbol{\mu}_\mathbf{a}\mathbf{(p')}$ and $l_a\mathbf{(p')}$ from (5.4) correspond to the linear attenuation function and thickness of the attenuator material along the ray path between the x-ray source and the concerned pixel. Finally, $\mathbf{N_P(p')}$ and $\mathbf{N_P^m(p')}$ denote the primary and modified (by the attenuators) primary signal, respectively.

Then, if, for each attenuator shadow pixel, one subtracts the associated modified acquisition total signal $\mathbf{N_T^m(p')}$ from its unmodified counterpart $\mathbf{N_T(p')}$, the following signal difference $\boldsymbol{\Delta}\mathbf{N(p')}$ can be obtained:

$$\boldsymbol{\Delta}\mathbf{N}(\mathbf{p'}) = \mathbf{N_T}(\mathbf{p'}) - \mathbf{N_T^m}(\mathbf{p'}) = \mathbf{N_P}(\mathbf{p'}) - \mathbf{N_P^m}(\mathbf{p'}) + \boldsymbol{\Delta}\mathbf{N_S}(\mathbf{p'}),\quad \forall\mathbf{p'}\in\mathbf{U}\,, \tag{5.5}$$

where $\boldsymbol{\Delta}\mathbf{N_S(p')}$ is the difference in scatter components between the two acquisitions for the considered pixel $\mathbf{p'}$.

Under the condition of a low attenuation (0.05–0.2 on average over energy) and x-ray field fill-factor (0.05–0.25) for the mask elements, the scatter components from the two different acquisitions for the pixel in question can be considered approximately equal (in other words $\mathbf{N_S(p')}\approx\mathbf{N_S^m(p')}$) and $\boldsymbol{\Delta}\mathbf{N_S(p')}$ can be considered negligible in (5.5). This is justified by scattered radiation being a global phenomenon, the amount of which is proportional to the total amount of radiation incident on the object. Thus, the change in local scatter induced by a relatively small change in overall incident radiation can be deemed negligi-

ble. Using the expanded versions of $\mathbf{N_P(p')}$ and $\mathbf{N_P^m(p')}$ from (5.3) and (5.4), respectively, and neglecting $\mathbf{\Delta N_S(p')}$, a more explicit form of (5.5) can be obtained:

$$\mathbf{\Delta N(p')} = \mathbf{D} \times \mathbf{W} \times \left[\mathbf{N_0(p')} \circ \exp\left(-\sum_{q=1}^{Q} \boldsymbol{\mu}_\mathbf{q}(\mathbf{p'}) l_q(\mathbf{p'}) \right) \right], \quad \forall \mathbf{p'} \in \mathbf{U}. \tag{5.6}$$

The quantity $\mathbf{W}$ from (5.6) is a diagonal matrix with its diagonal being a function of the attenuator material and thickness:

$$\mathbf{W} = diag\left(1 - \exp\left[-\boldsymbol{\mu}_\mathbf{a}(\mathbf{p'}) l_a(\mathbf{p'})\right]\right). \tag{5.7}$$

Taking (5.3) into account, one can derive the expression for primary radiation from (5.6):

$$\begin{aligned} \mathbf{N_P(p')} &= \mathbf{D} \times \mathbf{W}^{-1} \times \mathbf{D}^{-1} \times \left(\mathbf{D} \times \mathbf{W} \times \left[\mathbf{N_0(p')} \circ \exp\left(-\sum_{q=1}^{Q} \boldsymbol{\mu}_\mathbf{q}(\mathbf{p'}) l_q(\mathbf{p'}) \right) \right] \right) = \\ &= \mathbf{M} \times \mathbf{\Delta N(p')}, \quad \forall \mathbf{p'} \in \mathbf{U}. \end{aligned} \tag{5.8}$$

The quantity $\mathbf{M}=\mathbf{D}\times\mathbf{W^{-1}}\times\mathbf{D^{-1}}$ in (5.8) is the *transition matrix*, enabling the recovery of the primary $\mathbf{N_P(p')}$ (no attenuator) from $\mathbf{\Delta N(p')}$. Matrix $\mathbf{M}$ corresponds to a basis change for $\mathbf{W^{-1}}$. Unfortunately, due to the instability of $\mathbf{D}$ (condition number in the order of 10^5), its inverse is also unstable, which leads to $\mathbf{M}$ being unstable as well (condition number in the order of 10^4). To overcome this difficulty, a parametric form of $\mathbf{M}$ (condition number in the order of 10) can be used instead (Chapter 5.2.2).

The recovery of primary $\mathbf{N_P(p')}$ through the difference of totals for each attenuator shadow point gives the ability to obtain the scatter component $\mathbf{N_S(p')}$ for each one of such points via (4.1) and (5.8):

$$\mathbf{N_S(p')} = \mathbf{N_T(p')} - \mathbf{N_P(p')} = \mathbf{N_T(p')} - \mathbf{M} \times \mathbf{\Delta N(p')}, \quad \forall \mathbf{p'} \in \mathbf{U}. \tag{5.9}$$

Finally, when $\mathbf{N_S(p')}$ is obtained for all pixels from $\mathbf{U}$, spatial estimation is applied to recover the scatter radiation $\mathbf{\tilde{N}_S(p)}$ for the whole image region $\mathbf{\Omega}$:

$$\mathbf{\tilde{N}_S(p)} = T\{\mathbf{N_S(p')}\}, \quad \forall \mathbf{p'} \in \mathbf{U}, \quad \forall \mathbf{p} \in \mathbf{\Omega}. \tag{5.10}$$

where $T\{\bullet\}$ is the respective estimation operation detailed in Chapter 5.2.3. With the aid of the estimated scattered radiation $\mathbf{\tilde{N}_S(p)}$ an estimate of the primary radiation can be obtained by applying (5.2) to each image pixel. Note that in this case the acquisition considered is the one without the mask.

In order to provide a demonstration of different stages comprising PASSSA, a schematic depicting intermediate images from a single energy channel (50 keV) is presented in Figure 5.6. Firstly, a difference image is obtained by subtracting the modified (with attenuators) acquisition from the unmodified one. Note that the resulting image reflects the attenuator pattern, which is sparse. Next, the transition matrix is applied for each attenuator shadow pixel of the difference image in order to recover a sparse unmodified primary image, which is then subtracted from the unmodified total image resulting in a sparse scatter image. Finally, spatial estimation is applied in order to obtain a full scatter distribution. This completes the scatter estimation phase. Scatter correction is achieved through the separation phase, which is a straightforward subtraction of the estimated full scatter image from the unmodified total image. As a result an estimate of the unmodified primary image is recovered.

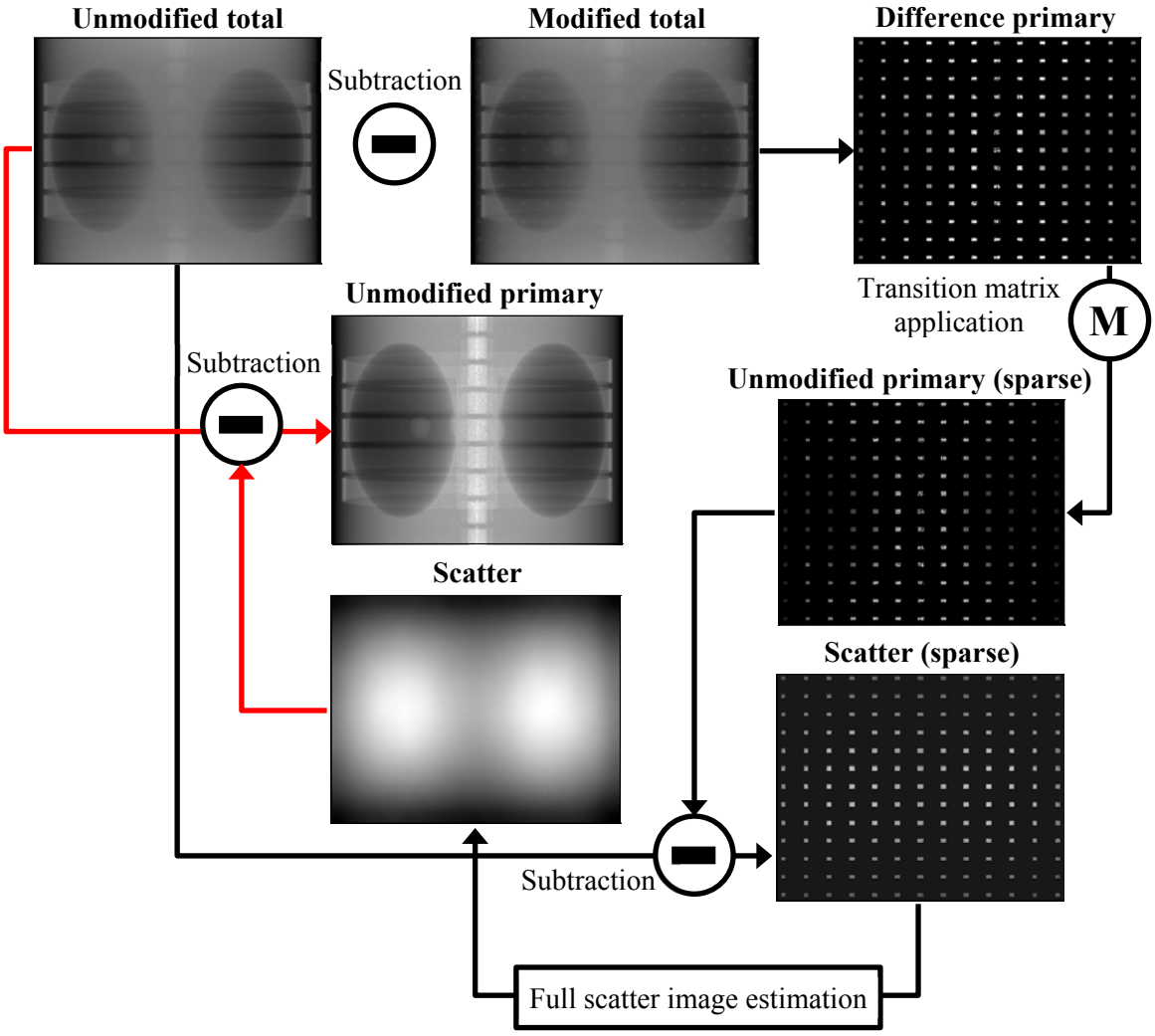

Figure 5.6. Schematic illustrating individual stages of PASSSA when applied on a radiographic projection. The procedure is divided into scatter estimation (black arrows) and separation (red arrows) phase. Images are taken from a single channel (50 keV). Scatter images are in number of photons, while the total and primary images are attenuation images (unitless)

It is important to note that PASSSA can be also subdivided in terms of *online* (performed during the acquisition) and *offline* (performed preliminary to the acquisition) operations. The online part is the one comprising the scatter estimation and correction procedures (Figure 5.6) while the offline part consists in determining the transition matrix **M** (Chapter 5.2.2).

As noted previously in Chapter 2.4.2, CT datasets are collections of radiographic projections taken at various angles. Thus, in order to correct for scatter in the context of CT imaging, one can apply PASSSA per projection and then apply a reconstruction algorithm (e.g. FDK) on the scatter corrected projection data.

Finally, despite the presentation of the PASSSA concept based on two total images (modified and unmodified), it does not necessarily imply that two acquisitions need to be performed. The unmodified version is only different from its modified counterpart in the attenuator shadow region. Thus, some form of spatial estimation can be employed to recover the unmodified total signal based on attenuator shadow information and its neigh-

borhood (Chapter 7.3.1). In the context of CT angular estimation (potentially coupled with spatial estimation) can also be applied (Chapter 7.3.2).

Note also that, compared to the BS approach (Chapter 5.1.3), information in the attenuator shadow region is only modified and not lost. This can be exploited to estimate the unmodified total signal in the respective region. Additionally, this indicates that PASSSA can be more readily implemented in single acquisition configuration than the BS approach. Another important virtue of PASSSA with respect to latter technique is that it does not require scatter level correction, due to the low influence of the attenuator mask on the incident tube flux.

5.2.2. Transition matrix

As outlined previously (Chapter 5.2.1), the transition matrix represents a basis change for the matrix $\mathbf{W}^{-1}$, which can be linked to the attenuator material and thickness via (5.7). Additionally, the analytical expression for $\mathbf{M}$ was:

$$\mathbf{M} = \mathbf{D} \times \mathbf{W}^{-1} \times \mathbf{D}^{-1} . \tag{5.11}$$

Before presenting the chosen parametric model for the transition matrix, some key observations can be given. Firstly, from expression (5.11), it can be stated that if $\mathbf{D}$ is non-singular and $\mathbf{D}$ and $\mathbf{W}^{-1}$ are square matrices, then $\mathbf{W}^{-1}$ can be considered *similar* to $\mathbf{M}$. Thus, several interesting properties apply: the trace and eigenvalues of $\mathbf{W}^{-1}$ are equal to those of $\mathbf{M}$. Moreover, if $\mathbf{D}$ is triangular then $\mathbf{M}$ will also be triangular given that $\mathbf{W}^{-1}$ is diagonal.

Using a DRM ($\mathbf{D}$) corresponding to realistic spectrometric detector (non-diagonal, 500 µm pixel, charge sharing corrected) with 110 energy channels (1 keV width) and $\mathbf{W}^{-1}$ corresponding to a 2 mm thickness aluminum attenuator, an example transition matrix is computed analytically using (5.7) and (5.11). The resulting $\mathbf{M}$ along with a horizontal (line) profile is presented in Figure 5.7.

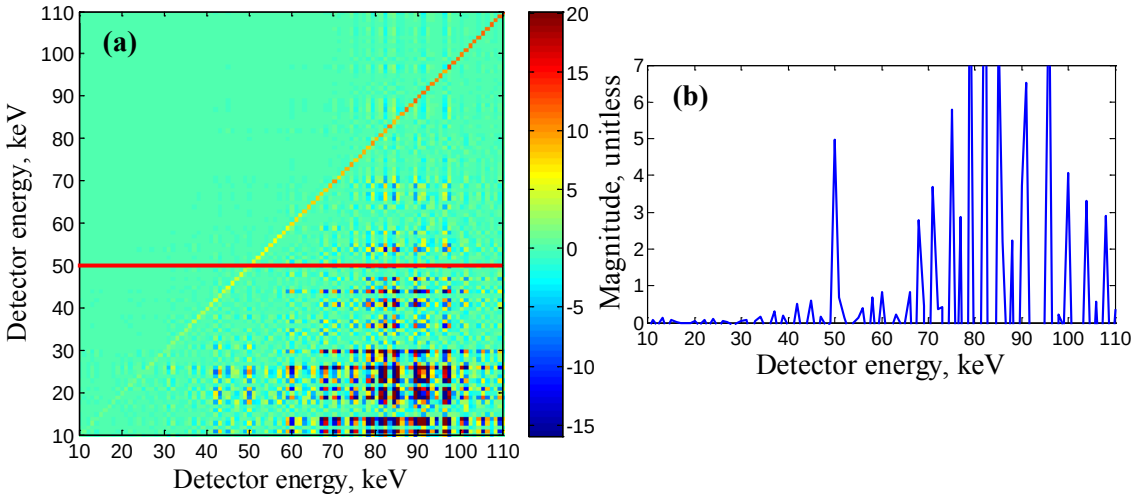

Figure 5.7. Example of the transition matrix $\mathbf{M}$ computed via (5.11) with a corresponding line profile at 50 keV (b). The condition number is about 7.5×10^4. An aluminum attenuator (2 mm thickness) was considered.

Analysis of Figure 5.7 indicates that the analytically calculated transition matrix is mostly triangular with a strongly pronounced diagonal and a high level of noise. The latter

is related to the poor conditioning of **D** (condition number of about 1.4×10^5). Furthermore, the line profile indicates a strongly peaked diagonal. The quasi-triangularity of the computed transition matrix can be directly linked to the quasi-triangularity of the DRM (Chapter 2.4.1) whilst the diagonal is related to the similarity with $\mathbf{W}^{-1}$. Indeed, if the diagonals of $\mathbf{W}^{-1}$ and **M** are compared (Figure 5.8), it can be seen that they are quite similar (within the limit of numerical noise in **M**). The diagonal preservation is not completely unexpected bearing the relationship of the transition matrix and $\mathbf{W}^{-1}$.

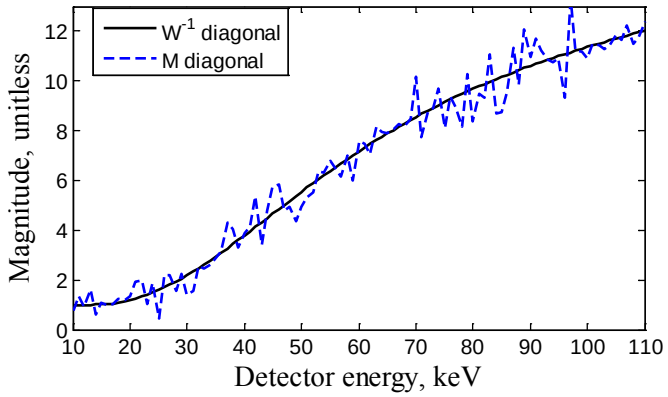

Figure 5.8. Comparison of **M** and $\mathbf{W}^{-1}$ diagonals as a function of energy for an aluminum attenuator (2 mm thickness).

The observations of the analytical form of **M** indicate that the diagonal is approximately preserved. However, they do not give a clear indication on how to manage the rest of the matrix coefficients. In order to reply to this question, a line profile (50 keV) of the considered **D** is examined Figure 5.9.

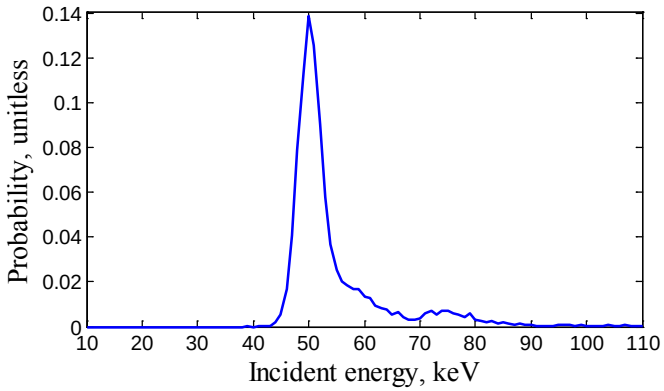

Figure 5.9. Line profile of the considered DRM (**D**) corresponding to realistic spectrometric detector (non-diagonal, 500 µm pixel, charge sharing corrected) taken at 50 keV. The condition number of **D** is about 1.4×10^5.

The examination of Figure 5.9 can give ideas on how the DRM deforms the incident tube spectrum. Namely, it does not only assign the incident photons, located at the correct energy (50 keV), to the corresponding measured energy, but also (predominantly) the photons located at energies higher than the considered one. In fact, it can be shown that this effect is even more pronounced for lower energies. Thus, globally, the spectrum shape will shift to lower energies. It is also worth noting that in the case of a perfect spectrometric detector, one would observe a single peak at 50 keV in the considered line profile.

Bearing in mind the diagonal preservation between **M** and $\mathbf{W^{-1}}$ and the dynamics of spectrum deformation produced by the DRM, the following parametric model for **M** is proposed:

$$\mathbf{M}(E^*,\bullet) = \left(W(E^*,E^*)\right)^{-1}\mathbf{f}\,, \tag{5.12}$$

where $\mathbf{M}(E^*,\bullet)$ is the line of **M** corresponding to a fixed detector energy bin E^* and $\mathbf{f} = f(E,E^*,\sigma,\alpha,\beta)$ is a parametric function with free parameters σ, α and β. The expression for **f** is given in (5.13).

$$f(E,E^*,\sigma,\alpha,\beta) = \begin{cases} (1-\beta)\exp\left(-\dfrac{(E^*-E)^2}{2\sigma^2}\right) + \beta\exp(-\alpha E), & E^* \geq E \\ \exp\left(-\dfrac{(E^*-E)^2}{2\sigma^2}\right), & E^* < E \end{cases}. \tag{5.13}$$

The matrix **M** obtained using (5.12) and (5.13) is, essentially, a deformed version of the diagonal matrix $\mathbf{W^{-1}}$. The model from (5.13) was chosen as it closely resembles the form of the photon detection probability distributions from the DRM (Figure 5.9).

For each energy channel E^*, the free parameters of the function from (5.12) need to be estimated. In order to do this, an offline calibration procedure in a scatter free geometry can be performed. Consider a set of K pairs of spectra $\{\mathbf{\Delta N}, \mathbf{N_P}\}_k$ generated with different levels of attenuation. Then, for each energy channel, the following minimization procedure, based on (5.8), can be applied to determine the set of optimal parametric function parameters:

$$\left[\hat{\sigma},\hat{\alpha},\hat{\beta}\right] = \underset{\sigma,\alpha,\beta}{\arg\min} \sum_{k=1}^{K} \left| \{N_P(E^*)\}_k - \mathbf{M}(E^*,\bullet) \times \{\mathbf{\Delta N}\}_k \right|, \tag{5.14}$$

In (5.14) it is important to note that $\mathbf{M}(E^*,\bullet)$ and $\{\mathbf{\Delta N}\}_k$ are row and column vectors, respectively. Once σ, α and β are estimated for each E^*, the transition matrix can be constructed with the aid of (5.12) and (5.13). Note that if the parameters are smooth functions in energy channel E, regularization in the energy channel dimension may also be considered. Additionally, the procedure of **M** estimation can be performed for each attenuator shadow pixel individually or for a group of attenuator shadow pixels.

An example of a transition matrix acquired through simulation with the aid of the previously used $\mathbf{W^{-1}}$ and **D** is provided in Figure 5.10. From the respective example one can note that the parametric **M** is mostly diagonal with a slight tail due to the exponential component of the model from (5.13). Moreover, the parametric version of **M** is much more stable than its analytical counterpart displayed in Figure 5.7 (condition number 10^4 times lower).

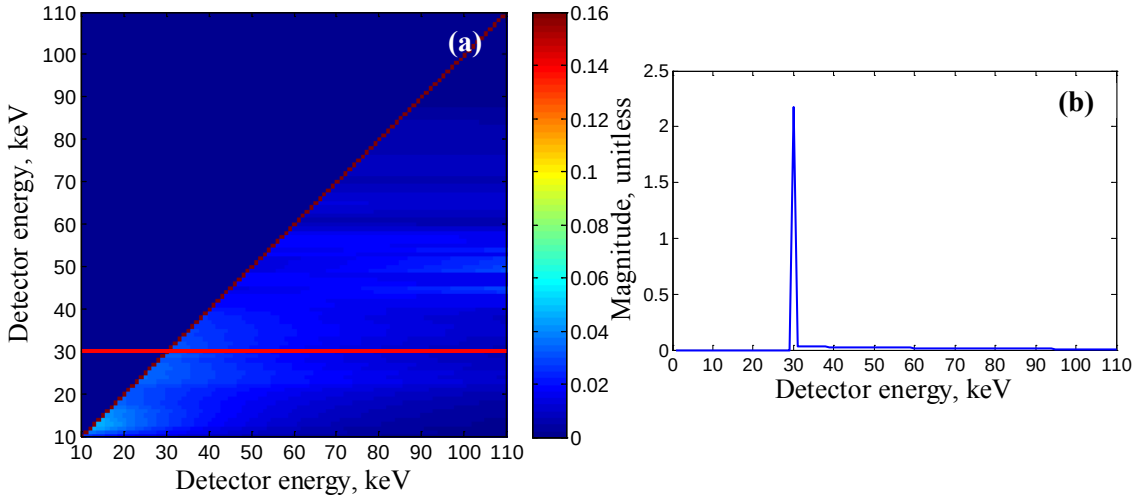

Figure 5.10. Example of the transition matrix **M** based on the parametric model from (5.13) (a) with a corresponding line profile at 30 keV (b). The condition number of the matrix is about 12.8. An aluminum attenuator (2 mm thickness) was considered. Note that the color bar of (a) has been adjusted to better view the non-diagonal coefficients. The diagonal values appear saturated as they are outside this range (c.f. Figure 5.8).

There are also other ways that can be considered for the estimation of the transition matrix. For example, one can apply linear least squares directly to (5.8) in combination with the known data samples described previously. However, such a procedure requires the determination of a larger number of parameters than in the case of a parametric model based **M**. The exception is only when the number of channels is small (≤ 3). Furthermore the least square estimation will lead to a less stable solution in the case of large **M** matrices than the parametric approach.

Another option is to generate an exhaustive offline calibration database where K is large. Then using grid search algorithms, one can derive a corresponding primary from the database each time a difference of primaries is calculated in the course of the PASSSA algorithm. In this case the major limit is the computational time, as the grid search is a much longer procedure than direct matrix multiplication. This is even more valid in the case of noisy measurement data.

5.2.3. Spatial estimation of scatter

By applying (5.9) for each detector element contained in the attenuator shadow region, a spatially sparse spectral scatter image is obtained. The goal is to recover the full scatter image $\tilde{\mathbf{N}}_S$.

Based on the findings of Chapters 3.1.2 and 3.1.3, it was concluded that for a range of acquisition configurations the spectrum shape of the scatter component can be considered preserved in the first approximation across different image pixels. This justifies the assumption that the scatter spectrum measured in an arbitrary image pixel **p** can be separated into a spatial g(**p**) and an energy **F** component:

$$\tilde{\mathbf{N}}_S(\mathbf{p}) = g(\mathbf{p})\mathbf{F}, \quad \forall \mathbf{p} \in \boldsymbol{\Omega}\,. \tag{5.15}$$

In (5.15) $g(\mathbf{p})$ is the level coefficient (scalar) and **F** is a discrete function of detector energy bin (vector). Next, the spatial component is expressed from (5.15):

$$g(\mathbf{p}) = \left(\sum_E \mathbf{N_S}(\mathbf{p}) \right) \left(\sum_E \mathbf{F} \right)^{-1}, \quad \forall \mathbf{p} \in \mathbf{\Omega}. \tag{5.16}$$

From the sparse scatter image it is possible to obtain an estimate of **F**. In order to do this, the mean scatter spectrum among the n_U points contained in the attenuator shadows is computed:

$$\widetilde{\mathbf{F}} = (n_U)^{-1} \sum_{\mathbf{p'}} \mathbf{N_S}(\mathbf{p'}), \quad \forall \mathbf{p'} \in \mathbf{U}. \tag{5.17}$$

Insertion of the estimate of the energy component from (5.17) into (5.16) leads to a sparse version of the spatial component:

$$z(\mathbf{p'}) = \left(\sum_E \mathbf{N_S}(\mathbf{p'}) \right) \left(\sum_E \widetilde{\mathbf{F}} \right)^{-1}, \quad \forall \mathbf{p'} \in \mathbf{U}. \tag{5.18}$$

Thus, if one recovers the spatial scatter component from $z(\mathbf{p'})$, the full scatter spectral image can be recovered via (5.15). This could be achieved by simple spatial interpolation. However, since the operations present in (5.9) tend to amplify noise, a regularized estimation approach is a better choice. One searches for a function $\widetilde{g}(\mathbf{p})$ that on one side best fits $z(\mathbf{p'})$ and on the other is smooth:

$$\widetilde{g}(\mathbf{p}) = \arg\min_g H(\mathbf{p}) \left\| g(\mathbf{p}) - z(\mathbf{p}) \right\|^2 + sR\{f(\mathbf{p})\}, \quad \forall \mathbf{p} \in \mathbf{\Omega}. \tag{5.19}$$

where $H(\mathbf{p})$ is an indicator function equal to 1 when $\mathbf{p} \in \mathbf{U}$, s is a positive scalar controlling the amount of smoothness and $R\{\}$ is an operator quantifying the roughness of the function of interest. The assumption on smoothness of the spatial scatter component is justified by the low frequency nature of scattered radiation (Chapter 3.1.1).

If R is chosen as the discrete version of the second derivative, then a discrete cosine transform (DCT) based spline (DCT-spline) approach can be used to iteratively solve the corresponding minimization problem of (5.19) [84]. However, the solution provided in [84] only provides isotropic smoothing. This can be limiting, for example, in the case of CT data, where images are of non-equal dimensions, and anisotropic smoothing is required. With the aid of more explicit formulations of some key algorithm parts [85] and a modified version of R [86], an updated version of the solution from [84] incorporating anisotropic smoothing was derived for a given M×N sized 2D image:

$$\begin{aligned} &\widetilde{\mathbf{g}}_{\mathbf{l}+1} = \mathbf{C}_{\mathbf{MN}}^{\mathbf{T}} \left(\mathbf{I_{MN}} + s\mathbf{\Lambda} \right)^{-1} \mathbf{C_{MN}} \left(\mathbf{H}(\mathbf{z} - \widetilde{\mathbf{g}}_{\mathbf{l}}) + \widetilde{\mathbf{g}}_{\mathbf{l}} \right), \\ &\Lambda_{ij} = \Lambda_{iN}^2 + 2k\Lambda_{iN}\Lambda_{jM} + k^3\Lambda_{jM}^2 \\ &\Lambda_{iN} = 2\left(1 - \cos\left[\frac{\pi(i-1)}{N} \right] \right), \quad \Lambda_{jM} = 2\left(1 - \cos\left[\frac{\pi(j-1)}{M} \right] \right). \end{aligned} \tag{5.20}$$

In (5.20) $\mathbf{C_{MN}}$ and $\mathbf{C_{MN}^T}$ are the DCT and inverse DCT, respectively, $\mathbf{I_{MN}}$ is an identity matrix, $\mathbf{\Lambda}$ is a diagonal matrix containing the eigenvalues of R and k is an additional positive smoothing parameter accounting for anisotropy. It is worth noting that the only difference of (5.20) from the solution provided in [84] is the supplemental smoothing parameter and thus a modified expression of $\mathbf{\Lambda}$. Note also that the eigenvalues can be pre-computed prior to the main iterative solution procedure.

In order to reduce or cancel the side effects of outliers on (5.20), a low weight can be assigned to them with the aid of an iterative reweighting process (outer to the current iterative loop of (5.20)), as is often done in robust local regression. The method used for this purpose consists in combining weights with a specified weighting function and with the aid

of current residuals, which are then iteratively updated (only a few iterations are required), until no change is observed [84]. For more details on the robust weight modification procedure the reader is referred to [84].

The smoothing parameters s and k can either be set by the user or determined in the course of the iteration procedure. In order to do this, various techniques can be applied [87]. In the current version of the DCT-spline method the generalized cross-validation (GCV) approach used in [84] for the determination of s while k was left to be specified by the user.

It is also worth noting that L2-norm data fidelity term in (5.19) can also be transformed into a L1-norm data fidelity term, in order to provide more robustness from outliers and large gaps in the data. An L1-derivative of the method from [84] has also been proposed and validated [88]. However, despite its potential improvements, the solution remains less stable than the L2 version.

Finally, by using the estimates from (5.20) and (5.17) in (5.15), the full spectral scatter image $\tilde{\mathbf{N}}_S$ can be recovered.

5.2.4. Conclusion

PASSSA represents a novel scatter correction method exploiting multi-energy information. The concept described in Chapter 5.2.1 along with its key elements (Chapters 5.2.2 and 5.2.3) clearly describes an innovative solution for the scatter correction problem in energy-resolved imaging. The method has the potential to substantially reduce scatter related spatial distortions and quantitative bias, which in turn will lead to better quality x-ray images. For this reason, the concept of PASSSA is the subject of a submitted patent.

In what follows, the developed method is evaluated through simulations and experiments in both radiographic and tomographic modes (Chapter 6). Additionally, an analysis of the method and corresponding x-ray system components (e.g. attenuator mask) is conducted and potential improvements are discussed (Chapter 7).

6. EVALUATION OF THE DEVELOPED SCATTER CORRECTION METHOD

In Chapter 5.2 a novel scatter correction approach for multi-energy x-ray imaging was presented and some key components were discussed. In the present chapter the aim is to evaluate PASSSA performance through simulated radiographic and tomographic acquisitions (Chapter 6.1) as well as through experimental multi-view radiographs (Chapter 6.2). Moreover, an analysis of material decomposition performance improvement after the application of the proposed method is examined in Chapter 6.3.

6.1. Evaluation through simulations

In order to analyze the efficacy of PASSSA, a simulation study was conducted. The simulations were done with the aid of the Sindbad-SFFD tool (Chapter 4.3). Chapter 6.1.1 provides detail on the x-ray system and geometry used for evaluations in radiographic (Chapter 6.1.2) and tomographic (Chapter 6.1.3) modes. Additionally, a detailed analysis of transition matrix performance is given in Chapter 6.1.4. Finally, a discussion of the results is provided in Chapter 6.1.5 followed by a conclusion in Chapter 6.1.6.

6.1.1. System description

A tungsten x-ray tube with 2.5 mm of aluminum filtration and an anode angle of 17° was set to 110 kV and 0.2 mAs. The tube parameters were aimed at matching those of a typical thoracic acquisition [89]. Additionally, a 64×680 pixel energy-resolved (1 keV width bins) CdTe detector with a pitch of 1 mm and a thickness of 5 mm was used. The bin width, pitch and thickness closely resemble a reported high count rate prototype linear 1D spectrometric detector [8]. The detector was also coupled with lead collimation in the horizontal direction in order to remove scatter coming outside the imaged object zone. The response of the detector was modelled with aid of a DRM corresponding to a realistic spectrometric detector (non-diagonal, 500 μm pitch, charge sharing corrected). Pile-up effects were not considered. According to [90], the Poisson model is a good representation of the photon noise in CT imaging. This model was used for the simulations. A total of 360 projections were acquired with and without the attenuator mask. The mask consisted of a 3×17 array of 1×1 mm aluminum square elements (thickness of 2 mm). The spacing between the attenuator centers in the horizontal and vertical directions was 4 mm and 3.2 mm, respectively.

The simplified thorax phantom (Figure 3.2, Chapter 3.1.2) placed in a typical CT geometry with a SDD distance of 100 cm and a SAD of 65 cm was used for both radiographic and tomographic simulations. The axis was aligned with the object center. Figure 6.1 gives an overview of the acquisition geometry.

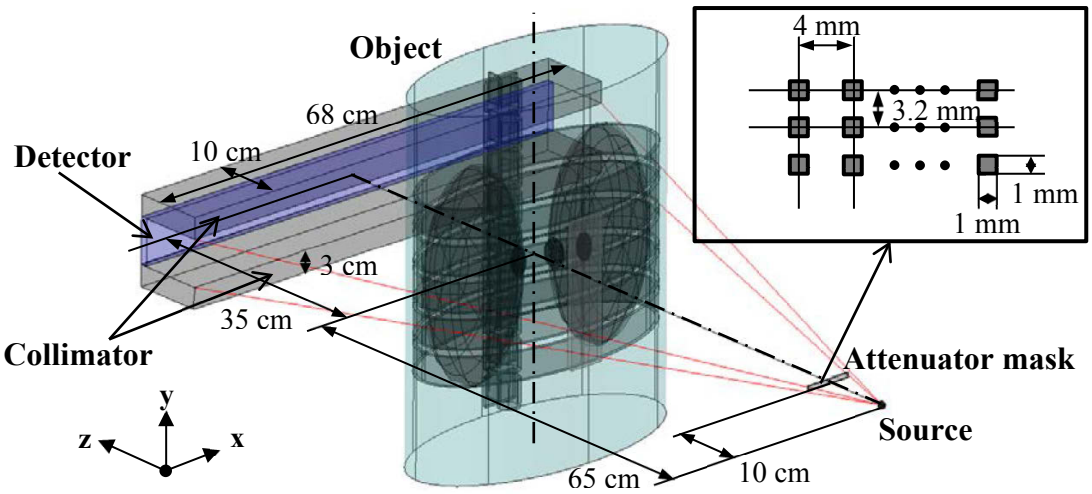

Figure 6.1. Schematic illustrating the acquisition geometry. A magnification of the attenuator mask is also displayed. The illustration corresponds to projection #91 (or at 90 degrees).

In order to estimate **M** prior to the actual acquisitions, a calibration database (scatter and noise free) was generated with the aid of two basis materials: water and aluminum. For each attenuator shadow pixel a set of $\{\mathbf{\Delta N}, \mathbf{N_p}\}_k$ pairs was produced by varying the thicknesses of water and aluminum. The range of thicknesses considered was 1-20 cm (1 cm steps) and 0.1-2 cm (0.1 cm steps) for water and aluminum, respectively. With the aid of (5.12)–(5.14), and the generated database an estimate of **M** was obtained for each attenuator shadow pixel to account for conicity effects. Model parameter σ was set to 0.2, in order to ensure a highly peaked **M** diagonal. The parameter was fixed, as relevant preliminary studies have shown it to be relatively constant if included in the minimization process. For the other two parameters, the Nelder-Mead simplex algorithm [91] was used for the minimization of (5.14) resulting in α and β values of -0.02–0.04 (0.01 on average) and 0–0.07 (0.02 on average), respectively for the considered energy interval of 0–110 keV.

In the DCT-spline scatter estimation algorithm, GCV was used to estimate the smoothing parameter *s*, while *k* was set to the ratio of detector dimensions: 10.625. Furthermore, (5.20) was iterated until no substantial change was observed.

6.1.2. Results in radiography

For a qualitative evaluation of PASSSA in a radiographic acquisition mode, a single projection from the acquired CT dataset was used (Figure 6.1). Comparison was made between three types of spectral images: total (with scatter), primary (no scatter) and corrected total (total after applying PASSSA). The SPR was between 14% and 22% (17% on average) for different projections.

Firstly, in order to examine the spatial performance of the scatter separation approach, the total attenuation image was computed by applying the following formula to each image pixel **p**:

$$A_T(\mathbf{p}) = -\log\left[\left(\sum_{E_{\min}}^{E_{\max}} N_T(\mathbf{p},E)E\right)\left(\sum_{E_{\min}}^{E_{\max}} N_0^d(\mathbf{p},E)E\right)^{-1}\right], \quad \forall \mathbf{p} \in \mathbf{\Omega}, \tag{6.1}$$

where $A_T(\mathbf{p})$ is the attenuation in pixel $\mathbf{p}$, $N_T(\mathbf{p},E)$ and $N_0^d(\mathbf{p},E)$ are the number of photons measured in pixel $\mathbf{p}$ and energy bin E corresponding to total radiation and the raw tube radiation ($\mathbf{N_0^d(p)=D\times N_0(p)}$). With the replacement of $N_T(\mathbf{p},E)$ by $N_P(\mathbf{p},E)$ and $\tilde{N}_P(\mathbf{p},E)$ in (6.1), primary and corrected total attenuation images were also obtained. The resulting attenuation images are presented in Figure 6.2.

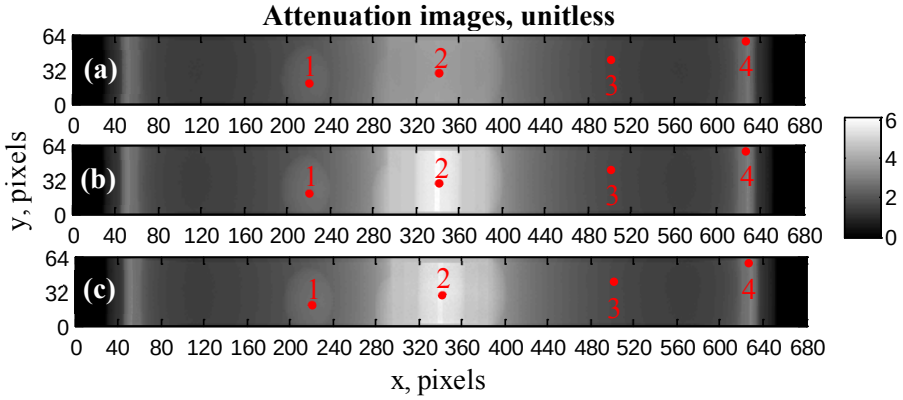

Figure 6.2. Total (a), primary (b) and corrected total (c) attenuation images obtained from their spectral counterparts. The full energy range was considered (0–110 keV). Pixels size was 1 mm. Red markers indicate pixels chosen for spectrum visualizations (Figure 6.4). These locations were chosen to analyze spectra with different levels and nature of object attenuation as well as a variable SPR.

Additionally, for each attenuation image, horizontal profiles were traced (Figure 6.3).

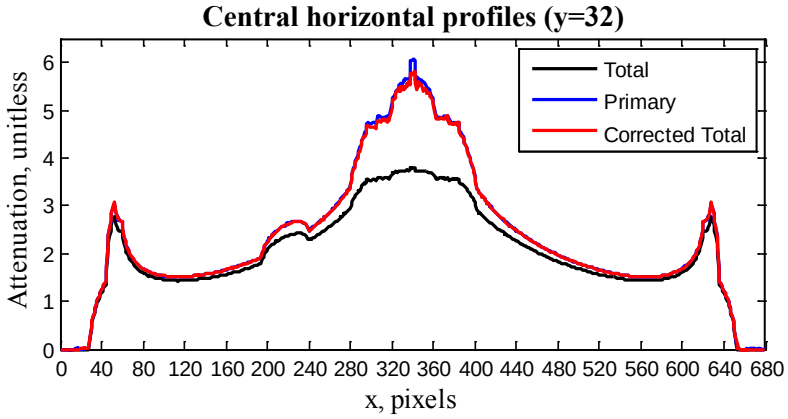

Figure 6.3. Central horizontal profiles from images presented in Figure 6.2. Pixels size was 1 mm. Note that the total profile is quite similar to the primary and corrected total profiles at the sides as the SPR in those zones is lower than in the central part. The SPR in the central part is higher due to the low primary signal in this region (high level of attenuation).

Finally, spectra from several control pixels (indicated in Figure 6.2) are presented in Figure 6.4.

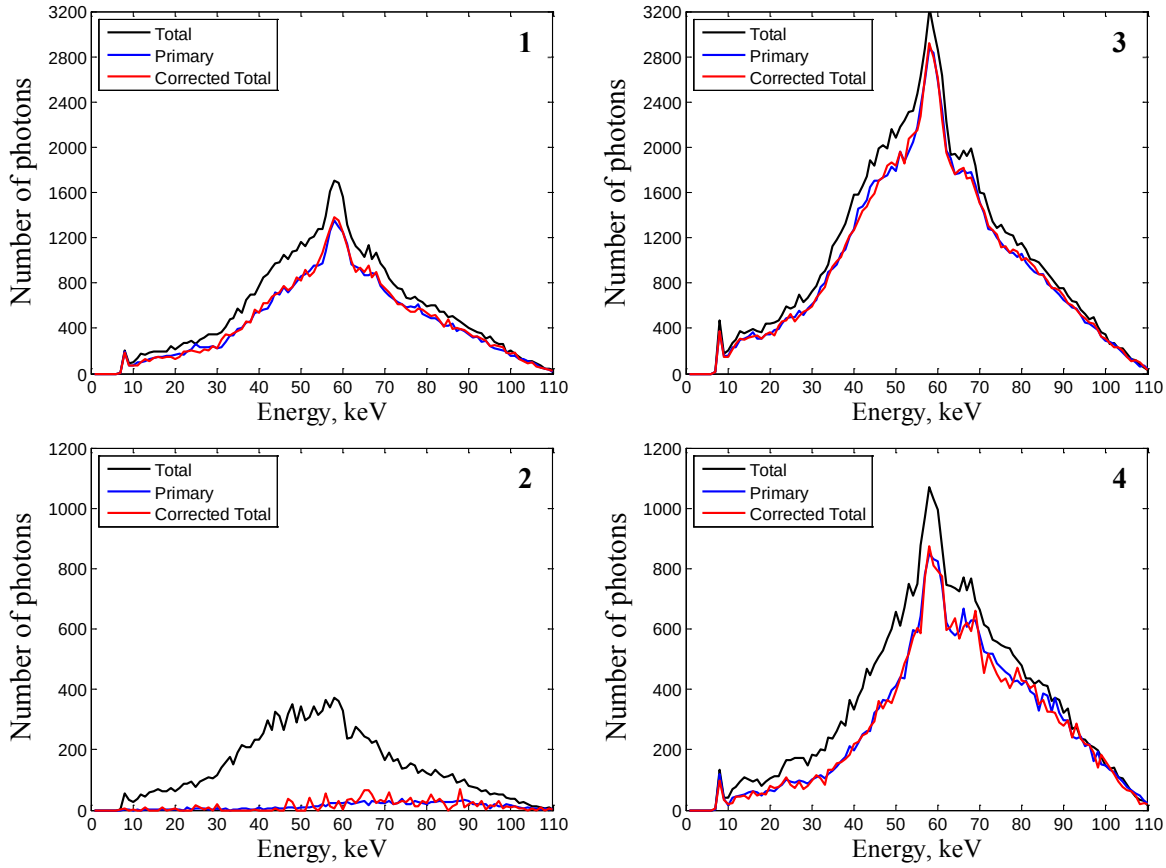

Figure 6.4. Total, primary and corrected total spectra taken from pixels indicated in Figure 6.2. Energy bin width was 1 keV. Spectra from point #2 exhibit a much different spectrum shape and level compared to spectra #1, #2 and #3. This is due to the strong attenuation in the respective region (level) as well as the presence of a substantial amount of bone structure (shape). Furthermore, the SPR in #2 is much higher compared to the other points, thus the total signal is dominated by the scatter component.

For the quantitative evaluation of PASSSA, the NRMSE was used. The $NRMSE_T$ between total and primary spectral images was computed in the following manner:

$$NRMSE_T = \overline{N}_P^{-1} \sqrt{\left(n_p n_E\right)^{-1} \left(\sum_{\mathbf{p},E} \left[N_T(\mathbf{p},E) - N_P(\mathbf{p},E) \right]^2 \right)} \times 100\% \,, \tag{6.2}$$

where n_p is the number of pixels, n_E is the number of energy bins and $\overline{N}_P$ is the number of photons averaged over E and $\mathbf{p}$. The $NRMSE_{PASSSA}$ for the corrected total was also calculated via (6.2) by replacing $N_T(\mathbf{p},E)$ by $\tilde{N}_P(\mathbf{p},E)$. The $NRMSE_T$ and $NRMSE_{PASSSA}$ for the radiographic projection used for the qualitative evaluation was 18.9% and 3.9%, respectively. For the different projections acquired for the CT dataset, $NRMSE_T$ was between 18.7% and 29.3% and 22.6% on average. Equivalently, $NRMSE_{PASSSA}$ was between 3.8% and 8.5% and 5.2% on average for the considered projection data.

Noise levels for different total radiation projections were also quantified in order to give an idea of method performance based on the noise in the input data. Relative noise $r(\mathbf{p})$ was computed for each total projection pixel as the ratio of the STD over the total number of arriving photons:

$$r(\mathbf{p}) = \left(\sqrt{\sum_E N_T(\mathbf{p},E)}\right)\left(\sum_E N_T(\mathbf{p},E)\right)^{-1} = \left(\sqrt{\sum_E N_T(\mathbf{p},E)}\right)^{-1}, \quad (6.3)$$

It is important to note that a noiseless version of $\mathbf{N_T}(\mathbf{p})$ is used for the calculation in (6.3) and pixels with inspected object information were considered. According to the Poisson model, the STD is the square root of the mean, which, in the current case, is the total number of photons. The relative photonic noise estimated via (6.3) was between 0.2% and 1.8% for all pixels in projections and 0.6% on average.

Finally, in order to provide a link between scatter induced error, correction performance and input data noise, $NRMSE_T$, $NRMSE_{PASSSA}$, and average $r(\mathbf{p})$ per projection were plotted as functions of projection number in Figure 6.5.

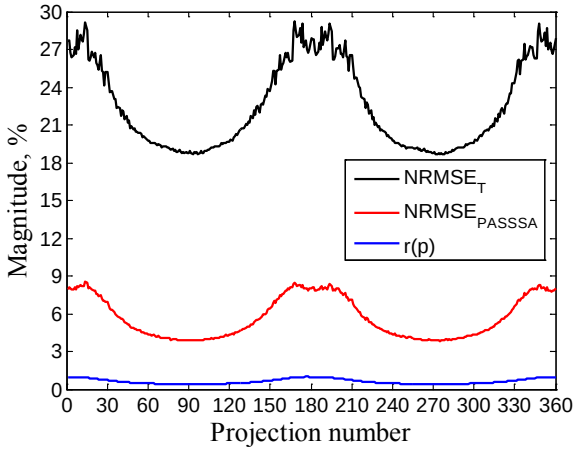

Figure 6.5. $NRMSE_T$, $NRMSE_{PASSSA}$, and average $r(\mathbf{p})$ for different projections. Note that curves follow the photon number change across projections: higher and lower error and noise level magnitudes for lower (around #0, #180 and #360) and higher (around #90 and #270) photon number projections, respectively.

6.1.3. Results in tomography

In order to provide an evaluation of performance for the developed scatter separation method in CT, object volumes were reconstructed from the collected radiographic projections using the FDK approach. Prior to reconstruction, energy-resolved radiographic projections were converted to attenuation images via (6.1). Note that in the case of primary and corrected total attenuation images $N_T(\mathbf{p},E)$ was replaced by $N_P(\mathbf{p},E)$ and $\tilde{N}_P(\mathbf{p},E)$ in (6.1), respectively. Figure 6.6 shows central CT slices corresponding to different types of volumes (total, primary and corrected total)

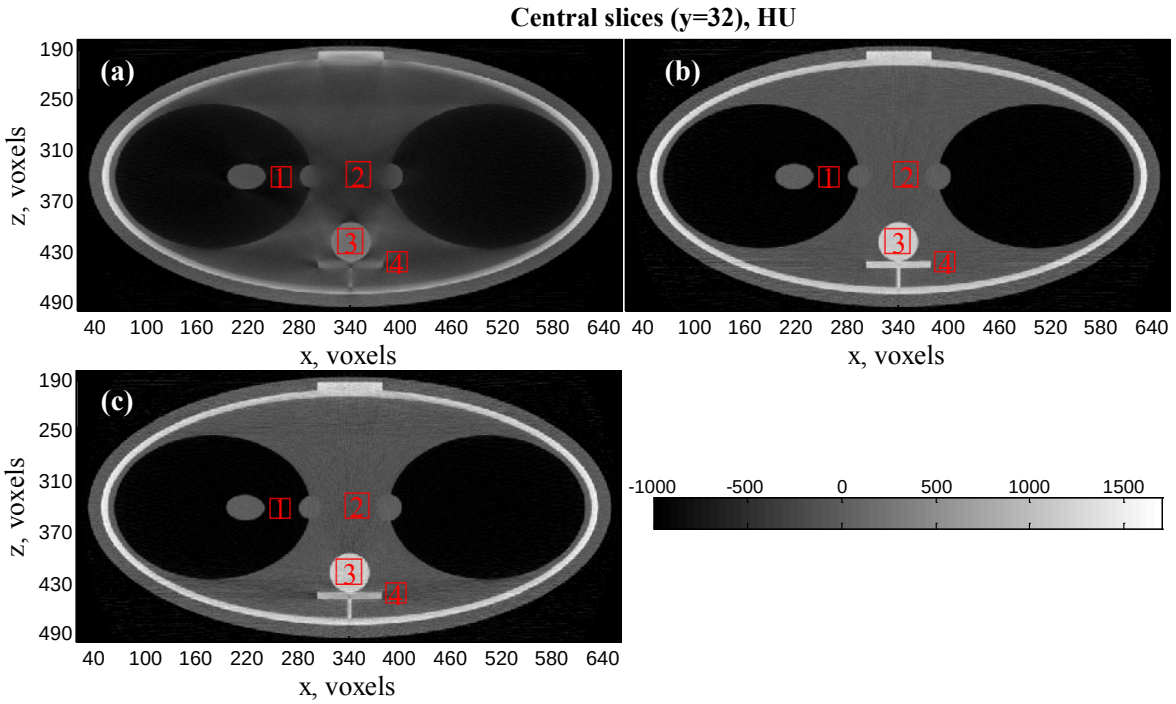

Figure 6.6. Total (a), primary (b) and corrected total (c) CT slices. Voxel size was 0.65 mm. Red squares indicate VOI locations chosen for HU curve visualizations (Figure 6.8). The VOIs aimed at quantifying scatter correction performance in different tissue regions: air (#1), water (#2) and bone (#3). Furthermore, VOIs #3 and #4 were placed to quantitatively analyze the visible artefact structures in the corrected total image.

Additionally, central horizontal profiles (Figure 6.7) were also traced on the slice images provided in Figure 6.6.

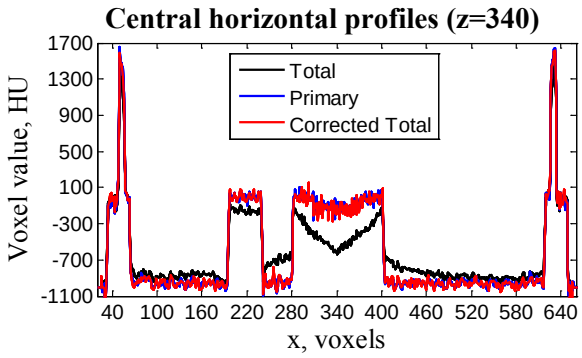

Figure 6.7. Central horizontal profiles taken from the slice images of Figure 6.6.

Further qualitative analysis was carried in the energy domain. In order to reduce noise amplified by the reconstruction procedure, spectral radiographic projections were grouped into 9 equally spaced energy channels (10 keV) on the interval 20–110 keV. Then, energy-resolved attenuation images were computed with the aid of (2.20) and (3.5). Finally, volume reconstructions using the FDK were carried out per energy bin. This means, that instead of obtaining a single volume per type (primary, total or corrected total), 9 volumes were obtained.

Using the VOI regions from Figure 6.6, mean voxel values as functions of energy (HU curves) were computed for total, primary and corrected total volumes (Figure 6.8). The STD was also calculated. The dimensions in x-y-z were 25×5×25 voxels for VOI #1 and #4. For VOI #2 and #3 the dimensions were 30×5×30 voxels, respectively.

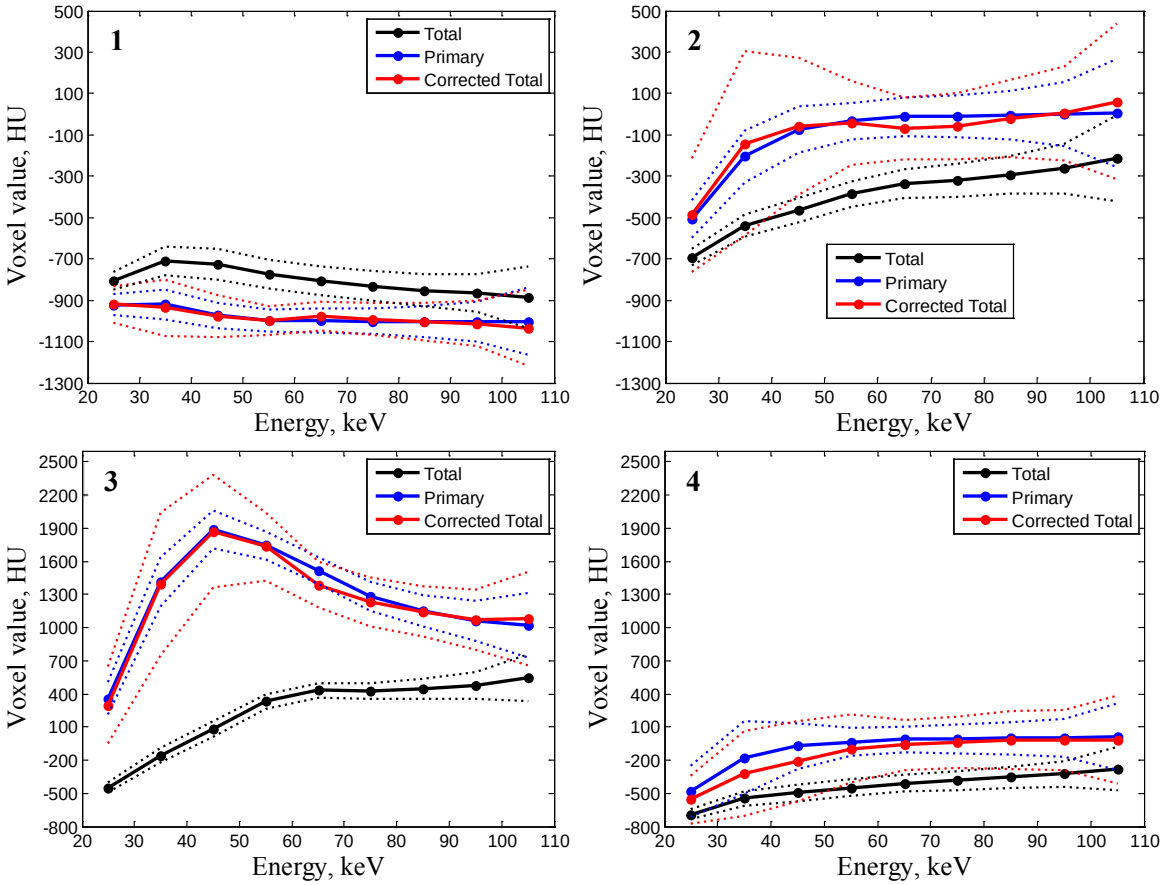

Figure 6.8. Total, primary and corrected total HU curves calculated from VOIs specified in the Figure 6.6. Solid and dashed lines indicate mean and STD values around the mean, respectively. Energy bin width was 10 keV. STD values corresponding to primary and corrected total curves are, in most cases, higher than those of the total curves.

In order to compute voxel values as functions of energy the classical HU conversion formula (2.26) can be applied per energy channel E:

$$V_{HU}(\mathbf{v},E)=\frac{V(\mathbf{v},E)-\mu_{water}(E)}{\mu_{water}(E)}\times 1000\,, \tag{6.4}$$

where $\mathbf{v}=(x,y,z)$ is a voxel, $V(\mathbf{v},E)$ and $V_{HU}(\mathbf{v},E)$ are the initial (in cm^{-1}) and converted (in HU) reconstructed voxel values per energy channel E, respectively. The quantity $\mu_{water}(E)$ corresponds to the value of the attenuation coefficient of water per energy channel E.

The standard deviation $\sigma(E)$ for each VOI per energy channel was computed using the following expression:

$$\sigma(E)=\sqrt{(n_{VOI}-1)^{-1}\sum_{\mathbf{v}}\left(V_{HU}(\mathbf{v},E)-\overline{V}_{HU}(E)\right)^2}\,, \tag{6.5}$$

where $\overline{V}_{HU}(E)$ is the mean voxel value in the given VOI for energy channel E and n_{VOI} is the number of voxels comprising the VOI.

The VOI information was also indicative of quantitative accuracy of PASSSA. Table 3 compares total and corrected total volumes with the ideal primary in terms of the average absolute error on energy per VOI.

Table 3. Average absolute HU error on energy per VOI between total and primary volumes as well as between corrected total and primary volumes.

VOI	Error (total vs primary), HU	Error (corrected total vs primary), HU
#1	173 HU	11 HU
#2	296 HU	32 HU
#3	1033 HU	41 HU
#4	151 HU	63 HU

6.1.4. Transition matrix performance evaluation

In Chapters 6.1.2 and 6.1.3 the performance of the full PASSSA chain has been validated in radiography and tomography with aid of simulations. As noted previously in Chapter 5.2.1, a key element in the method is the transition matrix **M**. Thus it is worth evaluating this component separately from the overall algorithm.

In the current chapter transition matrix performance is examined as function of number of energy channels, noise presence in the calibration and test data, mAs and DRM choice. The performance criterion is the NRMSE between the set of true primary spectra, corresponding to the ones used in the calibration database, and the set estimated with the aid of **M** and the corresponding difference signal **ΔN** via (5.8):

$$NRMSE_{DB} = \overline{N}_{ref}^{-1} \sqrt{(n_k n_E)^{-1} \left(\sum_{k,E} \left[N_{ref}(k,E) - N(k,E) \right]^2 \right)} \times 100\%, \qquad (6.6)$$

where $N_{ref}(k,E)$ and $N(k,E)$ are the number of photons in energy channel E of the kth reference primary spectrum and the corresponding estimated (with **M**) version, respectively (sub-index P has been omitted for simplicity of notation). Additionally, the quantity $\overline{N}_{ref}$ in (6.6) is the number of photons averaged over E and k and n_k is the number of calibration database samples. Finally, it is also important to note that $N_{ref}(k,E)$ and $\overline{N}_{ref}$ are noiseless.

The system settings described in Chapter 6.1.1 are used for calibration and test dataset generation (e.g. tube settings, geometry, calibration materials and thicknesses, DRM, etc.). **M** performance is evaluated for a single (central) image pixel located within the attenuator shadow region. The test dataset is identical to the calibration dataset with the exception of Poisson noise initialization. For each bin number the corresponding bin widths are considered equal.

Firstly, $NRMSE_{DB}$ is computed for varying calibration and test database noise settings. More precisely, four different cases are examined: case 1 – no noise in the calibration and test data, case 2 – no noise in the calibration and noisy test data, case 3 – noise in the calibration (averaging over 20 realizations) and test data, case 4 – noise in the calibration (no averaging) and test data. The result for the considered four cases is presented in Figure 6.9.

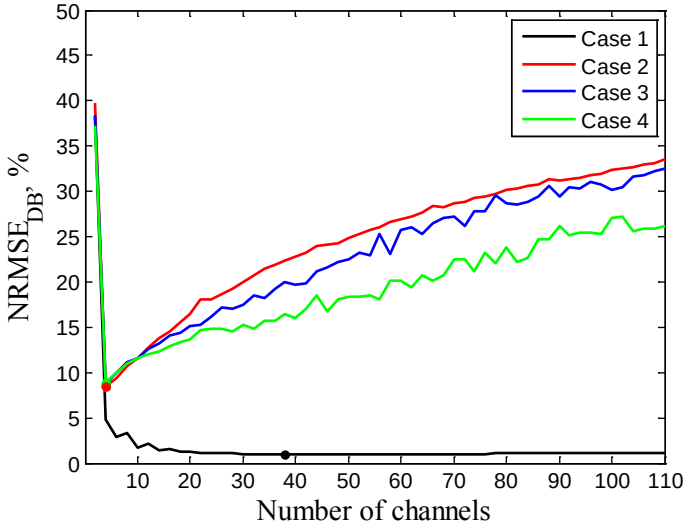

Figure 6.9. *NRMSE$_{DB}$* as function of the number of channels for different noise settings of the calibration and test data: case 1 (noiseless calibration and test data), case 2 (noiseless calibration and noisy test data), case 3 (noisy calibration data averaged over 20 realizations and noisy test data) and case 4 (noisy calibration and test data). The minimum point for each curve is indicated with a circular marker. For each bin number the corresponding bin widths are considered equal.

Next, the initial DRM (**D1**) is replaced by a different one (**D2**) and the same four cases are examined (Figure 6.10). The new DRM is equivalent to the previous one (non-diagonal, 500 μm pitch) with the exception of uncorrected charge sharing. Thus, it exhibits inferior spectral response characteristics than **D1**.

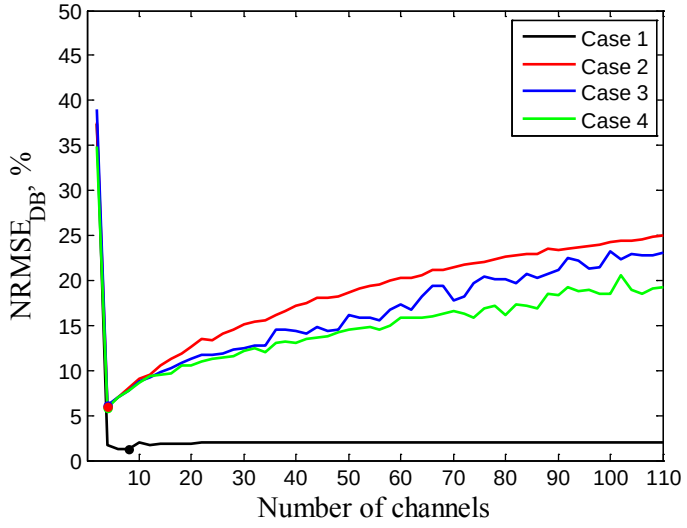

Figure 6.10. *NRMSE$_{DB}$* as function of the number of channels for different noise settings of the calibration and test data: case 1 (noiseless calibration and test data), case 2 (noiseless calibration and noisy test data), case 3 (noisy calibration data averaged over 20 realizations and noisy test data) and case 4 (noisy calibration and test data). Initial DRM replaced by one with uncorrected charge sharing. The minimum point for each curve is indicated with a circular marker. For each bin number the corresponding bin widths are considered equal.

Finally, the optimum number of channels (based on the $NRMSE_{DB}$ minimum value) is computed for both **D1** and **D2** as a function of mAs (Figure 6.11). In terms of noise settings, case 2 was considered.

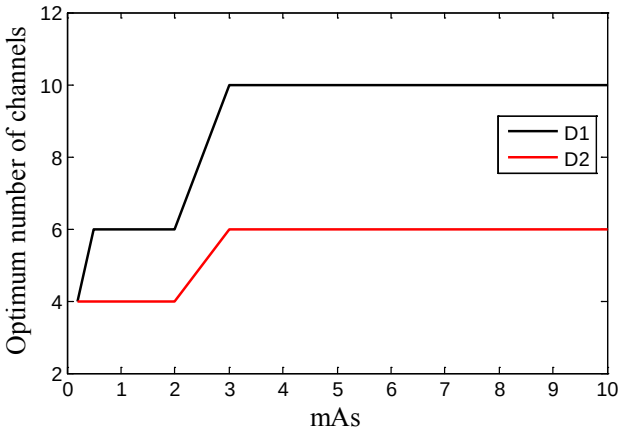

Figure 6.11. Optimum number of channels as a function of mAs for two different DRMs. Noiseless calibration and noisy test data were used. Note that in the simulations examining PASSSA performance (Chapters 6.1.2 and 6.1.3) 0.2 mAs was considered along with the **D1** DRM.

6.1.5. Discussion

PASSSA displayed an impressive level of performance in a radiographic setting (Chapter 6.1.2). The observation of attenuation images from Figure 6.2 reveals the effect of scattered radiation. When comparing the total image (a) with the ideal primary image (b) the loss of contrast and the decrease of internal structure border detectability are clearly visible. The bias induced by scatter radiation can be noticed when viewing the respective central horizontal profiles in Figure 6.3. The comparison of total and primary profiles clearly reveals a sub-estimation of attenuation due to the presence of scattered radiation. All of these effects are reduced to a substantial degree with the application of PASSSA. The corrected total attenuation image (Figure 6.2c) is almost identical to the primary attenuation image (Figure 6.2a). Corresponding profiles from Figure 6.3 display a similar tendency with an exception in the central area (vertebra), where a slight sub-estimation for the PASSSA corrected profile is observed with respect to the primary profile. Additionally, noise increase in this region is also visible.

Further examination of the proposed method performance in the energy domain reveals a high level of primary restoration (Figure 6.4). Corrected total spectra closely resemble the primary spectra even in the extreme cases where SPR is very high (spectrum #2). The accuracy of primary restoration with the aid of PASSSA is further confirmed by observing $NRMSE_{PASSSA}$. The analysis of $NRMSE_T$ and $NRMSE_{PASSSA}$ indicates that the PASSSA corrected total is substantially closer to the reference primary that the scatter corrupted total.

The observed relative noise levels in the total images varied within, approximately, one order of magnitude for different pixels and projections. This was not unexpected, as strong variations in recorded photon numbers arise due to substantial differences in attenuation. From a first glance at Figure 6.5, PASSSA performance ($NRMSE_{PASSSA}$) follows the same trend as the scatter induced error ($NRMSE_T$) and the input data noise (average $r(\mathbf{p})$ per total projection) for varying projections. However, if $NRMSE_T$ and $NRMSE_{PASSSA}$ are quantitatively compared, the error reduction in high noise (around #0 and #180) and low noise

(around #90 and #270) projections is around 3.7 and 4.6, respectively. For all projections, on average, $NRMSE_{PASSSA}$ is 4.3 times lower than $NRMSE_T$. This implies that there is some dependency in method performance as a function of noise level. Nevertheless, the change in PASSSA accuracy is not as substantial as the change in noise magnitude, which exhibits a much larger dynamic across different projections: about 9 times higher in the #0 and #180 projection regions than in the #90 and #270 regions.

In tomographic acquisition mode (Chapter 6.1.3) the developed scatter separation method also shows noteworthy results. Figure 6.6 shows that the corrected volume slice (c) exhibits almost no scatter induced artifacts visible in the total volume slice (b) and is visually close to the primary volume slice (a). The central horizontal profiles from Figure 6.7 further confirm the agreement. However, when comparing the corrected total and total profiles a noise increase in the former is visible.

The inspection of mean HU curves in several characteristic VOIs (Figure 6.8) reveals a high level of agreement between the volumes obtained from PASSSA corrected projections and the primary volumes. Noise increase in the former is again observed as the associated STDs are higher when compared to those calculated for total and primary HU curves. Nevertheless, the overall increase in HU value accuracy is substantial when comparing the errors between primary and total versus primary and corrected total. The decrease of HU value errors on average per energy was more than 10 times with the exception of VOI #4. This less impressive level of performance in this region is coherent with the residuals of streaking artefact still visible in this zone in Figure 6.6c.

The analysis of the transition matrix in Chapter 6.1.4 indicates that a performance gain can potentially be achieved by optimizing the number of energy channels and the calibration protocol. Firstly, for the considered acquisition settings, the accuracy of primary recovery can be improved by approximately a factor of 3 if the number of channels is reduced to 4 (Figure 6.9). Furthermore, performing the calibration on noisy data (case 3 and case 4) improves primary recovery when the number of bins is greater than the optimum (4 bins) as the $NRMSE_{DB}$ in that region is lower than for noiseless calibration case (case 1). A similar trend is observed, when a less perfect DRM (**D2**) is chosen (Figure 6.10). The optimum number of energy bins for the considered acquisition configuration also remains the same with a different DRM.

It is important to note, that $NRMSE_{DB}$ combines both the error due to data noise and model bias. When noise is not present in the data (case 1), a different optimum number of channels for both DRMs can be observed: 38 and 8 for **D1** and **D2**, respectively. Furthermore the behavior of the $NRMSE_{DB}$ curves (case 1) is also different for the different DRMs. Namely, the curve corresponding to **D1** exhibits lower values compared to its **D2** counterpart when the number of channels is higher than or equal to 10 while the **D2** curve exhibits values lower than the **D1** curve for channel numbers lower than 10. This implies that the chosen parametric model can be preferable for either detector for a different energy channel number range. Overall, case 1 considers purely the model error and from the previous observations one notes that the optimum energy channel number is thus dependent on the spectral qualities of the energy-resolved detector.

Additionally, the analysis of case 1 with respect to case 2 curves indicates a dependency of the optimum on noise in the measurement data. If noiseless calibration data is used and measurement data SNR is increased by increasing tube output (Figure 6.11), the optimum number of bins tends to grow both for **D1** (from 4 to 10) and **D2** (from 4 to 6). Thus, the selection of energy channel number should also be conditioned by measurement data noise. In practice, this means that for tomographic applications utilizing low tube outputs

per projection, a lower number of energy bins should be used than for radiographic applications where higher tube outputs can be exhibited.

Finally, another point worth noting with respect to the transition matrix analysis is the channel energy location choice. More precisely, the results presented in Chapter 6.1.4 may display a different error dynamic if a detector with non-uniform width energy channels were to be considered.

PASSSA displays an impressive performance for both radiographic and tomographic simulations. The differences observed between the ideal primary and the corrected total images and volumes can be attributed to several factors: noise in the corrected images and volumes, local spatial scatter estimation errors, residual scatter present in the difference signal, primary recovery error by the transition matrix.

As PASSSA is a scatter correction scheme based on scatter estimate subtraction, it is inherently prone to noise increase as well as other methods of this type (e.g. beam-stop, beam-hole, primary modulation, MC methods). Since a part of the measured total signal is subtracted, while the associated noise remains, the corrected total image obtains a lower SNR when compared to the primary image. The decrease in SNR of the projection images further propagates into the volumes reconstructed in CT contributing to streaking artifacts. The increase in noise could be resolved by application of post-processing (denoising) schemes either on projections or CT volumes. For the CT case regularized statistical reconstruction algorithms could also be applied.

Errors in spatial scatter estimation can be linked to the high level of noise exhibited by the initial sparse scatter data. This is due to the subtractions and matrix multiplication operations present in the method (e.g. (5.5) and (5.9)). Note, additionally, that the noise increase is not isotropic in energy as the diagonal of the transition matrix (c.f. Figure 5.8, Chapter 5.2.2) is not constant and the matrix is not completely diagonal. The following could be incorporated in the spatial estimation to improve performance. Another possible source of estimation inaccuracies is the scatter spectral shape hypothesis outlined in Chapters 3.1.2 and 3.1.3. In order to remedy this issue, the spatial interpolation method could be extended to interpolate directly from the noisy scatter spectra without the need for data separation into spatial and energy components.

Although negligible, the residual scatter is still present in the difference signal and further incorporated in the primary recovered by the application of the transition matrix. This can contribute to errors in the next stage of the method when the restored primary is subtracted from the total.

Since the transition matrix is approximated by a parametric model and measurement data is corrupted by noise, primary recovery errors can arise. As discussed previously, the pure model error of **M** matrix estimation for the considered acquisition settings is quite low (Figure 6.9, case 1) and the error magnitude is mainly due to the noise present in the measurement data. Detailed analysis of the transition matrix performance indicated that optimizing the number of detector energy bins and noise incorporation in the calibration data improves primary recovery performance.

An important virtue of the transition matrix is its ability to learn the detector imperfections in terms of energy response through a calibration protocol. This gives additional model flexibility and gives the possibility to perform estimation on a per pixel basis, which is important as the DRM of a given spectrometric detector can be pixel dependent.

Another important point worth discussing is the attenuator mask. In order to respect the quantitative constraints outlined in Chapter 5.2.1, materials and patterns other than the ones used in this work could be chosen. In fact, any material exhibiting a smooth attenua-

tion coefficient function (copper, iron, etc.) and sufficiently strong for the fabrication of necessary small scale elements can be used. In the case of materials exhibiting strong k-edges in their attenuation coefficient functions, (e.g. silver, gold, tungsten, etc.), the quality of primary recovery via (5.8) will degrade as the corresponding **M** would prove more difficult to parametrize with the model presented in (5.12) and (5.13). This could, possibly be resolved by adapting the parametric model of **M**. In terms of patterns, higher frequency regular or irregular patterns may be considered to improve the sampling of the scatter distribution and thus improving the overall scatter correction performance of PASSSA. Furthermore, the shape of the attenuators can be absolutely arbitrary proven that its magnified version in the image remains sufficiently large to detect.

6.1.6. Conclusion

The evaluation of PASSSA through simulations revealed impressive results for both radiographic projections and CT volumes in terms of scatter effect reduction. The attenuation images and CT slices obtained from corrected data showed a substantial increase in local contrast and internal structure detectability when compared to uncorrected images. Scatter induced bias was also substantially decreased for both radiographic and tomographic data. Visually the corrected total radiographic and CT images were close to their primary counterparts. Additionally, the spectra and HU curves obtained after the application of PASSSA displayed a high level of agreement with the corresponding primary quantities. In terms of quantitative performance, the developed approach proved to be quite efficient as well. Compared to the initial average error of 23% between the uncorrected total and the reference primary projections, the application of the proposed scatter correction scheme reduced this value to around 5%. Additionally, based on noise analysis in different projections, the method proved to be stable for varying noise levels. Finally, in terms of voxel value accuracy an increase by a factor greater than 10 was observed for most inspected VOIs, when comparing the corrected and uncorrected total volumes.

In terms of transition matrix analysis it can be concluded that the optimum number of channels is dependent on the spectral qualities of the energy-resolved detector and tube output of the system or mAs (photon statistics). In addition, it was noted that the transition matrix has an important virtue due to its ability to learn the detector imperfections in terms of energy response, which in turn gives additional model flexibility and the possibility to perform estimation on a per pixel basis. The latter is important as the DRM of a given spectrometric detector can be pixel dependent.

6.2. Evaluation through experiments

Simulations provided in Chapter 6.1 showed an impressive level of scatter correction performance by PASSSA. In the current chapter, the efficacy of the proposed approach is further validated through experimental multi-view radiographic acquisitions.

Chapter 6.2.1 outlines the geometry, phantom and x-ray system settings employed in the experiments followed by Chapter 6.2.2, which describes the reference primary estimation procedure. Chapter 6.2.3 presents the results corresponding to the multiple radiographic projections. Additionally, an analysis of the estimated transition matrix is also performed (Chapter 6.2.4). Finally, a discussion of the obtained results is given in Chapter 6.2.5 followed by a conclusion in Chapter 6.2.6.

6.2.1. System description

Several radiographic acquisitions were performed using a prototype x-ray system (Figure 6.12) in order to experimentally evaluate the performance of PASSSA.

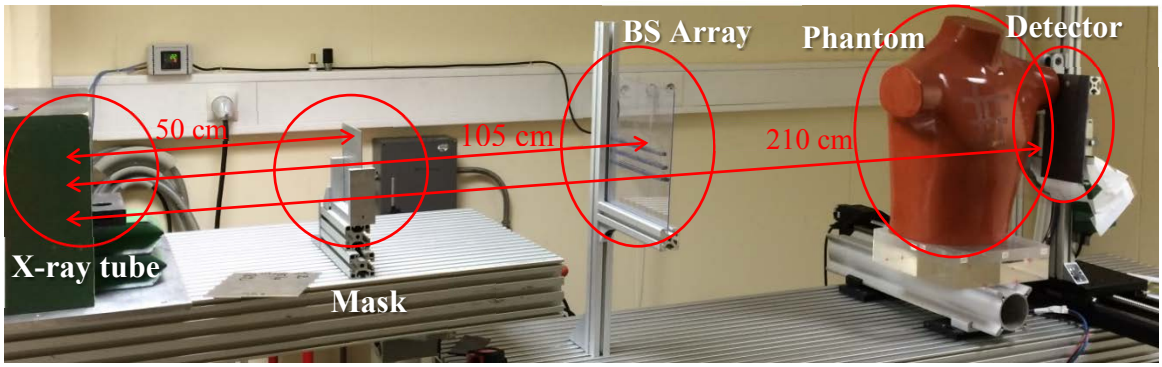

Figure 6.12. Prototype x-ray system used for the experiments. The considered air gap between the object and the detector was about 8 cm. The object is depicted in the lateral acquisition position.

It is worth noting that the system visualized in Figure 6.12 was not adapted for tomographic acquisitions. For this reason only several characteristic radiographic projections of the inspected object were performed.

The x-ray acquisitions were performed on an anthropomorphic thorax phantom (RSD RS-111), displayed in Figure 6.13.

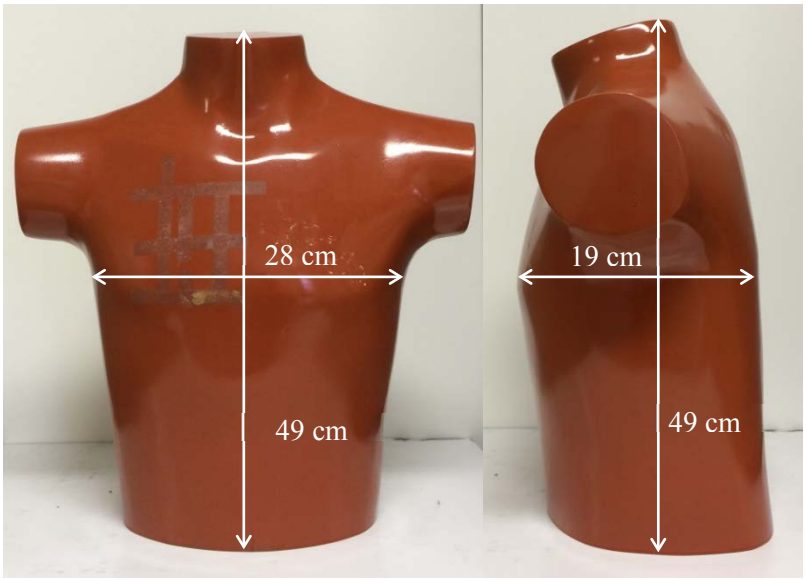

Figure 6.13. Anthropomorphic thorax phantom.

A tungsten x-ray tube (YXLON Y.TU 160-D06) with an anode angle of 11° and 2 mm of aluminum filtration was set to 110 kV and 4 mAs. The tube output (mAs) and voltage (kV) settings were chosen among the range used in a digital chest radiography optimization study [92]. Additionally, a 128×1 pixel MultiX® ME100 energy-resolved (37 channels, ≈2.5 keV width bins, energy threshold of ≈25 keV) CdTe detector with a pitch of 0.8 mm and a thickness of 3 mm was used. The linear 1D detector was translated horizontally to acquire 2D images of 128×451 pixel size. Lead collimation with an opening of 2.5 cm

was present on the detector. The large opening was used to better represent scatter distributions of a true 2D detector. AP (0°), oblique (45°), and lateral (90°) radiographic projections with and without the mask were taken. The mask consisted of a 11×21 array of cylinders with a 2 mm diameter and height placed on a 2 mm aluminum plate (Figure 6.14a). The spacing between the attenuator centers in both directions was 5 mm. Note that the plate was responsible for the 2 mm of tube filtration and was replaced by an equivalent plate (no attenuators) for the no-mask acquisitions. Additionally, a BS array was used in order to obtain scattered radiation images for reference primary radiation calculation. The array consisted of 3 lead strips (0.5×20 cm) with 1 cm thickness and 1.5 cm inter-strip spacing. The strips were supported on a PMMA sheet with a thickness of 1.5 mm. For acquisitions without the BS array, the support sheet presence was compensating by adding a 1.5 mm PMMA filter on the tube.

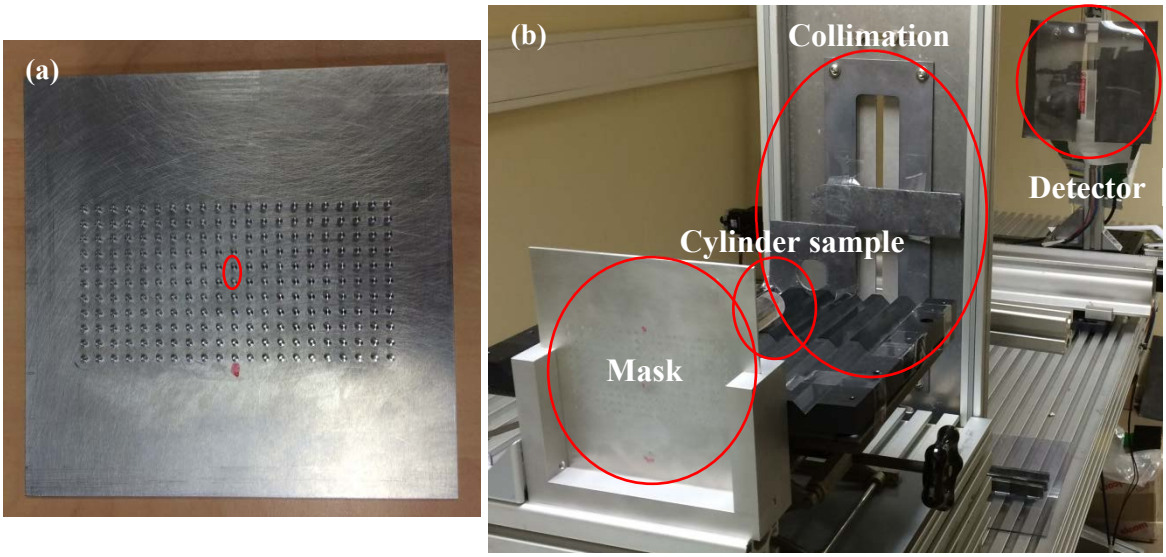

Figure 6.14. Attenuator mask (a) and transition matrix estimation geometry (b). The attenuator mask segment considered for the transition matrix estimation is marked in (a).

In order to estimate **M** prior to the acquisitions, a calibration dataset was established (preliminary to the object acquisitions) using 2 cm diameter cylinders with varying height (thickness) made of two materials: PMMA and aluminum. The considered range of thicknesses was 0–16 cm (4 cm step) and 0–3 cm (1 cm step) for PMMA and aluminum, respectively. Tube current was reduced to 1 mAs in the calibration acquisitions in order to reduce pile-up effects. Additionally, for photon noise reduction, 20 realizations of each sample acquisition were performed and averaged. In order to minimize the contribution of scatter, only a small segment of the mask was considered for the calibration (Figure 6.14a) and additional external collimation (opening of 2×0.4 cm) was incorporated between the samples and the detector (Figure 6.14b). For each attenuator shadow pixel of the considered mask segment a set of $\{\mathbf{\Delta N}, \mathbf{N_P}\}_k$ pairs (c.f. (5.14) from Chapter 5.2.2) was produced. Pixels with similar attenuator thicknesses were then grouped to further reduce photon noise. A total of 6 thickness groups were considered: 0.19–0.24 cm (0.01 cm step). With the aid of (5.12)–(5.14) and the generated dataset an estimate of **M** was obtained for each attenuator shadow pixel group. The pixels of the considered mask segment were then associated with the other attenuator shadow pixels, which were used for imaging and located outside the

segment, through the attenuator thickness. With the aid of this correspondence the estimated matrices were also linked to other attenuator shadow pixels outside the segment. Thus, every attenuator shadow pixel used in the imaging process obtained an associated transition matrix. Finally, a demonstration of mask segments (attenuation images) used for calibration and imaging are presented in Figure 6.15.

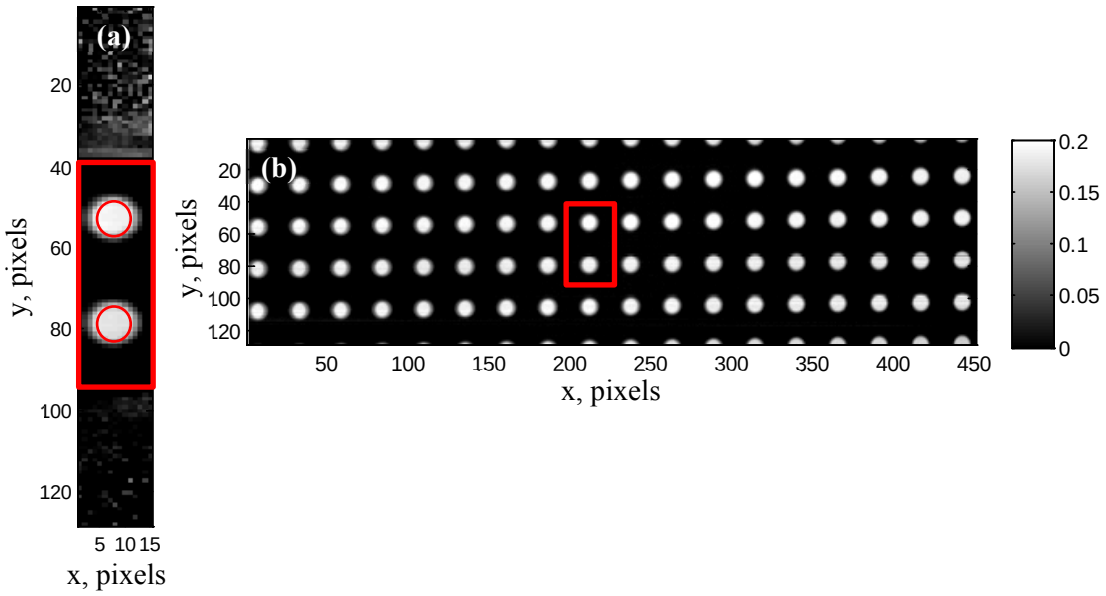

Figure 6.15. Attenuation images (unitless) of attenuator mask segments obtained in the calibration (a) and imaging (b) geometries. The localization of the segment (a) in image (b) is also indicated. Circles in (a) depict the zones used for transition matrix estimation. Note that the shadow borders are not used in order to exclude parts suffering from focal spot blurring.

6.2.2. Reference primary estimation

In order to acquire reference primary images for PASSSA performance evaluation, the BS approach was used (Chapter 5.1.3). With the aid of the array of lead strips described in Chapter 6.2.1 sparse scatter images were acquired for AP, oblique and lateral projections of the thorax phantom considered in the experiments.

Due to the relatively large vertical gaps and measurement data noise it was chosen to apply the DCT-spline based spatial estimation approach presented in Chapter 5.2.3. In order to justify the application of this estimation technique, a scatter spectrum shape analysis in the context of present acquisitions was also performed (Chapter 3.1.3).

Once the full energy-resolved scatter images have been obtained via the concerned estimation approach, a scatter level correction needed to be performed due to a large portion of the incident beam being blocked by the BS array. In order to do this, the initially estimated scatter images were subtracted from the total images acquired with the BS strips. This provided primary images with the BS array in place. Since the primary component in the image zones uninfluenced by the strips is identical to the one present in the images obtained without the BS array, scatter signal with a correct level can be obtained in these zones via subtraction from the corresponding total images (no BS). Once obtained, the scatter signal in these zones was compared with equivalent ones from the initial scatter images in order to determine the level coefficient. This coefficient was then applied on the initial scatter images in order to achieve scatter level adjustment.

Finally, an illustrative summary of the BS approach applied for reference primary image acquisition is provided in Figure 6.16. Note that since this technique is a subtraction type (as is PASSSA), one can divide it into two parts: scatter estimation and scatter separation.

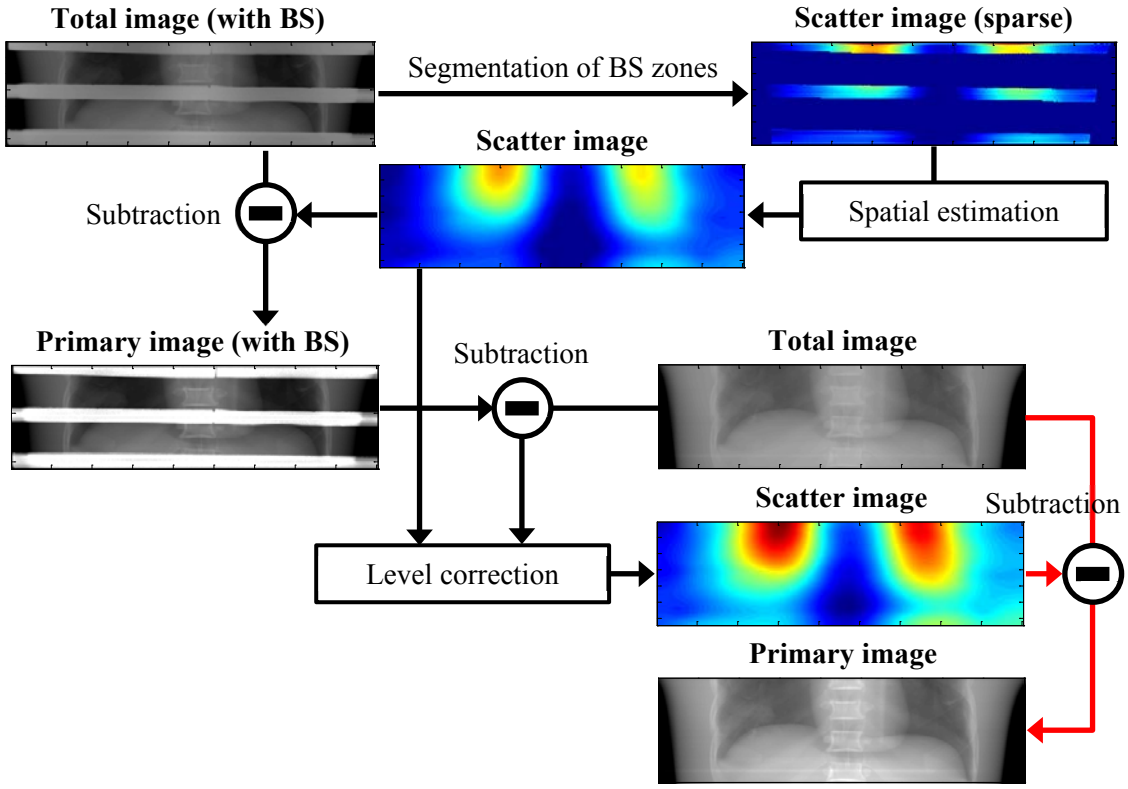

Figure 6.16. Schematic illustrating the reference primary image acquisition via the BS scatter correction method. The procedure is divided into scatter estimation (black arrows) and separation (red arrows) phase. Images are taken from a single channel (50 keV). Scatter images are in number of photons, while the total and primary images are attenuation images (unitless).

6.2.3. Results for multi-view radiography

As in Chapter 6.1, the evaluation of PASSSA was divided into qualitative and quantitative. AP, oblique and lateral radiographic projections were examined. Comparison was made between three types of energy-resolved images: total (with scatter), reference corrected total (total after applying the BS approach) and corrected total (total after applying PASSSA). The SPR for AP, oblique and lateral projections was 33%, 31% and 33%, respectively.

For the qualitative analysis, spatial performance of the developed scatter separation approach was analyzed through attenuation images and corresponding profiles. The total attenuation images were computed by applying (6.1) on each image pixel. With the replacement of $N_T(\mathbf{p},E)$ in (6.1) by the corresponding quantities from the corrected total acquisitions, total corrected with BS and total corrected with PASSSA attenuation images were also obtained. Additionally, spectra (total and corrected total) from characteristic image locations were also analyzed.

NRMSE was once again used for the quantitative evaluation of PASSSA. The $NRMSE_T$ between total and reference corrected total spectral images was computed via (6.2) by re-

placing $N_P(\mathbf{p},E)$ by the respective quantity from the reference corrected total acquisitions. Furthermore, $NRMSE_{PASSSA}$ was also obtained by replacing $N_T(\mathbf{p},E)$ and $N_P(\mathbf{p},E)$ in (6.2) by corresponding quantities from reference corrected total (BS approach) and corrected total (PASSSA) acquisitions

AP acquisition

Total, reference corrected total (BS method) and PASSA-corrected total attenuation images produced from their corresponding energy-resolved counterparts are presented in Figure 6.17.

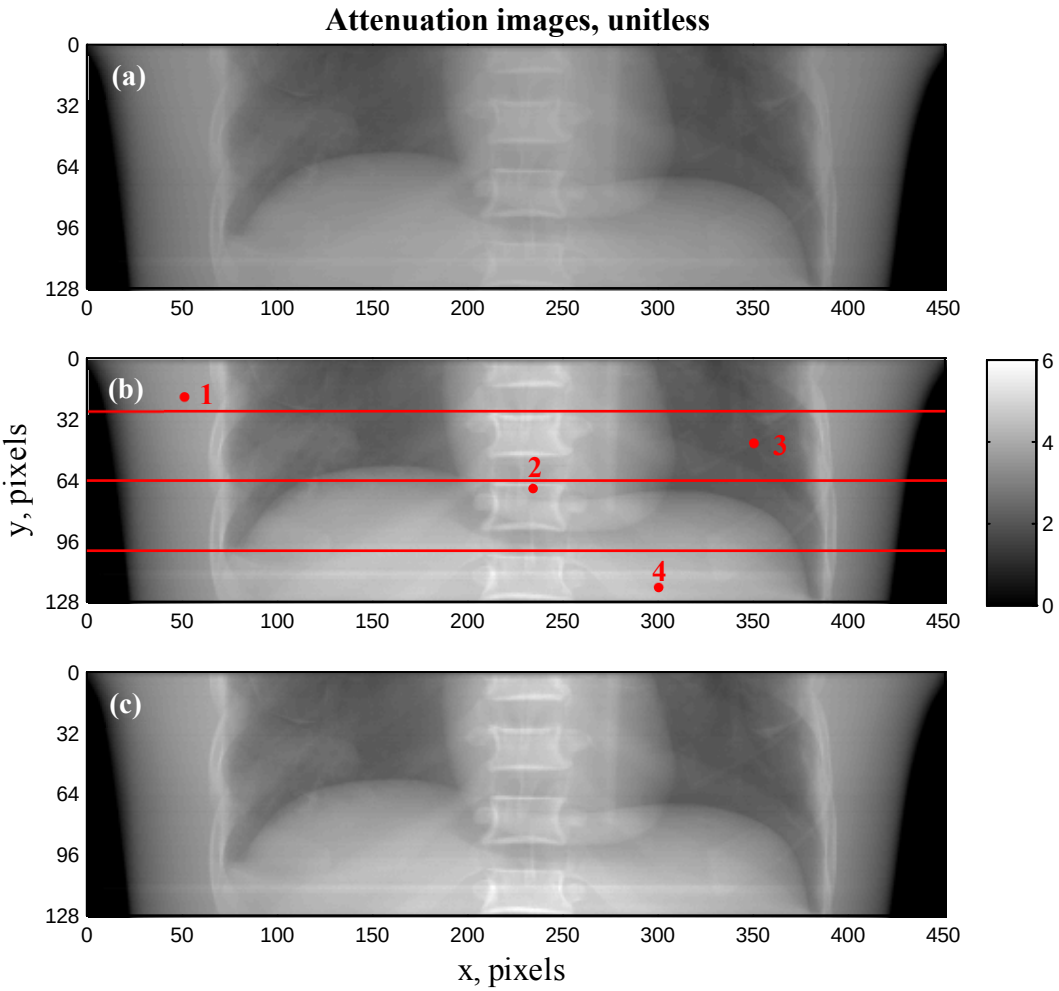

Figure 6.17. Total (a), reference corrected total (b) and corrected total (c) attenuation images obtained from their energy-resolved counterparts taken during the AP acquisition. The energy range considered was 25–110 keV. Pixel size was 0.8 mm. Locations for further profile (Figure 6.18) and spectrum (Figure 6.19) visualizations are also indicated on the reference corrected total image (b). These locations were chosen to examine areas with different levels and nature of object attenuation as well as a variable SPR. It also worth noting that the central profile (y=64) and pixels #2 and #4 are located in the area where reference scattered radiation was measured directly by the BS array.

Additionally, for each attenuation image, horizontal profiles in various locations are traced (Figure 6.18).

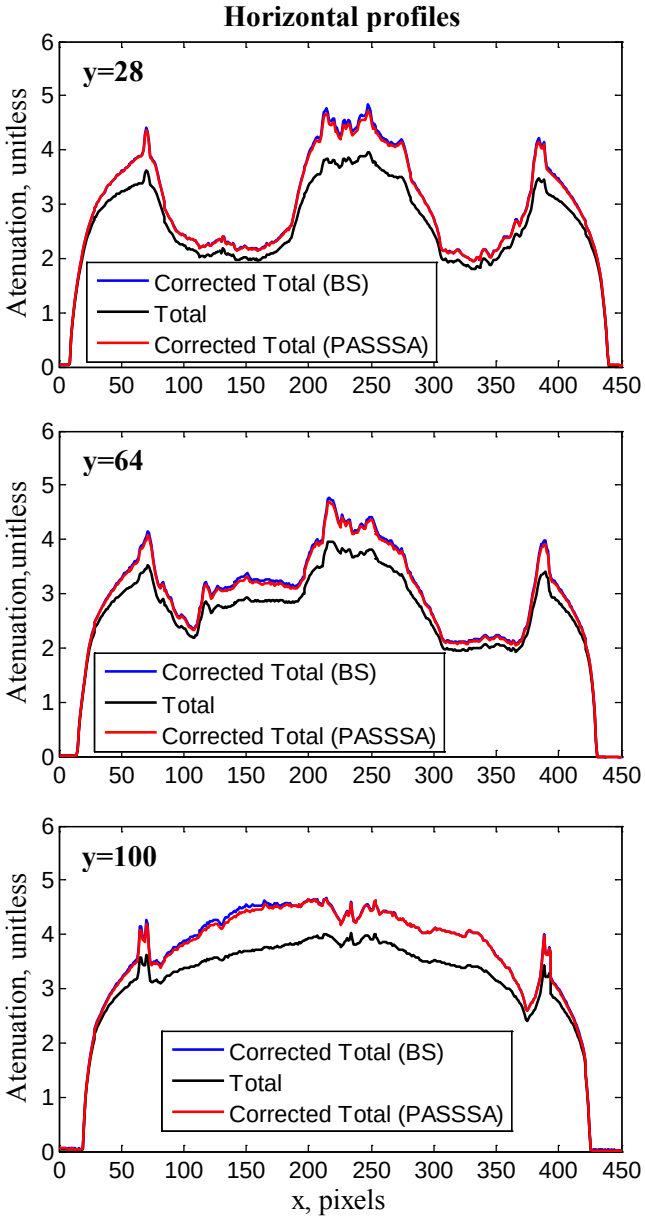

Figure 6.18. Horizontal profiles (AP acquisition) from images presented in Figure 6.17. Pixel size was 0.8 mm. One profile (y=64) was taken from the area where reference scatter was directly measured via the BS strips. Note that the total profiles are quite similar to the reference corrected total (BS) and corrected total (PASSSA) profiles at the sides and in lung regions as the SPR in these zones is lower than in parts where bone, vertebral column and diaphragm are present. The SPR in these parts is higher due to the low primary signal in this region (higher level of attenuation).

Total, BS-corrected total and PASSA-corrected total spectra from several control pixels (indicated in Figure 6.17) are presented in Figure 6.19.

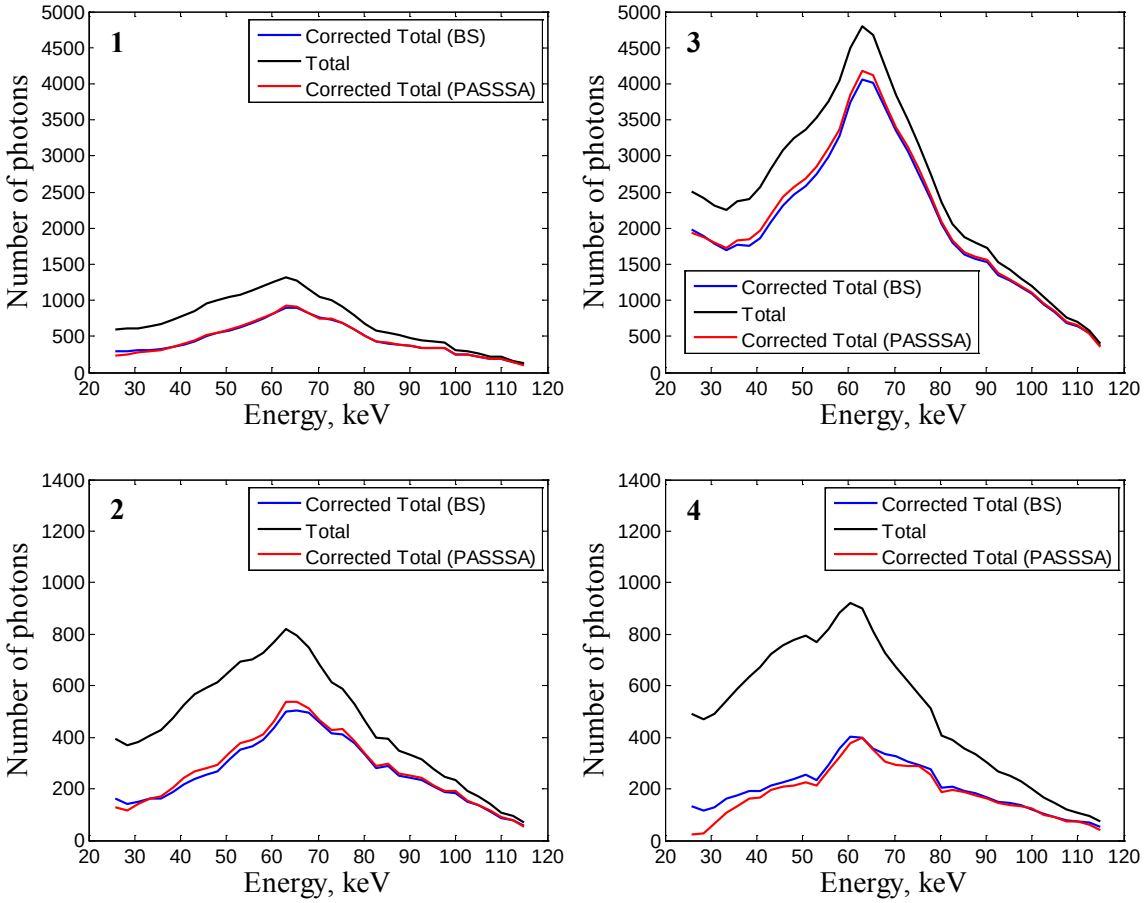

Figure 6.19. Total, reference corrected total and corrected total spectra (AP acquisition) taken from pixels indicated in Figure 6.17. Energy bin width was 2.5 keV. Spectra #2 and #4 are taken from image regions where the reference scatter data was measured directly via the BS array. The other two spectra (#1 and #3) are taken from zones where this data was spatially estimated. Corrected total spectrum shapes vary slightly across different sample locations with the exception of #3. This is due to the much lower attenuation exhibited in this part of the image (lung) compared to other regions. Additionally, note that the SPR is quite high for #4 due to the high level of attenuation present in this region (large amount of soft tissue).

Finally, a quantitative analysis of the energy-resolved images corresponding to the AP radiographic projection yielded a $NRMSE_T$ and a $NRMSE_{PASSSA}$ of 45.2% and 4.5%, respectively.

Oblique acquisition

As for the AP acquisition, total, reference corrected total (BS method) and PASSA-corrected total attenuation images produced from their corresponding energy-resolved counterparts are presented in Figure 6.20.

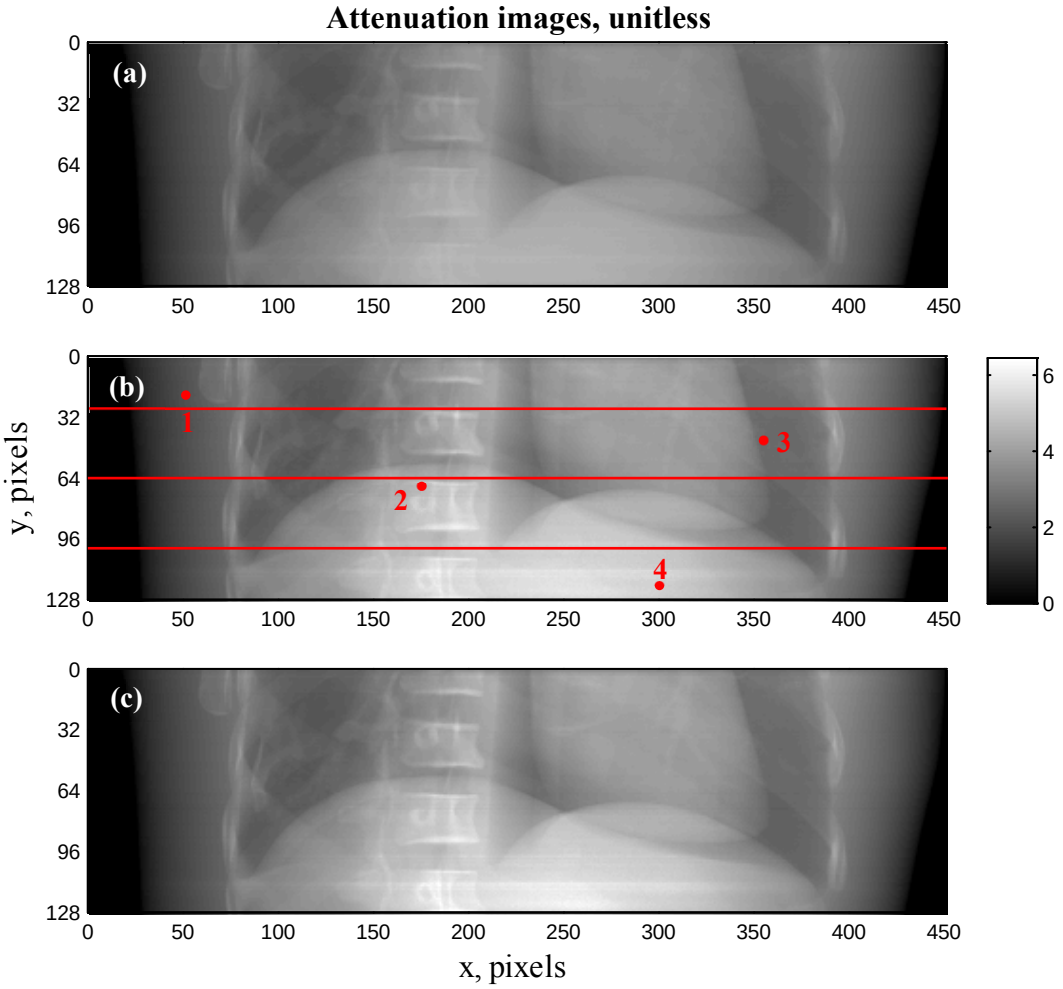

Figure 6.20. Total (a), reference corrected total (b) and corrected total (c) attenuation images obtained from their energy-resolved counterparts taken during the oblique acquisition. The energy range considered was 25–110 keV. Pixel size was 0.8 mm. Locations for profile (Figure 6.21) and spectrum (Figure 6.22) visualizations are also indicated on the reference corrected total image (b). These locations were chosen to examine areas with different levels and nature of object attenuation as well as a variable SPR. It also worth noting that the central profile (y=64) and pixels #2 and #4 are located in the area where reference scattered radiation was measured directly by the BS array.

Additionally, for each attenuation image, horizontal profiles in various locations are traced (Figure 6.21).

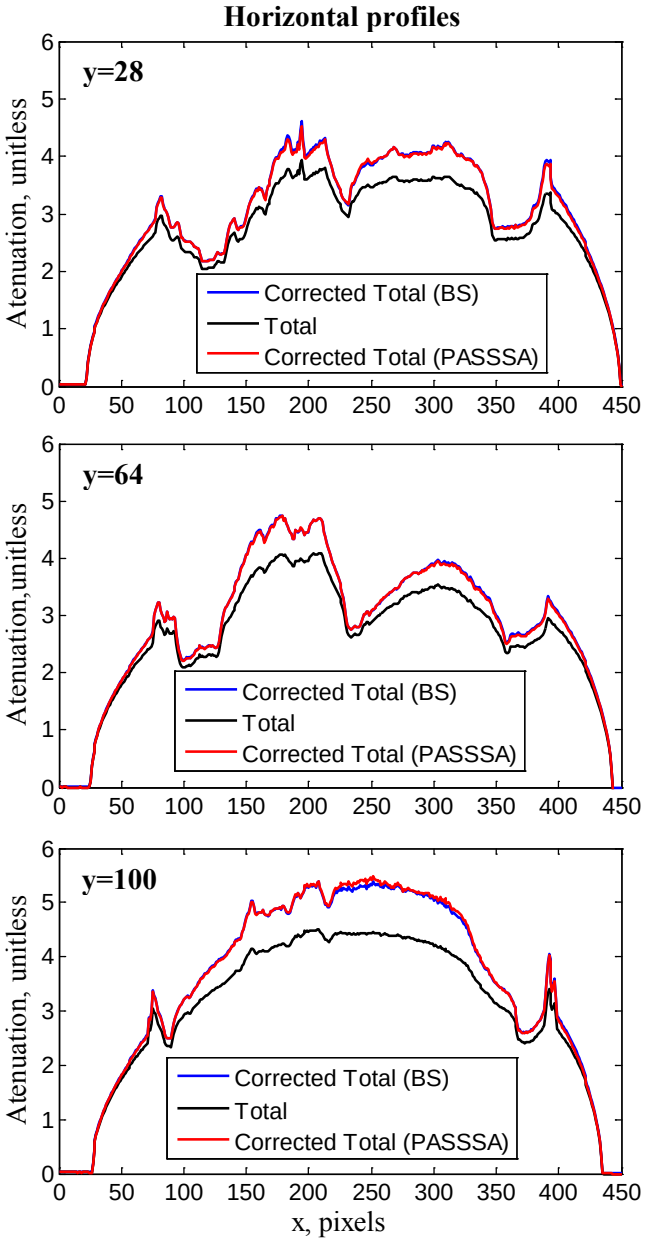

Figure 6.21. Horizontal profiles (oblique acquisition) from images presented in Figure 6.20. Pixel size was 0.8 mm. One profile (y=64) was taken from the area where reference scatter was directly measured via the BS strips. Note that the total profiles are quite similar to the reference corrected total (BS) and corrected total (PASSSA) profiles at the sides and in lung regions as the SPR in these zones is lower than in parts where vertebral column and diaphragm are present. The SPR in these parts is higher due to the low primary signal in this region (higher level of attenuation).

Total, BS-corrected total and PASSA-corrected total spectra from several control pixels (indicated in Figure 6.20) are presented in Figure 6.22.

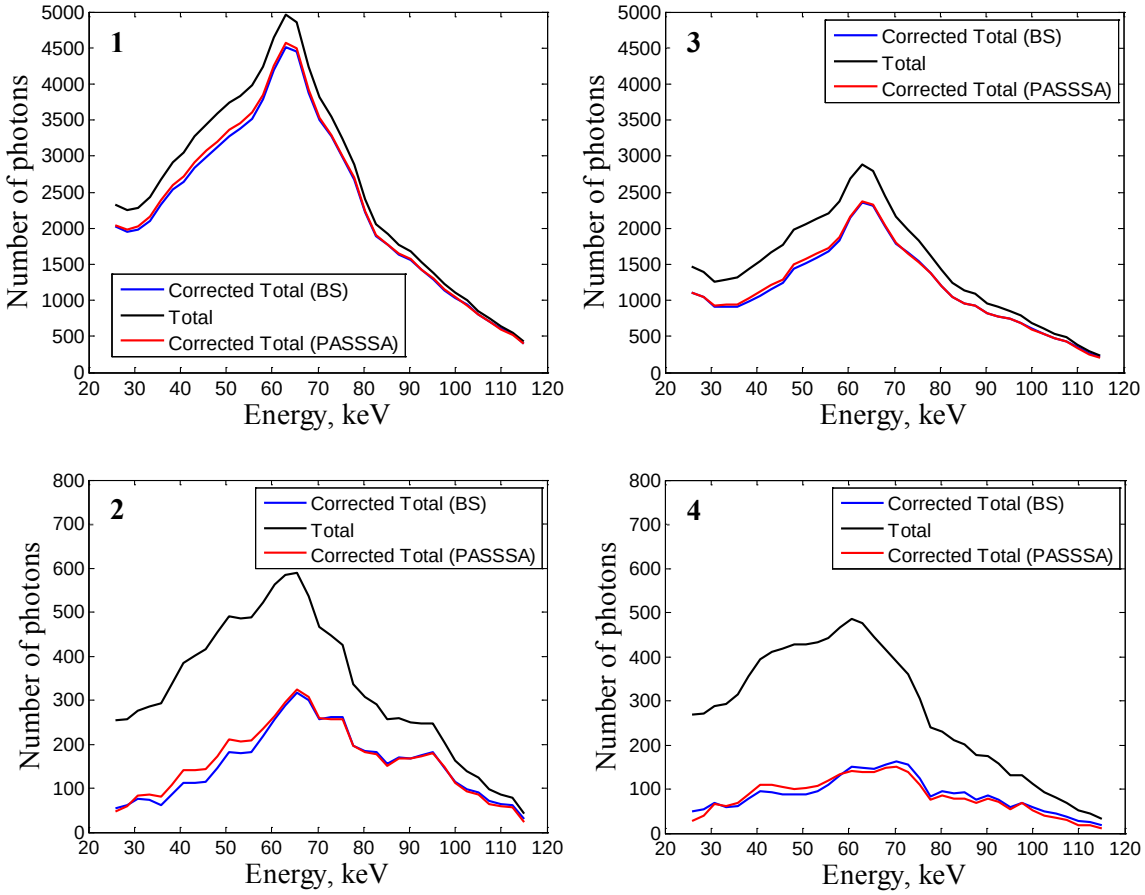

Figure 6.22. Total, reference corrected total and corrected total spectra (oblique acquisition) taken from pixels indicated in Figure 6.20. Energy bin width was 2.5 keV. Spectra #2 and #4 are taken from image regions where the reference scatter data was measured directly via the BS array. The other two spectra (#1 and #3) are taken from zones where this data was spatially estimated. Corrected total spectrum shapes are similar between points #1 and #3 as well as between #2 and #4. This is due to the similarities in levels of attenuation in these regions. Additionally, note that the SPR is quite high for #2 and #4 due to the high level of attenuation present in these regions (large amount of soft tissue and bone presence).

Finally, a quantitative analysis of the energy-resolved images corresponding to the oblique radiographic projection provided a $NRMSE_T$ and a $NRMSE_{PASSSA}$ of 41.5% and 5.3%, respectively.

Lateral acquisition

As for the AP and oblique acquisitions, total, reference corrected total (BS method) and PASSA-corrected total attenuation images produced from their corresponding energy-resolved counterparts are presented in Figure 6.23.

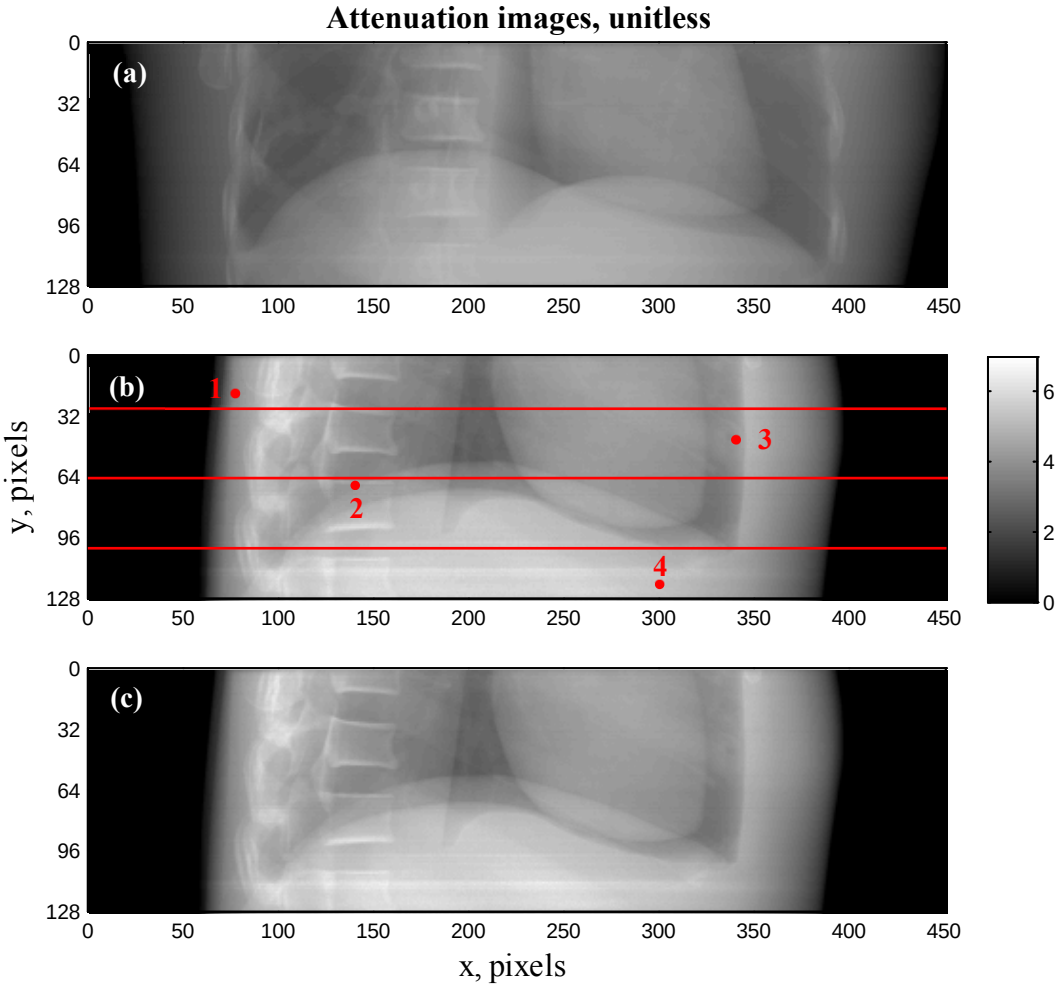

Figure 6.23. Total (a), reference corrected total (b) and corrected total (c) attenuation images obtained from their energy-resolved counterparts taken during the lateral acquisition. The energy range considered was 25–110 keV. Pixel size was 0.8 mm. Locations for profile (Figure 6.24) and spectrum (Figure 6.25) visualizations are also indicated on the reference corrected total image (b). These locations were chosen to examine areas with different levels and nature of object attenuation as well as a variable SPR. It also worth noting that the central profile (y=64) and pixels #2 and #4 are located in the area where reference scattered radiation was measured directly by the BS array.

Additionally, for each attenuation image, horizontal profiles in various locations are traced (Figure 6.24).

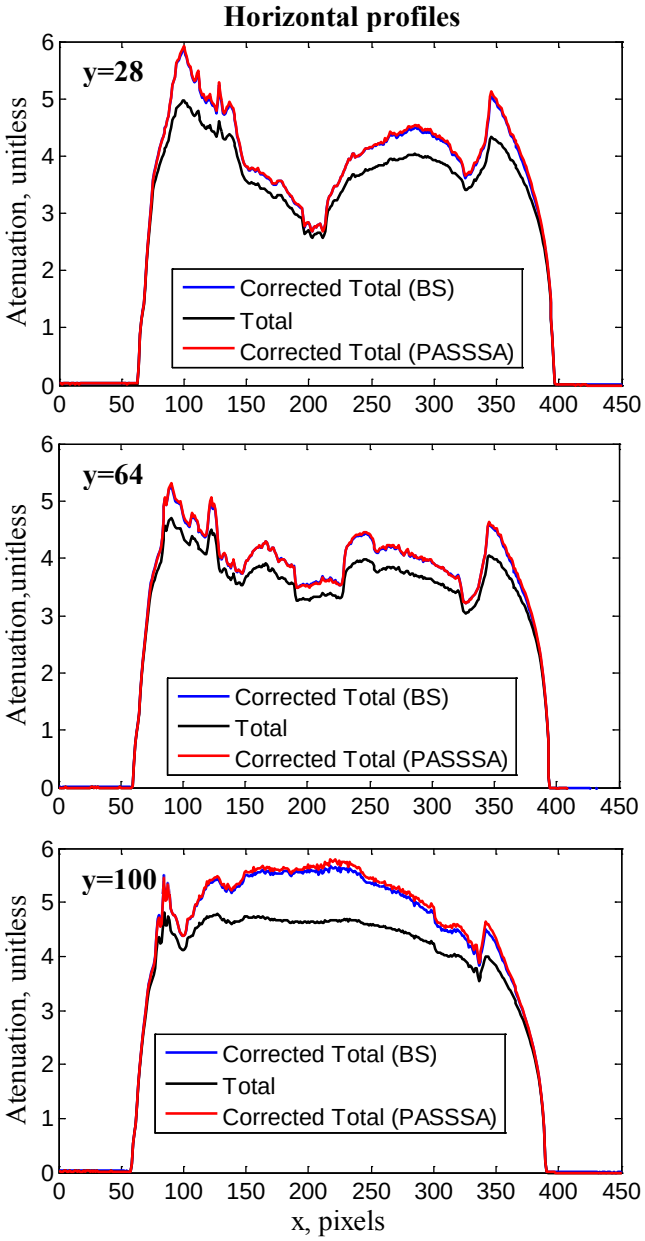

Figure 6.24. Horizontal profiles (lateral acquisition) from images presented in Figure 6.23. Pixel size was 0.8 mm. One profile (y=64) was taken from the area where reference scatter was directly measured via the BS strips. Note that the total profiles are quite similar to the reference corrected total (BS) and corrected total (PASSSA) profiles at the sides as the SPR in these zones is lower than in parts where vertebral column and diaphragm are present. The SPR in these parts is higher due to the low primary signal in this region (higher level of attenuation).

Total, BS-corrected total and PASSA-corrected total spectra from several control pixels (indicated in Figure 6.23) are presented in Figure 6.25.

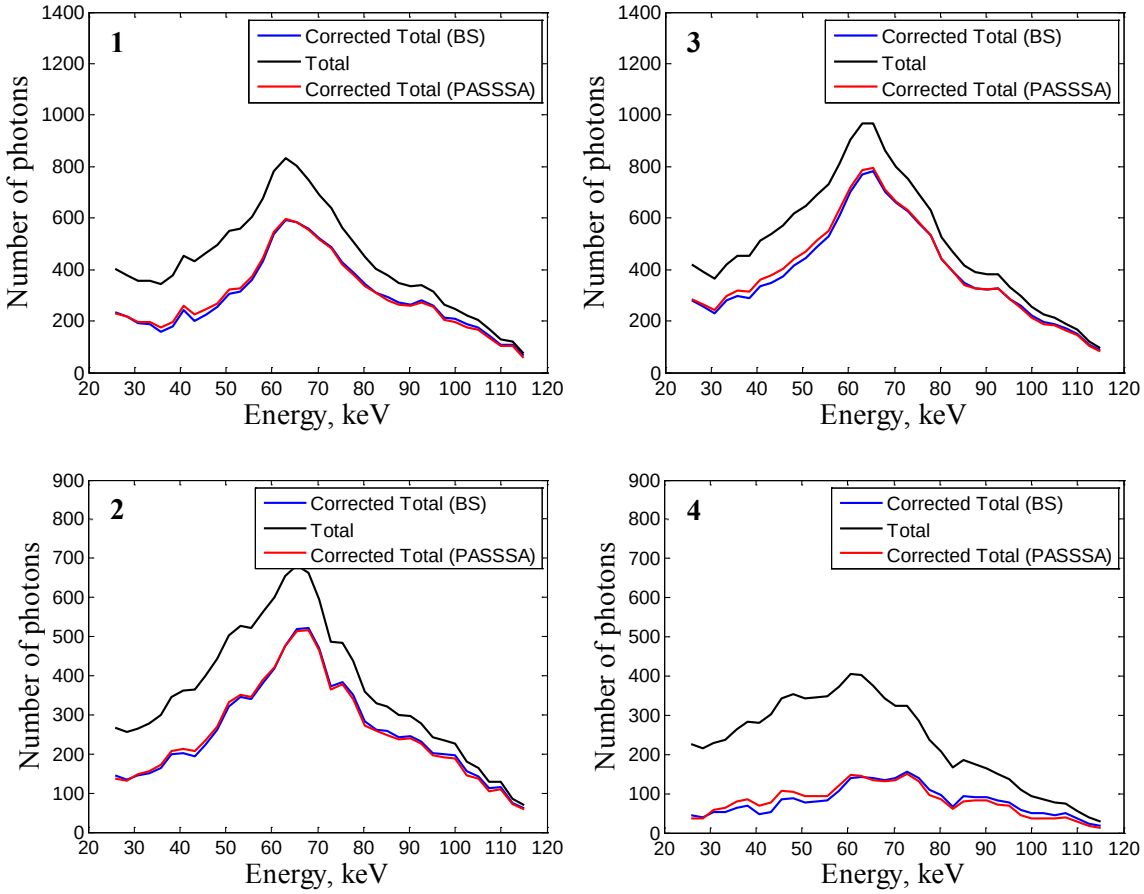

Figure 6.25. Total, reference corrected total and corrected total spectra (lateral acquisition) taken from pixels indicated in Figure 6.23. Energy bin width was 2.5 keV. Spectra #2 and #4 are taken from image regions where the reference scatter data was measured directly via the BS array. The other two spectra (#1 and #3) are taken from zones where this data was spatially estimated. Corrected total spectrum shapes vary slightly across different sample locations with the exception of #4. This is due to the much higher attenuation exhibited in this part of the image (diaphragm) compared to other regions. Additionally, note that the SPR is quite high for #4 due to the high level of attenuation present in this region (large amount of soft tissue).

Finally, a quantitative analysis of the energy-resolved images corresponding to the lateral radiographic projection resulted in a $NRMSE_T$ and a $NRMSE_{PASSSA}$ of 44.9% and 5.2%, respectively.

6.2.4. Transition matrix performance evaluation

Chapter 6.2.3 examined the performance of the full PASSSA algorithm for various radiographic projections. In the current chapter the aim is to analyze the key element of the method – the transition matrix. In order to do this, $NRMSE_{DB}$ as a function of number of energy channels between the set of true primary spectra, corresponding to the ones used in the calibration database, and the set estimated with the aid of **M** and the respective differ-

ence signal **ΔN** via (5.8) was computed via (6.6). It is important to note that $N_{ref}(k,E)$ in (6.6) was not completely noiseless as one was dealing with experimental data.

The system settings described in Chapter 6.2.1 were used for calibration and test dataset generation. **M** performance was evaluated for each thickness group considered in the calibration stage. The test dataset was identical to the calibration dataset. In addition, for each number of channels the corresponding widths were equal. It is also worth noting that the energy bin number was reduced by regrouping the initial measurement data corresponding to 37 bins into the required number of bins.

The $NRMSE_{DB}$ as a function of number of channels for each attenuator thickness group is visualized in Figure 6.26.

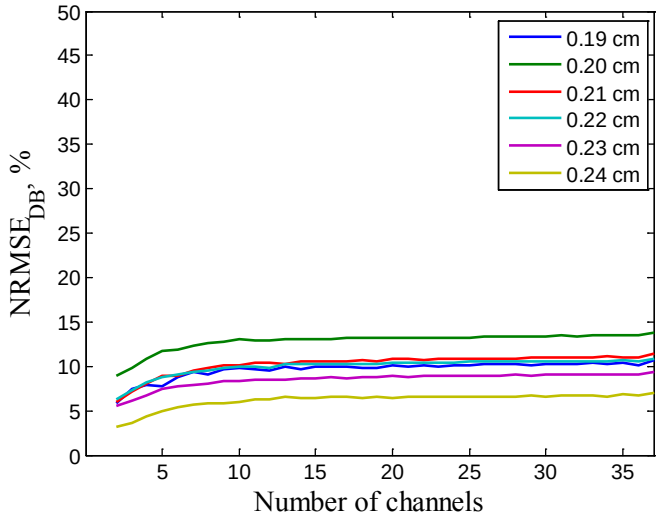

Figure 6.26. $NRMSE_{DB}$ as function of the number of channels for different attenuator thickness groups (0.19 cm – 0.24 cm).

6.2.5. Discussion

From a visual analysis of the different attenuation images (Figure 6.17, Figure 6.20 and Figure 6.23), the effect of scattered radiation becomes apparent. For all acquisitions (AP, oblique and lateral), the comparison of total images with the reference primary (BS correction) and the estimated primary (PASSSA correction) images, indicates insufficient local contrast and decrease of vertebra and heart contour detectability. The scatter induced bias can be noticed through the analysis of the respective central horizontal profiles presented in Figure 6.18, Figure 6.21 and Figure 6.24. The sub-estimation of attenuation due to the presence of scattered radiation is clearly apparent when comparing total and primary profiles. It is also strongest for the profiles traced in the lower part of the image (y=100) as local SPR is higher in this part of the image due to increase object attenuation.

BS-corrected (Figure 6.17b, Figure 6.20b and Figure 6.23b) and PASSSA-corrected (Figure 6.17c, Figure 6.20c and Figure 6.23c) attenuation images, generated from their energy-resolved counterparts, can be considered almost identical for AP, oblique and lateral acquisitions. Additionally, improved contrast and critical structure visibility (e.g. vertebra and heart) is obtained. Corresponding horizontal profiles from Figure 6.18, Figure 6.21 and Figure 6.24 further confirm this agreement. It also worth noting that the most discrepancy between BS-corrected and PASSSA-corrected profiles can be observed for pro-

file y=100 (especially for the lateral acquisition Figure 6.24). This can once again be linked to the increase of local SPR in this region.

The examination of the proposed scatter separation approach performance in the energy domain reveals a similar high degree of agreement between the primary spectra obtained via BS and via PASSSA. From Figure 6.19, Figure 6.22 and Figure 6.25, corresponding to spectra from the AP, oblique and lateral acquisitions, respectively, it can be seen that the estimated primary spectra closely resemble the reference primary spectra in all cases. A slightly higher deviation between BS- and PASSSA-estimated primary spectra can be visible for spectrum #4 in both AP (Figure 6.19) and lateral acquisitions (Figure 6.25). Note that spectrum #4 represents the case with the highest SPR among the examined spectra. In the oblique acquisition (Figure 6.22), BS-corrected and PASSSA-corrected spectra from point #2 exhibit the highest deviations.

The accuracy of primary recovery through the application of PASSSA is further validated by $NRMSE_{PASSSA}$. A reduction of scatter induced error by approximately a factor of 8–10 can be observed when comparing $NRMSE_T$ and $NRMSE_{PASSSA}$. The best and worst performance is achieved for the AP (factor about 10) and oblique (factor about 8) acquisitions, respectively. Note also that (based on NRMSE) the scatter induced error was reduced to about 5% for all projections, which is comparable with what was previously observed in simulations (Chapter 6.1).

Finally, the analysis of Figure 6.26 reveals $NRMSE_{DB}$ levels similar to the ones observed in simulations (Figure 6.9 and Figure 6.10, Chapter 6.1.4). However, the decrease in primary estimation error with decreasing energy channel number is slower. Thus, the potential improvement in primary estimation with reducing energy bin number is also lower in the considered acquisition settings. Additionally, the optimum in terms of $NRMSE_{DB}$ is located at 2 energy channels. The achieved improvement in primary estimation with the reduction of energy bin number from 37 to 2 is about 1.7 on average for the varying attenuator thickness groups. Note also that although the trend in $NRMSE_{DB}$ is similar for various attenuator thickness groups while the magnitude tends to vary. This is due to varying number of pixels corresponding to each individual attenuator thickness leading to a varying level of averaging.

PASSSA displays an impressive performance in terms of primary estimation for all radiographic projections considered. Results are consistent with what was previously observed in simulation (Chapter 6.1). The variations in BS- and PASSSA-corrected total images can be attributed to several factors: PASSSA model errors, transition matrix estimation errors, BS estimation errors, noise in the images.

The model errors for the proposed method include transition matrix model errors, residual scatter in the difference signal assumption and spatial interpolation. Each of these factors was previously discussed in detail in Chapter 6.1.5.

Although acquired with several realizations and with pixel grouping, the transition matrix can still exhibit errors as the calibration database is not completely noise free. Moreover, despite the added collimation, residual scatter can still be present from both the environment and the detector. Additionally, the fact of estimating transition matrices for a mask segment with further association with the other mask influenced pixels of the image may also introduce inaccuracies. Moreover, the fact of acquiring a 2D image through a translation of a 1D detector can also contribute to transition matrix estimation errors. Finally, as revealed by the transition matrix performance analysis, reducing the number of de-

tector energy bins can potentially improve **M** model performance under the conditions considered in the present study.

It is worth noting that the optimum number of channels as well as the behavior of the corresponding error curves was different from those observed in simulated studies (Chapter 6.1.4). There are several reasons that could explain such behavior. Firstly, the energy-response of the detector suffers from less charge sharing in the case of 1D detectors compared to the DRM of a 2D detector used in simulations. Secondly, signal thresholding at 25 keV may also induce differences compared to simulations. Finally, the noise properties for each number of bins obtained through the regrouping of initial data may not correspond to the actual noise properties corresponding to that number of bins. It is also worth noting that the dependency of the optimum number of channels on mAs was not evaluated.

As it is quite difficult to acquire an ideal primary (scatter free) image of a large object with the current prototype configuration, a reference primary is obtained through BS-estimation. Despite this technique being considered as the gold standard of scatter correction schemes, the obtained primary is still an estimate and thus incorporates a certain degree of error due to the estimation procedure. The BS-estimation procedure includes a number of error sources, namely gain adjustment, sample sufficiency, and the spatial interpolation from the samples. This means that the differences observed between PASSSA and BS primary estimates may also be in part due to the estimation method of the reference primary images.

Finally, as both BS and PASSSA are subtraction type scatter correction techniques, a noise increase is expected. The removal of a part of the total signal while leaving the associated noise results in a decrease in SNR for the corresponding corrected images. This aspect can also contribute to the differences observed between the BS- and PASSSA-estimated primary images.

6.2.6. Conclusion

Experimental evaluation of PASSSA using a prototype x-ray system with a linear 1D energy-resolved detector and an anthropomorphic thorax phantom displayed impressive results for various characteristic radiographic projections. The attenuation images obtained from PASSSA-estimated primary energy-resolved images showed a high level of agreement with corresponding BS estimates in terms of local contrast and internal structure contour visibility. Further analysis of the attenuation image profiles revealed a substantial scatter induced bias reduction for both radiographic projections considered. Additionally, the primary spectra acquired with the aid of PASSSA were closely matching their BS counterparts. Quantitatively, the developed method proved to be in relative agreement with the BS data. The application of the proposed scatter correction technique lowered the initial average error of 45% between the uncorrected total and the reference primary spectral images to around 5%. Thus, the scatter induced error for the PASSSA corrected spectral images is considered to be reduced by approximately a factor of 9.

The analysis of the transition matrix performance as a function of the number of detector channels concluded that an improvement by a factor of about 1.7 could be achieved if the number of channels was reduced from 37 to 2 in the considered configuration. However, a more detailed study with a true 2D energy-resolved detector would need to be conducted along with variable mAs, in order to better characterize the transition matrix behaviour as a function of detector energy bins. In addition, the effect of non-uniform energy channels on transition matrix performance should also be examined.

6.3. Performance analysis in basis material decomposition

In Chapters 6.1 and 6.2 PASSSA was examined through simulations (radiographic and CT acquisitions) and experiments (multi-view radiographic acquisitions), respectively. The resulting scatter correction efficacy proved to be quite promising both qualitatively and quantitatively.

The analysis of scatter effect on basis material decomposition of energy-resolved radiographic images (Chapter 3.2.3) concluded that the presence of scattered radiation in the acquisitions disturbs the resulting material image visual quality and quantitative accuracy. In the current chapter, material decomposition is applied on PASSSA-corrected simulated radiographic images in order to determine the performance improvement with respect to their uncorrected counterparts. Simulated images were provided by the developed Sindbad-SFFD simulation tool (Chapter 4.3).

In Chapter 6.3.1 the geometry, phantom, x-ray system settings and basis material decomposition protocol used in in the simulations are described. Additionally, Chapter 6.3.2 describes several adaptations made to PASSSA in order to better optimize the method for basis material decomposition. Chapter 6.3.3 provides decomposition results followed by the corresponding discussion in Chapter 6.3.4. Finally, Chapter 6.3.5 summarizes the most important findings.

6.3.1. System description

The x-ray acquisition settings used were similar to the ones previously employed in Chapter 3.2.3. A tungsten x-ray tube (17° anode angle and 2.5 mm aluminum filtration) was set to 110 kV and 1 mAs. Additionally, a 512×512 pixel energy-resolved (10 channels, 10 keV width bins with a 10 keV threshold) CdTe detector with a pitch of 1 mm and a thickness of 5 mm was used. The reduced number of channels was motivated by the transition matrix performance analysis (Chapter 6.1.4). The response of the detector was modelled with aid of a DRM corresponding to a realistic spectrometric detector (non-diagonal, 500 μm pitch, charge sharing corrected). Pile-up effects were not considered. Photonic noise (Poisson model) was also added. A supplemental (modified) acquisition with the attenuator mask was also considered for scatter correction via PASSSA. The mask consisted of a 17×17 array of 1×1 mm aluminum square elements (2 mm thickness). The spacing between the attenuator centers was 3 mm.

In order for the developed scatter correction method to function, the transition matrix **M** also needed to be estimated offline prior to the actual acquisition. The calibration protocol applied for the corresponding matrix estimation was identical to the one described in Chapter 6.1.1

The radiographic x-ray simulations were performed on the simplified numerical thorax phantom used throughout the thesis. Detailed specifications of this phantom can be found in Chapter 3.1.2 (Figure 3.2). The inspected object was placed in the geometry presented in Figure 6.27.

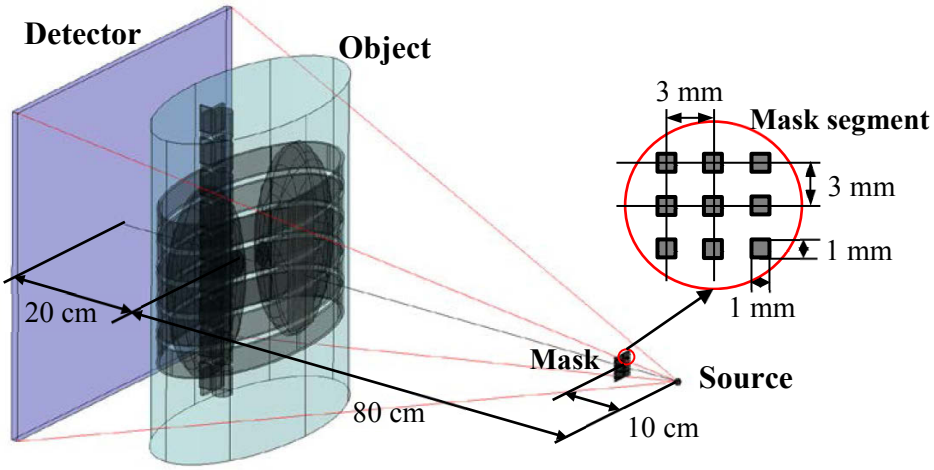

Figure 6.27. Modified x-ray acquisition depicting the object and geometry used for material decomposition. SDD, SAD and the corresponding air gap were 100 cm, 80 cm and 10 cm, respectively. An inset of the mask pattern is also shown. Note that the unmodified acquisition, used for obtaining primary and total images, was completely identical to the presented modified one with the exception of attenuator mask absence.

As in Chapter 3.2.3, various SPRs were considered: 60%, 30%, 12% and 3%. Note that the true scatter level for the considered acquisition set up was the one corresponding to the 60% SPR case. The other cases simulate partial loss of scatter level due to some form of preliminary correction or collimation. The 30%, 12% and 3% SPR cases correspond to 50%, 20% and 10% fractions of the initial scatter level. The energy-resolved primary (scatter free), total (with scatter) and corrected total (PASSSA) images were regrouped into 2 energy bins: 11–60 keV (LE) and 61–110 keV (HE). Then, attenuation as a function of energy channel was computed per image pixel via (2.20) and (3.5) for the primary and total images, respectively.

Material decomposition was performed on a water-bone material basis. The 3rd order polynomial presented in (3.7) was applied on each pixel of the energy-resolved primary, total and corrected total attenuation images. All polynomial terms were considered in the decomposition process. The polynomial coefficients for (3.7) were estimated via offline calibration on known water and bone thickness samples (scatter free setting). The considered thicknesses were 0–22 cm (0.5 cm step) and 0–7 cm (0.5 cm step) for water and bone, respectively. With the aid of the sample thicknesses and corresponding attenuations and linear least squares estimation polynomial coefficients were determined for (3.7).

6.3.2. Modified version of PASSSA

For scatter correction, a decomposition-optimized version of PASSSA was also considered (PASSSA2). PASSSA2 is essentially a derivative of the initial version. The difference consisted in the spatial scatter estimation (aimed at improving overall scatter estimation performance). Instead of applying the estimation procedure described in Chapter 5.2.3, the sparse scatter energy-resolved image was first regrouped in LE and HE channels (as specified in Chapter 6.3.1). Thus, the energy dimension of scatter was reduced from 10 channels with PASSSA to 2 channels with PASSSA2. Next, the DCT-spline estimation of (5.20) was applied per energy channel in order to recover the corresponding full scatter image.

Note that with the considered change to the spatial estimation procedure the method no longer relies on the scatter spectrum shape preservation hypothesis, as the estimation procedure no longer employs the corresponding shape.

The full scatter image (LE and HE channels) was then subtracted from the corresponding regrouped (in LE and HE channels) total image in order to obtain a scatter corrected image. Finally, attenuation as a function of energy bin, necessary for material decomposition, was computed for each PASSSA2-corrected total image pixel with the aid of (2.20).

6.3.3. Results

In order to qualitatively analyze the efficacy of developed scatter correction approach in the context of the considere multi-energy application, water and bone thickness images obtained from the decomposition of primary and total attenuation images (SPR 60% case) are presented in Figure 6.28.

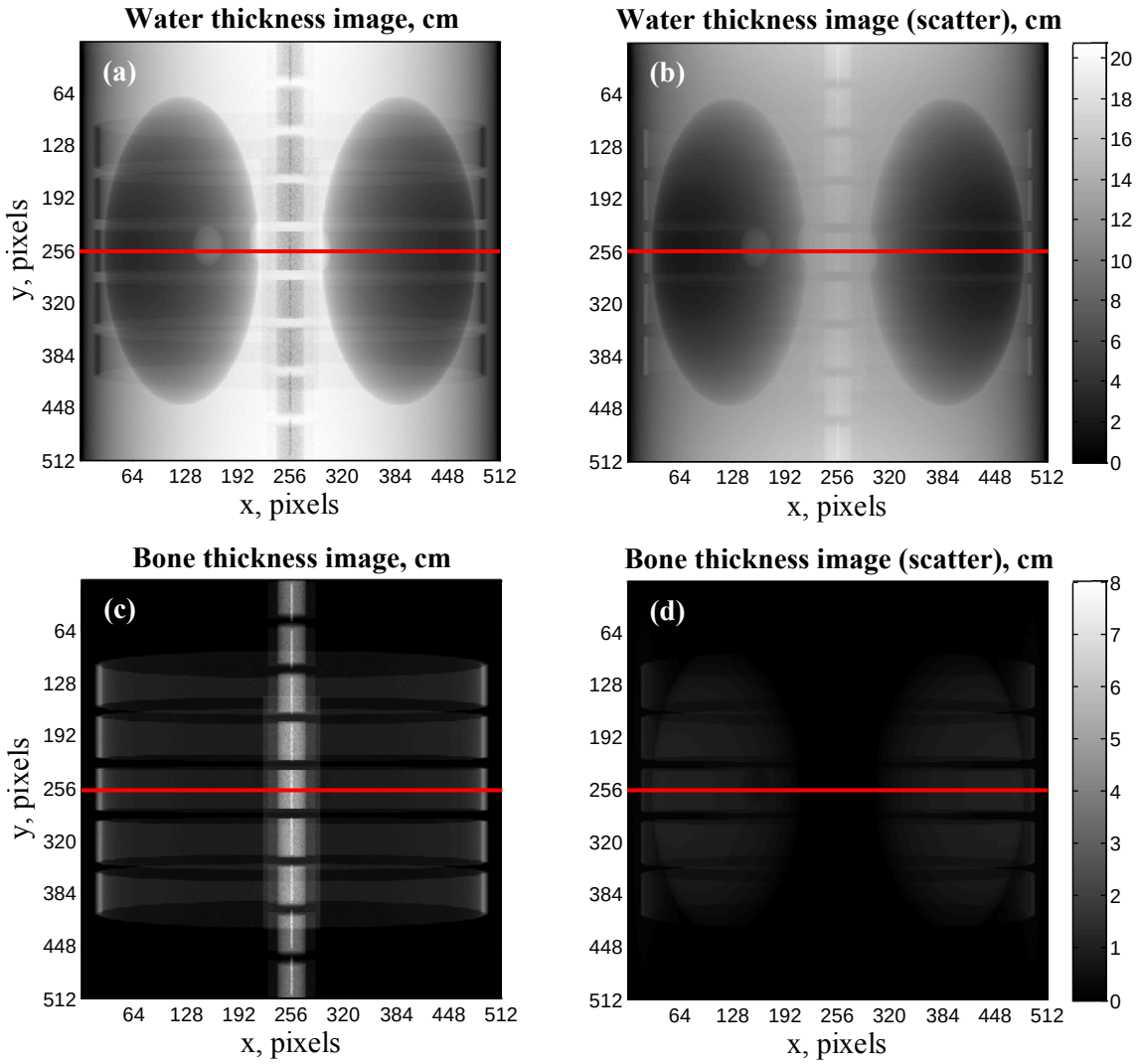

Figure 6.28. Water (a-b) and bone (c-d) thickness images. Images (a), (c) and (b), (d) were produced from primary (scatter free) and total (with scatter) attenuation images, respectively. The SPR was 60%. Additionally, locations for profile visualizations presented in Figure 6.30, Figure 6.31, Figure 6.32 and Figure 6.33 are marked in red.

Next, water and bone thickness images obtained from the decomposition of PASSSA- and PASSSA2-corrected total attenuation images (SPR 60% case) are also displayed (Figure 6.29).

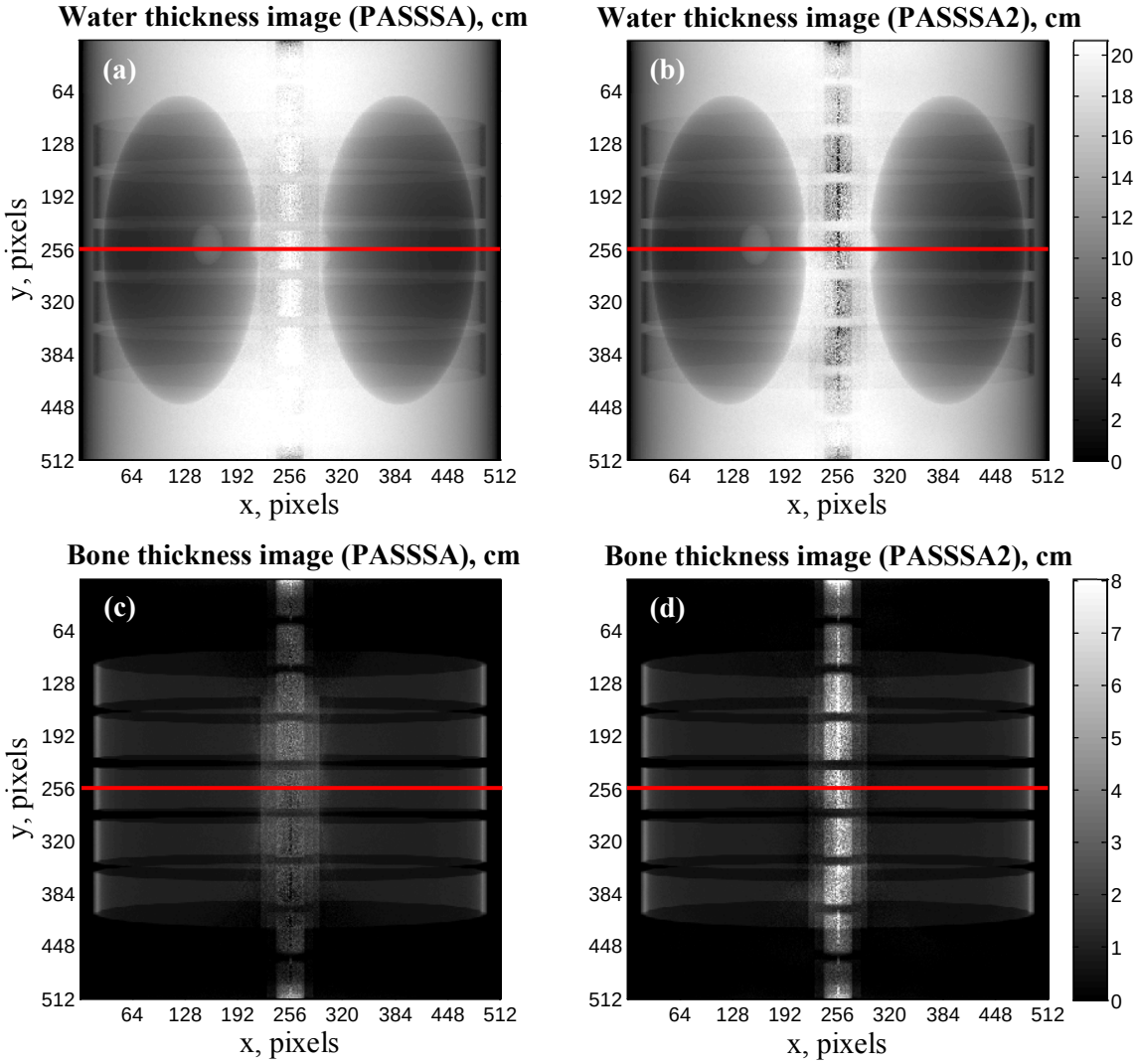

Figure 6.29. Water (a-b) and bone (c-d) thickness images. Images (a), (c) and (b), (d) were produced from PASSSA-corrected total and PASSSA2-corrected total attenuation images, respectively. The SPR was 60%. Additionally, locations for profile visualizations presented in Figure 6.30, Figure 6.31, Figure 6.32 and Figure 6.33 are marked in red.

Using the locations indicated in Figure 6.28 and Figure 6.29, horizontal primary, total, and corrected total (PASSSA and PASSSA2) image profiles were also traced for all the considered SPR levels. Figure 6.30, Figure 6.31, Figure 6.32 and Figure 6.33 display the profiles corresponding to the 60%, 30%, 12% and 3% SPR case, respectively.

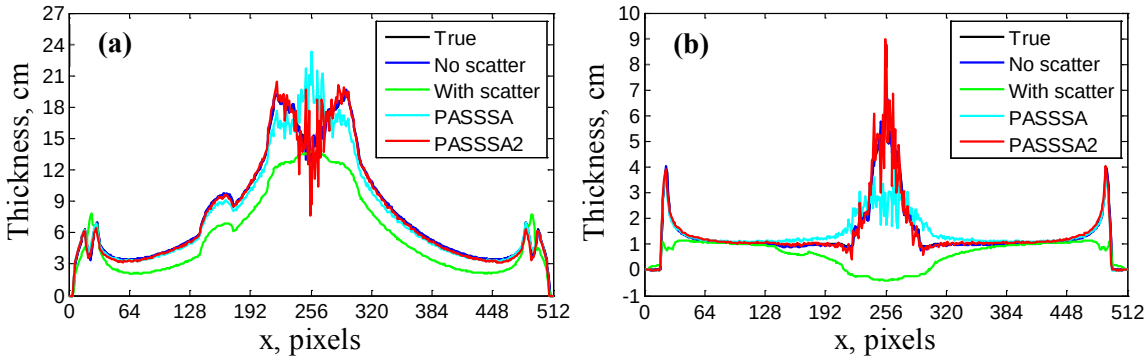

Figure 6.30. Water (a) and bone (b) thickness profiles from locations marked in Figure 6.28 and Figure 6.29. The considered SPR (with scatter curve) was 60%. The true water and bone thickness profiles are also visualized.

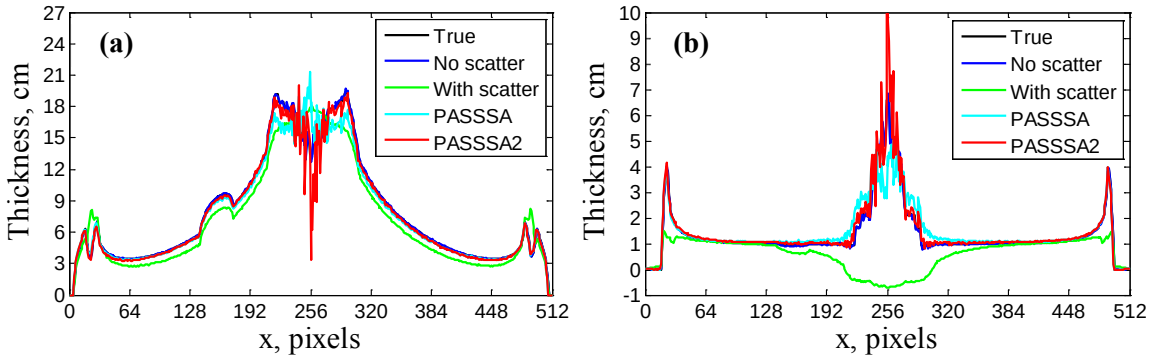

Figure 6.31. Water (a) and bone (b) thickness profiles from locations marked in Figure 6.28 and Figure 6.29. The considered SPR (with scatter curve) was 30%. The true water and bone thickness profiles are also visualized.

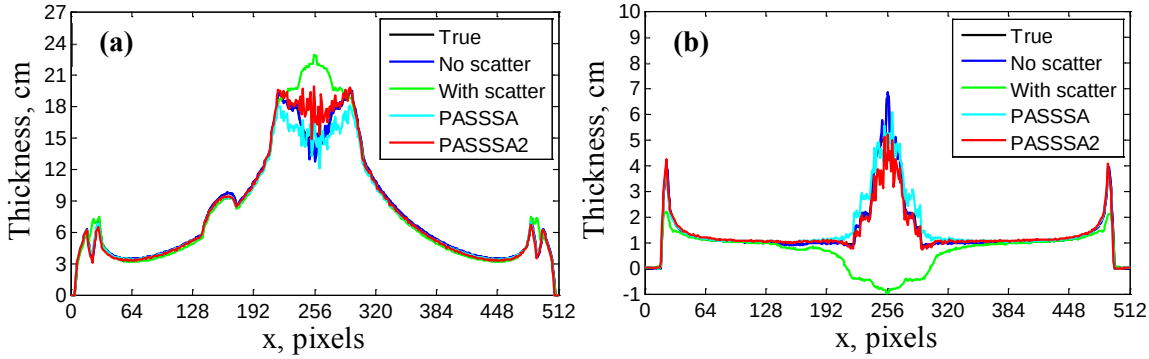

Figure 6.32. Water (a) and bone (b) thickness profiles from locations marked in Figure 6.28 and Figure 6.29. The considered SPR (with scatter curve) was 12%. The true water and bone thickness profiles are also visualized.

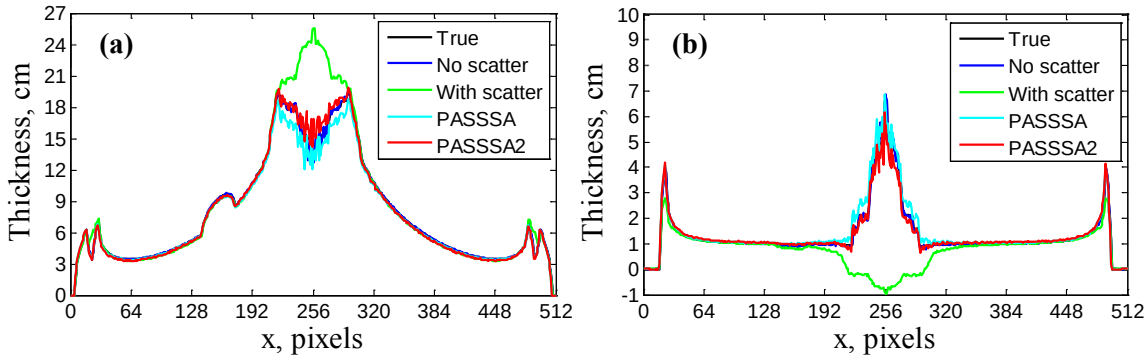

Figure 6.33. Water (a) and bone (b) thickness profiles from locations marked in Figure 6.28 and Figure 6.29. The considered SPR (With scatter curve) was 3%. The true water and bone thickness profiles are also visualized.

For the quantitative analysis of PASSSA performance, the average relative error between the true thickness images and the material thickness images obtained with varying SPRs and PASSSA corrections (PASSSA and PASSSA2) was computed via (3.6). Note that in this case attenuation in (3.6) is replaced by the thickness value contained in the respective material image.

In the absence of scatter the water and bone thickness estimation error was 0.7% and 2.1%, respectively. For the total images (with scatter, no correction), the water thickness estimation error was 5.6%–24.9% and 12.7% on average for the considered SPRs. The corresponding error on bone thickness was 28.3%–41.3% and 36.7% on average.

For the PASSSA-corrected images, a water thickness estimation error of 2.4%–4.8% (3.3% on average) was obtained for different SPRs. The respective bone thickness estimation error was 8.6%–14.9% (10.8% on average).

In the case of the images corrected by the adapted version of the developed method (PASSSA2), a water thickness estimation error of 2.3%–3.3% (2.7% on average) was obtained. Bone thickness error was 6.8%–9.6% and 7.8% on average.

Finally, the thickness estimation errors (total, primary, PASSSA- and PASSSA2-corrected case) for both water and bone as a function of SPR are presented in Figure 6.34.

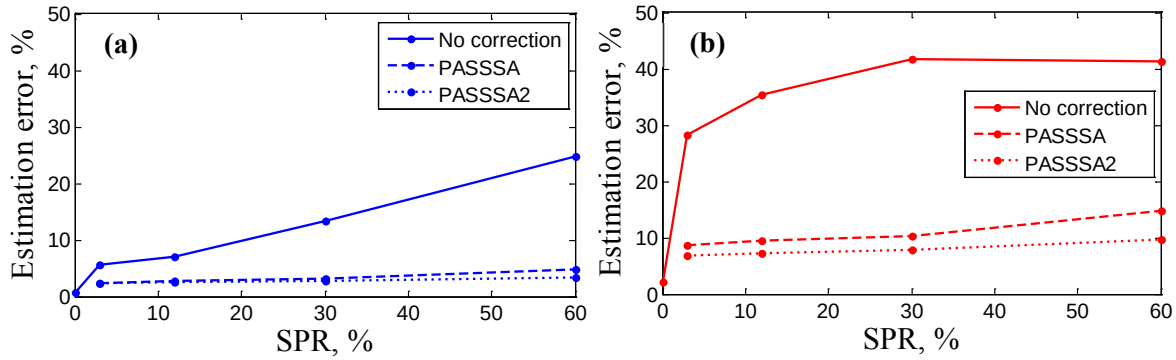

Figure 6.34. Water (a) and bone (b) thickness estimation errors as functions of SPR. Errors for material images obtained by decomposing the total (solid line), PASSSA-corrected (dashed line) and PASSSA2-corrected images (dotted line). Note that the estimation error for the thickness images obtained from primary images is also displayed on the solid line (0% SPR point).

6.3.4. Discussion

Material images from Figure 6.28 clearly demonstrate the effect of scattered radiation, which is especially prominent in the bone thickness image (d). A global thickness sub-estimation as well as a reduction of vertebral column and rib contour visibility can be observed in the water thickness image obtained from the total (b) attenuation images. The respective structures are even less apparent when the bone thickness image obtained in the presence of scatter (d) is compared with its scatter free counterpart (c). Additionally, lung structural detail has also propagated into the image. As noted in Chapter 3.2.3, this phenomenon can be linked to the low-energy shift characteristic to the scatter spectra (Chapters 3.1.1–3.1.3) resulting in a variable amount of scatter present in LE and HE bins, which in turn leads to material misinterpretation by the considered decomposition process.

Once PASSSA is applied on the scatter corrupted images, water and bone thickness images start to show substantial improvement (Figure 6.29). The initial version of PASSSA reduces the overall thickness estimation bias, improves critical structure (e.g. vertebral column and ribs) contour discernibility in both water (a) and bone images (c). However, the image zone around the vertebral column is not completely recovered and exhibits increased noise and substantial thickness over- and sub-estimation for water (a) and bone thickness (c) images, respectively. Additionally, some residual structural information (tumor inserts and lungs) is visible in the bone image (c). The noise increase is explained by the subtractive nature of PASSSA correction (note that PASSSA2 exhibits the same subtractive nature), high local SPR in the considered region and the application of a polynomial on the resulting images. The thickness estimation bias can arise from the relatively high (with respect to the rest of the image) local primary estimation error in the region and from the scatter spectrum shape hypothesis used in the method. For the former, high local SPR in vertebral column regions implies that the signal due to the scatter component is much stronger than that of the primary. This means that even a low estimation error of the scatter component will result in a high estimation error of the primary component. Thus, regions with high local SPR will be more sensitive to errors in scatter estimation that those exhibiting a low SPR. This in turn implies that the use of scatter spectrum shape approximations also has a higher influence on the efficacy of the scatter correction in the corresponding region. This explains the need of optimizing the initial version of PASSSA.

Indeed, when the developed scatter separation approach is optimized in terms of spatial scatter estimation (PASSSA2), water (Figure 6.29b) and bone (Figure 6.29d) material images superior to those obtained from images produced with the initial version of PASSSA (Figure 6.29a and Figure 6.29c) are acquired. More precisely, the image region around the vertebral column bears a much closer resemblance to the scatter free case (Figure 6.28a and Figure 6.28c). Additionally, almost no residual structural information in either material image is present. Finally, the critical region (vertebral column) also displays improvement in terms of noise for both water (Figure 6.29b) and bone thickness images (Figure 6.29d).

Thickness profiles (Figure 6.30) from images in Figure 6.28 and Figure 6.29 also support the previously made observations. The water and bone thickness corresponding to the scatter corrupted case exhibit thickness sub-estimation of a varying degree. The most prominent bias can be seen in the central part of the profile (high local SPR). One may also note the residual structure contour propagation (#210–#300 pixel part of the profile) observed previously in the material images (Figure 6.28b and Figure 6.28d). The application of PASSSA yields a thickness profile that is equivalent to the one obtained via primary

image decomposition with the exception of the middle part (#210–#300 pixel). This area, as seen previously, exhibits bias and noise increase with respect to scatter free case. Once the optimized PASSSA2 is used, both water in thickness profiles become almost identical to the corresponding ones obtained from the decomposed primary image.

With decreasing SPR the thickness profiles indicate a lower level of overall scatter induced degradation (Figure 6.31, Figure 6.32 and Figure 6.33). The exception, is, as expected due to its high local SPR, the vertebral column related section of the images. Even the case of a 3% SPR scatter induced bias is still visible in this region for both water (Figure 6.33a) and bone thickness profiles (Figure 6.33b). The profiles produced from PASSSA-corrected decomposed images reveal an improvement in thickness estimation accuracy. The biased profile area begins to shrink with the SPR decreasing from 12% (Figure 6.31) to 3% (Figure 6.33). The noise exhibited previously in this part of the profile (Figure 6.30) is also reduced. This is expected as the scatter contribution to the total signal decreases with decreasing SPR and thus, its subtraction from the respective signal leads to a less substantial noise increase. Once optimized, PASSSA correction leads to material thickness profiles that remain close to the true and scatter free thickness profiles with SPR being reduced from 12% (Figure 6.31) to 3% (Figure 6.33). As with the initial version of PASSSA, noise characteristics in the critical region (vertebral column) are improved. One notes that with decreasing noise in the respective area, slight differences between the thickness profiles obtained from decomposing PASSSA2-corrected images are revealed. This can be linked to spatial scatter estimation errors. As stated previously, decreasing SPR implies a decreased scatter signal. Taking this into account and bearing in mind the high level of noise associated with the acquisition of initial spatial sparse scatter data, one can assume that the spatial estimation procedure loses accuracy due to noise becoming more prominent than the signal with decreasing SPR.

Finally, the quantitative analysis of material images obtained from scatter free (primary), scatter corrupted (total) and scatter corrected (PASSSA and PASSSA2) images also indicates a high degree of thickness estimation error reduction by applying scatter correction on the initial energy-resolved data (Figure 6.34). Note that the application of the unmodified version of PASSSA already achieves a material thickness estimation error reduction by a factor of about 3.6 on average for all considered SPRs. However, both water (Figure 6.34a) and bone (Figure 6.34b) thickness error curves imply that the efficacy of PASSSA is dependent on SPR: higher and lower performance is achieved for the lower and higher SPR cases, respectively. When the optimized PASSSA2 is applied, this dependence is much less prominent as the corresponding thickness estimation error varies slower with SPR for both water (Figure 6.34a) and bone (Figure 6.34b). Furthermore, the corresponding estimation error is about 4.7 times lower (on average) than in scatter corrupted case for all SPRs. Moreover, it is much closer to the error exhibited when no scatter is present in the data (0% SPR). Thus, PASSSA performance increase becomes even more apparent with the applied optimization.

6.3.5. Conclusion

From the obtained results, one can conclude that the application of PASSSA on energy-resolved scatter corrupted data produced images, which, when subjected to decomposition, lead to material images closely matching the ones obtained from scatter free data and true thickness data. Quantitative analysis further confirmed these observations. The included optimization resulted in an estimation improvement in terms of bias in regions with low

primary signal (vertebral column). Moreover, thickness estimation error analysis revealed an about 30% increase in accuracy with the optimized version of PASSSA. Thus, the spatial estimation adaptation for the material decomposition task proved to be quite effective. It worth noting, however, that the applied PASSSA adjustment may not be as effective for other types of decomposition methods (e.g. direct model inversion [4]).

The most important conclusion that can be made, based on the presented results, is the need of scatter correction method optimization for a given multi-energy application. This is valid beyond the approach presented in the present thesis. As low scatter estimation errors in areas with high SPR (low primary signal) result in high primary estimation errors, any technique based on scatter distribution estimation (Chapters 5.1.2 and 5.1.3), if applied to multi-energy data, will suffer from substantial local errors in material decomposition. As seen from the results in the present chapter, the areas prone to the respective problem are the ones of most diagnostic interest (vertebral column). Thus, the chosen multi-energy scatter correction method must be conditioned by the respective application (e.g. basis material decomposition) and vice versa.

Based on this conclusion, one can analyze the potential of applying PASSSA2 instead of PASSSA in the context of the conducted method validation through radiographic and tomographic simulations (Chapter 6.1). If the goal is obtaining integration mode images from energy-resolved data (which means regrouping all channels), then PASSSA2 will definitely yield an improvement of the images obtained with PASSSA due to its adapted scatter estimation procedure. However, in this case the energy information is reduced, which means that if one requires maximum energy information, the initial version of PASSSA is the method of choice as it does not compromise energy information.

7. FURTHER ANALYSIS AND IMPROVEMENTS OF THE METHOD

Chapter 5.2 introduced PASSSA, a multi-energy adapted scatter correction method. Validation through simulations (Chapter 6.1) and experiments (Chapter 6.2) confirmed that the developed technique is highly efficient in substantially reducing scatter induced bias, structural distortions and artifacts. Furthermore, the application of PASSSA on multi-energy scatter corrupted data improved material thickness estimation accuracy in the context of basis material decomposition in radiography (Chapter 6.3).

The analysis of various method aspects in different x-ray applications (radiography, CT, material decomposition in radiography) opens up new perspectives in PASSSA improvement. In the present chapter, developments in some key points in method functionality are presented and discussed. These range from concrete propositions to more abstract and general concepts.

Chapter 7.1 presents developments in sparse scatter sample estimation and subsequent spatial estimation followed by propositions on attenuator mask optimization (Chapter 7.2). Finally, some concepts on method functionality with only a single (attenuator modified) acquisition are outlined in Chapter 7.3.

7.1. Scatter estimation improvements

In Chapters 6.1.5 and 6.3.4 it was mentioned that, when using PASSSA, scatter distribution estimation errors may arise due to high level of noise in the sparse scatter data recovered in the attenuator shadow regions and scatter spectrum shape preservation hypothesis. Moreover, Chapter 6.1.5 mentioned that the DCT-spline estimation method was not adapted to sample noise anisotropy in terms of energy channel.

In order to propose solutions for the noise-related part, noise propagation from input signals up to the sparse scatter signals needs be analyzed. Chapter 7.1.1 presents noise propagation models based on the various stages comprising PASSSA (Chapter 5.2.1). These models are the applied to analyze the behavior of noise as a function of key input parameters (Chapter 7.1.2). The analysis is then used to propose potential improvements in the management of scatter samples (Chapter 7.1.3). Furthermore, Chapter 7.1.3 also discusses spatial estimation method modifications that can be employed to reduce dependence on the spectrum shape hypothesis.

7.1.1. Noise propagation models

The present chapter aims at deriving three different noise propagation models that can be employed for noise propagation analysis in the scatter estimation part of PASSSA.

First noise propagation model

The first one is based on the input modified and unmodified total signals. Firstly, since the operations leading to the sparse scatter signals are applied per attenuator shadow pixel, a useful simplification of the notation of (5.9) can be made:

$$\mathbf{N_S} = \mathbf{N_T} - \mathbf{M} \times \mathbf{\Delta N}. \tag{7.1}$$

In (7.1), the dependence on the attenuator shadow pixel **p'** has been omitted. Using the definition of **ΔN** from (5.5) and rearranging leads to the following expression

$$\mathbf{N_S} = \left(\mathbf{I} - \mathbf{M}\right) \times \mathbf{N_T} + \mathbf{M} \times \mathbf{N_T^m}, \tag{7.2}$$

where **I** is an identity matrix.

For $\mathbf{N_S}$, $\mathbf{N_T}$ and $\mathbf{N_T^m}$, one can define associated variance vectors $(\boldsymbol{\sigma}_\mathbf{S})^2$, $(\boldsymbol{\sigma}_\mathbf{T})^2$ and $(\boldsymbol{\sigma}_\mathbf{T}^\mathbf{m})^2$. Thus, for example, $(\sigma_T(E))^2$ is the variance (in number of photons) associated with $N_T(E)$. Additionally, an absent or limited inter-channel correlation is assumed.

As noted previously in Chapter 6.1.1, a Poisson model is considered representable for noise modelling in x-ray imaging. Based on this model and using the previously outlined correlation assumption, the signal measured in each energy channel E represents the mean of the corresponding distribution. The associated noise is described by the respective STD, which, based on the Poisson model mean-variance equality, is equal to the square root of the mean.

Using the laws of uncertainty propagation, the considered Poisson nature of the input total signals ($\mathbf{N_T}$ and $\mathbf{N_T^m}$) and the associated variances ($(\boldsymbol{\sigma}_\mathbf{T})^2$ and $(\boldsymbol{\sigma}_\mathbf{T}^\mathbf{m})^2$), one can compute $(\boldsymbol{\sigma}_\mathbf{S})^2$ with the aid of (7.2):

$$\left(\boldsymbol{\sigma}_\mathbf{S}\right)^2 = \left(\mathbf{I} - \mathbf{M}\right)^2 \times \left(\boldsymbol{\sigma}_\mathbf{T}\right)^2 + \mathbf{M}^2 \times \left(\boldsymbol{\sigma}_\mathbf{T}^\mathbf{m}\right)^2, \tag{7.3}$$

where $\mathbf{M}^2 = \mathbf{M} \circ \mathbf{M}$. The STD associated with $\mathbf{N_S}$ can then be easily computed by taking the square root of (7.3):

$$\boldsymbol{\sigma}_\mathbf{S} = \sqrt{\left(\mathbf{I} - \mathbf{M}\right)^2 \times \left(\boldsymbol{\sigma}_\mathbf{T}\right)^2 + \mathbf{M}^2 \times \left(\boldsymbol{\sigma}_\mathbf{T}^\mathbf{m}\right)^2}. \tag{7.4}$$

Thus, with the aid of (7.4) and total signal variance data, a STD corresponding to the estimated scatter signal can be computed. The transition matrix **M** is estimated prior to the acquisitions. However, $(\boldsymbol{\sigma}_\mathbf{T})^2$ and $(\boldsymbol{\sigma}_\mathbf{T}^\mathbf{m})^2$ are not directly available. These variances can be obtained from $\mathbf{N_T}$ and $\mathbf{N_T^m}$ using the Poisson model property: $(\boldsymbol{\sigma}_\mathbf{T})^2 = \mathbf{N_T}$ and $(\boldsymbol{\sigma}_\mathbf{T}^\mathbf{m})^2 = \mathbf{N_T^m}$. However, in reality the measured $\mathbf{N_T}$ and $\mathbf{N_T^m}$ both include noise and thus the corresponding variances acquired through this property become approximations.

Second noise propagation model

The second noise propagation model is based on (7.4) and the corresponding assumptions. The difference is that it aims to link $\boldsymbol{\sigma}_\mathbf{S}$ to SPR, attenuator thickness (l_a) and $\boldsymbol{\sigma}_\mathbf{P}$, which is the STD associated with the primary signal $\mathbf{N_P}$ comprising $\mathbf{N_T}$. For this purpose, the variances present in (7.4) are further developed.

Assuming the independence of primary and scatter components comprising the total signal, the same scatter component both for the modified and unmodified totals and bearing in mind that the total is actually the sum of primary and scatter (limited to no pile-up assumption), one can write expanded versions of $(\boldsymbol{\sigma}_\mathbf{T})^2$ and $(\boldsymbol{\sigma}_\mathbf{T}^\mathbf{m})^2$:

$$\begin{aligned} \left(\boldsymbol{\sigma}_\mathbf{T}\right)^2 &= \left(\boldsymbol{\sigma}_\mathbf{P}\right)^2 + \left(\boldsymbol{\sigma}_\mathbf{S}^*\right)^2 \\ \left(\boldsymbol{\sigma}_\mathbf{T}^\mathbf{m}\right)^2 &= \left(\boldsymbol{\sigma}_\mathbf{P}^\mathbf{m}\right)^2 + \left(\boldsymbol{\sigma}_\mathbf{S}^*\right)^2 \end{aligned}, \tag{7.5}$$

where $(\boldsymbol{\sigma}_{\mathbf{P}}^{\mathbf{m}})^2$ and $(\boldsymbol{\sigma}_{\mathbf{S}}^{*})^2$ is the variance associated with the attenuator modified primary component and the scatter component present in the input total signal (non-estimated).

Next, $\boldsymbol{\sigma}_{\mathbf{S}}^{*}$ is expressed as a function of SPR and $\boldsymbol{\sigma}_{\mathbf{P}}$:

$$\left(\boldsymbol{\sigma}_{\mathbf{S}}^{*}\right)^2 = \mathbf{SPR} \times \left(\boldsymbol{\sigma}_{\mathbf{P}}\right)^2, \quad diag\left(\mathbf{SPR}\right) = \mathbf{N_S}\, o\left(\mathbf{N_P}\right)^{-1}, \tag{7.6}$$

where **SPR** is a diagonal matrix with the SPR as the diagonal. Additionally, the relationship between $(\boldsymbol{\sigma}_{\mathbf{P}}^{\mathbf{m}})^2$ and $(\boldsymbol{\sigma}_{\mathbf{P}})^2$ also needs to be established. In order to do this, one first expresses the unmodified primary signal as a function of the modified primary signal:

$$\mathbf{N_P^m} = \mathbf{B} \times \mathbf{N_P}, \quad \mathbf{B} = \mathbf{D} \times \mathbf{b} \times \mathbf{D}^{-1}. \tag{7.7}$$

Matrix **B** is called the *attenuation matrix*, as it describes the primary signal loss induced by the attenuator. Additionally, Matrix **b** in (7.7) is a diagonal matrix of the following form:

$$diag\left(\mathbf{b}\right) = \exp(-\boldsymbol{\mu}_{\mathbf{a}} l_a). \tag{7.8}$$

Note that **B** in (7.7) is similar to the transition matrix **M** as it also represents a basis-change for **b** as **M** did for $\mathbf{W^{-1}}$(c.f. (5.11)). Moreover, (7.8) is quite close to (5.7), which expresses **W** as a function of the corresponding attenuation coefficient function and attenuator thickness.

Based on (7.7) the relationship between $(\boldsymbol{\sigma}_{\mathbf{P}}^{\mathbf{m}})^2$ and $(\boldsymbol{\sigma}_{\mathbf{P}})^2$ can be established:

$$\left(\boldsymbol{\sigma}_{\mathbf{P}}^{\mathbf{m}}\right)^2 = \mathbf{B} \times \left(\boldsymbol{\sigma}_{\mathbf{P}}\right)^2. \tag{7.9}$$

The quantity **B** in (7.9) incorporates the dependence on attenuator thickness.

Inserting (7.9) and (7.6) in (7.5) leads to the following expanded expressions for the variances associated with the modified and unmodified total signals:

$$\begin{aligned} \left(\boldsymbol{\sigma}_{\mathbf{T}}\right)^2 &= \left(\boldsymbol{\sigma}_{\mathbf{P}}\right)^2 + \mathbf{SPR} \times \left(\boldsymbol{\sigma}_{\mathbf{P}}\right)^2 \\ \left(\boldsymbol{\sigma}_{\mathbf{T}}^{\mathbf{m}}\right)^2 &= \mathbf{B} \times \left(\boldsymbol{\sigma}_{\mathbf{P}}\right)^2 + \mathbf{SPR} \times \left(\boldsymbol{\sigma}_{\mathbf{P}}\right)^2 \end{aligned}. \tag{7.10}$$

Finally, (7.10) is used in (7.4) in order to obtain the second model for $\boldsymbol{\sigma}_{\mathbf{S}}$:

$$\boldsymbol{\sigma}_{\mathbf{S}} = \left(\sqrt{\left(\mathbf{I} - \mathbf{M}\right)^2 \times \left(\mathbf{I} + \mathbf{SPR}\right) + \mathbf{M}^2 \times \left(\mathbf{B} + \mathbf{SPR}\right)} \right) \times \boldsymbol{\sigma}_{\mathbf{P}}. \tag{7.11}$$

The observation of (7.11) reveals that the STD associated with the estimated scatter signal is directly proportional to the STD of the primary component present in the unmodified total signal. The dependence on SPR and attenuator thickness is, however, less apparent. Note also that there are several quantities in (7.11) that are not directly available: **SPR**, **B**, and $\boldsymbol{\sigma}_{\mathbf{P}}$. It may be possible that **B** can be obtained through calibrations as **M**. However, this was not tested within the scope of the present thesis. Overall, assuming that **B** can be obtained through calibration, the (7.11) model is more appropriate for system design, as in this case **B**, **SPR** and $\boldsymbol{\sigma}_{\mathbf{P}}$ can be considered as system optimization parameters.

Third noise propagation model

The problem of determining **B** has led to a third noise propagation model, which is an approximation of (7.11). The simplification lies in assuming a perfect detector (a diagonal DRM). In this case, **M** and **B** from (7.11) become equal to their diagonal matrix counterparts $\mathbf{W^{-1}}$ and **b**, respectively:

$$\boldsymbol{\sigma}_{\mathbf{S}} = \left(\sqrt{\left(\mathbf{I} - \mathbf{W}^{-1}\right)^2 \times \left(\mathbf{I} + \mathbf{SPR}\right) + \left(\mathbf{W}^{-1}\right)^2 \times \left(\mathbf{b} + \mathbf{SPR}\right)} \right) \times \boldsymbol{\sigma}_{\mathbf{P}}. \tag{7.12}$$

Using expanded versions of $\mathbf{W^{-1}}$ and **b**, the following more explicit version of (7.12) can be obtained:

$$\boldsymbol{\sigma}_{\mathbf{S}} = \left(\sqrt{\left(1-\left(1-\mathbf{e}_{\mathbf{a}}\right)^{-1}\right)^{2} \circ \left(1+diag\left(\mathbf{SPR}\right)\right) + \left(1-\mathbf{e}_{\mathbf{a}}\right)^{-2} \circ \left(\mathbf{e}_{\mathbf{a}}+diag\left(\mathbf{SPR}\right)\right)} \right) \circ \boldsymbol{\sigma}_{\mathbf{P}}, \tag{7.13}$$

where $\mathbf{e}_{\mathbf{a}}=\exp(-\boldsymbol{\mu}_{\mathbf{a}} l_a)$. Simplification of (7.13) then yields the third noise propagation model for estimated scatter:

$$\boldsymbol{\sigma}_{\mathbf{S}} = \left(1-\mathbf{e}_{\mathbf{a}}\right)^{-1} \circ \left(\sqrt{\left(\mathbf{e}_{\mathbf{a}}\right)^{2} \circ \left(1+diag\left(\mathbf{SPR}\right)\right) + \mathbf{e}_{\mathbf{a}} + diag\left(\mathbf{SPR}\right)} \right) \circ \boldsymbol{\sigma}_{\mathbf{P}}. \tag{7.14}$$

The (7.14) model is similar to the one previously presented in (7.11). However, it is substantially simpler, as matrix multiplications have been completely replaced by Hadamard products and the dependence on SPR is more tractable. Namely, since the values of $\mathbf{e}_{\mathbf{a}}$ are between 0 and 1 ($\boldsymbol{\mu}_{\mathbf{a}}>0$ and $l_a>0$) and SPR values can be between 0 and ∞ (limiting case), one can state that for large SPR values and assuming a fixed $\boldsymbol{\sigma}_{\mathbf{P}}$, $\boldsymbol{\sigma}_{\mathbf{S}}$ is approximately proportional to the square root of the respective SPR vector.

Conclusion

Having presented three different noise propagation models for the scatter estimation part of PASSSA it is worth summarizing the key aspects of each and indicate which will be used for the noise analysis in Chapter 7.1.2.

The first model, corresponding to expression (7.4), is an exact model based on variances associated with the total and modified total signals. The model can be applied directly on measurement data for noise propagation analysis provided the availability of associated variances.

The second model, corresponding to expression (7.11), is another exact model based on the variance associated with the primary signal, SPR and attenuator properties (attenuation matrix **B**). It is suitable for noise propagation based system optimization. However, due to the uncertainty related to the parametrization of **B**, the model remains not ready for testing.

The third model, corresponding to expression (7.14), is a simplified version of the second, assuming a perfect detector (diagonal DRM). As the second model, it is intended for system optimization. The virtue of the third model is the simplification of both the attenuation and transition matrices, which become diagonal. This eliminates the need for parametrization. However, due to the diagonal DRM assumption it is less exact than both the first and the second models.

In the noise analysis of Chapter 7.1.2 two models will be considered: the exact one from (7.4) and the simplified one from (7.14).

7.1.2. Noise analysis

Using the exact (7.4) and simplified (7.14) models presented in Chapter 7.1.1, a simulation analysis of estimated scatter sample noise ($\boldsymbol{\sigma}_{\mathbf{S}}$) as a function of unmodified primary noise ($\boldsymbol{\sigma}_{\mathbf{P}}$), attenuator thickness (l_a) and SPR was conducted for a single image pixel using the acquisition parameters (system settings, geometry, DRM, etc.) applied in Chapter 6.1.1 and Sindbad-SFFD (Chapter 4.3). Note that the exact model from (7.11) was not used, as no procedure for **B** estimation has yet been established.

Instead of using the thorax phantom, different water and aluminum thicknesses were used to simulate varied levels of primary signal and associated noise. The material thickness ranges were 1–17 cm (4 cm step) and 0.1–1.7 cm (0.4 cm step) for water and aluminum, respectively. The attenuator thickness range was 0.1–2 cm (0.1 cm step). For the ac-

quisition of $\boldsymbol{\sigma}_{\mathbf{P}}$, $\boldsymbol{\sigma}_{\mathbf{T}}$ and $\boldsymbol{\sigma}_{\mathbf{T}}^{\mathbf{m}}$, a total of 5000 Poisson realizations was used. The scatter component comprising the total signal remained unchanged.

Firstly, a fixed l_a (0.2 cm) was considered and $\boldsymbol{\sigma}_{\mathbf{P}}$, $\boldsymbol{\sigma}_{\mathbf{T}}$ and $\boldsymbol{\sigma}_{\mathbf{T}}^{\mathbf{m}}$ were varied via the proposed material thickness database. Note that in this case, according to (7.6), SPR also varies. With the aid of (7.4) and (7.14) $\boldsymbol{\sigma}_{\mathbf{S}}$ was computed for all possible material thickness combinations.

Figure 7.1 gives an example of the STD (as a function of energy) associated with estimated scatter sample for the lower (1 cm water and 0.1 cm aluminum) and upper (17 cm water and 1.7 cm aluminum) limit of the considered material database.

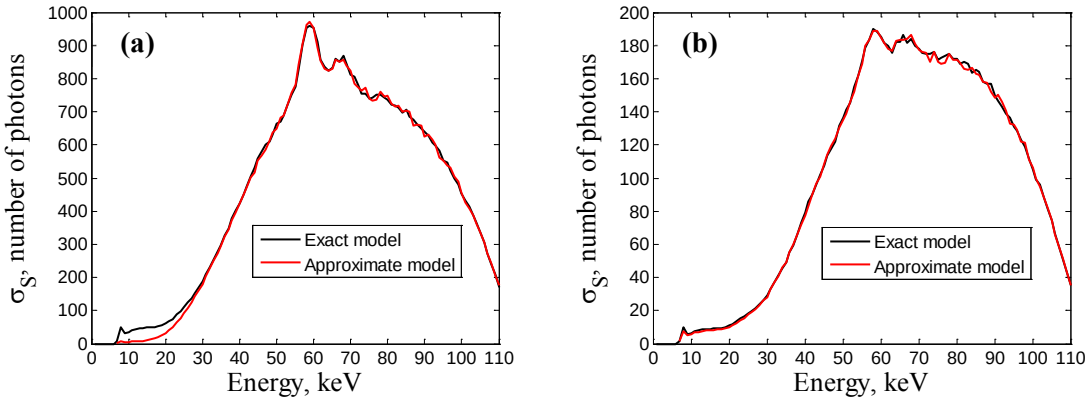

Figure 7.1. Estimated scatter sample STD as a function of energy ($\boldsymbol{\sigma}_{\mathbf{S}}$) obtained with the exact and approximate model for two different material thickness combinations: 1 cm water with 0.1 cm aluminum (a) and 17 cm water with 1.7 cm aluminum (b). The primary signal STD ($\boldsymbol{\sigma}_{\mathbf{P}}$) on average per energy was 75 (a) and 7 (b) photons, respectively. Additionally, average SPR per energy was 3% and 402%, respectively. Energy channel width was 1 keV.

The observation of Figure 7.1 indicates that the STD distribution is highly shifted towards the region of high energies. The shift becomes more prominent with increasing attenuation and the 60 keV peak becomes less visible. However, the overall shape change with the addition of attenuation is not as prominent. The shape is determined by both the primary spectrum shape and by the influence of **M**. More precisely, as larger quantity of material is encountered, the primary spectrum begins to lose magnitude, especially in the low-energy zone (c.f. Figure 2.12, Chapter 2.2.4). Thus, based on the Poisson model property, a similar behavior is also exhibited by $\boldsymbol{\sigma}_{\mathbf{P}}$, which is then modified by the transition matrix with a strongly pronounced diagonal favoring higher energies (Figure 5.8, Chapter 5.2.2). The fact that the diagonal dominates **M** and the DRM tends become more diagonal towards higher energies gives ground for the close results of both STD estimation models. Note additionally that the approximate model gives almost identical results for very high attenuation (b).

The curves in Figure 7.1 provide an illustration of the estimated scatter STD behavior as a function of energy. However, they are not as indicative of its dependence on SPR and the primary STD. For this purpose, two energies were isolated (20 keV and 80 keV), and the corresponding estimated scatter STD as a function of SPR (Figure 7.2) and primary STD (Figure 7.3) was traced.

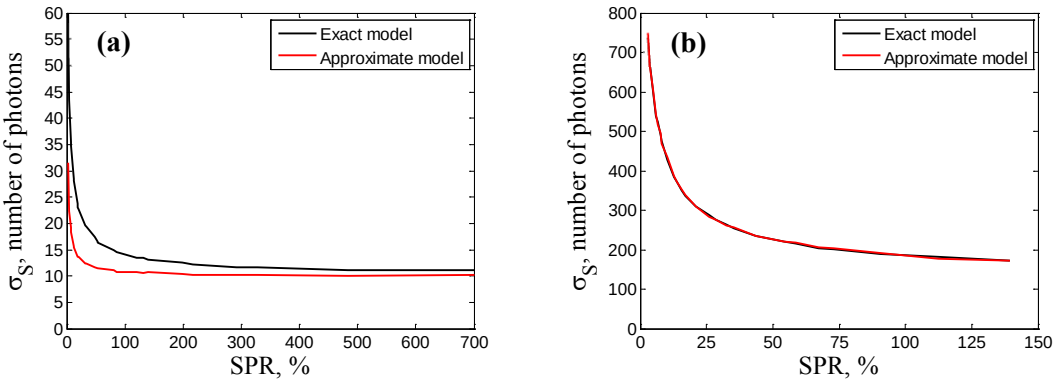

Figure 7.2. Estimated scatter STD as a function of SPR at 20 keV (a) and 80 keV (b).

Examination of Figure 7.2 reveals an exponential decrease in $\boldsymbol{\sigma_S}$ as function of SPR for fixed energies. Higher SPR bounds are exhibited for 20 keV (a), as scatter is shifted towards low energies (and is fixed) and the number of low-energy photons in the primary signal declines with attenuation. The 60 keV case (b) also displays identical results for both noise propagation models whilst for 20 keV (a) the difference is apparent and decreasing with SPR. This is similar to previous observations of Figure 7.1.

Figure 7.3 depicts a mostly linear increase of $\boldsymbol{\sigma_S}$ with increasing $\boldsymbol{\sigma_P}$ for both 20 keV (a) and 80 keV (b) cases. This means that as more primary signal comprising the total component is present (bearing a higher $\boldsymbol{\sigma_P}$), a higher level of noise ($\boldsymbol{\sigma_S}$) can be expected in the estimated scatter component. A steeper slope is exhibited for 80 keV. The models differ for the 20 keV case (a), which is consistent with Figure 7.1 and Figure 7.2.

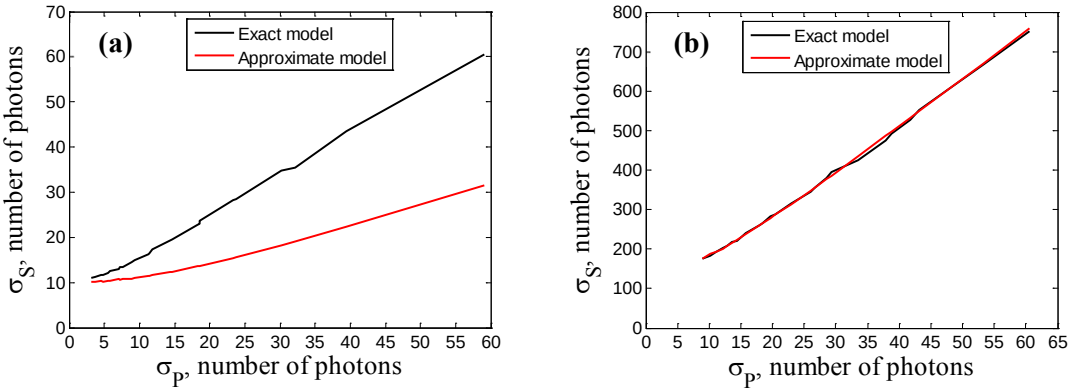

Figure 7.3. Estimated scatter STD as a function of primary STD at 20 keV (a) and 80 keV (b).

The next step was to fix $\boldsymbol{\sigma_P}$, $\boldsymbol{\sigma_T}$ and $\boldsymbol{\sigma_T^m}$, and vary l_a. Attenuator thicknesses from 0.1 cm to 2 cm (0.1 cm step) were considered. The material combination used for primary component generation was 10 cm of water and 0.5 cm of aluminum. Both primary and scatter components were fixed, resulting in a 29% SPR on average per energy. Example STD curves for a 0.2 cm and 2 cm attenuator thickness are presented in Figure 7.4.

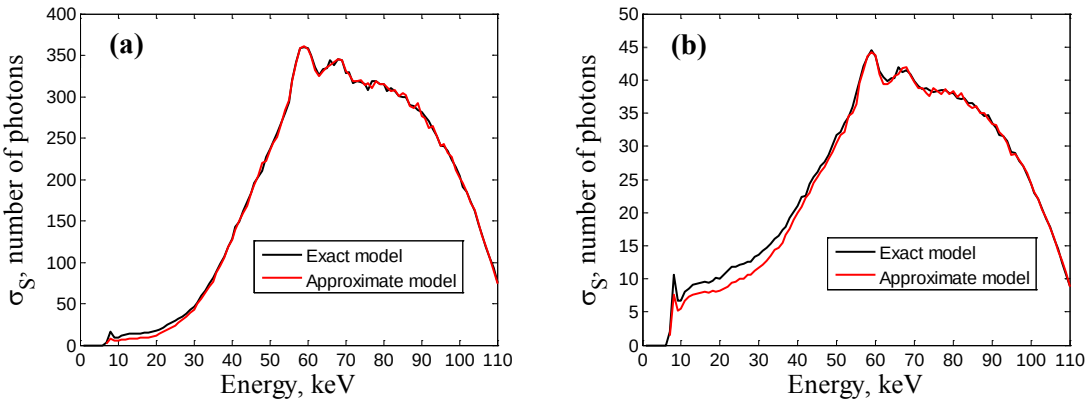

Figure 7.4. Estimated scatter sample STD as a function of energy ($\boldsymbol{\sigma_S}$) obtained with the exact and approximate model for two different attenuator thicknesses (l_a): 0.2 cm and 1.5 cm. Note that (a) corresponds to the attenuator thickness employed in PASSSA throughout the thesis. The primary signal STD ($\boldsymbol{\sigma_P}$) on average per energy was 23 photons with a corresponding 29% SPR. Energy channel width was 1 keV.

Similarly to Figure 7.1, the shape of the estimated scatter STD curve from Figure 7.4 bears resemblance to the primary spectrum shape and is shifted towards the high energy interval. For fixed total signals and an increasing attenuator thickness, one notes that for a larger attenuator thickness the values of $\boldsymbol{\sigma_S}$ in the low energy interval become more pronounced with respect to their higher-energy counterparts (b). Additionally, the relative change in overall STD magnitude is approximately equivalent to the relative change in attenuator thickness value. Finally, the approximate model, as previously, exhibits differences with the exact one. Note that this difference is even more apparent on the magnitude scale of (b).

In order to provide more insight on the dependence of $\boldsymbol{\sigma_S}$ on attenuator thickness, 20 keV and 80 keV energies were fixed and the corresponding STD as a function of attenuator thickness was traced (Figure 7.5).

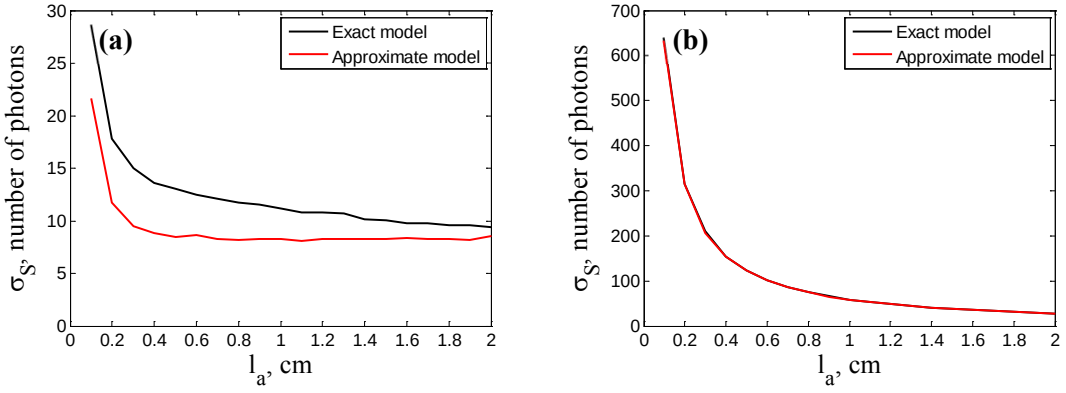

Figure 7.5. Estimated scatter STD as a function of attenuator thickness (l_a) at 20 keV (a) and 80 keV (b).

From Figure 7.5 one notes the exponential decrease in $\boldsymbol{\sigma_S}$ with increasing l_a for both the 20 keV (a) and 80 keV (b) cases. The observation of a relative STD magnitude change

being comparable to the relative attenuator thickness change is further confirmed as well as the approximate model consistency with the exact one for higher energies (b).

An important observation can be made from the noise propagation analysis conducted in the present chapter with aid of the exact (7.4) and simplified (7.14) models presented in Chapter 7.1.1. Namely, that the models provide highly similar results with the exceptions of the low-energy intervals. This is coherent with the corresponding DRM (c.f. Chapter 6.1.1) being more diagonal in the high-energy interval. It remains to be seen how the models would behave with respect to one another under a less diagonal DRM (e.g. with a high degree of charge sharing).

Another important point worth noting is that based on the observed model performance, the simplified model can be considered a reasonable tool for PASSSA linked scatter estimation noise propagation analysis given a detector with good spectral properties. This is justified as the DRM tends to become much closer to a diagonal matrix for such a detector.

7.1.3. Spatial scatter estimation

Based on the noise analysis conducted in Chapter 7.1.2, several propositions for the spatial scatter estimation routine comprising PASSSA can be outlined. These include the optimization of sample weighting as well as the spatial estimation method itself.

Firstly, given a preliminary estimated transition matrix and the availability of variance vector estimates for both modified and unmodified totals, one can apply the exact model from (7.4) per attenuator shadow pixel to compute the STD associated with each scatter sample estimated via (5.9). Then, instead of giving equal weight to each energy channel in the process of sparse scatter spatial component estimation in (5.18), an energy-dependent weight based on the obtained STD can be used instead. This will reduce the noise exhibited by the spatial component samples.

In addition to the energy weighting, spatial weighting can also be applied. Namely, since $\boldsymbol{\sigma}_S$ tends to decrease substantially with increasing SPR, more priority can be given to scatter samples obtained in image regions exhibiting high SPR (e.g. regions with high attenuation) than those where SPR is low (e.g. regions with low attenuation). SPR-based spatial weights can then be incorporated into $H(\mathbf{p})$ from (5.19).

Finally, the 2D DCT-spline estimation can be modified into a 3D version, thus excluding the need of the scatter spectrum shape hypothesis (Chapters 3.1.2 and 3.1.3). The extension of the spline-estimation approach to multiple dimensions has already been done in [84], although not considering the anisotropy aspect. This can be compensated with the aid of [85] and [86], similarly to what has been done in (5.20). In the case of a 3D DCT-spline estimation approach, both spatial (SPR based) and energy weights (STD based) can be combined in the respective 3D version of $H(\mathbf{p})$, in order provide noise-optimal weighting.

7.2. Attenuator mask optimization

The attenuator mask is a key system element necessary for the proper function of the developed scatter correction approach (Chapter 5.2.1). The spatial distribution as well as quality of the sparse scatter samples is directly linked to the design of the mask elements.

Chapter 6.1.5 outlined some aspects and limitations of attenuator mask design (e.g. element material, spatial pattern and shape). Based on the corresponding analysis as well as the noise propagation results from Chapter 7.1.2, some optimization strategies for attenua-

tor mask design in terms of element shape and positioning (Chapter 7.2.1) as well as element material selection (Chapter 7.2.2) are proposed.

7.2.1. Placement and dimensions

Given that the spatial distribution of the scatter samples is connected to the spatial pattern of the mask. Adapting the element placement for a particular x-ray imaging application can be considered.

As noted previously (Chapter 6.1.5), one can consider increasing the spatial frequency of the mask pattern, which in turn improves the sampling of the corresponding x-ray scatter distribution. Note that this has to be done bearing in mind the constraints in overall beam modification by the mask (Chapter 5.2.1).

The spatial distribution of attenuators can be further adapted based on the estimated scatter sample noise analysis conducted in Chapter 7.1.2. Namely, it was found that areas with high SPR exhibit superior scatter noise properties than their low SPR counterparts. With the aid of these observations, an object-adapted mask pattern can be designed. Consider thorax-type objects where clearly distinguished zones with low (lung region, high primary signal) and high (vertebral column, low primary signal) SPR can be identified. One can consider a mask with increased attenuator frequency in zones corresponding to lungs and vertebral column, respectively. A schematic illustrating this concept is provided in Figure 7.6.

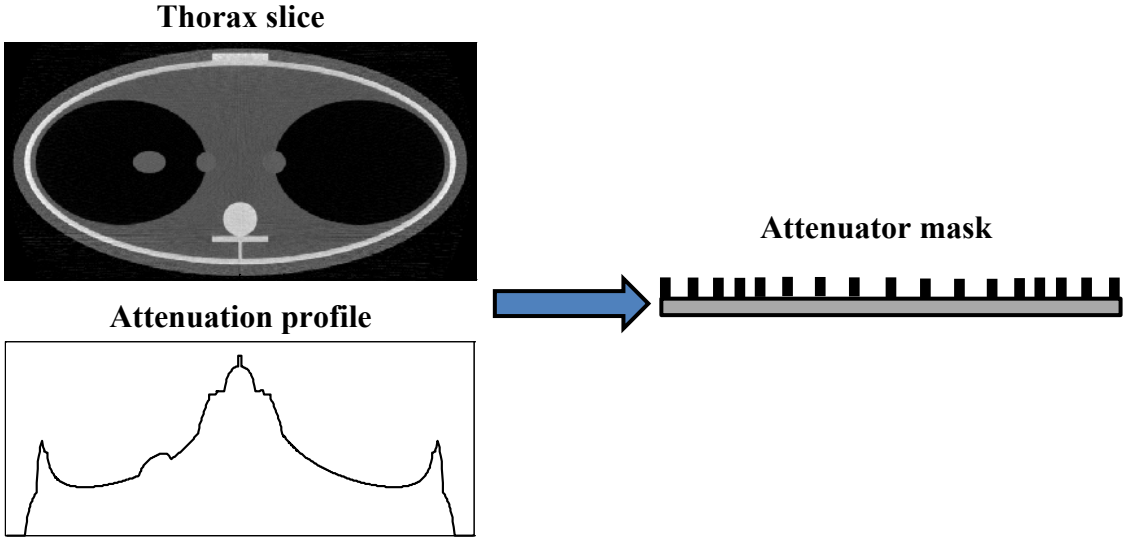

Figure 7.6. Schematic showing a thorax phantom slice and corresponding attenuation profile. A profile of the respective adapted attenuator mask is also displayed. Note that the frequency of mask elements increases/decreases in the lung/vertebral column region.

Another result from Chapter 7.1.2 is the exponential reduction in scatter sample associated STD with increasing attenuator element thickness. Thus, for the object considered until now (thorax), one can adapt the corresponding quantity based on the SPR behavior. More precisely, it would be advantageous to compensate the increase in STD due to low SPR with a higher attenuator thickness. Moreover, in order to further improve signal quality, one can also consider tilting the attenuator elements in the direction of the x-ray source.

This way the conicity effects are substantially reduced. Both modifications for the case of a thorax-type object are displayed in the schematic of Figure 7.7.

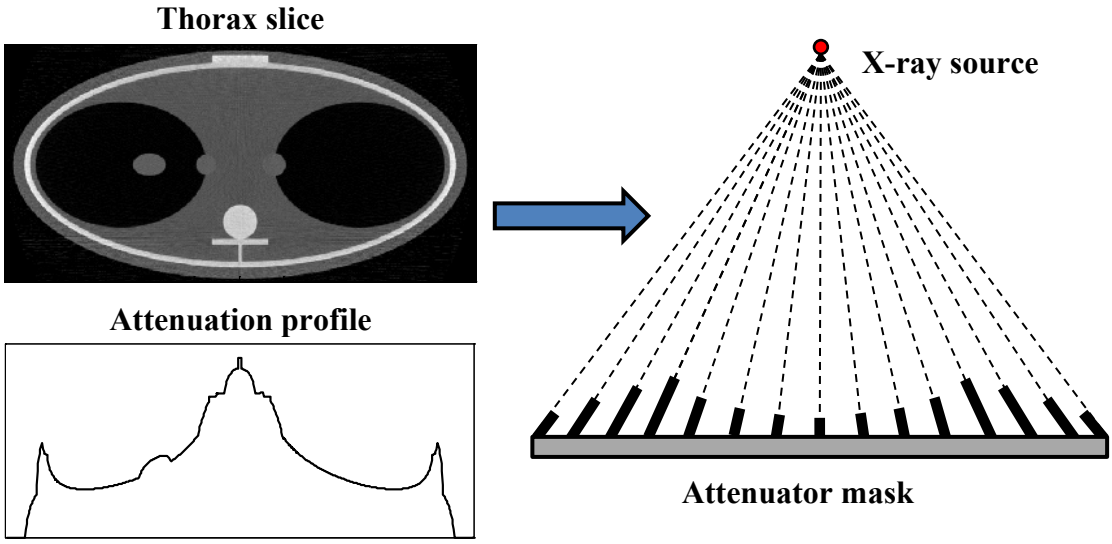

Figure 7.7. Schematic showing a thorax phantom slice and corresponding attenuation profile. A profile of the respective adapted attenuator mask is also displayed. The elements are directed towards the x-ray source, reducing conicity, and their thickness varies as function of object attenuation. Higher and lower thicknesses are considered for low SPR (lungs) and high SPR (vertebral column) regions, respectively.

It is also worth noting that both spatial pattern (Figure 7.6) and element thickness (Figure 7.7) optimizations can be combined. Additionally, one can consider performing similar adaptations for other anatomical regions (e.g. pelvis, extremities, head, etc.). In this manner, one obtains a collection of attenuator masks optimized for different anatomical examinations. The masks can then be changed by the operator or automatically by the system itself based on the corresponding acquisition protocol.

Another important note is that both pattern (Figure 7.6) and thickness (Figure 7.7) adaptations are best suited for radiography, as in CT a large dynamic in the placement of internal object structures can be observed across the projection data, which in turn results in a change of the spatial distribution of high and low SPR zones in the image. Thus, masks with dynamic properties (e.g. several moving masks) would need to be applied in order to provide similar SPR adaptive mask pattern and attenuation.

7.2.2. Material

Another important aspect of attenuator design is the corresponding material, which is in direct connection to the corresponding transition matrix **M** (c.f. (5.7)). Thus, element material selection influences the quality of primary recovery by **M** with the aid (5.8). This means that an attenuator material superior to aluminum in terms of transition matrix performance can be proposed.

Firstly, one can rewrite the signal difference expression (5.6), corresponding to a given attenuator pixel, in the following manner:

$$\mathbf{\Delta N} = \mathbf{D} \times \mathbf{W} \times \left[\mathbf{N_0} \circ \exp\left(-\sum_{q=1}^{Q} \boldsymbol{\mu}_\mathbf{q} \, l_q \right) \right]. \tag{7.15}$$

In (7.15), as in Chapter 7.1.1, the dependence on attenuator shadow pixel **p'** has been omitted for simplicity of notation.

The comparison of (7.15) and (5.3), which is the explicit expression for the primary radiation, reveals that the only difference between the expressions is the diagonal matrix **W** located between the DRM and the raw flux. Because of this, one needs to first apply an inverse of the DRM ($\mathbf{D^{-1}}$), then $\mathbf{W^{-1}}$ and then the DRM (**D**) to (7.15) in order to recover the primary $\mathbf{N_P}$. This, as stated in Chapter 5.2.1, leads to the expression of the transition matrix ($\mathbf{M}=\mathbf{D}\times\mathbf{W^{-1}}\times\mathbf{D^{-1}}$), which is applied to (7.15) in order to recover $\mathbf{N_P}$.

Consider now a non-realistic case where the diagonal **W** of is constant. In this case **W** can be switched with the DRM (**D**) leading to a more advantageous expression:

$$\mathbf{\Delta N} = \mathbf{W} \times \mathbf{D} \times \left[\mathbf{N_0} \circ \exp\left(-\sum_{q=1}^{Q} \boldsymbol{\mu}_\mathbf{q} \, l_q \right) \right]. \tag{7.16}$$

In order to recover the primary component from the signal difference in (7.16), it is sufficient to apply $\mathbf{W^{-1}}$, which is directly available through knowledge of attenuator parameters (material and thickness). Thus, the procedure of primary estimation has been substantially simplified. In reality, the diagonal of **W** is never constant, since this would imply a linear attenuation coefficient function constant in energy (c.f. (5.7)). However, one can assume that closer the respective function is to a constant (and thus the diagonal of **W** as well), closer **M** becomes to $\mathbf{W^{-1}}$. This implies a potential improvement in **M** parametrization accuracy.

If the diagonal of **W**, corresponding to the attenuator thickness (0.2 cm) and material (aluminum) considered throughout the thesis, is visualized (Figure 7.8), one can observe that it is only approximately constant (linear with a low slope) in the 70–110 keV region. Thus, there is ground for optimizing the attenuator material.

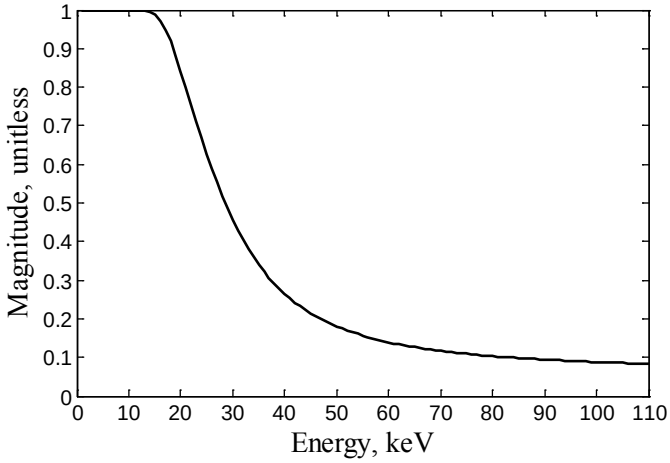

Figure 7.8. Diagonal of **W**, corresponding to an aluminum attenuator (0.2 cm thickness), as a function of energy.

In Chapter 2.2.4, the attenuation coefficient function was described as a combination of several physical photon-matter interactions effects. In fact, from Figure 2.10, one may note that the non-linear behavior of the respective function is mainly caused by photoelectric

effect and Rayleigh scattering. Additionally, the former has a more substantial contribution than the latter. With the aid of (2.3), it can be stated that photoelectric effect is less prominent for low Z materials. Based on these observations, several alternative attenuator materials can be proposed. More precisely, one needs a low Z material, which has sufficiently strong for the necessary small scale element fabrication. The density should be comparable or superior to the one of aluminum, in order to ensure small thicknesses (avoids potential mechanical fabrication issues). Finally, one can also consider that fabrication and exploitation also require a non-toxic material.

Based on the outlined criteria, two potential candidates have been selected: graphite and boron. The diagonals for corresponding **W** matrices are plotted for an equivalent 0.2 cm attenuator thickness in Figure 7.9.

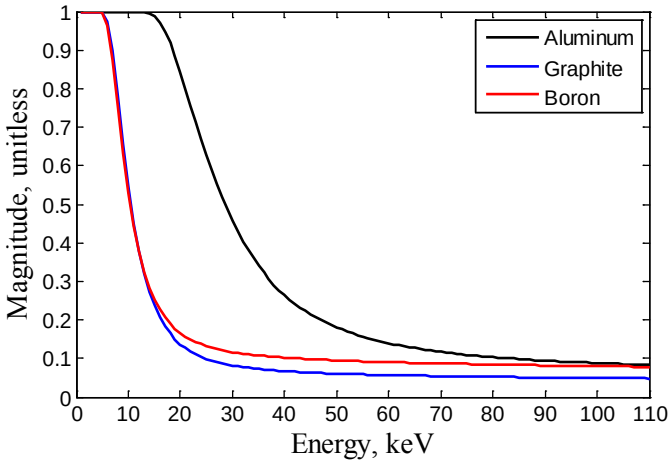

Figure 7.9. Diagonals of **W**, corresponding to a graphite and boron attenuators (0.2 cm thickness), as a function of energy. A diagonal of **W** obtained for the 0.2 cm aluminum attenuator is also displayed for comparison.

From Figure 7.9, one notes that the corresponding graphite and boron **W** diagonals exhibit a constant (in energy) behavior for a substantially larger interval than aluminum: 40–110 keV compared to 70–110 keV. However, since both material densities are lower than aluminum, a slight increase in attenuator thickness would be required to achieve an equivalent average attenuation per energy.

In conclusion, although the transition matrix **M** estimation procedure features a parametric model that can be adapted to given attenuator and detector properties, it can be advantageous to simplify the form of **M**, in order to improve parametrization accuracy, which in turn leads to a superior primary recovery performance. This can be achieved by choosing a strong non-toxic low Z material, such as graphite or boron, for the manufacturing of an attenuator mask.

7.3. Single acquisition

The concept of PASSSA was presented based on two acquisitions: modified (by attenuators) and unmodified (Chapter 5.2.1). The corresponding simulated and experimental validations were also conducted using this configuration (Chapter 6).

In the case of two acquisitions for medical applications each one needs to be performed at half of the dose considered for the given application, in order to avoid the increase in

patient dose. Reducing the dose per acquisition entails a tube output reduction. Thus, the measured x-ray signals will lose in SNR. Additionally, the supplemental acquisition leads to an increase in examination time and potential for patient motion related artifacts (especially in CT).

For NDT applications and security applications, dose is less of a constraint. However, the increase in acquisition time can pose a disadvantage as this would lead to longer industrial manufacturing times and security checks, respectively, for each of these modalities.

In Chapter 5.2.1, it was stated that PASSSA can also function in a single modified acquisition configuration provided the unmodified total signal was estimated in attenuator influenced zones of the image. Despite the non-trivial nature of such a task, possible solutions are proposed in both radiographic (Chapter 7.3.1) and tomographic acquisition modes (Chapter 7.3.2).

7.3.1. Radiography

As PASSSA is a scatter correction technique designed for radiographic projections, it would be sufficient to develop an unmodified (by attenuators) total signal estimation approach in the context of radiography in order for the method to function with a single acquisition both in radiographic and CT applications.

Firstly, an example attenuator influenced radiographic attenuation image with a corresponding attenuator shadow region surface plot from the 50 keV energy channel is presented in Figure 7.10, in order to visualize the problem.

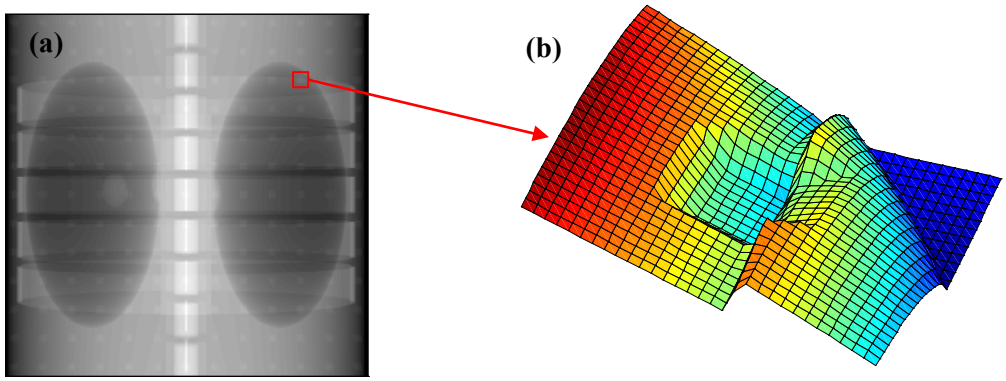

Figure 7.10. X-ray attenuation image under the influence of an attenuator mask (a) with a surface plot (number of photons) taken from region influenced by an attenuator at 50 keV (b). Note that the surface plot was obtained from the energy-resolved counterpart of (a).

The illustrations from Figure 7.10 indicate that the attenuators produce a localized signal level decrease in a given channel of the energy-resolved x-ray image (b). However, the high frequency information (e.g. contours and borders), still remains visible (a). Thus, using both the attenuator shadow region and its neighborhood, it may be possible to restore the corresponding zone (i.e. compensate for the effect of the attenuator).

One way of treating the issue of compensating the attenuator effect on the image is to treat it as an *inpainting* problem. In this case, one considers that no data is available in the attenuator shadows, and applies inpainting approaches to recover the corresponding areas. Possible solutions for the corresponding problem include diffusion processes [93], total variation [94] or neural networks [95]. Note that inpainting methods are used for 2D imag-

es and would need to be either applied per energy channel or adapted for the 3D images used in energy-resolved x-ray imaging. In any case the considered methods involve iterative processes (e.g. [93] and [94]) and thus the computational expense due to the 3D nature of the attenuator shadow compensation problem may become substantial. Furthermore, by default, these techniques deal with missing data, and in the current case the signal is just modified. However, this can potentially be incorporated as some form of prior for the considered inpainting approaches.

Another solution to the considered problem can be also found in the domain of old photograph restoration. More precisely, water blotches on old documents produce a semi-transparent artefact [96] similar to the one caused by the attenuators in an x-ray image. The difference is that it is less regular in spatial shape and borders exhibit more pronounced discontinuities due to residual dust. Thus, one can employ methods that aim to correct for such a distortion in the context of the present problem. These can include relatively simple linear [97] or logarithmic model based [96] approaches as well as methods based on Bayes statistics [98]. Compared to inpainting methods, these approaches require less computational time (especially [96] and [97]) and are more adapted to the current problem of attenuator effect compensation due to similarity in artefact nature. However, as in the case of inpainting methods, 2D images are considered and thus an adaptation to 3D energy-resolved x-ray data is necessary. Finally, the physical model behind the attenuator influence (i.e. the attenuation of a part of the primary signal) along with detector modelling (e.g. DRM) can be incorporated into techniques like [98] to yield an estimation approach more adapted to the current problem.

Finally, one can question the efficiency of applying an estimation approach for unmodified total recovery, since this implies the propagation of the respective estimation error toward the scatter samples and thus potentially compromising method efficiency. In essence, by inserting the attenuator mask into the x-ray beam, a tractable modification of the primary is created. The goal is to acquire a primary free of this modification. Thus, a method that corrects for attenuator influence and in the process estimates the scatter distribution could be developed based on the current version of PASSSA. The latter aspect gives the ability to provide scatter separation from the total signal via subtraction.

7.3.2. Tomography

In CT, the availability of multiple projections of the inspected object can be exploited to allow PASSSA to function in a single acquisition configuration. Since the collection of projections leads to a sinogram (Chapter 2.4.2), one can employ approaches similar to the ones proposed for radiography in Chapter 7.3.1 (e.g. inpainting or semi-transparent artefact correction) in the respective space. Changing the domain of the problem may potentially lead to a better performance of such methods.

A more adapted solution would be to exploit the additional angular information available in CT datasets. For this purpose, consider employing an attenuator mask that instead of remaining fixed (static) throughout the CT acquisition moves as a function of projection angle (dynamic). This in turn modifies the spatial position of the attenuator shadows for each projection. The concept is illustrated in Figure 7.11. In such a configuration, the unmodified total signal in the attenuator shadow regions can be estimated from adjacent projections. Furthermore, CT data consistency (or range) conditions, which describe redundancy or overlap in projection data [99], can be employed to aid the estimation process. Indeed, projection data redundancies have been exploited in the past to improve the per-

formance of SK approaches [100] and to restore missing primary radiation in the context of single acquisition BS scatter correction approach [29]. The latter is of particular interest, as it also utilizes a moving mask and deals with missing data (due to the BS array blocking the x-ray beam). The availability of information in the attenuator shadow regions combined with the CT data redundancy based approach from [29], can lead to the most optimal unmodified total estimation technique.

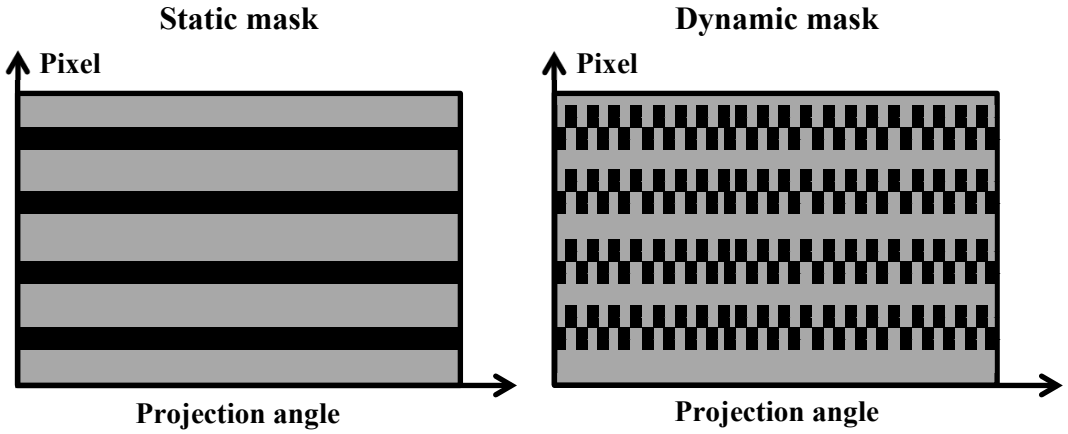

Figure 7.11. Schematic drawing of a CT sinogram when a static/dynamic attenuator mask is used. In the case of the dynamic mask the attenuator shadows (black) change their spatial position with projection angle.

Despite its advantages for CT acquisitions, there are some mechanical considerations of the moving mask. Namely, due to gantry rotation speeds (full rotation in less than 1 s) [38], the mask would never achieve the idealistic pattern displayed in Figure 7.11 due to limited speed of electronic displacement circuits. This would lead to an attenuator shadow spatio-angular distribution which is smoother and exhibiting some degree of motion blurring, which will need to be accounted for. Additionally, questions of grid movement stability under a rapidly rotating gantry can also be raised. The influence of gantry rotations can also add residual motions (tilting) to the default movement of the mask and thus contribute to the production of artifacts in the sinogram.

As discussed in Chapter 7.3.1, a single acquisition PASSSA-derivative method can be developed providing both attenuator influence correction and scatter distribution estimation (and thus being capable of scatter correction through subtraction). In addition, in the context of CT, the exploitation of projection data consistency conditions can be considered. Moreover, coupling of the algorithm with a corresponding iterative statistical tomographic reconstruction approach is also an option.

8. CONCLUSION AND PERSPECTIVES

The primary goal of the thesis was to develop an x-ray scatter correction method adapted for multi-energy imaging. As energy-resolved PCDs are a relatively recent technology, there have been very few studies examining the behavior of scattered radiation in the energy domain as well as its influence on multi-energy x-ray applications. In addition, currently employed energy-resolved PCDs are evolving in the direction of 2D detectors. Finally, a scatter correction method dedicated to energy-resolved x-ray data has not yet been proposed.

In the context of the lack of scatter analysis in the energy domain, a secondary objective was formulated. It was chosen to develop a simulation tool based on the existing Sindbad software (conceived at the LDET laboratory), which would be capable of providing energy-resolved scatter simulation within a reasonable time. In Chapter 4.3, Sindbad-SFFD, a tool fulfilling this requirement was introduced and validated through GATE simulations and experiments. Results showed that Sinbad-SFFD produces simulations that are highly consistent with ones provided by GATE and experimental data. Furthermore, the tool proved to be sufficiently fast, providing energy-resolved images in about 1.5 h on a single core processor. Future developments will focus on overall and CT-dedicated acceleration through parallelization and angular sub-sampling, respectively. Additionally, Rayleigh interaction related point artifacts and photon number optimization will also be investigated.

Once Sindbad-SFFD was designed and validated, an analysis of scatter in the energy domain was conducted (Chapter 3.1.2) in order to complement existing studies on the phenomenon reviewed in Chapter 3.1.1. In addition to simulations, experiments studying scattered radiation with the aid of energy-resolved PCDs were also performed (Chapter 3.1.3). Based on the corresponding scatter simulations and experiments, it was concluded that the spectrum shape of scattered radiation can be globally preserved for a number of different air gaps and objects. Additionally, based on a multi-projection experiment with the anthropomorphic phantom (Chapter 3.1.3), it was observed that scatter may also preserve spectrum shape across varying projections of the same object. This property can prove useful in the development of both scatter simulation and estimation algorithms. Further investigations, especially in CT, are, however required to establish the limits of scatter shape preservation.

Having examined scattered radiation in both spatial and energy domains in Chapter 3.1, it was important to evaluate its effect both qualitatively and quantitatively in various x-ray applications (Chapter 3.2). Simulations conducted with Sindbad-SFFD showed that in both integration mode radiography (Chapter 3.2.1) and tomography (Chapter 3.2.2) the presence of scatter introduced bias and a loss of local contrast. For CT, artifacts were also present. The observations were consistent with what was indicated by numerous other scattered radiation related studies discussed in Chapter 3.1.1. For the considered multi-energy appli-

cation (basis material decomposition), scatter also induced bias, contrast loss and object structure related artifacts (Chapter 3.2.3). It was concluded that scatter poses a great issue, especially in basis material decomposition, which is sensitive to energy-resolved data accuracy. Thus, a way of managing the presence of scatter in the measured data is necessary.

In Chapter 5.1, a literature review on existing scatter correction techniques, used in integration mode imaging, was conducted. The approaches were classified and analyzed in terms of their virtues and disadvantages. It was concluded that some of the methods can be applied directly to energy-resolved imaging whilst others will suffer from an increase in model complexity and execution time. Additionally, since the scatter correction methods discussed in Chapter 5.1 applied for integration mode x-ray detectors, they do not exploit the energy information provided by energy-resolved PCDs. In order to fill the gap in existing scatter correction methods and fulfill the primary objective of the thesis, PASSSA, a method exploiting multi-energy information was developed (Chapter 5.2). The concept was then validated though simulations (provided by Sindbad-SFFD) and experiments (Chapter 6).

The evaluation of PASSSA through simulations (Chapter 6.1) revealed noteworthy results for both radiographic projections and CT volumes in terms of scatter effect reduction. Attenuation images and CT slices obtained from corrected energy-resolved data showed a substantial increase in local contrast and internal structure detectability. A high degree of bias reduction was also achieved. Moreover, x-ray spectra obtained after correction were highly close to their scatter free counterparts. Compared to the initial average error of 23% between the uncorrected and scatter-free projections, the application of PASSSA reduced this value to around 5%. Additionally, based on noise analysis in different projections, the method proved to be stable for varying noise levels. In terms of voxel value accuracy, an increase by a factor greater than 10 was observed for most inspected volumes of interest, when comparing the corrected and uncorrected total volumes. Finally, it was also noted that the transition matrix enabled the method to adapt to various non-idealities of the detector (e.g. its response).

Radiographic experiments performed with an anthropomorphic thorax phantom further proved the efficacy of the developed scatter separation approach (Chapter 6.2). In terms of attenuation images, PASSSA-corrected energy-resolved data resulted in images comparable to those obtained through BS correction. The same was true for the corresponding spectra. Moreover, the improvement upon the images generated from uncorrected data in terms of contrast and bias was apparent. Quantitatively, the developed method proved to be in relative agreement with the BS-corrected data (within 5%). The application of PASSSA lowered the initial average error between the scatter corrupted and BS-corrected energy-resolved images by approximately a factor of 9.

In Chapter 6.3 basis material decomposition was applied on energy-resolved simulated radiographic images corrected by PASSSA in order to determine the performance with respect to their uncorrected counterparts. The respective chapter also examined some application related optimizations in the developed method. It was concluded that the application of PASSSA on energy-resolved scatter corrupted data results in material images closely matching the ones obtained from scatter free data and true thickness data. Quantitative analysis further supported these observations with an average thickness estimation error reduction by a factor of about 3.6. The included method optimization resulted in an estima-

tion improvement both in terms of local bias and noise. The thickness estimation accuracy improved by 30% with respect to the initial version of PASSSA. An important conclusion was the need for any given multi-energy scatter correction method to be conditioned by the respective application and vice versa.

Based on the analysis of PASSSA in Chapter 6, further method developments were proposed (Chapter 7). These ranged from specific propositions, such as spatial scatter estimation improvements (Chapter 7.1) and attenuator element optimization (Chapter 7.2) to more general ideas, such as method functioning with a single acquisition (Chapter 7.3). In Chapter 7.1.3, a proposition of data weighting based on noise propagation analysis was formulated in order to improve scatter estimation. Moreover, the corresponding analysis also provided ground for attenuator dimension adaptations (Chapter 7.2.1). The mask design evaluation also revealed some other materials, such as graphite and boron, capable of improving the performance of the key element of PASSSA – the transition matrix. From the discussions in Chapter 7.3, it was concluded that the functioning of the method with a single acquisition may be possible through an estimation of the supplemental data through inpainting, old-photograph restoration and data consistency driven approaches (CT). The former can also be coupled with a moving attenuator mask.

The method developed within the framework of this thesis opens the door for other scatter correction methods exploiting multi-energy information. Firstly, an approach not requiring a supplemental acquisition is much more attractive for medical x-ray imaging due to both dose and acquisition time considerations (Chapter 7.2) as well as due to an increased probability of motion related artifacts. The adaptation of PASSSA to such a configuration will be thus the primary priority for future work. In addition, in the CT case, it would be advantageous to utilize the redundancy of CT data through consistency conditions (Chapter 7.3) and potentially couple the scatter correction method with a projection data reconstruction approach. These developments will open up the second direction of future work. Finally, it is worth noting that since PASSSA corrects scatter via the respective distribution estimation, supplemental measurement data (scatter) is available. It would be interesting to explore the potential of using the energy-resolved scatter data to improve the performance of x-ray imaging applications.

APPENDIX A: TEXTE DE SYNTHESE EN FRANÇAIS

1. Introduction

Depuis la découverte des rayons X par Röntgen en 1895, de nombreuses applications pour l'imagerie à rayons X sont apparues, allant de diagnostic médical à la sécurité et le contrôle non-destructif (CND) des échantillons industriels. Des avancées significatives peuvent être observées dans la conception des différents composants du système à rayons X tels que des tubes, des générateurs, des détecteurs, collimateurs, des portiques de tomodensitométrie (TDM), supports de patients, etc.

Au cours des dernières décennies, plusieurs changements importants dans la technologie de détection de rayons X se sont produits. En particulier, dans le début des années 1990, la détection de film analogique a été remplacée par la technique dite « semi-numérique » connu sous le nom de « Computed Radiography » (CR). L'idée était basée sur l'utilisation de plaques de phosphore photo-stimulable, qui ont été traitées après exposition par un lecteur. [1]. Puis, au début du XXI^{ème} siècle, la technologie de détection de rayons X entièrement numérique, connu sous le nom de « Digital Radiogrpahy » (DR), a été introduite. Ces types de détecteurs convertis rayons X en signaux électriques après l'exposition, soit par une conversion directe ou directe. [2]. Les deux CR et DR ont permis l'application de techniques de traitement d'image pour les images à rayons X résultant. Ces techniques permettent l'amélioration et le rétablissement d'image et la capacité d'effectuer la segmentation d'images, ainsi que le développement des méthodes de détection de la maladie automatiques, etc. [3].

En cours des dernières années, de nouvelles capacités de détecteur de rayons X numérique ont été étudiés. Pour un pixel donné, des détecteurs à rayons X classiques fournissent un signal proportionnel à l'énergie photonique déposée dans l'élément détecteur, intégré sur la plage totale d'énergie [2]. Les nouveaux détecteurs en comptage de photons à base de semi-conducteurs ont la capacité de classer les photons en plusieurs canaux discrets d'énergie, dont le nombre varie de quelques canaux (typiquement de 2 à 8) [4]–[6] pour une centaine d'une largeur d'environ 1 keV, en fonction du circuit électronique [7], [8]. Cette nouvelle technologie permet le développement de l'imagerie résolue en énergie pour toutes les applications à rayons X actuels. L'information sur l'énergie supplémentaire permet d'augmenter le rapport contraste-bruit [9], réduire la dose et artéfacts [10]. De plus, les composants matériels présents dans l'objet peuvent être différenciés et leurs épaisseurs équivalentes et les rapports relatifs (tissu mou, tissu osseux, tissu glandulaire, etc.) estimées par le traitement d'une image unique d'acquisition de tir à la fois la radiographie et TDM [4], [10], [11]. Afin de bénéficier de la capacité matérielle différentiation de l'imagerie multi-énergie, un haut degré de précision dans les acquisitions est nécessaire (faible biais, faible bruit, absence d'artéfacts, etc.), en particulier pour les matériaux proches en termes d'atténuation.

Un tel objectif est difficile à atteindre dans le cas des géométries non-collimatées en raison de rayonnement diffusé qui induit divers effets indésirables dans l'imagerie à rayons X tels que le biais, la perte de contraste et les artéfacts en TDM [12]. En outre, cet effet est dépendant d'objet et de géométrie [13]. Plusieurs études ont démontrées l'impact de la diffusion des rayons X sur les applications d'imagerie multi-énergies [14], [15] et une approche d'estimation de diffusion d'ordre un a également été proposée [16].

Un nombre important de méthodes ont été développées pour la correction du diffusé en utilisant des détecteurs conventionnels en intégration [17]. Ces approches comprennent des méthodes directes, comme les grilles anti-diffusantes [18], l'augmentation de l'écart d'air [19] et la collimation supplémentaire [20], les méthodes basées sur la modélisation numérique tels que méthodes Monte Carlo (MC) [21]–[23], et les « Scatter kernels » (SK) [24]–[26], les méthodes basées sur des mesures physiques, telles que « Beam Stop » (BS) [27]–[29], un « Beam Hole » (BH) [30], [31], modulation primaire (PM) [32]–[34]et d'autres [35], [36], et les méthodes de post-traitement d'image [37]. Certaines de ces techniques peuvent être appliquées directement dans l'imagerie multi-énergies (méthodes directes, méthodes basées sur des mesures physiques) tandis que d'autres vont souffrir d'une augmentation de la complexité du modèle et le temps d'exécution (méthodes basées sur la modélisation numérique, méthodes de post-traitement d'image). Il est important de noter que les méthodes de correction du rayonnement diffusé utilisées pour les détecteurs à rayons X conventionnels n'exploitent pas l'information sur l'énergie. L'évolution à taille relativement importante 2D des détecteurs résolus en énergie donne plus d'importance au développement d'une méthode de correction du diffusé adaptée pour l'imagerie multi-énergies.

La thèse inclus deux objectifs principaux. Le premier est le développement d'un outil de simulation capable de fournir des images du diffusé résolues en énergies dans un temps raisonnable. Avec l'aide de l'outil concernée il serait possible d'étudier le comportement du diffusé dans le domaine d'énergie et obtenir des connaissances plus profond sur le sujet en général. Le deuxième et le principal objectif de cette thèse est le développement d'une méthode de correction du diffusé adaptée à l'imagerie multi-énergies et qui utilise l'information énergétique fournie par les détecteurs correspondants.

2. Outil de simulation du rayonnement diffusé spectral

Un des objectifs de la thèse actuelle était de concevoir un outil de simulation permettant la simulation du rayonnement primaire et diffusé résolus en énergie pendant un temps acceptable. Cet outil était basé sur le code existant d'un outil, *Sindbad* interne (développé au laboratoire LDET) [62]. Le nouveau logiciel de simulation permettrait de réaliser diverses études visant à fournir plus d'information sur le comportement du diffusé dans l'espace d'image et, surtout, dans le domaine d'énergie.

Chapitre 2.1 présente les principes clés derrière l'outil développé. Ensuite, la validation croisée (Chapitre 2.2) et la validation expérimentale (Chapitre 2.3) du logiciel respectif sont effectuées. Finalement, une conclusion est donnée dans le Chapitre 2.4

2.1. Sindbad-SFFD

Une image résolue en énergie peut être représentée par une matrice 3D (Fig. 1) où chaque pixel **p** (fait partie de la région **Ω** d'image entière) contient un spectre échantillonné avec un certain pas (dépendant du nombre de canaux du détecteur).

Sous l'hypothèse d'absence des effets d'empilement (ou empilements limités), ce spectre est une somme de deux components, le rayonnement primaire $\mathbf{N_P(p)}$, correspondant aux photons atténués dans l'objet traversé, et le rayonnement diffusé $\mathbf{N_S(p)}$, correspondant aux photons déviés par les effets Compton et Rayleigh (ou fluorescence dans certains cas) :

$$\mathbf{N_T(p)} = \mathbf{N_P(p)} + \mathbf{N_S(p)}, \quad \forall \mathbf{p} \in \mathbf{\Omega}. \tag{1}$$

Les deux signaux (primaire et diffuse) sont des fonctions discrètes du nombre de canaux d'énergie d'un détecteur spectrométrique. Donc, par exemple, pour un pixel **p** et canal E donnés, $N_P(\mathbf{p},E)$ correspond au nombre de photons primaire mesurés dans ce pixel et canal d'énergie.

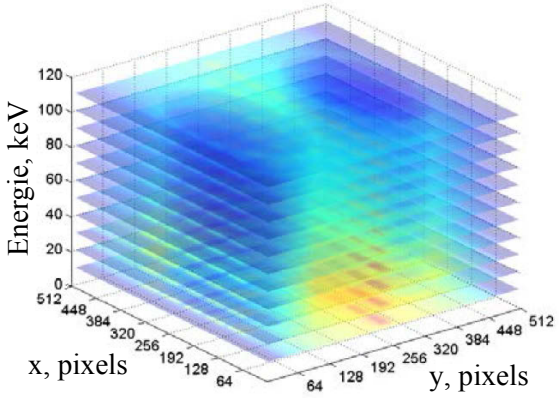

Fig. 1. Exemple d'une image radiographique résolue en énergie.

La simulation du premier terme était déjà possible avec la version récente de Sindbad. Pour le deuxième (diffusé) une simulation MC analogique peut être utilisée. Cela a été fait dans plusieurs études sur le rayonnement diffusé résolu en énergie [14], [15], [58]. Cependant, dans ce cas, l'introduction d'information sur l'énergie augmente de façon significative la demande de calcul. Afin d'avoir les spectres du diffusé avec une bonne résolution énergétique dans chaque point d'image, un nombre plus élevé de photons devrait être utilisé dans la simulation.

Afin de fournir des temps de calcul raisonnables sans sacrifier la précision, une approche dite « Spectral Fixed Forced Detection » (SFFD) a été utilisé en combinaison avec Sindbad. Le nouveau logiciel de simulation, appelé *Sindbad-SFFD*, est capable de simuler le primaire et le diffusé résolus en énergie dans un temps raisonnable. L'approche SFFD, responsable de la partie simulation du diffusé, est basé sur une combinaison de MC et de calcul déterministe [65] avec une addition de sous-échantillonnage spatial du détecteur. Fig. 2 fournit un résumé illustratif de cette technique.

D'abord, la partie MC détermine l'ensemble de points de diffusion $\{P_1,\ldots, P_{i-1}, P_i, P_{i+1},\ldots, P_I\}$ dans l'objet par le suivi de chaque particule du point d'émission jusqu'à ce qu'elle soit absorbée ou sortie des limites de la simulation. Coordonnées, direction de propagation, l'énergie incidente des photons, type d'événement (Compton ou Rayleigh) et l'ordre des événements sont enregistrés pour chaque point d'interaction P_i. Fluorescence n'est pas traitée comme elle commence à ajouter une contribution significative seulement quand une bonne quantité de matériau avec un numéro atomique élevé est présente dans l'objet.

La deuxième partie de la méthode applique un calcul déterministe des fractions de particules $f_{ij}(E_i,E_{ij}^*)$ arrivant de chaque point P_i sur un nœud donnée du détecteur $S_J \in \{S_1,\ldots, S_J\}$:

$$f_{ij}\left(E_i,E_{ij}^*\right)=\frac{1}{\sigma_i\left(E_i\right)}\frac{d\sigma\left(\theta_{ij},E_i\right)}{d\Omega}\exp\left(-\sum_{q=1}^{Q}\mu^q\left(E_{ij}^*\right)l_{ij}^q\right)\Omega_{ij}\,, \tag{2}$$

où $\sigma_i(E_i)$ est la section efficace totale en fonction de l'énergie des photons incidents E_i pour une diffusion de P_i sur 4π sr, $d\sigma(\theta_{ij},E_i)/d\Omega$ est la section efficace différentielle, θ_{ij} est l'angle de diffusion, $\mu_q(E_{ij}^*)$ est le coefficient d'atténuation (fonction de l'énergie des photons diffusés E_{ij}^*) d'un matériau donné $q \in \{1, ..., Q\}$ constituant l'objet, l_{ij}^q est la longueur du chemin parcouru par la fraction de particules diffusées dans le matériau respectif et Ω_{ij} est l'angle solide vu par la source de diffusion P_i sur le nœud S_j correspondant à un pixel donné du détecteur. En supposant un détecteur parfait, le spectre du diffusé continue $N_j(E_{ij}^*)$ (le sous-indice S a été omis pour simplifier la notation) dans chaque nœud S_j peut être calculé en utilisant l'expression suivante:

$$N_j\left(E_{ij}^*\right) = \sum_{i=1}^{I} f_{ij}\left(E_i, E_{ij}^*\right). \tag{3}$$

La partie finale de SFFD consiste à déterminer les spectres pour le détecteur entier en utilisant une interpolation spatiale sur les échantillons S_j. Le sous-échantillonnage a été implémenté prenant compte du fait que le rayonnement diffusé a une distribution spatiale contenue dans les basses fréquences [57].

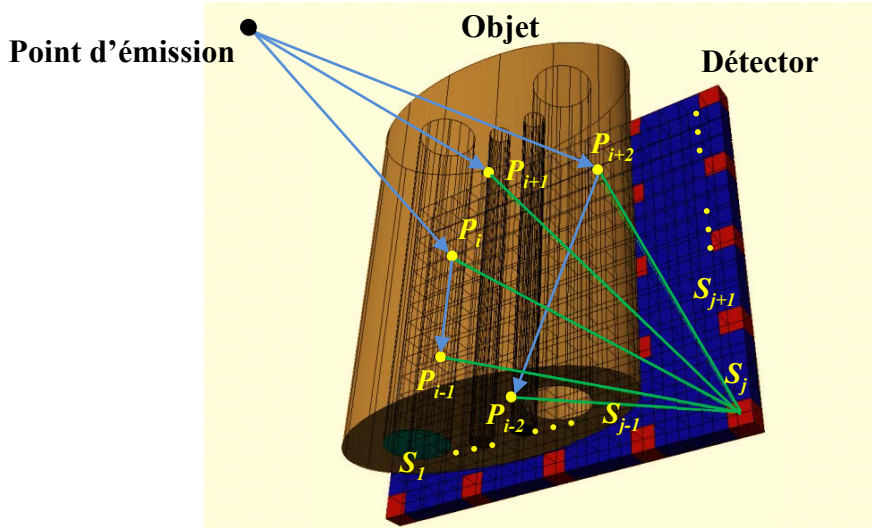

Fig. 2. Schématique reflétant différentes parties de l'approche SFFD de simulation du diffusé. Les particules générés par le MC interagissent avec l'objet et produisent un ensemble de points diffusant d'ordre différent, suivi par une somme de fractions de particules dans la direction du nœud donné.

À ce point, on ne considérait qu'un détecteur parfait. Afin de tenir compte d'un détecteur réaliste, il faut appliquer *une matrice de réponse du détecteur* (DRM) sur (3). L'outil de simulation développé prend la DRM en tant que paramètre pour simuler la réponse du détecteur. Une option d'ajout de bruit photonique au signal est également présente. Un exemple d'une telle matrice est donné dans Fig. 3.

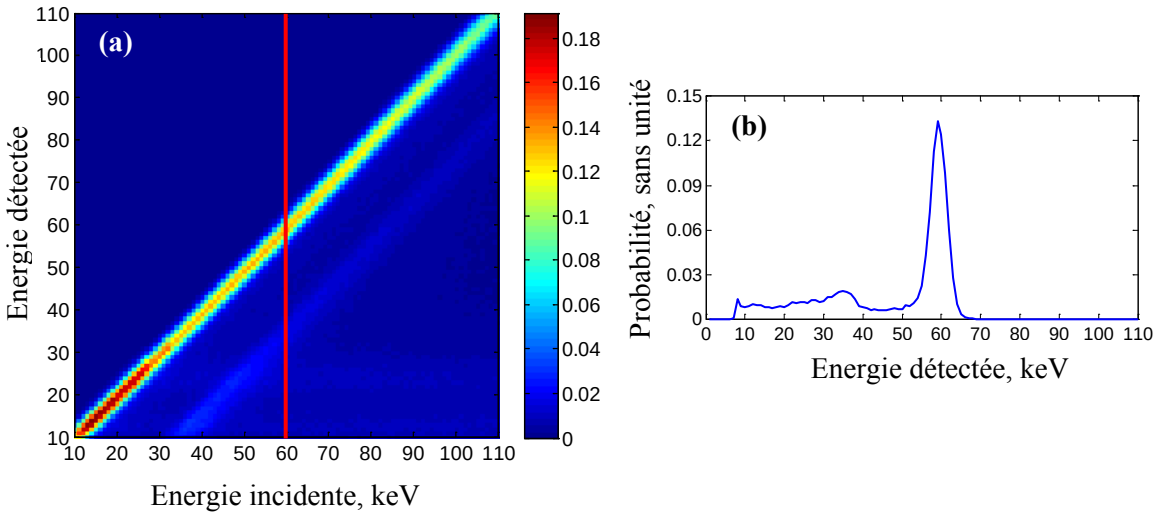

Fig. 3. DRM d'un détecteur CdTe avec un pixel de 800 µm (épaisseur de 3 mm) (a). Un profil de la matrice à l'énergie incidente de 60 keV est aussi présenté (b).

Pour la présente étude, un modèle précis, capable de prédire la réponse du détecteur à toute énergie, a été utilisé [70]. Basé sur un code MC (Penelope [71]), ce premier modèle simule toutes les interactions physiques des photons et des électrons à l'intérieur d'un semi-conducteur donné pour fournir la position et le nombre de charges créés à chaque interaction. La seconde étape effectue une intégration numérique de l'équation de transport pour chaque nuage de charge le long de leurs trajectoires vers les anodes de collecte. En utilisant le théorème de Schockley-Ramo [72], la dérive du transport, la diffusion, le piégeage, la répulsion de Coulomb et le partage de charge sont pris en compte pour fournir une estimation précise des signaux transitoires induits sur l'anode de collecte ces voisines. Enfin, la modélisation de l'électronique, y compris le bruit réaliste, est effectuée pour obtenir les formes d'onde d'impulsions finales. La réponse du détecteur est calculée pour toutes les énergies et les résultats stockés dans le format d'une DRM.

Une autre façon d'estimer la DRM est avec de l'aide d'expériences. Un exemple d'effectuer une telle estimation consiste à mesurer la réponse du détecteur avec plusieurs sources de rayonnement à différentes énergies et appliquer un modèle paramétrique [45].

Enfin, il est intéressant de noter que pour des simulations du diffusé en TDM, la procédure SFFD décrite jusqu'à présent peut être appliqué pour chaque projection séparément.

Dans les chapitres suivants Sindbad-SFFD est validé par des simulations et des expériences dans une mode radiographique. Cela donne la possibilité de découpler la validation des différentes parties composant l'outil développé. Chapitre 2.2 (validation croisée) ne considérera pas la modélisation du détecteur, mettant ainsi l'accent sur les interactions de particules et la géométrie. Ensuite, Chapitre 2.3 (validation expérimentale) intégrera la modélisation du détecteur, évaluant ainsi la chaîne de simulation complète.

2.2. Validation croisée

Afin d'examiner la précision du logiciel développé en termes de performances de simulation de diffusion de rayons X (approche SFFD), une comparaison avec les acquisitions fournies par un autre simulateur (GATE [73]) a été réalisée. Les simulations GATE peuvent être considérées comme des simulations MC analogiques comme aucune technique

supplémentaire de réduction de la variance n'a été appliquée. La validation de la génération des images du rayonnement primaire n'a pas été considérée comme elle est entièrement basée sur la version précédente du logiciel (Sindbad) qui a été validée dans [47].

Un fantôme numérique du poly méthacrylate de méthyle (PMMA) a été utilisé pour valider le logiciel de simulation (Fig. 4). Le fantôme et la géométrie ont été choisis de telle sorte que la distribution spatiale du diffusé ne serait pas entièrement plat. Une raison supplémentaire était d'adapter au mieux aux équipements expérimentaux disponibles.

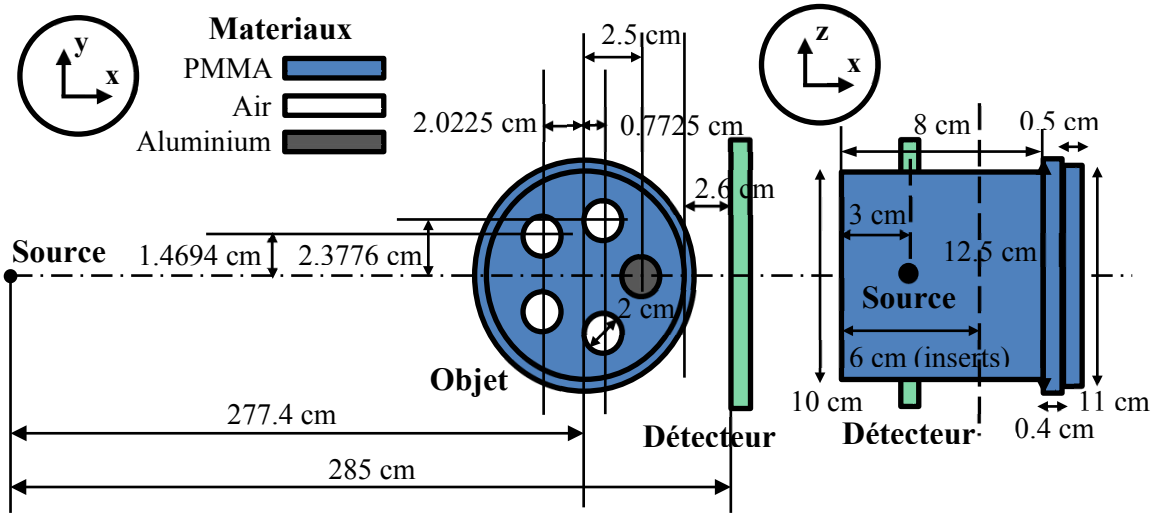

Fig. 4. Objet et géométrie utilisés dans la procédure de validation (vues y-x et z-x)

Des représentations en géométrie de construction de solides (CSG) et voxels ont été créés pour les simulations Sindbad-SFFD et GATE, respectivement. Les paramètres de tube ont été fixés à 110 kV, 1 mAs et 10.4 ° émission conique avec 2 mm de filtration d'aluminium, respectivement. La modélisation du spectre de tube à rayons X était basé sur le modèle semi-empirique proposée par Birch et Marshall [74]. Un détecteur parfait (DRM identité, canaux de 1 keV) de 16 × 201 pixels (pas de pixel de 0.8 mm) a été modélisée. Le choix d'un tel détecteur a été motivée par le prototype disponible dans le laboratoire, ainsi que par la structure de l'objet (relativement homogène dans la direction y). Les simulations GATE ont été mises en place avec 3.17×10^{11} photons initiaux. Pour Sindbad-SFFD, 10^7 photons initiaux et une grille de nœud régulière (4×50) suivi par une interpolation spline cubique entre les points nodaux ont été appliqués. En outre, pour les deux simulateurs, une boîte d'air de 6 m^3 centrée sur l'objet a été ajoutée pour simuler l'environnement. Le code de Sindbad-SFFD a été exécuté sur un CPU de 2.83 GHz, tandis que GATE a été exécuté sur un cluster avec 2,6 GHz en moyenne par noyau. Le temps utilisé pour les simulations avec le logiciel développé était ≈1.5 h par rapport au ≈2417 h (par CPU) pour GATE.

Tout d'abord, une image d'atténuation a été calculée à partir de l'image du primaire résolu en énergie (Figure 4.6). Cette image aidera à relier les structures d'objet (par exemple des cavités et insert en aluminium) avec les images du diffusé.

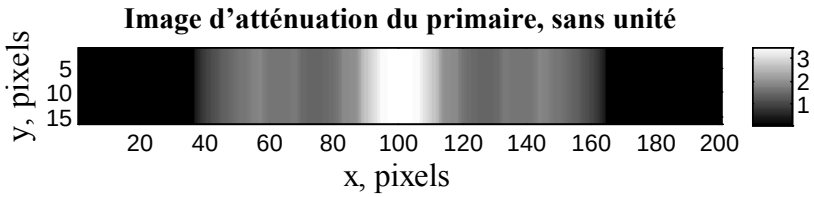

Fig. 5. Image d'atténuation du primaire obtenue avec Sindbad-SFFD.

On voit clairement les cavités des ainsi que l'insert d'aluminium sur Fig. 5. De plus, l'image indique que l'objet occupe l'intervalle de pixels #38–#162 dans la direction *x*.

Afin de comparer l'outil développé en terme de précision de la distribution spatiale du diffusé, des images du diffusé en énergie incidente totale ont été générées (Fig. 6). De plus, dans le cas de Sindbad-SFFD, une moyenne de 10 réalisations avec l'écart-type (STD) correspondant ont été utilisés pour évaluer la dépendance sur l'initialisation du MC.

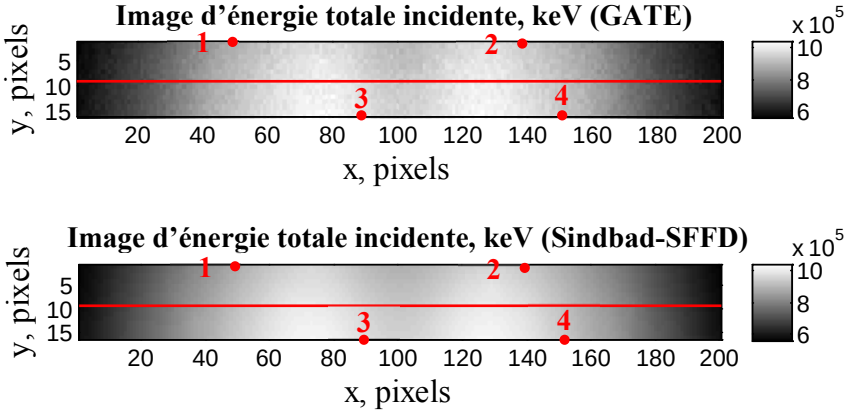

Fig. 6. Images du diffuse en énergie incidente totale obtenues avec GATE et Sinbad-SFFD. Les lieus de profiles et spectres utilisés pour les visualisations de Fig. 7 et Fig. 8, respectivement, sont marqués rouge sur les images.

En plus des images en énergie incidente totale présentées dans la Fig. 6 profils horizontaux centraux ont également été tracés (Fig. 7).

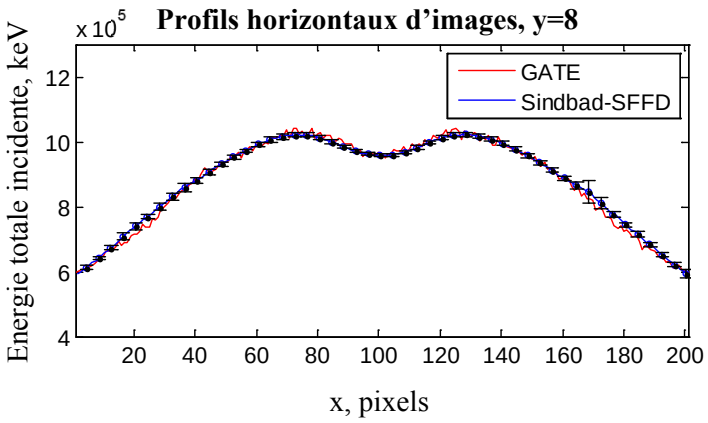

Fig. 7. Profils horizontaux centraux des images de GATE et Sindbad-SFFD affichées dans Fig. 6. Des marqueurs avec des barres d'erreur (STD) correspondent aux points de la grille SFFD. STDs pour GATE ne sont pas présents car ils ne seraient pas visibles à cette échelle.

Les résultats présentés dans la Fig. 6 montrent des images du diffusé compatibles avec la géométrie d'objet. Notez les maxima dans le profil dans les parties où des cavités d'air sont présentes. De plus, le minimum au centre du profilé (Fig. 7) est dû à l'augmentation de l'atténuation dans cette région (forte épaisseur du PMMA et un insert en aluminium). Globalement, les images et les profils de diffusé, obtenus à partir de deux simulateurs différents, représentent un niveau élevé d'accord. Simulations avec GATE sont, comme prévu, plus bruyant par rapport à Sindbad-SFFD. Cela est dû à la nature partiellement analytique de l'approche SFFD. De plus, les faibles STD, qu'on peut observer sur le profil horizontal tracé, montrent que le nombre de photons choisi est suffisant pour fournir une simulation stable par rapport à l'initialisation de MC. Enfin, il peut aussi être vu du profil qu'il existe des zones où le STD est plus élevé que dans d'autres lieus de profil (autour de pixel #160). Ceci indique que dans une ou plusieurs réalisations fournies par Sindbad-SFFD un pic était présent.

L'accord entre Sindbad-SFFD et GATE est confirmée dans le domaine de l'énergie grâce à l'observation des spectres du diffusé incident dans la Fig. 8. Les différences entre les spectres sont principalement dues à la présence de bruit photonique présent dans les simulations GATE. Notez que les spectres #1 et #2 de Sindbad-SFFD montre une augmentation de STD dans l'intervalle de 40–50 keV – une indication de la présence d'artéfacts pics dans une des réalisations.

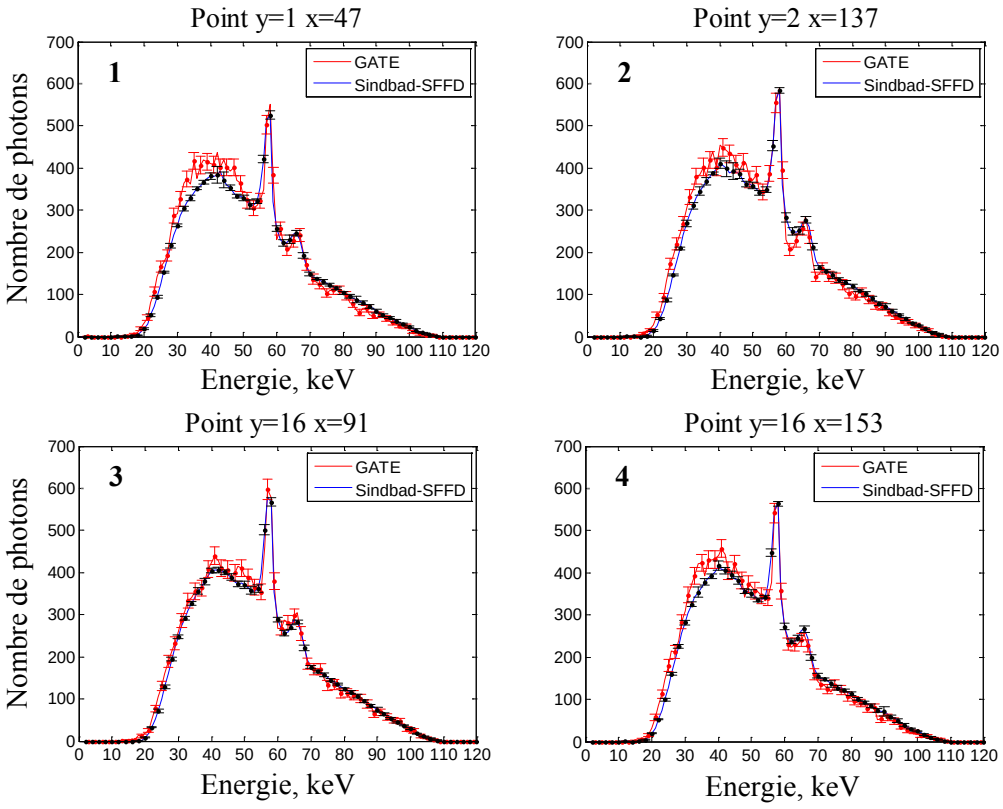

Fig. 8. Spectres du diffusé incident sur plusieurs pixels de contrôle (Fig. 6). Les courbes fournies par l'outil développé et GATE sont marqués en bleu et rouge, respectivement. Les spectres sont échantillonnés à des intervalles réguliers de 1 keV. STDs sont également ajoutés à la fois pour les spectres de Sindbad-SFFD et les spectres de GATE.

Afin de quantifier les différences entre les images d'énergie totale incidente, une métrique dite « normalized root-mean-square error » (NRMSE) a été utilisée :

$$NRMSE_I = \frac{1}{\overline{I_{GATE}(\mathbf{p})}} \sqrt{\frac{\sum_{\mathbf{p}} [I_{GATE}(\mathbf{p}) - I_{SFFD}(\mathbf{p})]^2}{n_p}}, \quad (4)$$

Où I_{GATE} et I_{SFFD} sont des images d'énergie totale incidente générées par GATE et SFFD, respectivement.

Pour les spectres générés, une métrique similaire a été appliquée sur l'intervalle d'énergie de 22–100 keV. Cela élimine la contribution des canaux avec un bas nombre de photons :

$$NRMSE_S = \frac{1}{\overline{\mathbf{N_{GATE}}(\mathbf{p})}} \sqrt{\frac{\sum_{E} [\mathbf{N_{GATE}}(\mathbf{p}) - \mathbf{N_{SFFD}}(\mathbf{p})]^2}{n_E}}. \quad (5)$$

Dans (5) $\mathbf{N_{GATE}(p)}$ et $\mathbf{N_{SFFD}(p)}$ sont les spectres du diffusé (le sous-indice *S* a été omis pour simplifier la notation) générés par GATE et SFFD, respectivement, et est le nombre de canaux du détecteur.

Le $NRMSE_I$, lorsqu'on compare l'outil conçu avec GATE, était de 1,5%. Il est également plus représentatif de la performance SFFD spatiale globale en termes des images d'énergie totale du diffusé. Pour quantifier la performance spectrale de l'outil, $NRMSE_S$ a été calculé en donnant les résultats suivants pour les quatre spectres présentés à la Fig. 8 : 6.2% – spectre #1, 5.5% – spectre #2, 3.7% – spectre #3, 5.1% – spectre #4. Comme indiqué précédemment, ces différences sont principalement dues à l'absence de bruit dans les simulations Sindbad-SFFD. Ceci est confirmé par le calcul de la STD relative moyenne pour les données GATE, ce qui donne environ 7% pour chaque spectre.

Les pics locaux responsables de l'augmentation des STDs dans les simulations fournies par l'outil développé sont dus à des événements parcimonieux de la diffusion de Rayleigh du premier ordre avec une forte probabilité de diffusion [75]. Si le nombre de photons augmente, les événements deviendront moins rares et l'artefact aura tendance à disparaître. Cependant, une telle tactique va conduire à une augmentation proportionnelle du temps de calcul. A noter, de plus, que l'augmentation de la distance réduira également ces pics comme le nombre de d'événements du premier ordre atteignant le plan de détection est plus faible en raison de l'angle solide réduit. La dernière option ne convient pas pour des simulations radiographiques comme l'objet est souvent situé à proximité du détecteur. Il y a plusieurs solutions que peuvent être appliquées pour remédier cet artefact sans aucune dépendance géométrique. Tout d'abord, le modèle décrit par (2) peut être élargie pour inclure une pondération basée sur la probabilité de type interaction (Rayleigh ou Compton). Une telle opération donnerait moins de poids aux événements isolés Rayleigh responsables de l'artefact. Cependant, le temps de calcul sera également doublé, comme le calcul de la fraction de particules serait maintenant fait par type d'événement. La deuxième solution consiste à subdiviser le nombre total de photons lancés dans les ensembles à différentes initialisations MC avec une application ultérieure d'une moyenne-médiane. Ce dernier pourrait, malheureusement, biaiser le résultat.

2.3. Validation expérimentale

Une étude plus approfondie de l'outil développé a été effectuée par comparaison avec les acquisitions expérimentales. L'accent restait encore sur la partie simulation du diffusé.

La géométrie et le fantôme considérés ont été les mêmes que celles utilisées pour la validation croisée (Fig. 4). Une image du banc d'essai expérimental correspondant est présentée à la Fig. 9. Paramètres de tube ont également été maintenus sans changement. Les expériences utilisaient un tube à rayons X YXLON Y.TU 160-D02 et un détecteur linéaire CdTe spectrométrique (16×1 pixels, canaux de 1.2 keV) avec un pas de 0.8 mm et une épaisseur de 3 mm qui était translaté horizontalement pour acquérir des images équivalents à un détecteur de 16×201 pixels. Un seuil de 21 keV a été appliqué pour réduire le bruit dans les spectres de sortie. Une correction de gain a également été appliquée. Une grille BS 11 × 11 composé de petits éléments de plomb a été utilisé pour bloquer le rayonnement primaire dans certaines zones. Donc, ces zones enregistraient seulement des signaux de diffusé. L'espacement entre les centres d'éléments était de 10 mm et l'épaisseur maximale de chaque était d'environ 7 mm. La grille a été insérée à une distance de 218 cm de la source en face de l'objet inspecté. Une moyenne de 10 acquisitions a été utilisée pour réduire le bruit de photons.

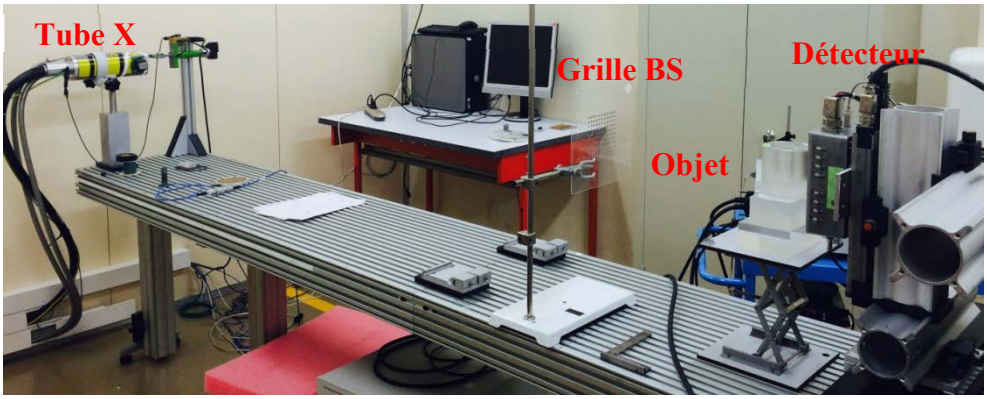

Fig. 9. Banc de test correspondant à la géométrie présentée dans Fig. 4.

Afin de créer une simulation réaliste avec Sindbad-SFFD, un DRM caractérisant le détecteur expérimental a été appliqué. En outre, les spectres ont été convolués avec une gaussienne pour tenir compte du bruit électronique. Basé sur des études précédentes, un sigma de 3.7 keV était choisi [47]. D'autres effets, tels que la diffusion et les empilements n'ont pas été considérés comme l'expérience a été optimisée pour les rendre négligeables. Pour tenir compte de l'environnement dans l'expérience, la boîte d'air considérée dans la partie validation croisée a été laissée en place.

Tout d'abord, une image sans objet présent a été expérimentalement acquise pour vérifier si la forme et le niveau du spectre de sortie du tube ont été correctement modélisés par l'outil de simulation développé (Fig. 10).

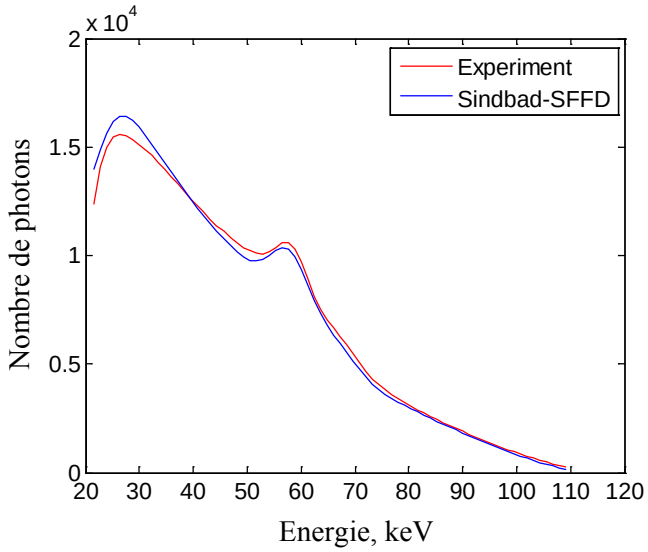

Fig. 10. Spectres du plein flux expérimental et simulé échantillonné aux intervalles réguliers de 1.2 keV.

Les deux spectres présentés à la Fig. 10 semblent assez similaires, à l'exception de la région de faible énergie où le spectre expérimental a une légère déformation. L'accord a été considéré comme suffisant pour effectuer la mesure et comparaison du diffusé.

Ensuite, une acquisition expérimentale de l'objet avec la grille BS a été réalisée et convertie en une image d'atténuation. Le résultat est affiché dans la Fig. 11. Notez le segment 2×11 de la grille visible sur l'image. Les cavités d'air et l'insert en aluminium sont également clairement visibles.

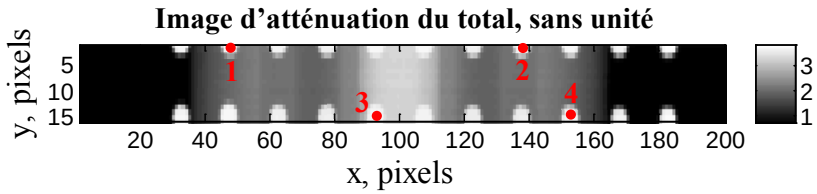

Fig. 11. Image expérimentale d'atténuation du total du fantôme examiné avec l'addition de la grille BS. Les pixels d'image utilisés pour la visualisation des spectres dans Fig. 14 sont marqués rouge.

Afin d'isoler des points concernés par la modification BS, une acquisition avec seulement la grille en place a été produite et des points avec une atténuation maximale par projection d'élément BS ont été déterminées par seuillage.

Après avoir obtenue une mesure parcimonieuse du diffusé, une interpolation spline cubique a été appliquée pour acquérir une image du diffusé complète présentée à la Fig. 12, qui a été comparée à une image équivalente produite par Sindbad-SFFD. En outre, deux profils horizontaux correspondants contenant les mesures initial parcimonieuse du diffusé ont été tracées (Fig. 13). Enfin, les images et les profils ont été limités à un intervalle de 45–155 pixels dans la direction *x* afin de ne pas considérer les pixels influencés par l'environnement (table, grille, objet et support de détecteur, etc.).

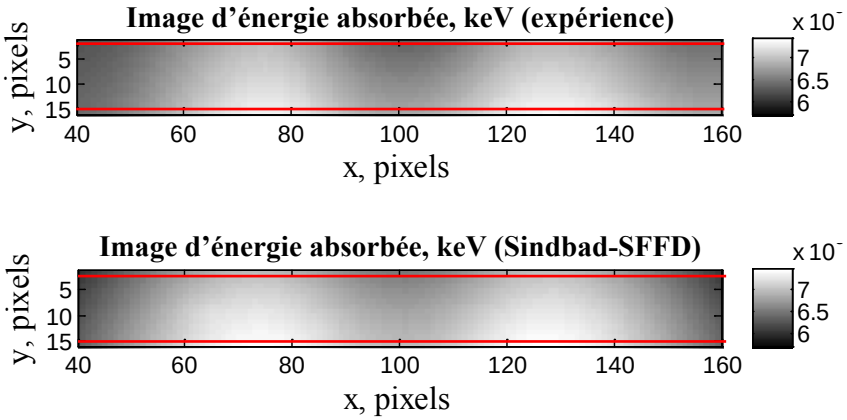

Fig. 12. Images d'énergie absorbée du diffusé : expérience et Sindbad-SFFD. Les lieus utilisés pour les visualisations des profils dans fig. sont marqués rouge sur les deux images.

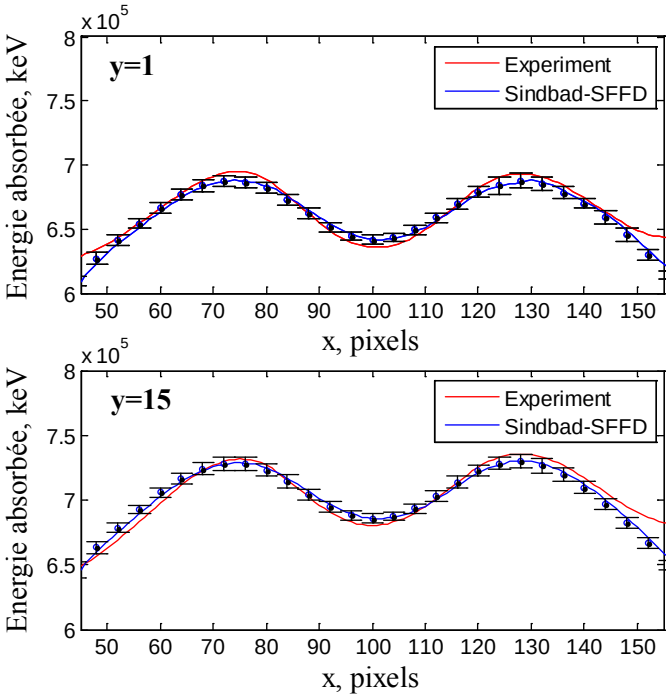

Fig. 13. Profils horizontaux des positions indiquées dans Fig. 12. Des marqueurs avec des barres d'erreur (STD) correspondent aux points de la grille SFFD.

Bien que l'analyse de la Fig. 12 montre un degré globalement élevé de similarité entre les résultats expérimentaux et simulés, il y a certaines différences qui apparaissent. Tout d'abord, en observant les profils horizontaux (Fig. 13), il est clairement visible que le niveau expérimental du diffusé est plus élevé à partir de pixel # 145 pour les deux profils. La même chose peut être vu pour le y=1 profil pour les pixels avant pixel #50. Ces différences peuvent être expliquées par l'influence du diffusé ambiant provenant de l'environnement qui est encore près des bords de la projection de l'objet. En outre, l'asymétrie dans les écarts entre les courbes expérimentales et simulées peut être expliquée par le fait que l'environnement vu par le plan du détecteur est également asymétrique. Une analyse plus détaillée des profils d'image montre que la courbe expérimentale présente une légère asy-

métrie entre les maxima. Cela pourrait être dû à une erreur dans l'alignement géométrique de l'objet par rapport au plan du détecteur. Enfin, les différences de composition d'aluminium peuvent être la cause de la dissemblance des minima centraux dans les profils expérimentaux et simulés.

En outre, la comparaison des simulations Sindbad-SFFD avec les données expérimentalement obtenues considérait des spectres du diffusé mesurés dans plusieurs points de contrôle contenus dans les projections des éléments de BS (Fig. 14).

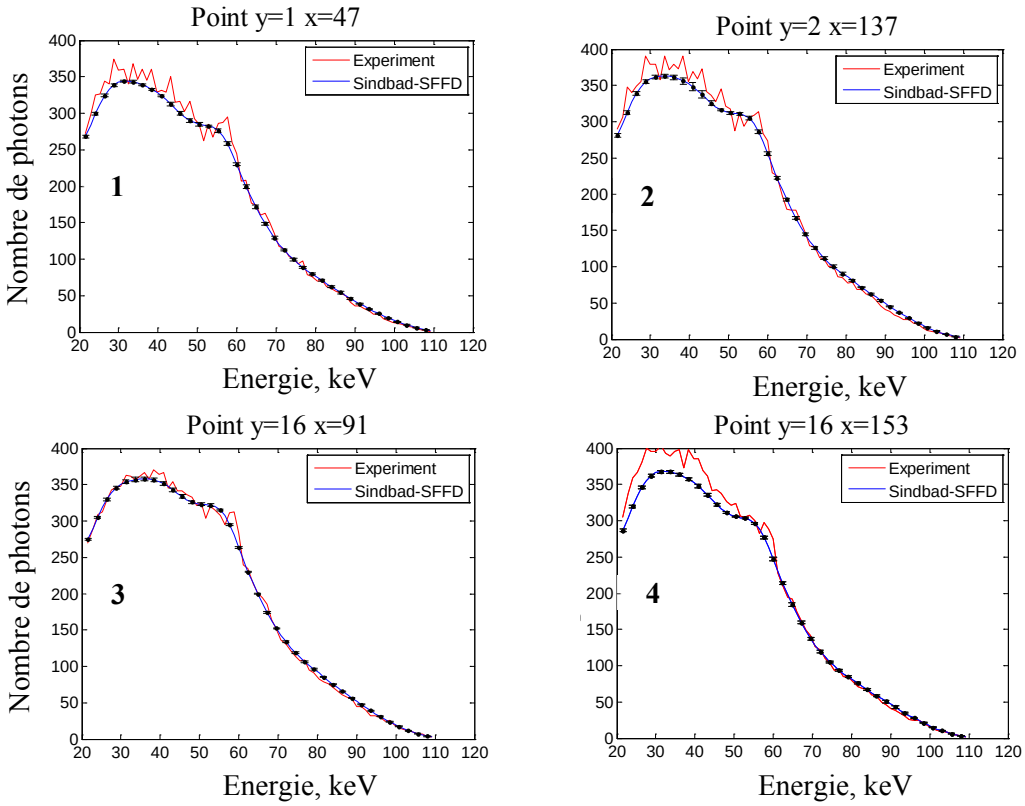

Fig. 14. Spectres du diffusé incident sur plusieurs pixels de contrôle (Fig. 11). Les courbes fournies par l'outil développé et expériences sont marqués en bleu et rouge, respectivement.

Une évaluation quantitative des résultats présentés dans Fig. 12 et Fig. 14 a été effectuée en utilisant les métriques fournis par (4) et (5) où les quantités indexées GATE sont remplacées par les quantités expérimentales correspondantes.

Le $NRMSE_I$ calculé pour les images présentées à la Fig. 12 était égale à 1.8%, ce qui confirme l'accord global entre les expériences et l'outil développé en termes de distribution spatiale du diffusé. En termes d'aspect spectral du diffusé, pour les quatre spectres présentés à Fig. 14, le $NRMSE_S$ était de 6.4% (#1), 6.5% (#2), 3.6% (#3), 8.4% (#4), respectivement. Comme prévu, le spectre #4 présente la plus grande erreur en raison de la différence de niveau de photons de basse énergie pour ce point. Autres spectres représentent également des différences quantitatives comparables avec celles qui ont été observées dans Fig. 14.

2.4. Conclusion et perspectives

En générale, les simulations Sindbad-SFFD étaient compatibles avec celles fournies par GATE avec une erreur de 1.5% observée pour les images d'énergie incidente totale et une erreur maximale de l'ordre de 6% pour les spectres des points de contrôle. De telles différences peuvent être liées au bruit photonique (présent dans les simulations GATE) des moteurs MC différents, représentations de fantôme (voxels vs CSG). Il est également intéressant de noter que, tout en étant relativement proche de simulations GATE, l'outil développé nécessite beaucoup moins de temps de calcul.

On observe en outre un accord entre les simulations obtenues à partir de l'outil développé et des expériences avec une différence dans les images d'énergie absorbée de 1.8% et une différence maximale des spectres étudiés de l'ordre de 8.5%. Le diffusé ambiant, des inexactitudes de positionnement géométrique et le bruit de photons ont été identifiés comme les causes les plus probables de dissemblance. Dans l'ensemble, la performance résultant de l'outil de simulation présenté confirme son potentiel de devenir un instrument important les études d'estimation et de correction du rayonnement diffusé en imagerie à rayons X multi-énergies.

Les travaux futurs seront consacrés à éliminer l'artefact de diffusion de Rayleigh. De plus, une sélection automatique des nœuds de grille et photons initiaux seront également étudiés. Pour les simulations TDM, sous-échantillonnage angulaire de la distribution respective du diffusé suivi par une interpolation seront également exploités, comme il a été montré que le diffusé varie lentement avec l'angle de projection [57]. Enfin, d'autres techniques de réduction de la variance et parallélisation sur GPU peuvent également être explorées.

3. Méthode de correction du diffusé spectral

Dans le Chapitre 1 il a été mentionné que les techniques actuelles de correction du diffusé ne sont pas adapté à l'imagerie multi-énergies. Dans ce chapitre une méthode de correction du diffusé dite « Partial Attenuation Spectral Scatter Separation Approach » (PASSSA) est introduite (Chapitre 3.1). Cette technique exploite l'information énergétique fournie par les détecteurs spectrométriques.

PASSSA est ensuite validé (Chapitre 3.2) en simulation et expérimentalement (Chapitre 3.3). De plus, une discussion de ces résultats est présente dans Chapitre 3.3.

3.1. Concept

Auparavant, dans le Chapitre 2.1, il a été mentionné que sous hypothèse d'un modèle linéaire de détecteur résolu d'énergie (absence ou quantité limitée d'empilements), il peut être considéré que chaque pixel de détecteur mesure une somme de composantes primaire et diffusé, ce qui conduit à (1). Donc, pour chaque pixel, on a une équation à deux inconnues: le rayonnement primaire et le rayonnement diffusé. Étant donné un estimateur $\tilde{\mathbf{N}}_{\mathbf{S}}(\mathbf{p})$ du rayonnement diffusé, un estimateur du rayonnement primaire $\tilde{\mathbf{N}}_{\mathbf{P}}(\mathbf{p})$ peut être trouvé via une soustraction du rayonnement total mesuré par le pixel:

$$\widetilde{\mathbf{N}}_{\mathbf{P}}(\mathbf{p}) = \mathbf{N}_{\mathbf{T}}(\mathbf{p}) - \widetilde{\mathbf{N}}_{\mathbf{S}}(\mathbf{p}), \quad \forall \mathbf{p} \in \boldsymbol{\Omega}. \tag{6}$$

Afin de corriger le rayonnement diffusé par (6), une approche pour obtenir $\tilde{\mathbf{N}}_S(\mathbf{p})$ pour l'ensemble de l'image spectrale est nécessaire.

Considérons maintenant une acquisition radiographique modifiée par l'insertion d'un masque des éléments atténuants (*atténuateurs*) entre l'objet et la source (Fig. 15).

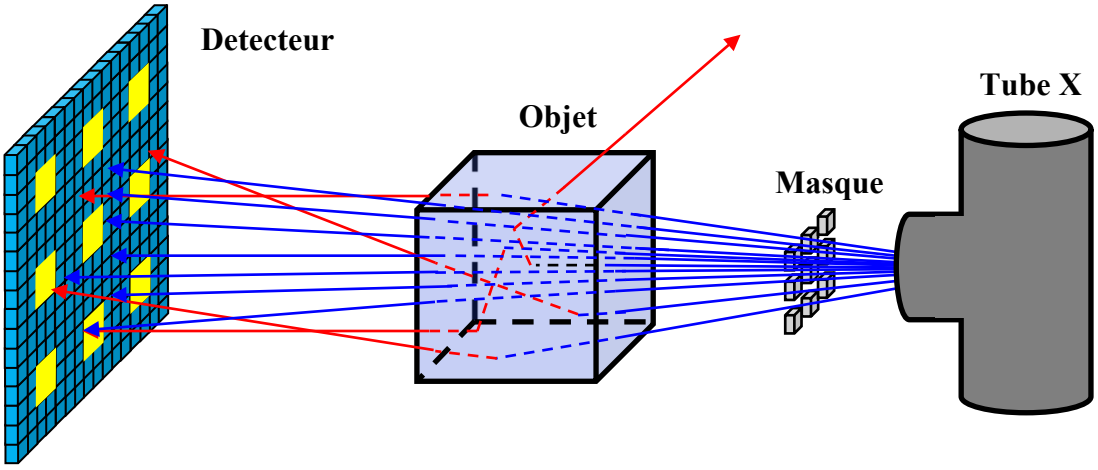

Fig. 15. Schéma d'une acquisition radiographique modifiée par un masque d'atténuateurs. Le rayonnement primaire et le rayonnement diffusé sont marqués bleu et rouge, respectivement. Les zones du détecteur influencées par l'insertion du masque sont marque jaune sur le détecteur.

L'insertion du masque produit des zones (ombres) sur le détecteur avec une quantité d'atténuation supplémentaire due au masque. La forme de ces ombres correspond au motif spatial magnifié du masque d'atténuateurs. De ce point, deux acquisitions de l'objet inspecté sont considérés (avec et sans le masque). Soient le total, primaire et diffusé de l'acquisition contenant le masque d'atténuateurs indiqués avec un exposant *m*.

D'abord, on peut écrire des expressions explicites pour le component primaire dans un pixel $\mathbf{p'}$ donné d'une sous-région $\mathbf{U} \subset \mathbf{\Omega}$ correspondant aux ombres des atténuateurs dans les deux acquisitions :

$$\mathbf{N_P}(\mathbf{p'}) = \mathbf{D} \times \left[\mathbf{N_0}(\mathbf{p'}) \circ \exp\left(-\sum_{q=1}^{Q} \boldsymbol{\mu}_\mathbf{q}(\mathbf{p'}) l_q(\mathbf{p'}) \right) \right], \quad \forall \mathbf{p'} \in \mathbf{U} \tag{7}$$

et

$$\mathbf{N_P^m}(\mathbf{p'}) = \mathbf{D} \times \left[\mathbf{N_0}(\mathbf{p'}) \circ \exp\left(-\boldsymbol{\mu}_\mathbf{a}(\mathbf{p'}) l_a(\mathbf{p'}) - \sum_{q=1}^{Q} \boldsymbol{\mu}_\mathbf{q}(\mathbf{p'}) l_q(\mathbf{p'}) \right) \right], \quad \forall \mathbf{p'} \in \mathbf{U}\,. \tag{8}$$

Dans (7) et (8) $\mathbf{N_0(p)}$ est le spectre du plein flux. De plus, les quantités $\boldsymbol{\mu}_\mathbf{a}(\mathbf{p'})$ et $l_a(\mathbf{p'})$ de (8) correspondent au coefficient d'atténuation et l'épaisseur du matériau d'atténuateur sur le chemin de la source au pixel concerné.

Après, si pour chaque pixel d'ombre d'atténuateurs on soustrait le signal total associé à l'acquisition modifié $\mathbf{N_T^m(p')}$ de son équivalent non-modifié $\mathbf{N_T(p')}$, la différence des signaux suivante $\mathbf{\Delta N(p')}$ peut être obtenue :

$$\mathbf{\Delta N}(\mathbf{p'}) = \mathbf{N_T}(\mathbf{p'}) - \mathbf{N_T^m}(\mathbf{p'}) = \mathbf{N_P}(\mathbf{p'}) - \mathbf{N_P^m}(\mathbf{p'}) + \mathbf{\Delta N_S}(\mathbf{p'}), \quad \forall \mathbf{p'} \in \mathbf{U}\,, \tag{9}$$

où $\mathbf{\Delta N_S(p')}$ est la différence des components diffusé de deux acquisitions pour le pixel $\mathbf{p'}$ considéré.

Sous la condition d'une faible atténuation (0.05–0.2 en moyenne par énergie) et un bas facteur de remplissage du champ d'irradiation (0.05–0.25) pour les éléments du masque, les components diffusé de deux acquisitions peuvent être considéré comme approximativement égaux (autrement dit $\mathbf{N_S(p')}\approx\mathbf{N_S^m(p')}$) et $\mathbf{\Delta N_S(p')}$ peut être considéré comme négligeable dans (9). Cela se justifie par le rayonnement diffusé étant un phénomène global, dont le montant est proportionnel à la quantité totale de rayonnement incident sur l'objet. Donc, le changement local du diffusé induit par un changement relativement faible du rayonnement incident peut être considéré comme négligeable. En utilisant des versions plus développées de $\mathbf{N_P(p')}$ et $\mathbf{N_P^m(p')}$ de (7) et (8), respectivement, et en négligeant $\mathbf{\Delta N_S(p')}$, une forme plus explicite de (9) peut être obtenue :

$$\mathbf{\Delta N(p')} = \mathbf{D}\times\mathbf{W}\times\left[\mathbf{N_0(p')}\circ\exp\left(-\sum_{q=1}^{Q}\boldsymbol{\mu}_\mathbf{q}(\mathbf{p'})l_q(\mathbf{p'})\right)\right],\quad \forall\mathbf{p'}\in\mathbf{U}. \tag{10}$$

La quantité **W** de (10) est une matrice diagonale. La diagonal est une fonction du matériau et d'épaisseur d'atténuateur :

$$\mathbf{W} = diag\left(1-\exp\left[-\boldsymbol{\mu}_\mathbf{a}(\mathbf{p'})l_a(\mathbf{p'})\right]\right). \tag{11}$$

Prenant compte du (7), on peut dériver une expression du rayonnement primaire de (10) :

$$\begin{aligned}\mathbf{N_P(p')} &= \mathbf{D}\times\mathbf{W}^{-1}\times\mathbf{D}^{-1}\times\left(\mathbf{D}\times\mathbf{W}\times\left[\mathbf{N_0(p')}\circ\exp\left(-\sum_{q=1}^{Q}\boldsymbol{\mu}_\mathbf{q}(\mathbf{p'})l_q(\mathbf{p'})\right)\right]\right)= \\ &= \mathbf{M}\times\mathbf{\Delta N(p')},\quad \forall\mathbf{p'}\in\mathbf{U}.\end{aligned} \tag{12}$$

La quantité $\mathbf{M}=\mathbf{D}\times\mathbf{W^{-1}}\times\mathbf{D}$ dans (12) est *la matrice de passage* qui permets de récupérer le primaire $\mathbf{N_P(p')}$ (pas d'atténuateur) de $\mathbf{\Delta N(p')}$. La matrice M correspond à un changement d'espace pour $\mathbf{W^{-1}}$. Malheureusement, à cause de l'instabilité de **D** (nombre de conditionnement d'environ 10^5), son inverse est aussi instable, ce qui amène à une version instable de M (nombre de conditionnement d'environ 10^4). Afin de s'affranchir de cette difficulté, une forme paramétrique de **M** peut être utilisée (nombre de conditionnement d'environ 10). En ce cas un modèle dit gaussienne-exponentielle peut être appliqué pour chaque ligne de **M** (qui correspond à un canal du détecteur). Pour établir les paramètres libres de ce modèle une base de calibrage est utilisée en combinaison avec une approche de minimisation.

La récupération du primaire $\mathbf{N_P(p')}$ à travers la différence des totaux pour chaque point d'ombre d'atténuateur permet d'obtenir le component diffusé $\mathbf{N_S(p')}$ pour chacun de ces points avec l'aide de (1) et (12) :

$$\mathbf{N_S(p')} = \mathbf{N_T(p')} - \mathbf{N_P(p')} = \mathbf{N_T(p')} - \mathbf{M}\times\mathbf{\Delta N(p')},\quad \forall\mathbf{p'}\in\mathbf{U}. \tag{13}$$

Finalement, dès que le $\mathbf{N_S(p')}$ est obtenu pour tous les pixels de **U**, une estimation spatiale est appliquée pour récupérer le rayonnement diffuse pour l'ensemble de l'image $\mathbf{\Omega}$:

$$\widetilde{\mathbf{N}}_\mathbf{S}(\mathbf{p}) = T\left\{\mathbf{N_S(p')}\right\},\quad \forall\mathbf{p'}\in\mathbf{U},\quad \forall\mathbf{p}\in\mathbf{\Omega}. \tag{14}$$

Où est l'opération d'estimation respective. Avec l'aide du rayonnement diffusé estimé $\mathbf{\tilde{N}_S(p)}$ une estimation du rayonnement primaire peut être obtenue en appliquant (6) à chaque pixel d'image. Il est à noter que dans ce cas l'acquisition considérée est celle qui est sans masque d'atténuateur.

Afin de fournir une démonstration de différentes étapes comprenant PASSSA, un schéma représentant des images intermédiaires à partir d'un canal unique de l'énergie (50 keV) est présenté à la Fig. 16. D'abord, une image de différence est obtenue en soustrayant l'acquisition modifiée (avec atténuateurs) celle qui est non-modifiée. Il est à noter que l'image qui en résulte reflète le motif d'atténuateur, qui est parcimonieux. Ensuite, la

matrice de passage est appliquée au signal de différence de chaque pixel d'ombre d'atténuateurs afin de récupérer une image primaire non-modifiée parcimonieuse, qui est ensuite soustraite de l'image totale non-modifiée qui donne une image du diffusé parcimonieuse. Enfin, l'estimation spatiale est appliquée afin d'obtenir une distribution du diffusé complète. Ceci termine la phase d'estimation du diffusé. La correction diffusé est obtenue par la phase de séparation, qui est une soustraction pure de l'image du diffusé estimée complète de l'image totale non-modifiée. En résultat, une estimation de l'image primaire non-modifiée est récupéré.

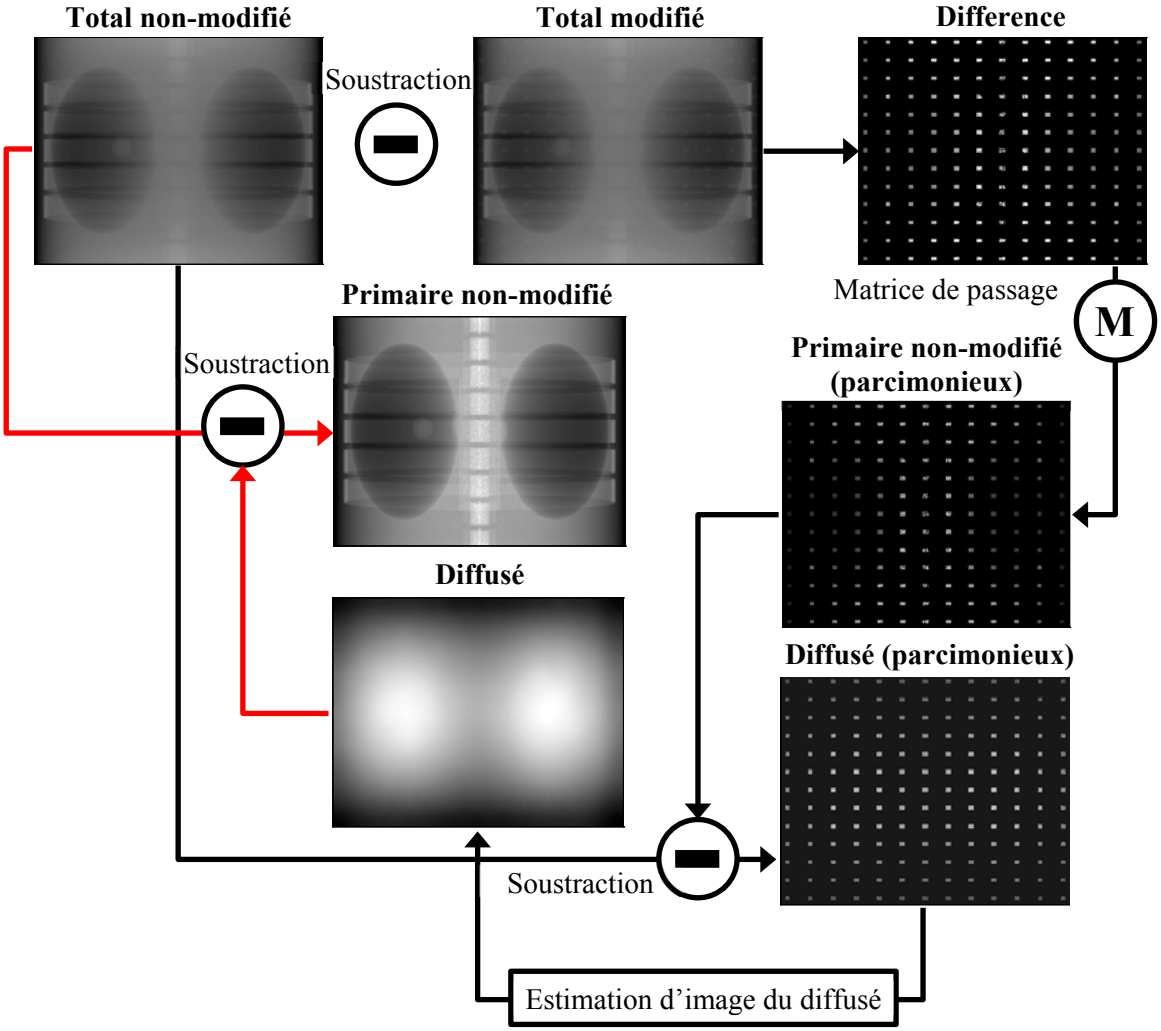

Fig. 16. Schéma illustrant des phases différentes de PASSSA pour une projection radiographique. La procédure est devisée en estimation (flèches noires) et séparation du diffusé (flèches rouge). Les images sont prises d'un canal unique (50 keV). Les images du diffusé sont en nombre de photons et les images du total et du primaire sont des images d'atténuation (sans unité).

Comme les données TDM sont des collections des projections radiographiques prises aux angles différents, on peut appliquer PASSSA par chaque vue est ensuite utiliser un algorithme de reconstruction (e.g. FDK) pour obtenir un volume d'objet à partir des données corrigées.

Enfin, malgré la présentation du concept PASSSA sur la base de deux images totales (modifiées ou non), cela ne signifie pas nécessairement que les deux acquisitions doivent

être effectuées. La version non-modifiée ne diffère de son homologue modifié que dans la région d'ombre d'atténuateurs. Donc, une certaine forme d'estimation spatiale peut être utilisée pour récupérer ce signal à partir de l'information contenue dans chaque ombre et son voisinage. Dans le contexte TDM, une estimation angulaire (potentiellement combinée avec une estimation spatiale) peut également être appliquée. Notez également que, par rapport à l'approche BS, l'information dans la région d'ombre d'atténuateurs est seulement modifiée et n'est pas perdue. Ceci peut être exploité pour estimer le signal total non-modifié dans la région respective.

3.2. Validation en simulation

Afin d'analyse l'efficacité de PASSSA, une étude en simulation a été conduite. Les simulations ont été faites avec l'aide de l'outil Sindbad-SFFD (Chapitre 2). Chapitre donne une description du système (paramètres du tube, géométrie, fantôme, etc.). En suite des résultats pour la mode radiographique (Chapitre 3.2.2) et tomographique (Chapitre 3.2.3) sont présentés.

3.2.1. Description du system

Un tube à rayons X de tungstène avec une filtration de 2 mm d'aluminium et un angle d'anode de 17° a été réglé à 110 kV et 0.2 mAs. Les paramètres de tube correspondent à ceux utilisés pour une acquisition thoracique typique [89]. En outre, un détecteur CdTe de 64×680 pixels résolu en énergie (canaux 1 keV) avec un pas de 1 mm et une épaisseur de 5 mm a été utilisé. La largeur du canal, la hauteur et l'épaisseur ressemblent à un prototypé détecteur linéaire spectrométrique rapporté dans [8]. Le détecteur est également couplé à une collimation en plomb. La réponse du détecteur a été modélisée avec l'aide d'une DRM correspondante à un détecteur spectrométrique réaliste (pixel de 500 μm, DRM non-diagonale, partage de charge corrigé). Les effets d'empilement ne sont pas considérés. Selon [90], le modèle de Poisson est une bonne représentation du bruit de photons dans l'imagerie TDM. Ce modèle a été utilisé pour les simulations. Pour la mode TMD 360 projections ont été acquises avec et sans le masque d'atténuateurs. Le masque consistait d'une grille (3×17) d'éléments carrés d'aluminium de 1×1 mm (épaisseur de 2 mm). L'espacement entre les centres d'atténuateurs dans les directions horizontale et verticale était de 3 mm et 2.2 mm, respectivement.

Un fantôme simplifié du thorax a été placé dans une géométrie TDM typique avec une distance source-détecteur de 100 cm et une distance source-objet de 65 cm. Cette géométrie a été utilisée pour les deux modes de simulation. L'axe de rotation a été aligné avec le centre de l'objet. La Fig. 17 donne une vue de la géométrie d'acquisition.

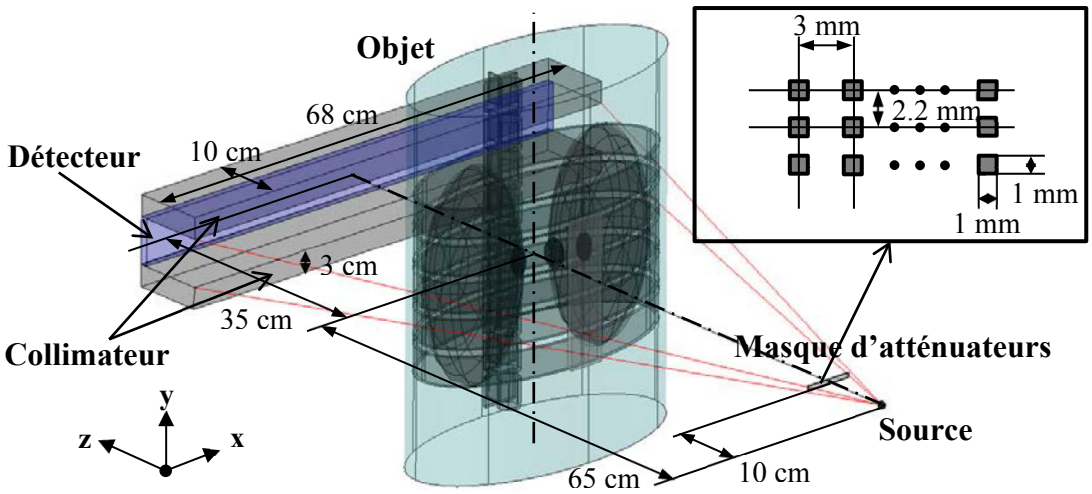

Fig. 17. Schéma illustrant la géométrie d'acquisition. Une magnification du masque d'atténuateurs est aussi montrée. L'illustration correspond à la projection #91 (ou de 90°). La colonne vertébrale, le sternum et les côtes sont modélisé avec de l'os cortical. Les poumons consistent de l'air. Les petits inserts ellipsoïdaux sont du PMMA et le corps du fantôme est de l'eau.

Afin d'estimer **M** hors des acquisitions actuelles, une base de calibrage (sans diffuse et bruit) a été générée avec l'aide de deux matériau : eau et aluminium. Pour chaque pixel d'atténuateur cela a permis d'établir des paires de $\mathbf{\Delta N}$ et $\mathbf{N_P}$ en changeant les épaisseurs d'eau et d'aluminium. La gamme d'épaisseurs considérée était 1–20 cm (pas de 1 cm) et 0.1–2 cm (pas de 0.1 cm) for water and aluminium, respectivement. En utilisant le modèle paramétrique mentionné dans le Chapitre 3.2.1 et l'algorithme de minimisation dit simplex [91], une estimation de **M** a été obtenue.

3.2.2. Radiographie

Pour une évaluation quantitative de PASSSA dans la mode radiographique, une projection unique (Fig. 17) des données TDM acquises a été utilisée. Une comparaison entre trois types d'image spectrales a été effectuée : image du total (avec diffusé), image du primaire (sans diffusé) et image du total corrigé (après avoir appliqué PASSSA). Le ratio diffusé sur primaire (SPR) était entre 14.1% et 22.2% (en moyenne 17.1%) pour des projections différentes.

D'abord, afin d'examiner la performance spatiale de l'approche de séparation du diffusé, une image d'atténuation totale a été générée en appliquant la formule suivante à chaque pixel **p** de l'image :

$$A_T(\mathbf{p}) = -\log\left[\left(\sum_{E_{\min}}^{E_{\max}} N_T(\mathbf{p},E)E\right)\left(\sum_{E_{\min}}^{E_{\max}} N_0^d(\mathbf{p},E)E\right)^{-1}\right], \quad \forall \mathbf{p} \in \mathbf{\Omega}, \tag{15}$$

où $A_T(\mathbf{p})$ est l'atténuation dans le pixel **p**, $N_T(\mathbf{p},E)$ et $N_0^d(\mathbf{p},E)$ sont les nombres de photons mesurés dans le pixel **p** et canal d'énergie E correspondant au rayonnement total et au plein flux ($\mathbf{N_0^d(p)=D\times N_0(p)}$). Avec le remplacement de $N_T(\mathbf{p},E)$ par $N_P(\mathbf{p},E)$ et $\tilde{N}_P(\mathbf{p},E)$ dans (15) les images du primaire et du total corrigé ont aussi été obtenues. Les images d'atténuation résultantes sont présentées dans Fig. 18.

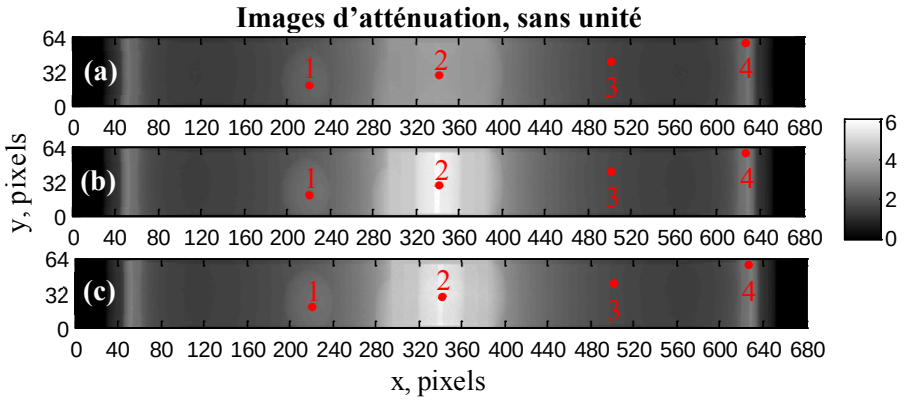

Fig. 18. Images d'atténuation du total (a), primaire (b) et total corrigé (c) obtenues à partir de leurs équivalents spectrales. La gamme d'énergie considérée était de 0–110 keV. La taille de pixel était de 1 mm. Des marqueurs rouges indiquent les pixels choisis pour la visualisation des spectres (Fig. 20). Ces lieus ont été choisis pour analyser des spectres avec un niveau différent de l'atténuation ainsi qu'un SPR variable.

De plus, pour chaque image d'atténuation, des profils horizontaux ont été tracés.

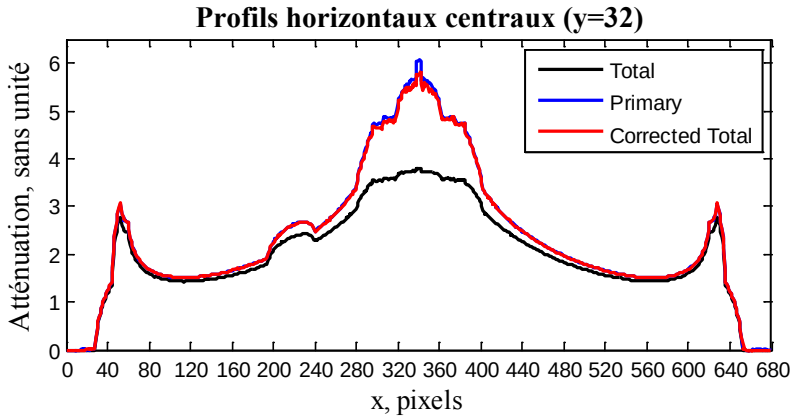

Fig. 19. Profils horizontaux centraux des images présentées à la Fig. 18. Taille de pixel était de 1 mm. Il est à noter que le profil du total similaire aux profils total corrigé et primaire sur les côtés come le SPR dans ces zones est plus faible que dans la partie centrale. Le SPR dans la partie centrale est plus élevé en raison du faible signal primaire dans cette région (haut niveau d'atténuation).

Finalement, des spectres des points de contrôle différents (indiqués dans Fig. 18) sont présentés dans Fig. 20.

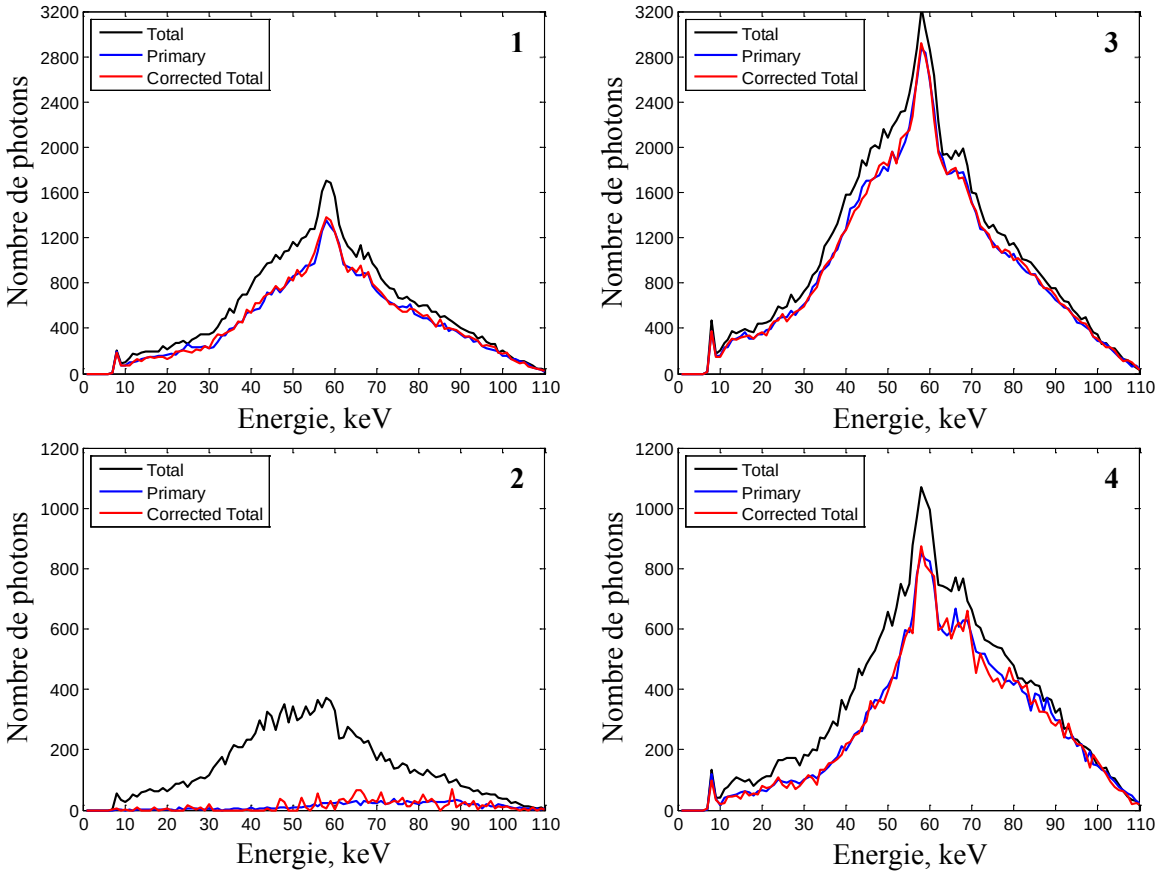

Fig. 20. Spectres du total, primaire et total corrigé pris des pixels indiqués à la Fig. 18. Les spectres du point #2 montrent une forme de spectre très différent et le niveau par rapport aux spectres #1, #2 et #3. Ceci est dû à la forte atténuation dans la région respective (niveau), ainsi que à la présence d'une quantité substantielle de la structure osseuse (forme). En outre, le SPR dans #2 est beaucoup plus élevé par rapport aux autres points, donc le signal total est dominé par le component diffusé.

Pour l'analyse quantitative de PASSSA, la NRMSE a été utilisée. La $NRMSE_T$ entre les images spectrales du total et du primaire peut être calculée dans la manière suivante :

$$NRMSE_T = \overline{N}_P^{-1}\sqrt{\left(n_p n_E\right)^{-1}\left(\sum_{\mathbf{p},E}\left[N_T(\mathbf{p},E)-N_P(\mathbf{p},E)\right]^2\right)}\times 100\%\,, \qquad (16)$$

où n_p est le nombre de pixels, n_E est le nombre de canaux d'énergie et $\overline{N}_P$ est le nombre de photon moyen sur E et $\mathbf{p}$. La $NRMSE_{PASSSA}$ pour l'image corrigée a aussi été calculée avec (16) en remplaçant $N_T(\mathbf{p},E)$ par $\tilde{N}_P(\mathbf{p},E)$. Les $NRMSE_T$ et $NRMSE_{PASSSA}$ pour la projection radiographique utilisée étaient de 18.9% et 3.9%, respectivement. Pour les différentes projections acquises pour les données TDM, la était entre 18.7% et 29.3% et 22.6% en moyenne. De façon équivalente, $NRMSE_{PASSSA}$ était entre 3.8% et 8.5% et 5.2% en moyenne pour les données tomographiques considérées.

Le niveau du bruit pour les différentes projections du total a aussi été quantifié afin de donner une idée de la performance de la méthode en fonction du bruit et des données d'entrée. Le bruit $r(\mathbf{p})$ relatif a été calculé pour chaque pixel d'une projection du total comme le ratio du STD sur le nombre total de photons :

$$r(\mathbf{p}) = \left(\sqrt{\sum_E N_T(\mathbf{p}, E)} \right) \left(\sum_E N_T(\mathbf{p}, E) \right)^{-1}, \quad (17)$$

Il est important de noter qu'une version sans bruit du $\mathbf{N_T(p)}$ est utilisée dans le calcul de (17) et seulement des pixels contenants l'information sur l'objet ont été considérés. Selon le modèle Poissonien, le STD est la racine de la moyenne qui, dans le cas actuel, est les nombres totaux de photons. Le bruit photonique relatif estimé avec (17) était entre 0.2% et 1.8% pour tous les pixels de toutes les projections et 0.6% en moyenne.

Finalement, afin de établir le lien entre l'erreur induite par le diffusé, la performance de correction et le bruit dans les données d'entrée, $NRMSE_T$, $NRMSE_{PASSSA}$, et $r(\mathbf{p})$ moyen par projection ont été calculés en fonction de numéro de projection (Fig. 21).

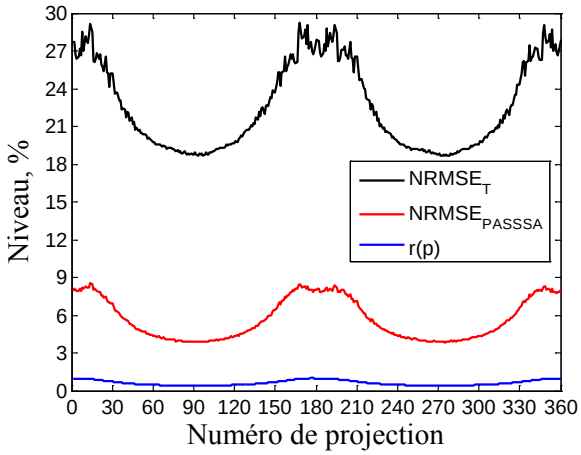

Fig. 21. $NRMSE_T$, $NRMSE_{PASSSA}$, et $r(\mathbf{p})$ moyen pour des projections différentes. Il à noter que les courbe suivent le changement du nombre de photons à travers les projections : erreur et bruit élevés et faible pour un faible (vers #0, #180 et #360) et grand (vers #90 et #270) nombre de photons, respectivement.

3.2.3. Tomographie

Afin de faire une évaluation des performances de la méthode de séparation du diffusé développée en TMD, des volumes d'objet ont été reconstruits à partir des projections radiographiques acquises à l'aide de l'approche FDK. Avant la reconstruction, les projections radiographiques résolues en énergie ont été converties en images d'atténuation en mode intégration. Figure 6.6 montre des tranches TDM centrales correspondantes aux différents types de volumes (total, primaire et total corrigé)

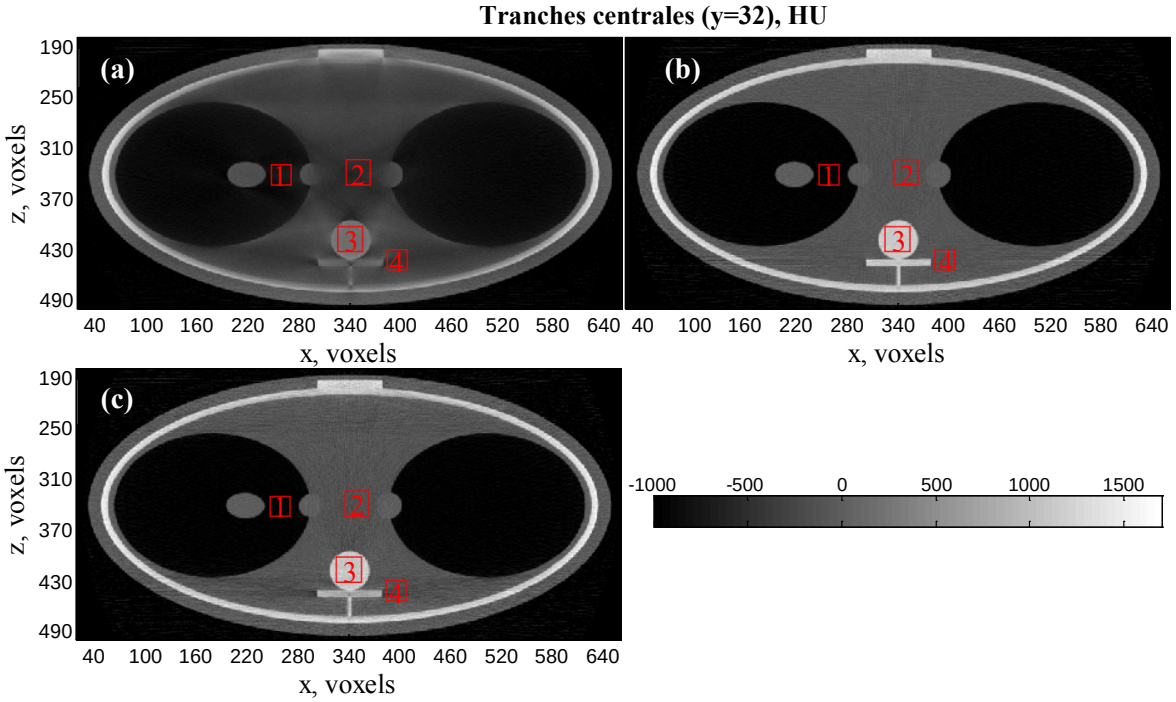

Fig. 22. Tranches TDM du total (a), du primaire (b) et du total corrigé (c). Taille de voxel était de 0.65 mm. Les carrés rouges indiquent des lieus des « volumes of interest » (VOIs) choisis pour les visualisations des courbes HU (Fig. 24). Les VOIs cible à quantifier la performance de la correction du diffusé dans des régions de tissu diffèrent : air (#1), eau (#2), os (#3). En autre, VOIs #3 et #4 ont été places afin d'analyser de façon quantitative l'artefact visible sur l'image du total corrigé.

De plus, des profils centraux horizontaux ont aussi été traces sur les images de tranche de Fig. 22.

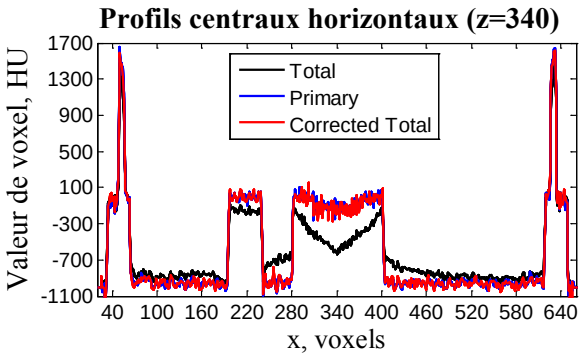

Fig. 23. Profils centraux horizontaux pris des images de tranche de Fig. 22.

Une analyse qualitative supplémentaire a été réalisée dans le domaine de l'énergie. Afin de réduire le bruit amplifié par la procédure de reconstruction, les projections radiographiques spectrales ont été regroupées en 9 canaux d'énergie également espacés (10 keV) sur l'intervalle de 20–110 keV. Ensuite, les images d'atténuation correspondant à chaque niveau d'énergie ont été calculées. Enfin, les reconstructions de volume à l'aide du FDK ont été réalisées pour chaque canal. Cela signifie qu'au lieu d'obtenir un seul volume par type (primaire, total ou total corrigé), 9 volumes ont été obtenus.

En utilisant les régions VOI de la Fig. 22, les valeurs moyennes de voxel en fonction de l'énergie (courbes HU) ont été calculées pour les volumes du total, du primaire et du total corrigé (Fig. 24). Le STD a également été calculé. Les dimensions en x-y-z étaient 25×5×25 voxels pour VOI #1 et #4. Pour VOI #2 et #3 les dimensions étaient de 30×5×30 voxels, respectivement.

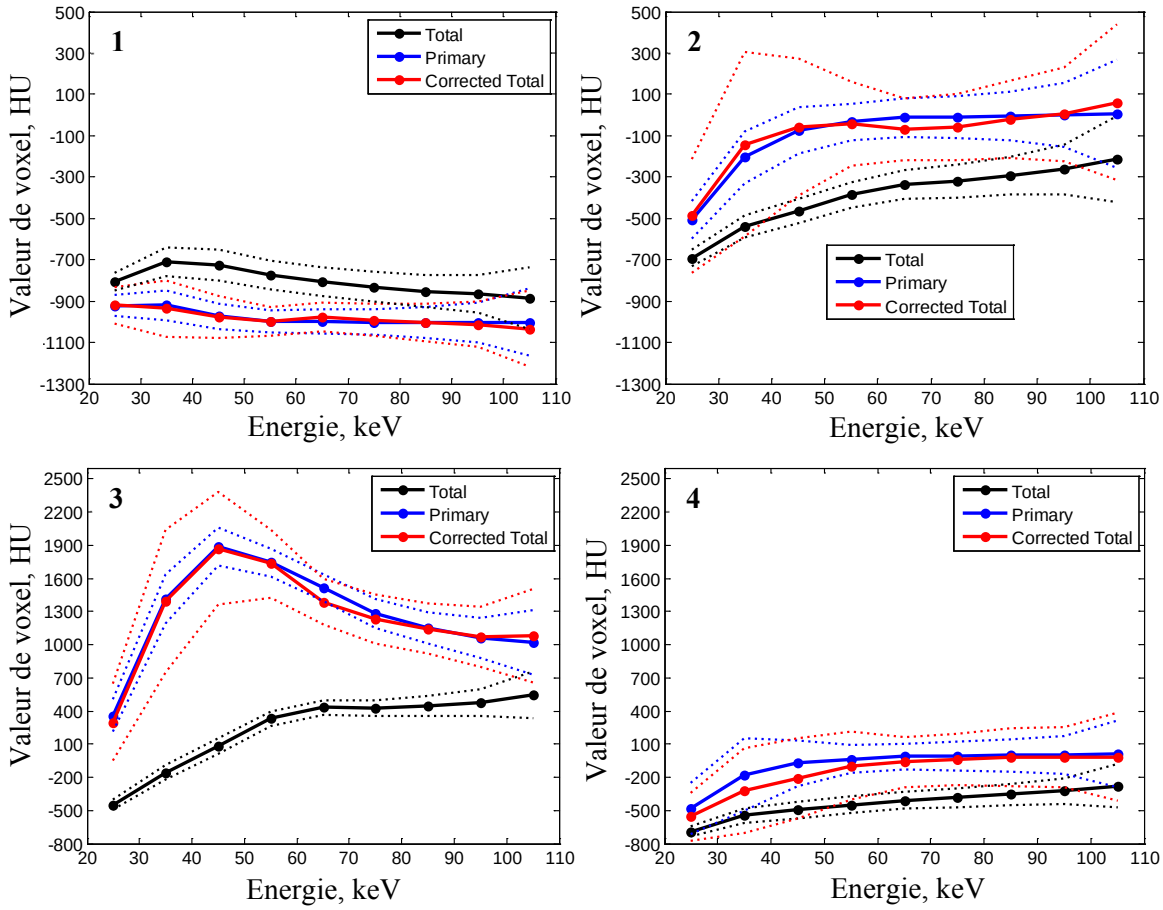

Fig. 24. Courbes HU du total, du primaire et du total corrigé calculées à partir des VOIs spécifiées dans Fig. 22. Les lignes solides et pointillées indiquent les valeurs moyennes et les STDs autour de la moyenne, respectivement. Les valeurs du STD correspondantes à des courbes du total corrigé et du primaire sont, dans la plupart des cas, supérieures à celles des courbes du total.

Afin de calculer les valeurs de voxel en fonction d'énergie la formule classique pour la conversion en HU peut être utilisée par canal d'énergie E :

$$V_{HU}(\mathbf{v},E)=\frac{V(\mathbf{v},E)-\mu_{water}(E)}{\mu_{water}(E)}\times 1000\,, \tag{18}$$

où $\mathbf{v}=(x,y,z)$ est un voxel, $V(\mathbf{v},E)$ et $V_{HU}(\mathbf{v},E)$ sont les valeurs initial (en cm^{-1}) et converti (en HU), respectivement, du voxel reconstruit. La quantité $\mu_{water}(E)$ correspond à la valeur du coefficient d'atténuation de l'eau par canal d'énergie E.

L'écart type $\sigma(E)$ pour chaque VOI par canal d'énergie a été calculé en utilisant l'expression suivante :

$$\sigma(E)=\sqrt{(n_{VOI}-1)^{-1}\sum_{\mathbf{v}}\left(V_{HU}(\mathbf{v},E)-\overline{V}_{HU}(E)\right)^2}\,, \tag{19}$$

où $\overline{V}_{HU}(E)$ est la valeur moyenne de voxel dans un VOI et canal d'énergie E donnés et n_{VOI} est le nombre de voxel constituant la VOI.

L'information VOI est également indicative de la précision quantitative de PASSSA. Lorsqu'on compare l'image du total corrompu par le diffusé avec le primaire idéal, l'erreur HU moyenne sur l'énergie était de 296 HU, 173 HU, 1033 HU, 151 HU pour VOI #1, #2, #3 et #4, respectivement. La comparaison équivalente du volume du total corrigé avec le primaire donnée une erreur de 32 HU, 11 HU, 41 HU, 63 HU pour VOI #1, #2, #3 et #4, respectivement.

3.3. Validation expérimentale

Les simulations du Chapitre 3.2 ont montré un niveau impressionnant de performance de correction du diffusé par PASSSA. Dans le chapitre actuel, l'efficacité de l'approche proposée est aussi validée par des acquisitions radiographiques expérimentales.

Chapitre 3.3.1 souligne la géométrie, le fantôme et les paramètres du system utilisé dans les expériences. Ce chapitre est suivi par une présentation des résultats correspondants aux acquisitions radiographiques (Chapitre 3.3.2).

3.3.1. Description du system

Plusieurs projections radiographiques ont été faites en utilisant un prototype d'un system à rayons X (Fig. 25) afin d'évaluer expérimentalement la performance de PASSSA.

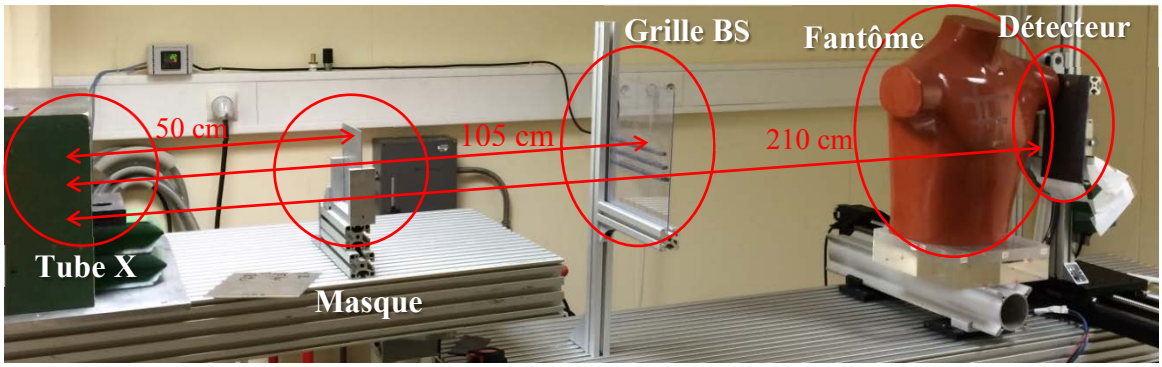

Fig. 25. Prototype du system à rayons X utilisé pour les expériences. L'écart d'air considéré entre l'objet et le détecteur était d'environ 8 cm. L'objet est dans la position latérale d'acquisition.

Les acquisitions ont été effectuées sur un fantôme anthropomorphique du thorax (RSD RS-111) affiché dans Fig. 26.

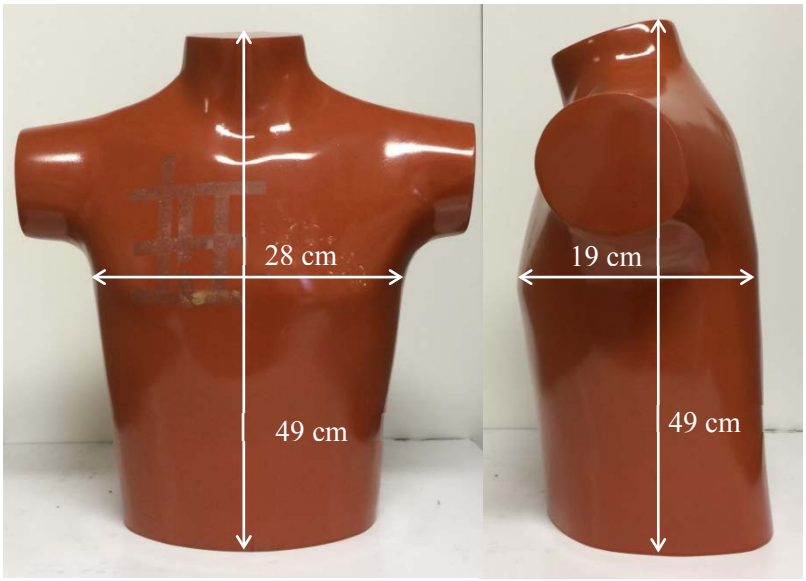

Fig. 26. Fantôme anthropomorphique du thorax.

Un tube à rayons X de tungstène (160 YXLON Y.TU-D06) avec un angle d'anode de 11° et une filtration de 2 mm d'aluminium a été mis sur 110 kV et 4 mAs. La sortie de tube (mAs) et la tension (kV) ont été choisies parmi la gamme des paramètres utilisés dans une étude d'optimisation de la radiographie thoracique numérique [92]. En outre, un détecteur CdTe MultiX® ME100 (128×1 pixels) résolu en énergie (37 canaux, ≈2.5 keV canal avec un seuil de ≈25 keV) avec un pas de 0.8 mm et une épaisseur de 3 mm a été utilisé. Le détecteur linéaire a été translaté horizontalement pour acquérir des images 2D de 128×451 pixels. Une collimation en plomb avec une ouverture de 2.5 cm était présente sur le détecteur. Des projections radiographiques antéropostérieure (AP) (0 °) et latérale (90 °) avec et sans le masque ont été prises. Le masque d'aluminium était composé d'une grille 11×21 de cylindres d'un diamètre et d'une hauteur de 2 mm placé sur une plaque de 2 mm (Fig. 27a). L'espacement entre les centres d'atténuateurs dans les deux directions était de 5 mm. Il est à noter que la plaque était responsable de 2 mm de filtration de tube et a été remplacé par une plaque équivalente (sans atténuateurs) pour les acquisitions sans-masque. En outre, une grille BS a été utilisé afin d'obtenir des images du rayonnement diffusé pour le calcul du rayonnement primaire de référence. La grille était composée de 3 bandes de plomb (0.5×20 cm) avec une épaisseur de 1 cm et un espacement inter-bande de 1.5 cm. Les bandes étaient supportées sur une plaque de PMMA d'une épaisseur de 1.5 mm. Pour les acquisitions sans la grille BS, la présence de la plaque de support a été compensée en ajoutant un filtre de PMMA de 1.5 mm sur le tube.

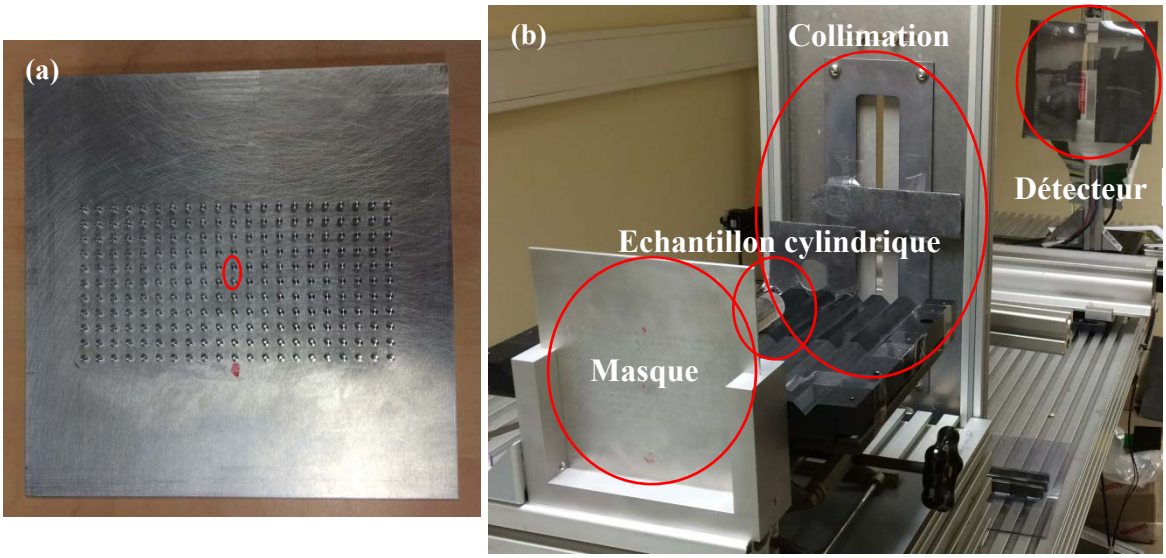

Fig. 27. Masque d'atténuateurs (a) et la géométrie d'estimation de la matrice de passage (b). Le segment du masque d'atténuateurs considéré pour l'estimation de la matrice de passage est marqué dans (a)

Afin d'estimer **M** préalablement aux acquisitions, un ensemble de données de calibrage a été établi (préliminaire aux acquisitions d'objet) en utilisant des cylindres de diamètre de 2 cm avec différentes hauteurs (épaisseur) fait de deux matériaux: PMMA et aluminium. La gamme d'épaisseur considérée était 0–16 cm (pas de 4 cm) et 0–3 cm (pas de 1 cm) pour PMMA et aluminium, respectivement. Le courant de tube a été réduit à 1 mAs dans les acquisitions de calibrage afin de réduire les effets d'empilement. En outre, pour réduire le bruit de photons, 20 réalisations de chaque acquisition d'échantillon ont été effectuées et moyennées. Afin de minimiser la contribution du diffusé, seulement un petit segment du masque a été considéré pour le calibrage (Fig. 27a) et une collimation externe supplémentaire (ouverture de 2×0.4 cm) a été incorporé entre les échantillons et le détecteur (Fig. 27b). Pixels avec des épaisseurs des atténuateurs similaires ont ensuite été regroupés afin de réduire l'influence du bruit de photons. Un total de 6 groupes d'épaisseur ont été considérés: 0.19–0.24 cm (pas de 0.01 cm). A l'aide de la procédure de minimisation simplex, le modèle paramétrique choisi (gaussienne-exponentielle) et la base de données générée une estimation de **M** a été obtenue pour chaque groupe de pixels d'ombre d'atténuateurs. Les pixels du segment du masque considérés étaient ensuite associés aux autres pixels d'ombre d'atténuateurs à travers l'épaisseur d'atténuateur. Grâce à cette procédure, les matrices estimées ont également été liés aux autres pixels d'ombre d'atténuateurs. Enfin une démonstration de segments de masque (images d'atténuation) utilisés pour le calibrage et l'imagerie est faite dans la Fig. 28.

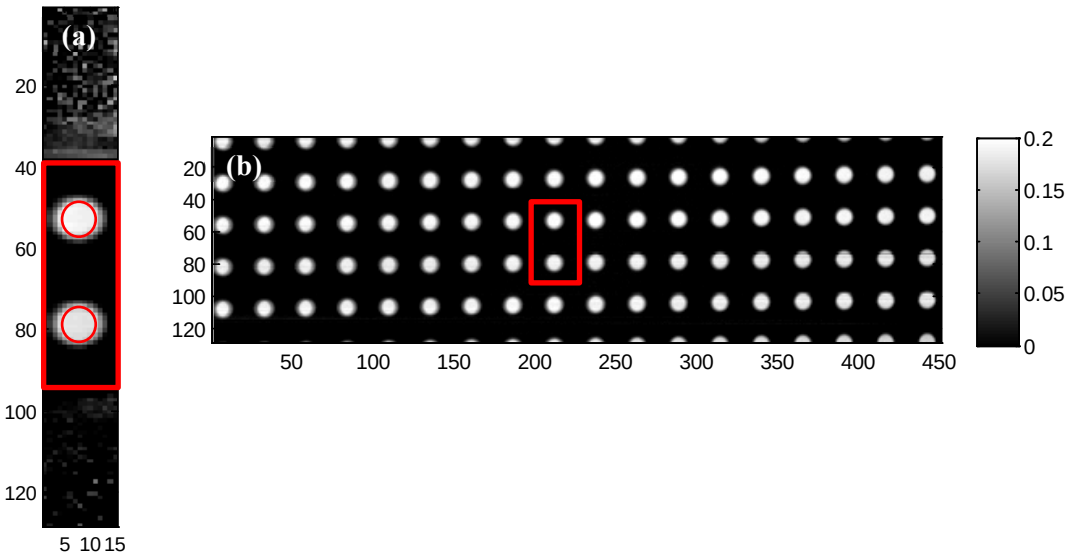

Fig. 28. Images d'atténuation (sans unité) des segments du masque d'atténuateurs obtenus avec la géométrie de calibrage (a) et d'imagerie (b). La localisation du segment (a) dans l'image (b) est aussi indiquée. Cercles dans (a) montre les zones utilisées pour l'estimation. Il est à noter que les bords de l'ombre ne sont pas utilisés afin d'exclure les parties souffrantes du flou de la tache focale.

3.3.2. Radiographie

Comme dans le Chapitre 3.2, l'évaluation de PASSSA a été divisée en qualitative et quantitative. Des projections radiographiques AP et latérale ont été examinées. Une comparaison a été faite entre les trois types d'images résolu d'énergie: du total (avec diffusé), du total corrigé de référence (total après application de l'approche BS) et total corrigé (total après application de PASSSA). Le SPR pour des projections AP et latérale était de 32,8%, et de 33,1%, respectivement.

Pour l'analyse qualitative, la performance spatiale de l'approche de séparation du diffusé développée a été analysée à travers des images d'atténuation et leurs profils correspondants. Les images d'atténuation ont été obtenues en appliquant (15) à chaque pixel d'image. Avec le remplacement du $N_T(\mathbf{p},E)$ dans (15) par les quantités correspondantes des acquisitions du total corrigé, les images d'atténuation du total corrigé avec BS et du total corrigé avec PASSSA ont également été obtenues. En outre, les spectres (total et total corrigé) à partir des lieus d'image caractéristiques ont également été analysés.

La NRMSE a été encore utilisée pour une analyse quantitative de PASSSA. La $NRMSE_T$ entre les images spectrales du total et du total corrigé de référence a été calculée avec (16) en remplacent $N_P(\mathbf{p},E)$ par la quantité respective des acquisitions du total de référence corrigé. De plus, $NRMSE_{PASSSA}$ a aussi été obtenue en remplacent $N_T(\mathbf{p},E)$ et $N_P(\mathbf{p},E)$ dans (16) par les quantités correspondantes des acquisitions du total corrigé de référence (approche BS) et du total corrigé (PASSSA).

Acquisition AP

Les images d'atténuation du total, du total corrigé de référence (méthode BS) et du total corrigé par PASSSA produite de leurs équivalents correspondants résolus en énergie sont présentées dans Fig. 29.

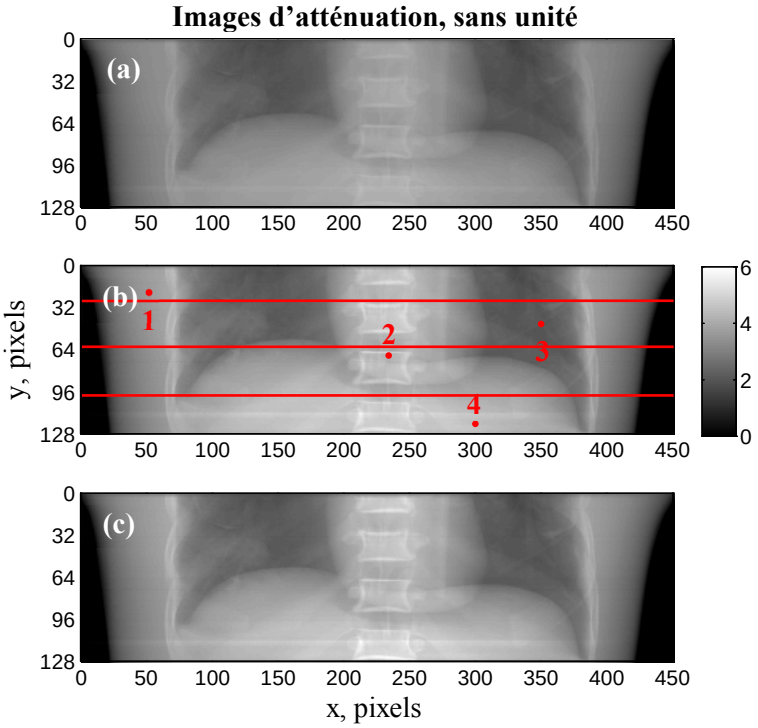

Fig. 29. Images d'atténuation du total (a), du total corrigé de référence (b) et du total corrigé (c) obtenue de leurs équivalents résolus en énergie pris pendant l'acquisition AP. La gamme d'énergie considérée était de 24–110 keV. La taille de pixel était de 0.8 mm. Les lieus pour les visualisations des profils (Fig. 30) et des spectres (Fig. 31) sont aussi indiqués sur l'image du total corrigé de référence (b). Ces lieus ont été choisis afin d'examiner des zones avec un niveau et une nature différents d'atténuation ainsi qu'un SPR variable. Il est aussi important de noter que le profil central (y=64) et pixels #2 et #4 sont dans la zone où le diffusé de référence a été mesuré par la grille BS.

De plus, pour chaque image d'atténuation, profils horizontaux sont tracés dans des lieus différents (Fig. 30).

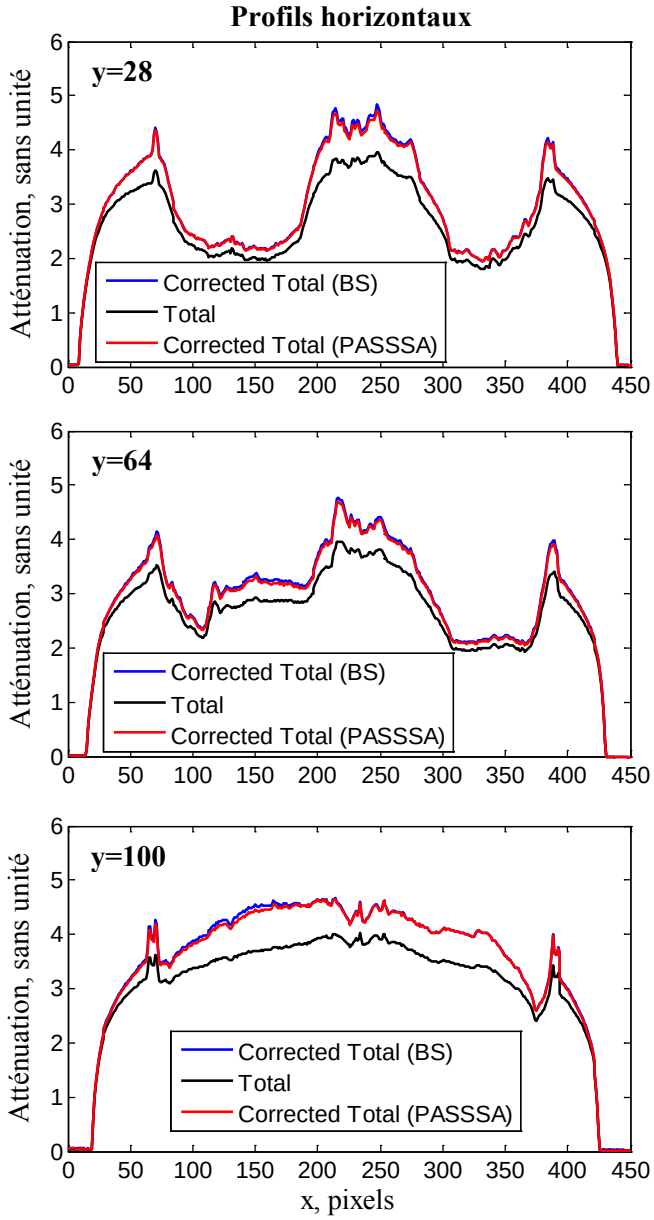

Fig. 30. Profils horizontaux (Acquisition AP) des images présentées dans Fig. 29. La taille de pixel était de 0.8 mm. Un profil (y=64) a été pris de la zone où le diffusé de référence a été mesuré directement par les bande de la grille BS. Il à noter que les profils totaux sont assez similaires aux profils du total corrigé (BS) de référence et du total corrigé (PASSSA) sur les côtés et dans les régions pulmonaires comme le SPR dans ces zones est plus faible que dans les régions où la colonne vertébrale et le diaphragme sont présents. Le SPR dans ces régions est plus élevée en raison du faible signal primaire dans cette région (niveau plus élevé d'atténuation).

Les spectres du total, du total corrigé par BS et du total corrigé par PASSSA des plusieurs points de contrôle (indiqué dans Fig. 29) sont présenté dans Fig. 31.

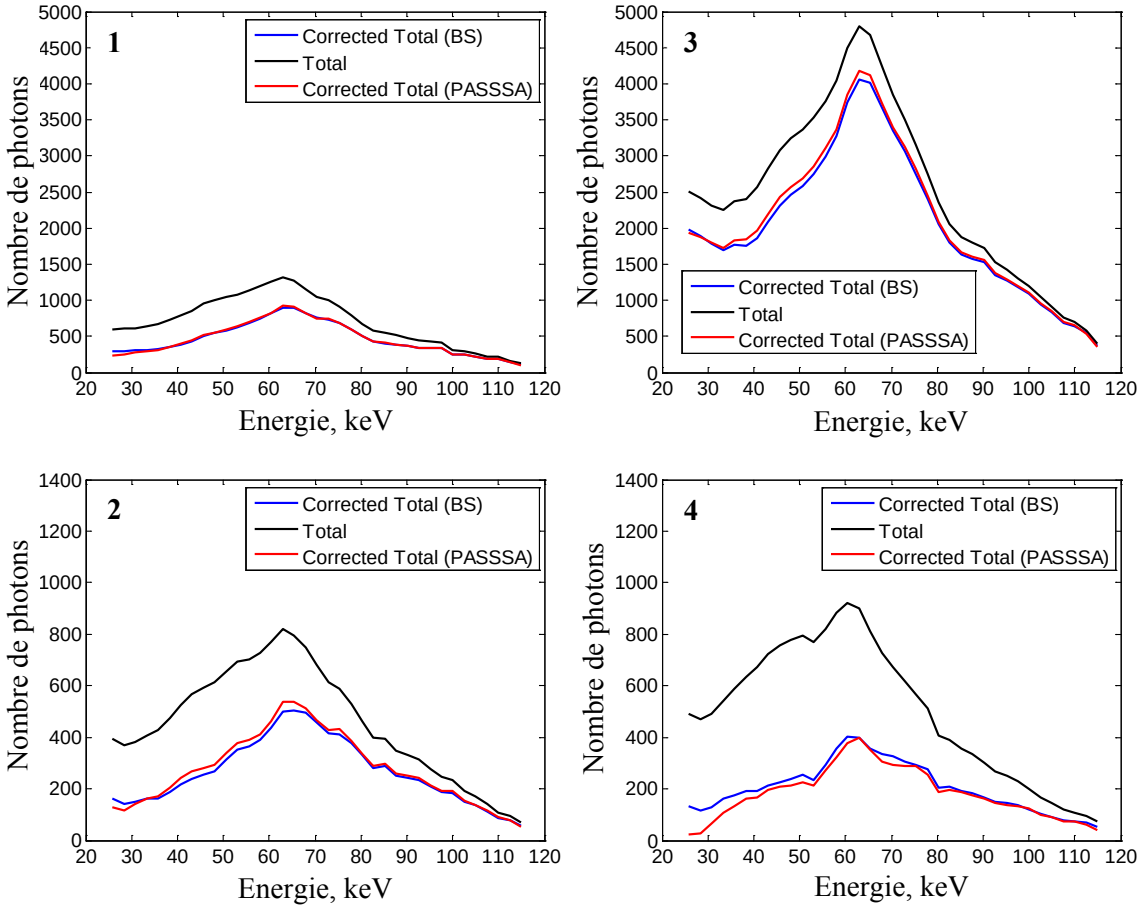

Fig. 31. Spectres du total, total corrigé de référence et du total corrigé (acquisition AP) pris des pixels indiqués sur la Fig. 29. Les spectres # 2 et # 4 sont pris à partir des zones d'image où les données du diffusé de référence ont été mesurées directement par la grille BS. Les deux autres spectres (#1 et #3) sont pris à partir des zones où ces données ont été estimées spatialement. Les formes du spectre total corrigé varient légèrement entre les différents lieux d'échantillonnage à l'exception du #3. Ceci est dû à l'atténuation beaucoup plus faible dans cette partie de l'image (poumon) par rapport à d'autres régions. En outre, notez que le SPR est assez élevé pour #4 en raison du niveau élevé d'atténuation présente dans cette région (grande quantité de tissus mous).

Finalement, une analyse quantitative des images résolues en énergie correspondantes à la projection radiographique AP a donné une $NRMSE_T$ et une $NRMSE_{PASSSA}$ de 45.2% et de 4.5%, respectivement.

Acquisition latérale

Comme pour l'acquisition AP, les images d'atténuation du total, du total corrigé de référence (méthode BS) et du total corrigé par PASSSA produite de leurs équivalents correspondants résolus en énergie sont présentées dans Fig. 32.

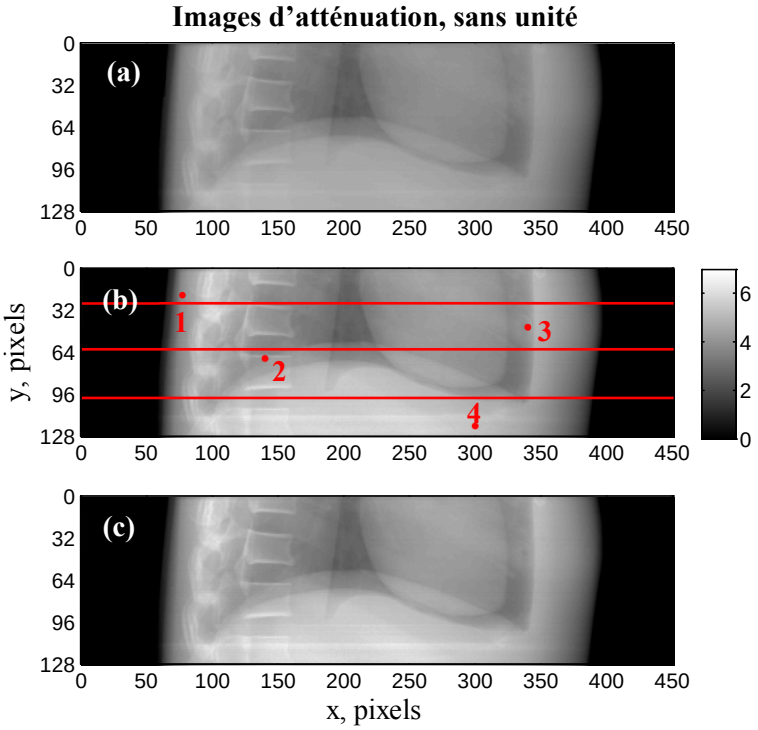

Fig. 32. Images d'atténuation du total (a), du total corrigé de référence (b) et du total corrigé (c) obtenue de leurs équivalents résolus en énergie pris pendant l'acquisition latérale. La gamme d'énergie considérée était de 24–110 keV. La taille de pixel était de 0.8 mm. Les lieus pour les visualisations des profils (Fig. 30) et des spectres (Fig. 31) sont aussi indiqués sur l'image du total corrigé de référence (b). Ces lieus ont été choisis afin d'examiner des zones avec un niveau et une nature différents d'atténuation ainsi qu'un SPR variable. Il est aussi important de noter que le profil central (y=64) et pixels #2 et #4 sont dans la zone où le diffusé de référence a été mesuré par la grille BS.

De plus, pour chaque image d'atténuation, profils horizontaux sont tracés dans des lieus différents (Fig. 33).

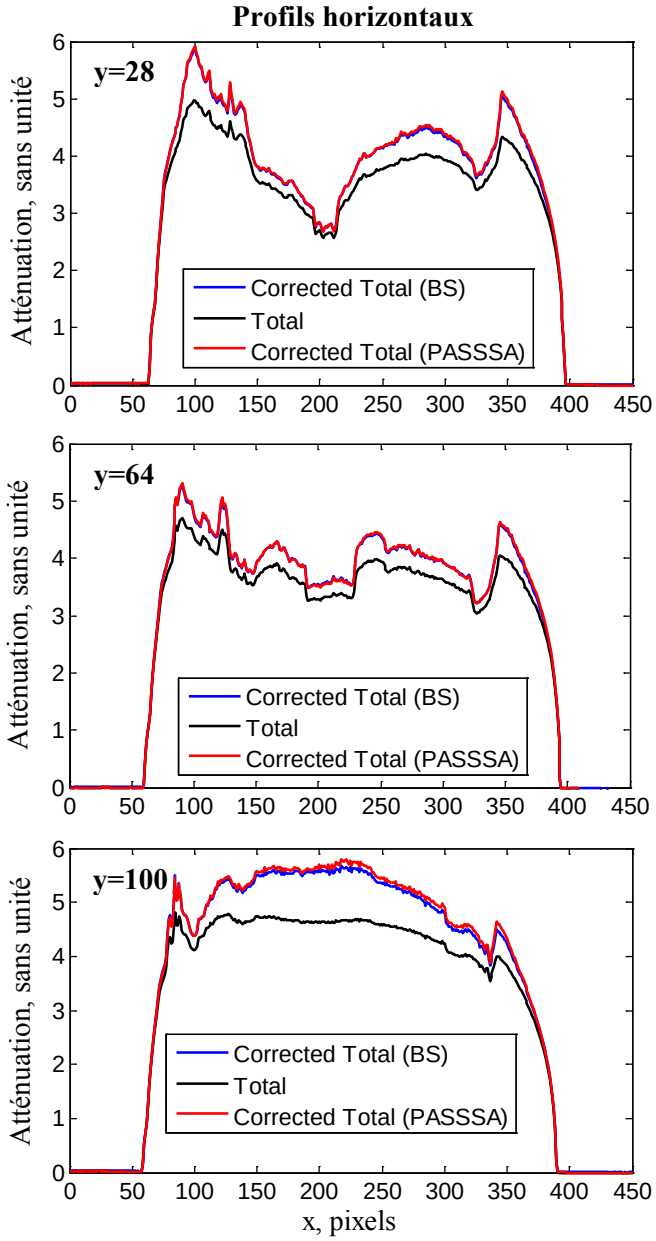

Fig. 33. Profils horizontaux (Acquisition AP) des images présentées dans Fig. 32. La taille de pixel était de 0.8 mm. Un profil (y=64) a été pris de la zone où le diffusé de référence a été mesuré directement par les bande de la grille BS. Il à noter que les profils totaux sont assez similaires aux profils du total corrigé (BS) de référence et du total corrigé (PASSSA) sur les côtés le SPR dans ces zones est plus faible que dans les régions où la colonne vertébrale et le diaphragme sont présents. Le SPR dans ces régions est plus élevée en raison du faible signal primaire dans cette région (niveau plus élevé d'atténuation).

Les spectres du total, du total corrigé par BS et du total corrigé par PASSSA des plusieurs points de contrôle (indiqué dans Fig. 32) sont présenté dans Fig. 34.

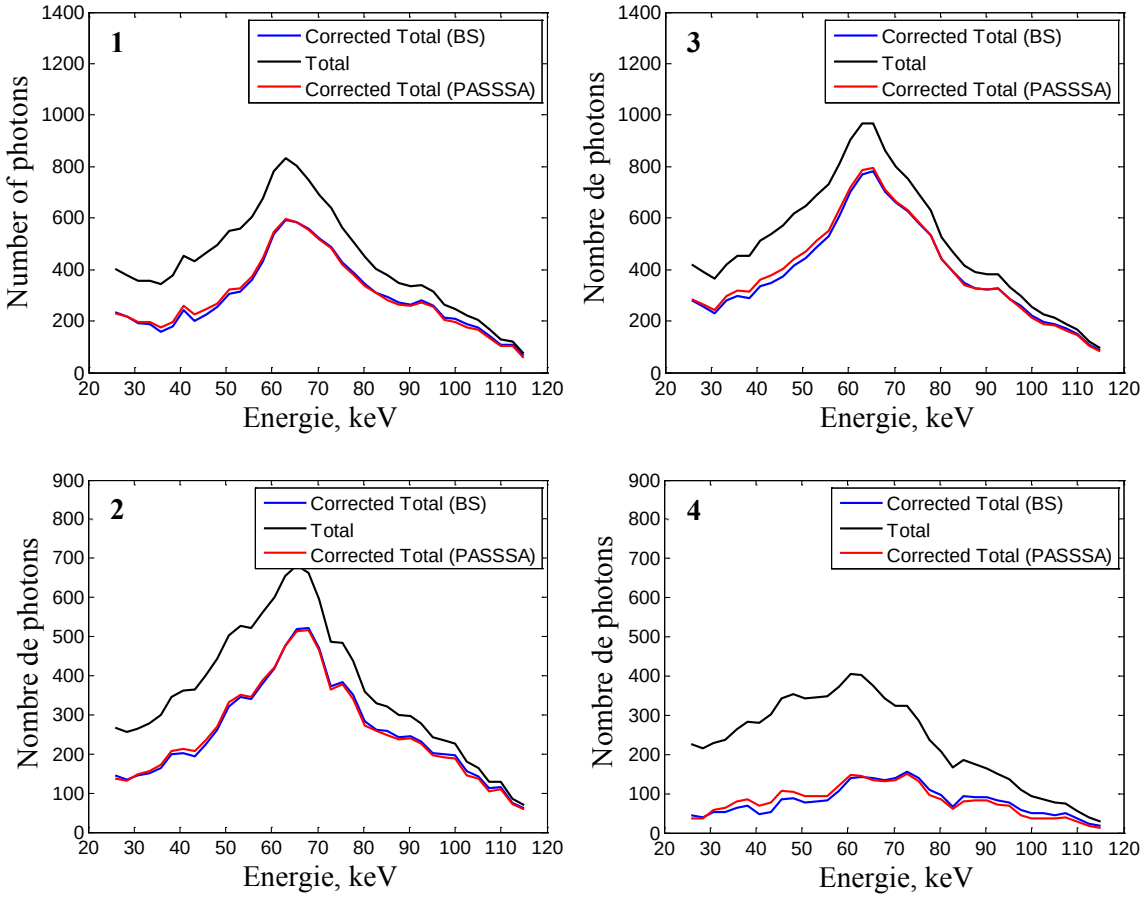

Fig. 34. Spectres du total, total corrigé de référence et du total corrigé (acquisition AP) pris des pixels indiqués sur la Fig. 29. Les spectres # 2 et # 4 sont pris à partir des zones d'image où les données du diffusé de référence ont été mesurées directement par la grille BS. Les deux autres spectres (#1 et #3) sont pris à partir des zones où ces données ont été estimées spatialement. Les formes du spectre total corrigé varient légèrement entre les différents lieux d'échantillonnage à l'exception du #4. Ceci est dû à l'atténuation beaucoup plus grande dans cette partie de l'image (diaphragme) par rapport à d'autres régions. En outre, notez que le SPR est assez élevé pour #4 en raison du niveau élevé d'atténuation présente dans cette région (grande quantité de tissus mous).

Finalement, une analyse quantitative des images résolues en énergie correspondantes à la projection radiographique AP a donné une $NRMSE_T$ et une $NRMSE_{PASSSA}$ de 44.9% et de 5.2%, respectivement.

3.4. Discussion

3.4.1. Simulations

PASSSA montre un niveau de performance impressionnant dans un cadre radiographique (Chapitre 3.2.2). L'observation des images d'atténuation de la Fig. 18 révèle l'effet du rayonnement diffusé. Lorsqu'on compare l'image totale (a) avec l'image primaire idéale

(b), la perte de contraste et la diminution de la détectabilité des frontières des structures internes sont clairement visibles. Le biais induit par le rayonnement diffusé peut être remarqué lorsqu'on affiche les profils horizontaux centraux respectifs à la Fig. 19. La comparaison des profils totaux primaires montre clairement une sous-estimation de l'atténuation due à la présence d'un rayonnement diffusé. Tous ces effets sont réduits à un degré important par l'application de PASSSA. L'image d'atténuation totale corrigée (Fig. 18c) est presque identique à l'image d'atténuation primaire (Fig. 18a). Des profils correspondants de la Fig. 19 montrent une tendance similaire avec une exception dans la zone centrale (vertèbre), où une légère sous-estimation pour le profil corrigé par PASSSA est observée par rapport au profil du primaire. En outre, l'augmentation du bruit dans cette région est également visible.

Une analyse plus approfondie de la performance de la méthode proposée dans le domaine de l'énergie révèle un niveau élevé de la restauration du primaire (Fig. 20). Les spectres du total corrigé ressemblent beaucoup les spectres du primaire, même dans les cas extrêmes où le SPR est très élevé (spectre #2). La précision de restauration du primaire à l'aide de PASSSA est en outre confirmée en observant $NRMSE_{PASSSA}$. L'analyse des $NRMSE_T$ et $NRMSE_{PASSSA}$ indique que le total corrigé par PASSSA est substantiellement plus proche du primaire de référence que le total corrompu par le diffusé.

Les niveaux du bruit relatif observés dans les images totales variaient dans la gamme d'environ un ordre de grandeur pour les différents pixels et projections. Ce n'était pas inattendu, car des fortes variations dans le nombre de photons enregistrés apparaissent en raison de différences substantielles dans l'atténuation. D'un premier coup d'œil à la Fig. 21, les performances PASSSA ($NRMSE_{PASSSA}$) suivent la même tendance que l'erreur induite par le diffusé ($NRMSE_T$) et le bruit des données d'entrée ($r(\mathbf{p})$ moyenné par projection du total) pour les projections diverses. Cependant, si $NRMSE_T$ et $NRMSE_{PASSSA}$ sont quantitativement comparées, la réduction d'erreur pour des projections avec un bruit élevé (environ #0 et #180) et un faible bruit (environ #90 et #270) est d'environ 3.7 et 4.6, respectivement. Pour toutes les projections, en moyenne, $NRMSE_{PASSSA}$ est 4.3 fois inférieure à $NRMSE_T$. Ceci implique qu'il existe une certaine dépendance des performances du procédé en fonction du niveau de bruit. Néanmoins, le changement de précision de PASSSA n'est pas aussi important que le changement du niveau de bruit, qui présente une dynamique beaucoup plus grande entre les différentes projections: environ 9 fois plus élevé dans les projections #0 et #180 que dans les projections #90 et #270.

En mode tomographique d'acquisition (Chapitre 3.2.3), le procédé de séparation du diffusé développé montre également des résultats remarquables. Fig. 22 montre que la tranche du volume corrigé (c) est presque sans des artéfacts induits par le diffusé visibles dans la tranche du volume total (b) et est visuellement proche de la tranche du volume du primaire (a). Les profils horizontaux centraux de la Fig. 23 confirment cet accord. Cependant, lorsqu'on compare les profils du total et du total corrigé une augmentation du bruit dans le dernier est visible.

L'inspection des courbes HU moyennes dans plusieurs VOIs caractéristiques (Fig. 24) révèle un niveau élevé d'accord entre les volumes obtenus à partir des projections corrigées par PASSSA les volumes primaires. Une augmentation du bruit dans l'ancien est à nouveau observée comme les STDs associés sont plus élevés par rapport à ceux qui ont été calculés pour les courbes HU du total et du primaire. Néanmoins, l'augmentation globale de la précision de la valeur HU est importante lorsqu'on compare les erreurs entre le primaire et le total par rapport et le primaire et le total corrigé. La diminution des erreurs des

valeurs HU en moyenne par énergie était plus de 10 fois à l'exception du VOI #4. Ce niveau moins impressionnant de la performance dans cette région est cohérente avec les résidus d'artefact du trait encore visibles dans cette zone à la Fig. 22c.

PASSSA montre une performance impressionnante pour les deux simulations : radiographiques et tomographiques. Les différences observées entre le primaire idéal et les images et les volumes du total corrigés peuvent être attribués aux plusieurs facteurs: le bruit dans les images et les volumes corrigés, erreurs locale dans l'estimation spatiale du diffusé, diffusé résiduel présent dans le signal de différence, erreur de récupération du primaire par la matrice de passage.

Comme PASSSA est un procédé de correction du diffusé basé sur une soustraction de l'estimation du diffusé, il est intrinsèquement enclin à l'augmentation du bruit comme les autres méthodes de ce type (par exemple BS, BH, modulation primaire, les méthodes MC). Etant donné qu'une partie du signal total mesuré est soustrait, tandis que le bruit associé reste, l'image corrigée obtient un ratio signal sur bruit (SNR) plus faible par rapport à l'image primaire. La diminution du SNR des images de projection se propage dans les volumes reconstruits en TDM contribuant à des artéfacts du trait. L'augmentation du bruit pourrait être résolue par l'application d'une méthode de post-traitement (technique de débruitage), soit sur des projections ou des volumes TDM. Pour le cas de TDM des algorithmes statistiques régularisés de reconstruction pourraient également être appliquées.

Des erreurs dans l'estimation spatiale du diffusé peuvent être liées au niveau élevé de bruit présent dans les données initiales parcimonieuses. Ceci est dû aux opérations de soustraction et la multiplication matricielle présentes dans le procédé (e. g. (13)). Il est à noter, en outre, que l'augmentation du bruit n'est pas isotrope en énergie comme la diagonale de la matrice de passage n'est pas constante et la matrice n'est pas complètement diagonale. Cela pourrait être incorporé dans l'estimation spatiale pour améliorer les performances.

Même si négligeable, le diffusé résiduel est toujours présente dans le signal de différence et est incorporé dans le primaire récupéré par l'application de la matrice de passage. Cela peut contribuer à des erreurs dans la prochaine étape de la méthode lorsque le primaire restauré est soustrait du total.

Un avantage important de la matrice de transition est sa capacité à apprendre les imperfections du détecteur en termes de réponse grâce à un protocole du calibrage. Cela donne une plus grande souplesse du modèle et donne la possibilité d'effectuer une estimation sur une base par pixel, ce qui est important puisque le DRM d'un détecteur spectrométrique donné peut dépendre du pixel.

Un autre point important qui mérite d'être discuté est le masque d'atténuateurs. Afin de respecter les contraintes quantitatives décrites dans le Chapitre 3.1, des matériaux et des motifs autres que ceux qui sont utilisés dans ce travail pourraient être choisis. En fait, un quelconque matériau avec un coefficient d'atténuation lisse en énergie (cuivre, fer, etc.) et suffisamment fort pour la fabrication de petits éléments à l'échelle nécessaire peut être utilisé. Dans le cas de matériaux présentant des k-edge forts dans leurs coefficients d'atténuation (par exemple l'argent, l'or, le tungstène, etc.), la qualité de la récupération du primaire par (12) se dégradera comme la **M** correspondante serait plus difficile à paramétrer. Cela pourrait, peut-être, résolu en adaptant le modèle paramétrique de **M**. En termes de motifs, des motifs réguliers ou irréguliers avec une fréquence spatiale plus élevée peuvent être envisagés pour améliorer l'échantillonnage de la distribution du diffusé et améliorer aussi la performance globale de correction du diffusé par PASSSA. De plus, la forme

des atténuateurs peut être absolument arbitraire s'ils restent suffisamment grands pour les détecter.

3.4.2. Experiences

A partir d'une analyse visuelle des images différentes d'atténuation (Fig. 29 et Fig. 32), l'effet du rayonnement diffusé devient apparent. Pour toutes les deux acquisitions (AP et latérale) la comparaison des images du total avec les images du primaire de référence (correction par BS) et les images du primaire estimé (correction PASSSA) indique un contraste local insuffisant et une diminution de la détectabilité du contour de la vertèbre et du cœur. Le biais induit par le diffusé peut être aussi remarqué par l'analyse des profils horizontaux centraux respectifs présentés dans la Fig. 30 et la Fig. 33. La sous-estimation de l'atténuation due à la présence du rayonnement diffusé apparaît clairement lorsqu'on compare les profils du primaire et du total. Elle est également plus forte pour les profils tracés dans la partie basse de l'image (y=100) comme le SPR local est plus élevé dans cette partie de l'image due à l'augmentation d'atténuation.

Les images d'atténuation produites des images résolues en énergie corrigées par BS (Fig. 29b et Fig. 32b) et PASSSA (Fig. 29c et Fig. 32c) peuvent être considérées comme presque identique pour les acquisitions AP et latérale. En outre, une amélioration du contraste et de la visibilité des structures critiques (par exemple les vertèbres et le cœur) est obtenue. Des profils horizontaux correspondant de la Fig. 30 et Fig. 33 confirment encore cet accord. Il est également intéressant de noter que le plus d'écart entre les profils de corrigée par BS et corrigé par PASSSA peut être observé pour le profil y=100 (en particulier pour l'acquisition latérale Fig. 32). Ceci peut à nouveau être lié à l'augmentation du SPR local dans cette région.

L'analyse de la performance de l'approche de séparation du diffusé proposée dans le domaine de l'énergie révèle un degré élevé d'accord entre les spectres du primaire obtenu par BS et par PASSSA. Sur les Fig. 31 et Fig. 34, ce qui correspond aux spectres de l'acquisition AP et de l'acquisition latérale, respectivement, on peut voir que les spectres du primaire estimé ressemblent aux spectres du primaire de référence dans tous les cas. Un écart légèrement plus élevé entre et les spectres BS et les spectres PASSSA peut être visible pour le spectre #4 dans le cas AP (Fig. 31) et le cas latéral (Fig. 34). Il est à noter que le spectre #4 représente le cas du SPR le plus élevé parmi les spectres examinés.

La précision de la récupération du primaire par l'application de PASSSA est encore validée par la $NRMSE_{PASSSA}$. Une réduction d'erreur induite par le diffusé d'un facteur d'environ 10 peut être observé lorsqu'on compare $NRMSE_T$ et $NRMSE_{PASSSA}$. Les performances atteintes sont presque égale pour le cas AP et le cas latéral. Il est à noter également que (basé sur la NRMSE) l'erreur induite par le diffusé a été réduite à environ 5% pour tous les projections, ce qui est comparable à ce qui a déjà été observé précédemment dans les simulations (Chapitre 3.2).

PASSSA montre une bonne performance en termes d'estimation du primaire pour les deux projections radiographiques considérées. Les résultats sont cohérents avec ce qui a été précédemment observé dans les simulations (Chapitre 3.2). Les différences entre les images du total corrigées par BS et PASSSA peuvent être attribués aux plusieurs facteurs: erreurs de modèle de PASSSA, erreurs d'estimation de la matrice de passage, erreurs d'estimation BS, bruit dans les images.

Les erreurs de modèle pour la méthode proposée incluent des erreurs de modèle de la matrice de passage, l'hypothèse d'absence du diffusé résiduel dans le signal de différence

et l'interpolation spatiale. Chacun de ces facteurs a déjà été discuté en détail dans le chapitre 3.4.1.

Bien qu'elle ait été acquise en utilisant plusieurs réalisations et un regroupement de pixels, la matrice de passage peut encore présenter des erreurs comme la base de données du calibrage n'était pas complètement sans bruit. De plus, malgré de la collimation ajoutée, le diffusé résiduel peut encore être présente à la fois de l'environnement et du détecteur. En outre, le fait d'estimer des matrices de passage pour un segment de masque avec une association avec les autres pixels d'image influencés par le masque peut également introduire des inexactitudes. Finalement, le fait d'acquérir une image 2D à travers une translation d'un détecteur linéaire peut également contribuer aux erreurs d'estimation de la matrice de passage.

Comme il est assez difficile d'acquérir une image idéale du primaire (sans diffusé) d'un objet de grande taille avec la configuration du prototype actuel, un primaire de référence est obtenue par l'estimation BS. Malgré le fait que cette technique est considérée comme l'étalon des méthodes de correction du diffusé, le primaire obtenu est toujours une estimation et intègre donc un certain degré d'erreur en raison de la procédure d'estimation. La procédure d'estimation BS comprend un certain nombre de sources d'erreur, correction du gain, échantillonnage suffisant, et l'interpolation spatiale à partir des échantillons. Cela signifie que les différences observées entre les primaires estimés par PASSSA et les primaires estimés par BS peuvent également être en partie due à la méthode d'estimation des images primaires de référence (méthode BS).

Enfin, comme BS et PASSSA sont des techniques de correction de type soustraction du diffusé, une augmentation du bruit peut être anticipée. L'enlèvement d'une partie du signal total, tout en laissant le bruit associée fournie une diminution du SNR pour les images corrigées correspondantes. Cet aspect peut également contribuer aux différences observées entre les images BS et les images PASSSA.

4. Conclusion et perspectives

Le principal objectif de la thèse était de développer une méthode de correction du rayonnement diffusé adapté pour l'imagerie multi-énergies. Malheureusement, comme les détecteur résolus en énergie sont une technologie relativement récente, il y a eu très peu d'études sur le comportement du rayonnement diffusé dans le domaine de l'énergie, ainsi que son influence sur les applications à rayons X multi-énergies. En outre, un procédé de correction du diffusé dédié aux données résolues en énergie n'a pas encore été proposée.

Dans le contexte de l'absence d'une analyse du diffusé dans le domaine de l'énergie, un objectif secondaire a été formulé. Il a été choisi de développer un outil de simulation sur la base du logiciel existant Sindbad (conçu au laboratoire de LDET), qui serait capable de fournir une simulation du diffusé résolu en énergie dans un délai raisonnable. Dans le Chapitre 2, Sindbad-SFFD, un outil satisfaisant ce critère a été introduit et validé par simulations GATE et des expériences. Les résultats ont montré que Sinbad-SFFD produit des simulations qui sont très compatibles avec ceux fournis par GATE et les données expérimentales. En outre, l'outil était suffisamment rapide, fournissant des images résolues en énergie dans environ 1.5 h sur un processeur seul processeur. Les développements futurs se focaliseront sur l'accélération globale dédiée-TDM en utilisant le parallélisation et le sous-

échantillonnage angulaire, respectivement. En outre, les artéfacts de point liés aux interactions Rayleigh et l'optimisation du nombre de photons seront également étudiés.

L'évaluation de PASSSA en simulation (Chapitre 3.2) a fournie des résultats remarquables pour les projections radiographiques et des volumes TDM en termes de réduction de l'effet du diffusé. Les images d'atténuation et les tranches TDM obtenues à partir des données corrigées résolues en énergie ont montrées une augmentation substantielle du contraste local et la détectabilité des structures internes. Un degré élevé de réduction du biais a également été atteint. En outre, les spectres de rayons X obtenu après correction ont été très proches de leurs homologues sans diffusé. Par rapport à l'erreur moyenne initiale de 23% entre les projections non corrigées et les projections sans diffusé, l'application de PASSSA a réduit cette valeur à environ 5%. En outre, prenant compte de l'analyse du bruit dans les différentes projections, la méthode est considérée stable pour les niveaux de bruit variables. Enfin, en termes de précision de la valeur de voxel, une augmentation d'un facteur >10 a été observé pour la plupart des VOIs inspectées, lorsqu'on compare les volumes du total corrigé et non corrigés.

Les expériences radiographiques réalisées avec un fantôme anthropomorphique du thorax ont encore prouvé l'efficacité de l'approche de séparation du diffusé développée (Chapitre 3.3). En termes d'images d'atténuation, les données résolues en énergie corrigées par PASSSA ont donné lieu à des images comparables à celles obtenues avec la correction BS. La même chose était vraie pour les spectres correspondants. En outre, l'amélioration sur les images générées à partir des données non corrigées en termes de contraste et du biais était aussi évidente. Quantitativement, la méthode développée a prouvé d'être en accord avec les données corrigées par BS (dans la limite de 5%). L'application de PASSSA a réduit l'erreur moyenne initiale entre les images résolues en énergie corrompu par le diffusé et corrigé par BS par un facteur d'environ 9.

La méthode développée dans le cadre de cette thèse ouvre la porte à d'autres méthodes de correction du diffusé exploitant des informations multi-énergies. Tout d'abord, une approche ne nécessitant pas une acquisition supplémentaire est beaucoup plus attractive pour l'imagerie médicale à rayons X en raison des considérations du temps d'acquisition et de la dose. L'adaptation de PASSSA à une telle configuration sera donc la priorité principale pour les travaux futurs. En outre, dans le cas TDM, il serait avantageux d'utiliser la redondance des données TDM grâce à des conditions de consistance et potentiellement coupler la méthode de correction du diffusé avec une approche de reconstruction de données de projection. Ces développements ouvriront la deuxième orientation des travaux futurs. Enfin, il est important de noter que comme PASSSA corrige le diffusé en utilisant une estimation de la distribution respective, des données de mesure supplémentaires (diffusé) sont disponibles. Il serait intéressant d'explorer la possibilité d'utiliser les données du diffusé résolues en énergie pour améliorer les performances des applications d'imagerie à rayons X.

LIST OF SCIENTIFIC CONTRIBUTIONS

Publications

A. Sossin, J. Tabary, V. Rebuffel, J. M. Létang, N. Freud, and L. Verger, "*Fast scattering simulation tool for multi-energy x-ray imaging*," Nuclear Instruments and Methods in Physics Research Section A, vol. 802, pp. 60–66, 2015

A. Sossin, J. Tabary, V. Rebuffel, J. M. Létang, N. Freud, and L. Verger, "*A novel scatter separation method for multi-energy x-ray imaging*," Physics in Medicine and Biology, vol. 61, no. 12, pp. 60–66, 2016

A. Sossin, J. Tabary, V. Rebuffel, J. M. Létang, N. Freud, and L. Verger, "*Experimental validation of a multi-energy x-ray adapted scatter separation method*," submitted to Physics in Medicine and Biology, 2016

Conference proceedings

A. Sossin, V. Rebuffel, J. Tabary, J. M. Létang, N. Freud, and L. Verger, "*Influence of Scattering on Material Quantification Using Multi-Energy X-ray Imaging*," in IEEE NSS/MIC, 2014

A. Sossin, V. Rebuffel, J. Tabary, J. M. Létang, N. Freud, and L. Verger, "*Fast scattering simulation tool for multi-energy x-ray imaging*," in IEEE NSS/MIC, 2014

Patents

A. Sossin, V. Rebuffel, J. Tabary, "*Procédé de correction d'un spectre*," submitted in 2015

Conferences

Poster at the 2014 IEEE Nuclear Science Symposium and Medical Imaging Conference. A. Sossin, V. Rebuffel, J. Tabary, J. M. Létang, N. Freud, and L. Verger. *Influence of Scattering on Material Quantification Using Multi-Energy X-ray Imaging.*

Poster at the 2014 IEEE Nuclear Science Symposium and Medical Imaging Conference. A. Sossin, V. Rebuffel, J. Tabary, J. M. Létang, N. Freud, and L. Verger. *Fast scattering simulation tool for multi-energy x-ray imaging.*

Poster at the 2016 Congrés National d'Imagerie du Vivant. A. Sossin, V. Rebuffel, J. Tabary, J. M. Létang, N. Freud, and L. Verger. *A novel scatter correction method for multi-energy x-ray imaging.*

Poster at the 2016 SPIE Medical Imaging Conference. A. Sossin, V. Rebuffel, J. Tabary, J. M. Létang, N. Freud, and L. Verger. *A novel scatter correction method for multi-energy x-ray imaging.*

Presentation at the 2016 IEEE Nuclear Science Symposium and Medical Imaging Conference. A. Sossin, V. Rebuffel, J. Tabary, J. M. Létang, N. Freud, and L. Verger. *Improving basis material decomposition in the presence of x-ray scatter with the aid of a Partial Attenuation Spectral Scatter Separation Approach (PASSSA).*

REFERENCES

[1] J. T. Bushberg, J. A. Siebert, E. M. Jr. Leidholdt, and J.M. Boone, The essential physics of medical imaging. 2nd edition. Philadelphia 2002, Lippincott Williams & Wilkins. 933 p.

[2] L. Lança and A. Silva, Digital Imaging Systems for Plain Radiography. New York 2013, Springer-Verlag. 115 p.

[3] G. Dougherty, Digital image processing for medical applications. New York 2009, Cambridge University Press. 462 p.

[4] J. P. Schlomka, E. Roessl, R. Dorscheid, S. Dill, G. Martens, T. Istel, C. Bäumer, C. Herrmann, R. Steadman, G. Zeitler, A. Livne, and R. Proksa, "Experimental feasibility of multi-energy photon-counting K-edge imaging in pre-clinical computed tomography," Physics in Medicine and Biology, vol. 53, no. 15, pp. 4031–4047, 2008.

[5] R. Ballabriga, M. Campbell, E. Heijne, X. Llopart, L. Tlustos, and W. Wong, "Medipix3: A 64k pixel detector readout chip working in single photon counting mode with improved spectrometric performance," Nuclear Instruments and Methods in Physics Research Section A, vol. 633, pp. S15–S18, 2011.

[6] A. Vincenzi, P. L. de Ruvo, P. Delogu, R. Bellazzini, A. Brez, M. Minuti, M. Pinchera, and G. Spandre, "Energy characterization of Pixirad-1 photon counting detector system," Journal of Instrumentation, vol. 10, no. 4, p. C04010–C04010, 2015.

[7] A. Brambilla, P. Ouvrier-Buffet, J. Rinkel, G. Gonon, C. Boudou, and L. Verger, "CdTe Linear Pixel X-Ray Detector With Enhanced Spectrometric Performance for High Flux X-Ray Imaging," IEEE Transactions on Nuclear Science, vol. 59, no. 4, pp. 1552–1558, 2012.

[8] A. Brambilla, P. Ouvrier-Buffet, G. Gonon, J. Rinkel, V. Moulin, C. Boudou, and L. Verger, "Fast CdTe and CdZnTe Semiconductor Detector Arrays for Spectroscopic X-Ray Imaging," IEEE Transactions on Nuclear Science, vol. 60, no. 1, pp. 408–415, 2013.

[9] P. M. Shikhaliev, "Computed tomography with energy-resolved detection: a feasibility study," Physics in Medicine and Biology, vol. 53, no. 5, pp. 1475–1495, 2008.

[10] S. Faby, S. Kuchenbecker, D. Simons, H.-P. Schlemmer, M. Lell, and M. Kachelrieß, "CT calibration and dose minimization in image-based material decomposition with energy-selective detectors," in Proceeding of SPIE, 2014, vol. 9033.

[11] K. C. Zimmerman and T. G. Schmidt, "Experimental comparison of empirical material decomposition methods for spectral CT," Physics in Medicine and Biology, vol. 60, no. 8, pp. 3175–3191, 2015.

[12] J. H. Siewerdsen and D. A. Jaffray, "Cone-beam computed tomography with a flat-panel imager: Magnitude and effects of x-ray scatter," Medical Physics, vol. 28, no. 2, pp. 220–231, 2001.

[13] A. Sisniega, W. Zbijewski, A. Badal, I. S. Kyprianou, J. W. Stayman, J. J. Vaquero, and J. H. Siewerdsen, "Monte Carlo study of the effects of system geometry and antiscatter grids on cone-beam CT scatter distributions," Medical Physics, vol. 40, no. 5, p. 051915, 2013.

[14] J. Wiegert, K. J. Engel, and C. Herrmann, "Impact of scattered radiation on spectral CT," in Proceeding of SPIE, 2009, vol. 7258.

[15] T. G. Schmidt, "CT energy weighting in the presence of scatter and limited energy resolution," Medical Physics, vol. 37, no. 3, pp. 1056–1067, 2010.

[16] A. M. T. Opie, A. P. H. Butler, and P. J. Bones, "Energy-resolved Compton scatter estimation for micro-CT," in Proceeding of SPIE, 2012, vol. 8506.

[17] E.-P. Rührnschopf and K. Klingenbeck, "A general framework and review of scatter correction methods in x-ray cone-beam computerized tomography. Part 1: Scatter compensation approaches," Medical Physics, vol. 38, no. 7, pp. 4296–4311, 2011.

[18] J. H. Siewerdsen, D. J. Moseley, B. Bakhtiar, S. Richard, and D. A. Jaffray, "The influence of antiscatter grids on soft-tissue detectability in cone-beam computed tomography with flat-panel detectors," Medical Physics, vol. 31, no. 12, pp. 3506–3520, 2004.

[19] J. Persliden and G. A. Carlsson, "Scatter rejection by air gaps in diagnostic radiology. Calculations using a Monte Carlo collision density method and consideration of molecular interference in coherent scattering," Physics in Medicine and Biology, vol. 42, no. 1, pp. 155–175, 1997.

[20] C.-J. Lai, L. Chen, H. Zhang, X. Liu, Y. Zhong, Y. Shen, T. Han, S. Ge, Y. Yi, T. Wang, W. T. Yang, G. J. Whitman, and C. C. Shaw, "Reduction in x-ray scatter and radiation dose for volume-of-interest (VOI) cone-beam breast CT–a phantom study," Physics in Medicine and Biology, vol. 54, no. 21, pp. 6691–6709, 2009.

[21] G. Jarry, S. A. Graham, D. J. Moseley, D. J. Jaffray, J. H. Siewerdsen, and F. Verhaegen, "Characterization of scattered radiation in kV CBCT images using Monte Carlo simulations," Medical Physics, vol. 33, no. 11, p. 4320–4329, 2006.

[22] G. Poludniowski, P. M. Evans, V. N. Hansen, and S. Webb, "An efficient Monte Carlo-based algorithm for scatter correction in keV cone-beam CT," Physics in Medicine and Biology, vol. 54, no. 12, p. 3847–3864, 2009.

[23] G. J. Bootsma, F. Verhaegen, and D. A. Jaffray, "Efficient scatter distribution estimation and correction in CBCT using concurrent Monte Carlo fitting," Medical Physics, vol. 42, no. 1, pp. 54–68, 2015.

[24] J. Rinkel, L. Gerfault, F. Estève, and J.-M. Dinten, "A new method for x-ray scatter correction: first assessment on a cone-beam CT experimental setup," Physics in Medicine and Biology, vol. 52, no. 15, pp. 4633–4652, 2007.

[25] J. S. Maltz, B. Gangadharan, S. Bose, D. H. Hristov, B. A. Faddegon, A. Paidi, and A. R. Bani-Hashemi, "Algorithm for X-ray Scatter, Beam-Hardening, and Beam Profile Correction in Diagnostic (Kilovoltage) and Treatment (Megavoltage) Cone Beam CT," IEEE Transactions on Medical Imaging, vol. 27, no. 12, pp. 1791–1810, 2008.

[26] M. Sun and J. M. Star-Lack, "Improved scatter correction using adaptive scatter kernel superposition," Physics in Medicine and Biology, vol. 55, no. 22, pp. 6695–6720, 2010.

[27] R. Ning, X. Tang, and D. Conover, "X-ray scatter correction algorithm for cone beam CT imaging," Medical Physics, vol. 31, no. 5, p. 1195–1202, 2004.

[28] A. Peterzol, J. M. Létang, and D. Babot, "A beam stop based correction procedure for high spatial frequency scatter in industrial cone-beam X-ray CT," Nuclear Instruments and Methods in Physics Research Section B: Beam Interactions with Materials and Atoms, vol. 266, no. 18, pp. 4042–4054, 2008.

[29] H. Yan, X. Mou, S. Tang, Q. Xu, and M. Zankl, "Projection correlation based view interpolation for cone beam CT: primary fluence restoration in scatter measurement with a moving beam stop array," Physics in Medicine and Biology, vol. 55, no. 21, pp. 6353–6375, 2010.

[30] Y. Zhou, T. Mathur, and S. Molloi, "Scatter and veiling glare estimation based on sampled primary intensity," Medical Physics, vol. 26, no. 11, pp. 2301–2310, 1999.

[31] K. Yang, G. Burkett, and J. M. Boone, "A breast-specific, negligible-dose scatter correction technique for dedicated cone-beam breast CT: a physics-based approach to improve Hounsfield Unit accuracy," Physics in Medicine and Biology, vol. 59, no. 21, pp. 6487–6505, 2014.

[32] L. Zhu, N. R. Bennett, and R. Fahrig, "Scatter Correction Method for X-Ray CT Using Primary Modulation: Theory and Preliminary Results," IEEE Transactions on Medical Imaging, vol. 25, no. 12, pp. 1573–1587, 2006.

[33] K. Schorner, M. Goldammer, K. Stierstorfer, J. Stephan, and P. Boni, "Scatter Correction Method by Temporal Primary Modulation in X-Ray CT," IEEE Transactions on Nuclear Science, vol. 59, no. 6, pp. 3278–3285, 2012.

[34] L. Ritschl, R. Fahrig, M. Knaup, J. Maier, and M. Kachelrieß, "Robust primary modulation-based scatter estimation for cone-beam CT," Medical Physics, vol. 42, no. 1, pp. 469–478, 2015.

[35] J. H. Siewerdsen, M. J. Daly, B. Bakhtiar, D. J. Moseley, S. Richard, H. Keller, and D. A. Jaffray, "A simple, direct method for x-ray scatter estimation and correction in digital radiography and cone-beam CT," Medical Physics, vol. 33, no. 1, pp. 187–197, 2006.

[36] T. Niu, M. Sun, J. Star-Lack, H. Gao, Q. Fan, and L. Zhu, "Shading correction for on-board cone-beam CT in radiation therapy using planning MDCT images," Medical Physics, vol. 37, no. 10, pp. 5395–5406, 2010.

[37] E. Meyer, C. Maas, M. Baer, R. Raupach, B. Schmidt, and M. Kachelries, "Empirical scatter correction (ESC): A new CT scatter correction method and its application to metal artifact reduction," in IEEE Nuclear Science Symposium Conference Record (NSS/MIC), 2010, pp. 2036–2041.

[38] J. Hsieh, Computed Tomography Principles, Design, Artifacts, and Recent Advances. 2nd edition. Bellingham 2009, SPIE Press. 510 p.

[39] D. R. Dance, S. Christophides, A. D. A. Maidment, I. D. McLean, and K. H. Ng, Diagnostic Radiology Physics: A Handbook for Teachers and Students. Vienna 2014, International Atomic Energy Agency. 682 p.

[40] R. Behling, Modern Diagnostic X-Ray Sources: Technology, Manufacturing, Reliability. Boca Raton 2015, CRC Press. 423 p.

[41] Q. Chen and G. A. Thouas, "Metallic implant biomaterials," Materials Science and Engineering R, vol. 87, pp. 1–57, 2015.

[42] J. H. Hubbell, Wm. J. Veigele, E. A. Briggs, R. T. Brown, D. T. Cromer, and R. J. Howerton, "Atomic form factors, incoherent scattering functions, and photon scattering cross sections," Journal of Physical and Chemical Reference Data, vol. 4, no. 3, pp. 471–538, 1975.

[43] D. E. Peplow and K. Verghese, "Measured molecular coherent scattering form factors of animal tissues, plastics and human breast tissue," Physics in Medicine and Biology, vol. 43, no. 9, pp. 2431–2452, 1998.

[44] M. Persson, B. Huber, S. Karlsson, X. Liu, H. Chen, C. Xu, M. Yveborg, H. Bornefalk, and M. Danielsson, "Energy-resolved CT imaging with a photon-counting silicon-strip detector," Physics in Medicine and Biology, vol. 59, no. 22, pp. 6709–6727, 2014.

[45] J. Cammin, J. Xu, W. C. Barber, J. S. Iwanczyk, N. E. Hartsough, and K. Taguchi, "A cascaded model of spectral distortions due to spectral response effects and pulse pileup effects in a photon-counting x-ray detector for CT," Medical Physics, vol. 41, no. 4, p. 041905, 2014.

[46] T. G. Schmidt, "An empirical method for correcting the detector spectral response in energy-resolved CT," in Proceeding of SPIE, 2012, vol. 8313.

[47] V. Rebuffel, J. Tabary, P. Hugonnard, E. Popa, A. Brambilla, G. Montemont, and L. Verger, "New functionalities of SINDBAD simulation software for spectral X-ray imaging using counting detectors with energy discrimination," in IEEE Nuclear Science Symposium and Medical Imaging Conference (NSS/MIC), 2012, pp. 2550–2554.

[48] S. Yun, H. K. Kim, H. Youn, J. Tanguay, and I. A. Cunningham, "Analytic Model of Energy-Absorption Response Functions in Compound X-ray Detector Materials," IEEE Transactions on Medical Imaging, vol. 32, no. 10, pp. 1819–1828, Oct. 2013.

[49] L. A. Lehmann, R. E. Alvarez, A. Macovski, W. R. Brody, N.J. Pelc, S.J. Rieder, and A.L. Hall, "Generalized image combinations in dual KVP digital radiography," Medical Physics, vol. 8, no. 5, pp. 649–667, 1981.

[50] B. Brendel, E. Roessl, J.-P. Schlomka, and R. Proksa, "Empirical projection-based basis-component decomposition method," in Proceedings of SPIE, 2009, vol. 7258.

[51] K. C. Zimmerman and T. G. Schmidt, "Experimental comparison of empirical material decomposition methods for spectral CT," Physics in Medicine and Biology, vol. 60, no. 8, pp. 3175–3191, 2015.

[52] L. A. Feldkamp, L. C. Davis, and J.W. Kress, "Practical cone-beam algorithm," Journal of the Optical Society of America A, vol. 1, no. 6, pp. 612–619, 1984.

[53] J. Jan, Medical image processing, reconstruction and restoration: concepts and methods. Boca Raton 2006, CRC Press. 730 p.

[54] B. J. Heismann, J. Leppert, and K. Stierstorfer, "Density and atomic number measurements with spectral x-ray attenuation method," Journal of Applied Physics, vol. 94, no. 3, pp. 2073–2079, 2003.

[55] N. Freud, P. Duvauchelle, S. A. Pistrui-Maximean, J.-M. Létang, and D. Babot, "Deterministic simulation of first-order scattering in virtual X-ray imaging," Nuclear Instruments and Methods in Physics Research Section B: Beam Interactions with Materials and Atoms, vol. 222, no. 1–2, pp. 285–300, Jul. 2004.

[56] W. Yao and K. W. Leszczynski, "An analytical approach to estimating the first order x-ray scatter in heterogeneous medium," Medical Physics, vol. 36, no. 7, p. 3157–3167, 2009.

[57] G. J. Bootsma, F. Verhaegen, and D. A. Jaffray, "Spatial frequency spectrum of the x-ray scatter distribution in CBCT projections," Medical Physics, vol. 40, no. 11, p. 111901, 2013.

[58] D. J. Platten, "A Monte Carlo study of the energy spectra and transmission characteristics of scattered radiation from x-ray computed tomography," Journal of Radiological Protection, vol. 34, no. 2, pp. 445–456, 2014.

[59] F. E. Boas and D. Fleischmann. Computed tomography artifacts: Causes and reduction techniques. Imaging in Medicine, vol. 4, no. 2, pp. 229–240, 2012.

[60] A. Sossin, V. Rebuffel, J. Tabary, J. M. Létang, N. Freud, and L. Verger, "Influence of Scattering on Material Quantification Using Multi-Energy X-ray Imaging," in IEEE Nuclear Science Symposium and Medical Imaging Conference (NSS/MIC), 2014, pp. 1–5.

[61] E. B. Podgorsak. Radiation oncology physics: a handbook for teachers and students. Vienna 2005, International Atomic Energy Agency. 657 p.

[62] A. Glière, "Sindbad. From CAD model to synthetic radiographs," Review of Progress in QNDE, Vol. 17A, pp. 387–394, 1998.

[63] J. Tabary and A. Glière, "Coupling Photon Monte Carlo Simulation and CAD Software. Application to X-ray Nondestructive Evaluation," MONTE CARLO 2000, Lisbon, Portugal, 2000.

[64] A. Sossin, J. Tabary, V. Rebuffel, J. M. Létang, N. Freud, and L. Verger, "Fast scattering simulation tool for multi-energy x-ray imaging," Nuclear Instruments and Methods in Physics Research Section A, vol. 802, pp. 60–66, Dec. 2015.

[65] N. Freud, J.-M. Létang, and D. Babot, "A hybrid approach to Simulate X-ray imaging techniques, combining Monte Carlo and deterministic algorithms," IEEE Transactions on Nuclear Science, vol. 52, no. 5, pp. 1329–1334, 2005.

[66] E. Mainegra-Hing and I. Kawrakow, "Variance reduction techniques for fast Monte Carlo CBCT scatter correction calculations," Physics in Medicine and Biology, vol. 55, no. 16, pp. 4495–4507, 2010.

[67] A. Badal and A. Badano, "Accelerating Monte Carlo simulations of photon transport in a voxelized geometry using a massively parallel graphics processing unit," Medical Physics, vol. 36, no. 11, pp. 4878–4880, 2009.

[68] W. P. Segars, M. Mahesh, T. J. Beck, E. C. Frey, and B. M. W. Tsui, "Realistic CT simulation using the 4D XCAT phantom," Medical Physics, vol. 35, no. 8, pp. 3800–3808, 2008.

[69] J. Tabary, R. Guillemaud, F. Mathy, and P. Hugonnard, "Combination of high resolution analytically computed uncollided flux images with low resolution Monte Carlo computed scattered flux images," IEEE Transactions on Nuclear Science, vol. 51, no. 1, pp. 212–217, 2004.

[70] G. Montémont, M-C. Gentet, O. Monnet, J. Rustique and L. Verger, "Simulation and Design of Orthogonal Capacitive Strip CdZnTe Detectors," IEEE Transactions on Nuclear Science, vol. 54, no. 4, pp. 854–859, 2007.

[71] J. Sempau, E. Acosta, J. Baro, J. M. Fernandez-Varea, and F.Salvat, "An algorithm for Monte Carlo simulation of the coupled electron-photon transport," Nuclear Instruments and Methods in Physics Research Section B, vol. 132, no 3, pp. 377–390, 1997.

[72] S. Ramo, "Currents Induced by Electron Motion," in Proceeding of the IRE. vol. 27, no. 9, pp. 584–585, 1939.

[73] S. Jan, D. Benoit, E. Becheva E, T. Carlier, F. Cassol, P. Descourt, T. Frisson, L. Grevillot, L. Guigues, L. Maigne, C. Morel, Y. Perrot, N. Rehfeld, D. Sarrut, D.R. Schaart, S. Stute, U. Pietrzyk, D. Visvikis, N. Zahra, and I. Buvat, "GATE V6: a major enhancement of the GATE simulation platform enabling modelling of CT and radiotherapy," Physics in Medicine and Biology, vol. 56, no. 4, pp. 881–901, 2011.

[74] R. Birch and M. Marshall, "Computation of bremsstrahlung X-ray spectra and comparison with spectra measured with a Ge(Li) detector," Physics in Medicine and Biology, vol. 24, no. 3, pp. 505–517, 1979.

[75] N. Freud, J. M. Létang, and D. Babot, "A hybrid approach to simulate multiple photon scattering in X-ray imaging," Nuclear Instruments and Methods in Physics Research B, vol. 227 no. 4, pp. 551–558, 2005.

[76] N. Bhatia, D. Tisseur, F. Buyens, and J. M. Létang, "Scattering correction using continuously thickness-adapted kernels," NDT & E International, vol. 78, pp. 52–60, Mar. 2016.

[77] H. Lee, L. Xing, R. Lee, and B. P. Fahimian, "Scatter correction in cone-beam CT via a half beam blocker technique allowing simultaneous acquisition of scatter and image information," Medical Physics, vol. 39, no. 5, pp. 2386–2395, 2012.

[78] K. Schörner, M. Goldammer, and J. Stephan, "Comparison between beam-stop and beam-hole array scatter correction techniques for industrial X-ray cone-beam CT," Nuclear Instruments and Methods in Physics Research Section B: Beam Interactions with Materials and Atoms, vol. 269, no. 3, pp. 292–299, 2011.

[79] H. Gao, L. Zhu, and R. Fahrig, "Modulator design for x-ray scatter correction using primary modulation: Material selection," Medical Physics, vol. 37, no. 8, pp. 4029–4037, 2010.

[80] B. Meng, H. Lee, L. Xing, and B. P. Fahimian, "Single-scan patient-specific scatter correction in computed tomography using peripheral detection of scatter and compressed sensing scatter retrieval," Medical Physics, vol. 40, no. 1, p. 011907, 2013.

[81] T. Niu, A. Al-Basheer, and L. Zhu, "Quantitative cone-beam CT imaging in radiation therapy using planning CT as a prior: first patient studies," Medical physics, vol. 39, no. 4, pp. 1991–2000, 2012.

[82] Y.-K. Park, G. C. Sharp, J. Phillips, and B. A. Winey, "Proton dose calculation on scatter-corrected CBCT image: Feasibility study for adaptive proton therapy," Medical Physics, vol. 42, no. 8, pp. 4449–4459, Aug. 2015.

[83] B. Ohnesorge, T. Flohr, and K. Klingenbeck-Regn, "Efficient object scatter correction algorithm for third and fourth generation CT scanners," European Radiology, vol. 9, no. 3, pp. 563–569, 1999.

[84] D. Garcia, "Robust smoothing of gridded data in one and higher dimensions with missing values," Computational Statistics & Data Analysis, vol. 54, no. 4, pp. 1167–1178, 2010.

[85] M. J. Buckley, "Fast computation of a discretized thin-plate smoothing spline for image data," Biometrika, vol. 81, no. 2, pp. 247–258, 1994.

[86] S. N. Wood, "Modelling and smoothing parameter estimation with multiple quadratic penalties," Journal of the Royal Statistical Society: Series B, vol. 62, no. 2, pp. 413–428, 2000.

[87] D. Aydın, M. Memmedli, and R. E. Omay, "Smoothing parameter selection for nonparametric regression using smoothing spline," European Journal of Pure and Applied Mathematics, vol. 6, no. 2, pp. 222–238, 2013.

[88] M. Tepper and G. Sapiro, "Fast L1 smoothing splines with an application to Kinect depth data," in IEEE International Conference on Image Processing (ICIP), 2013, pp. 504–508.

[89] P. Hoskin and V. Goh, Radiotherapy in Practice – Imaging. Oxford 2010, Oxford University Press. 352 p.

[90] G. M. Lasio, B. R. Whiting, and J. F. Williamson, "Statistical reconstruction for x-ray computed tomography using energy-integrating detectors," Physics in Medicine and Biology, vol. 52, no. 22, pp. 47–66, 2007.

[91] J. A. Nelder and R. Mead, "A Simplex Method for Function Minimization," The Computer Journal, vol. 7, no. 4, pp. 308–313, 1965.

[92] Z. Sun, C. Lin, Y. Tyan, and K.-H. Ng, "Optimization of chest radiographic imaging parameters: a comparison of image quality and entrance skin dose for digital chest radiography systems," Clinical Imaging, vol. 36, no. 4, pp. 279–286, 2012.

[93] D. Tschumperlé and R. Deriche, "Anisotropic Diffusion Partial Differential Equations in Multi-Channel Image Processing: Framework and Applications," Advances in Imaging and Electron Physics (AIEP), vol. 145, pp. 145–209, 2007.

[94] P. Getreuer, “Total Variation Inpainting using Split Bregman,” Image Processing On Line, vol. 2, pp. 147–157, 2012.

[95] V. K. Alilou and F. Yaghmaee, “Application of GRNN neural network in non-texture image inpainting and restoration,” Pattern Recognition Letters, vol. 62, pp. 24–31, 2015.

[96] A. Greenblatt, S. Agaian, and K. Panetta, “Restoration of images damaged by semi-transparent water blotches using localized image enhancement,” in Proceedings of SPIE, 2008, vol. 6982.

[97] M. A. Elgharib, F. Pitié, and A. Kokaram, “Blotch and scratch removal in archived film using a semi-transparent corruption model and a ground-truth generation technique,” EURASIP Journal on Image and Video Processing, vol. 2013, no. 1, pp. 1–20, 2013.

[98] F. Stanco, L. Tenze, and G. Ramponi, “Virtual restoration of vintage photographic prints affected by foxing and water blotches,” Journal of Electronic Imaging, vol. 14, no. 4, 2005.

[99] R. Clackdoyle and L. Desbat, “Full data consistency conditions for cone-beam projections with sources on a plane,” Physics in Medicine and Biology, vol. 58, no. 23, pp. 8437–8456, 2013.

[100] C. Kim, M. Park, Y. Sung, J. Lee, J. Choi, and S. Cho, “Data consistency-driven scatter kernel optimization for x-ray cone-beam CT,” Physics in Medicine and Biology, vol. 60, no. 15, pp. 5971–5994, 2015.

FOLIO ADMINISTRATIF

THESE DE L'UNIVERSITE DE LYON OPEREE AU SEIN DE L'INSA LYON

NOM : SOSSIN
(avec précision du nom de jeune fille, le cas échéant)

DATE de SOUTENANCE : 20/10/2016

Prénoms : Artur

TITRE : Correction of scattered radiation in multi-energy radiography and tomography

NATURE : Doctorat

Numéro d'ordre : 2016LYSEI104

Ecole doctorale : Électronique, Électrotechnique et Automatique (EEA)

Spécialité : Traitement du Signal et de l'Image

RESUME : L'imagerie à rayons X couplée aux détecteurs résolus en énergie permet de différencier les matériaux présents et d'estimer leurs contributions respectives. Cependant, ces techniques nécessitent des images très précises. La présence du rayonnement diffusé conduit à une perte du contraste spatial et un biais dans l'imagerie radiographique ainsi que des artéfacts dans la tomodensitométrie (TDM). L'objectif principal de cette thèse était de développer une approche de correction du rayonnement diffusé adaptée à l'imagerie multi-énergies. Pour réaliser cette tâche, un objectif secondaire a été défini : la conception et la validation d'un outil de simulation capable de fournir des images du diffusé résolu en énergie dans un temps raisonnable. Une fois validé, cet outil a permis d'étudier le comportement du diffusé dans le domaine spatial et énergétique. Sur la base de cette analyse du diffusé, une approche originale dite « Partial Attenuation Spectral Scatter Separation Approach » (PASSSA) adaptée à l'imagerie multi-énergies a été développée. L'évaluation de PASSSA en mode radiographique par des simulations numériques et des mesures expérimentales a révélé des résultats remarquables en termes d'amélioration du contraste d'image et de la réduction du biais induit par la présence du diffusé. De plus, des études de simulation ont permis d'évaluer la performance de l'approche développée dans la TDM, où PASSSA s'est révélée d'être très efficace pour corriger les distorsions induites par le rayonnement diffusé. D'autre part, l'amélioration de la performance dans le contexte de la décomposition des matériaux de base en radiographie après avoir appliqué la méthode développée a également été analysée : l'application de PASSSA se traduit par une amélioration substantielle de l'estimation des épaisseurs des matériaux de base. Finalement, sur la base des différents résultats de validation obtenus, une analyse des développements potentiels a été menée.

MOTS-CLÉS : radiographie, tomographie, rayonnement diffusé, résolu en énergie, simulation, correction

Laboratoire (s) de recherche : LDET (CEA, Grenoble), CREATIS (INSA Lyon)

Directeur de thèse: Jean Michel Létang

Président de jury :

Composition du jury :

A. MOHAMMAD-DJAFARI, Directeur de Recherche (LSS-CNRS)
C. MOREL, Professeur (CPPM)
G. POLUDNIOWSKI, Chercheur (Univ. de Surrey)
V. REBUFFEL, Ingénieur Chercheur (CEA LETI)
J. M. LETANG, Maître de Conférences (INSA Lyon)